University of Sussex

Unravelling the influence of environment, redshift and confusion on the star formation in dusty galaxies

Steven Duivenvoorden

Submitted for the degree of Doctor of Philosophy

University of Sussex

June 2018

Declaration

Chapter two was published in Monthly Notices of the Royal Astronomical Society: HELP: star formation as a function of galaxy environment with *Herschel*, Duivenvoorden et al. 2016, Monthly Notices of the Royal Astronomical Society, Volume 462, Issue 1, p.277-289. I contributed to all aspects of this paper, with co-authors giving comments and advice on the science and the writing.

Chapter three was published in Monthly Notices of the Royal Astronomical Society: Red, redder, reddest: SCUBA-2 imaging of colour-selected *Herschel* sources, Duivenvoorden et al. 2018, Monthly Notices of the Royal Astronomical Society, Volume 477, Issue 1, p.1099-1119. I contributed to all aspects of this paper with the exception of the SMA data reduction (done by J. Greenslade) and the `INTERROGATOR` photometric redshift calculations (done by S. M. Wikins). The SCUBA-2 data was observed by J. M. Scudder and myself. All co-authors helped by giving comments and advice on the science and the writing.

Chapter four is sent for comments to a select group of potential co-authors: Have we seen all the galaxies that comprise the cosmic infrared background at $250\,\mu\text{m} \leq \lambda \leq 500\,\mu\text{m}$?, Duivenvoorden et al. in preparation. I contributed to all aspects of this paper, with other authors giving comments and advice on the science and the writing.

I hereby declare that this thesis has not been and will not be submitted in whole or in part to another University for the award of any other degree.

Signature:

Steven Duivenvoorden

UNIVERSITY OF SUSSEX

Steven Duivenvoorden, Doctor of Philosophy

Unravelling the influence of environment, redshift and confusion on the star formation in dusty galaxies

Summary

Over the last three decades, the far-infrared emission from distant galaxies has been revealed to us. This far-infrared light is emitted by dust clouds heated by UV radiation from young stars. This reveals to us some of the most remarkable and highly star-forming galaxies in the Universe. The *Herschel space observatory* was able to capture this light. With this thesis I have attempted to get a better understanding of the underlying galaxy population. I have done this by observing the most extreme forms of star formation in the early Universe seen in maps obtained by the SPIRE instrument and using prior information from deep high resolution surveys. In particular I have examined the dependencies of dusty galaxy properties on their environment.

I have confirmed that star formation is primarily dependent on both galaxy mass and whether a galaxy lies in the "blue cloud". Environment is the primary influence on the fraction of galaxies lying in the blue cloud and has a minor, but significant, affect on the average star formation rate of star forming galaxies. The highest redshift galaxies directly detected in the *Herschel* SPIRE maps are very rare, but due to the large area of the HerMES surveys we are able to find a statistical significant sample. With the addition of longer wavelength SCUBA-2 data I further confine the redshift of the dusty galaxies and find that the star formation rates of those sources are extremely high and exceed 1000 $M_\odot$ a year. The observed number counts of these extremely bright sources have been a problem for galaxy evolution models. I am able to explain the observed number count of red SPIRE sources by adding correlated confusion noise and Gaussian instrumental noise to simulated galaxy catalogues. My results emphasise that it is crucial to correct for noise and selection effects for comparison with simulations. I exploit a novel way of fitting the full SPIRE maps using prior information from deep high resolution surveys, obtained from wavelengths ranging from optical to radio. In doing so I obtain the most accurate values of the cosmic infrared background (CIB) at the SPIRE wavelengths. With these results we have a better indication of which sources are producing the CIB, and therefore the bulk of star formation. My results indicate that future large area surveys like LSST are likely to resolve a substantial fraction of the population responsible for the CIB at $250\,\mu\mathrm{m} \leq \lambda \leq 500\,\mu\mathrm{m}$.

Acknowledgements

Firstly and most importantly, a huge thanks goes to Seb Oliver for his supervision of this thesis. This project would not have been possible without his remarkable expertise and inspiring support.

Thanks go to each of the co-authors on my papers: M. Béthermin, V. Buat, S. C. Chapman, D. L. Clements, A. Cooray, K. E. K. Coppin, H. Dannerbauer, B. Darvish, G. De Zotti, J. S. Dunlop, S. A. Eales, A. Efstathiou, D. Farrah, J. E. Geach, J. Greenslade, M. Griffin, W. S. Holland, P. D. Hurley, E. Ibar, R. J. Ivison, M. Jarvis, G. Lagache, L. Marchetti, S. Oliver, A. Papadopoulos, G. Petitpas, D. A. Riechers, M. T. Sargent, D. Scott, J. M. Scudder, R. Shirley, M. Symeonidis, M. Vaccari, M. P. Viero, J. D. Vieira, L. Wang, J. Wardlow, S. M. Wilkins, M. Zemcov and G. De Zotti for their invaluable help and support.

Thanks also to the far-infrared research group, Charlotte, Ian, Jillian, Pete, Raphael, Seb and Yannick, for creating such a collegiate atmosphere, always ready to share their knowledge and give encouragement.

I would like to thank Ivo Labbé and Henk Hoekstra of Leiden University for setting me such interesting and motivating research projects during my BSc and MSc degrees. Elena Rossi and Marcello Cacciato provided fantastic supervision of my MSc thesis, which inspired me to pursue this PhD in Astrophysics.

Embarking on a PhD is a daunting and often stressful pursuit, yet one that I have enjoyed immensely. This is largely due to the friendship, fun and camaraderie I've found with fellow PhD students and office mates. My housemates Hannah and Panka have similarly lent support and cracked open cold beers at crucial moments.

Finally, deepest thanks go to my parents Inge and Jaap, brother Rutger and partner Caroline. They, alongside so many of my oldest friends and family, have helped to make this extraordinary time so happy and rewarding in ways personal as well as professional.

Official acknowledgements

This project has received funding from the European Unions Horizon 2020 research and innovation programme under grant agreement No. 607254; this thesis reflects only the authors view and the European Union is not responsible for any use that may be made of the information contained therein. Funding for this thesis was supported by the Science and Technology Facilities Council (grant number ST/M503836/1).

The James Clerk Maxwell Telescope is operated by the East Asian Observatory on behalf of The National Astronomical Observatory of Japan, Academia Sinica Institute of Astronomy and Astrophysics, the Korea Astronomy and Space Science Institute, the National Astronomical Observatories of China and the Chinese Academy of Sciences (Grant No. XDB09000000), with additional funding support from the Science and Technology Facilities Council of the United Kingdom and participating universities in the United Kingdom and Canada.

The Herschel spacecraft was designed, built, tested, and launched under a contract to ESA managed by the Herschel/Planck Project team by an industrial consortium under the overall responsibility of the prime contractor Thales Alenia Space (Cannes), and including Astrium (Friedrichshafen) responsible for the payload module and for system testing at spacecraft level, Thales Alenia Space (Turin) responsible for the service module, and Astrium (Toulouse) responsible for the telescope, with in excess of a hundred subcontractors

SPIRE has been developed by a consortium of institutes led by Cardiff University (UK) and including University of Lethbridge (Canada); NAOC (China); CEA, LAM (France); IFSI, University of Padua (Italy); IAC (Spain); Stockholm Observatory (Sweden); Imperial College London, RAL, UCL-MSSL, UKATC, University of Sussex (UK); and Caltech, JPL, NHSC, University of Colorado (USA). This development has been supported by national funding agencies CSA (Canada); NAOC (China); CEA, CNES, CNRS (France); ASI (Italy); MCINN (Spain); SNSB (Sweden); STFC, UKSA (UK); and NASA (USA).

Contents

List of Tables

List of Figures

Chapter 1

Introduction

1.1 The electromagnetic radiation from a distant galaxy

The origin and evolution of galaxies is one of the most interesting questions facing modern day astronomers. Different populations of galaxies have to be observed over various cosmic epochs in order to gather enough information to obtain a coherent theory about galaxy evolution. This information could, until recently, only be obtained by observations of electromagnetic radiation with telescopes. The recent observations of gravitational waves by the Laser Interferometer Gravitational-Wave Observatory (LIGO, e.g. Abbott et al. 2016, 2017) provides astronomers with a new way to observe the sky, though in this thesis we will focus on the light we receive from distant galaxies.

Galaxies emit electromagnetic radiation over a huge range of wavelengths, from the highly energetic gamma rays down to metres-long radio emission. The total light from every component within the galaxy contributes to the galaxy spectral energy distribution (SED). This SED describes how either the brightness or flux changes as a function of frequency from an astrophysical object. The SED is what we observe, and can be used to obtain physical parameters of the galaxy, like stellar mass, size, and star formation rate. In practice, however, we only observe a small part of this total SED which makes our information incomplete. To get a physical understanding of the underlying process in a galaxy, one has to understand how the SED is built up from the several components of a galaxy, and how incompleteness of the data affects estimates of the obtained physical parameters. In the following sections we will describe the different components within a galaxy and how they contribute to the total galaxy SED.

1.1.1 Stars

Stars are the most well known component of a galaxy. A star is only a star if it is bound by self-gravity and if it radiates energy from an internal source of nuclear fusion. Planets lack the second condition and emit a neglectable amount of radiation compared to stars. We therefore ignore planets in our explanation of the total radiation emitted by galaxies. The minimum mass needed for a star to ignite nuclear fusion is $\sim$ 4100 Earth masses. As stars radiate from an internal source it forces the star to evolve, which will eventual cause the star to violate its bounding by self gravity or to stop radiating from an internal source, leading to the death of the star. During the main part of the star's lifetime, the internal source of energy is the nuclear fusion of hydrogen, and when the core of the star runs out of hydrogen a complex sequence begins with the burning of heavier elements. The lifetime of a star depends mainly on its mass, where massive stars have shorter lives. Stars are typically located in stellar clusters within a galaxy which host roughly $\sim 10^5$ stars, where a complete galaxy typically hosts between 10^8 and 10^{14} stars.

Stars are classified according to their spectral absorption lines in 7 categories: O, B, A, F, G, K and M. The hottest stars (O and B) have very few absorption lines and produce ionizing photons. The contribution to the full galaxy SED from individual low mass (non-ionizing) stars within the galaxy is primary emitted at optical and near-infrared (NIR) wavelengths. The outer layer for these Sun-like stars could be crudely approximated by a blackbody with a peak temperature (T) around several thousand Kelvin. The peak at optical and NIR wavelengths for low mass stars can be explained given the peak temperature range of these stars and the given shape of the blackbody function:

$$B_\nu(\nu, T) = \frac{2h\nu^3}{c^2} \frac{1}{e^{\frac{h\nu}{k_B T}} - 1}. \tag{1.1}$$

However, the output from a star is more complex than this blackbody shape i.e. another peak for this cool stars lies at 1.6 μm due to a minimum in the H^- opacity (e.g. John, 1988). Low mass stars are long-lived and this information can be used to calculate the total stellar mass of a galaxy by assuming an Initial Mass Function (IMF). This function describes the distribution of initial masses for a newly born population of stars. When you assume a certain type of IMF, in combination with the lifetime of certain stars, one can calculate the evolution of stellar mass and calculate how the total stellar emission will appear over time. With this information, potentially only one wavelength has to be observed to determine the stellar mass, instead of a full SED. Commonly used IMF's are Salpeter (1955), Kroupa (2001) and Chabrier (2003). The different IMF's disagree on

the number of high-mass stars formed for every low-mass star. It is also not clear if a universal IMF exists or how exactly the IMF is different for galaxies formed in the early Universe. Obtaining a more accurate measure of the IMF is an important aim for future observations, such as those provided by the new space telescope, the James Web Space Telescope.

Due to their higher temperature, the more massive, shorter-lived stars emit a much larger part of their radiation in the ultra-violet (UV). Due to their short lifetime, this UV emission from massive stars can be used to trace the star formation of the whole galaxy (e.g. Kennicutt, 1998b). For newly formed stellar populations the total luminosity is dominated by the UV emission from young stars. The lifetime of these massive stars is of the order 10^6 year, consequently the UV emission probes the star formation over the same time scale. An SED of a galaxy therefore reflects a combination of the history of star formation and stellar evolution. The UV light from massive stars dominates the radiation output from nearly formed stellar clusters, but due to their short lifetime the light blueward of 1000 Å diminishes after 10^7 year where the light in the NIR increases due to evolution of massive stars into red giant stars. These red giant stars are a late phase for a stellar evolution of a 0.3-8 $M_\odot$ star where the outer atmosphere is inflated and drops in temperature, causing the red colour. After $\sim 10^9$ year the radiation output is dominated by these red giant stars.

Metals in the stellar atmosphere will absorb radiation on the blue-end of 4000 Å. This drop in the SED from the normal blackbody curve only appears if the stars have a high metal content. A higher metal content indicates that a star is of a later generation because these metals are only made and ejected in the interstellar medium by supernovae and stellar winds.

When a star with a mass > 9 $M_\odot$ dies it will form a Type II or Type Ib supernova (for a review about supernovae see Filippenko, 1997). A supernova is an extremely energetic burst which occurs when the core of a star collapses, causing the outer layers of the star to be exploded away. Supernovae are short-lived bursts (<100 days) but very energetic. The supernova itself is mainly visible in the UV and optical, even though most of the energy is radiated away in the form of neutrinos. The shock fronts of the remnants of this explosion cause synchrotron radiation in the X-ray and radio (for a review about supernovae remnants see Reynolds, 2008). This synchrotron radiation traces the recent star formation, as the stars which form supernovae are short lived. In particular, the radio emission from these remnants is often used to get an un-obscured estimate of the recent

star formation. Supernovae Ia result from a thermonuclear runaway of a white dwarf, and are primarily used as standard candles to calculate cosmological distances and not as a star formation tracer.

1.1.2 AGN

It is commonly accepted that a super massive black hole (SMBH) resides in the centre of every massive galaxy. The accretion of matter onto a SMBH releases roughly 10 per cent of the rest mass energy of the accreted matter, which is a factor of ten more efficient than the nuclear fusion occurring in stars. The energy output from this accretion is responsible for the majority of non-nuclear radiation we receive, except for the afterglow of the Big Bang, the Cosmic Microwave Background (CMB, Penzias and Wilson, 1965). Gas falling towards a SMBH and its accretion disc radiate over a large range in wavelengths, from radio up to X-ray and gamma radiation. The optical and UV radiation of these so called Active Galactic Nuclei (AGN) can show broad emission lines ($\Delta\lambda/\lambda \sim 0.3$) and can dominate the total SED of a galaxy. The width of the emission lines is caused by Doppler broadening due to the extremely high random velocities of the surrounding gas of the SMBH (for a review about AGN see Fabian, 2012).

The radiation from AGN can vary over time and the total energy output can differ by orders of magnitude for different galaxies, making it sometimes difficult to calculate the AGN contribution to the galaxy SED. This variation in time-scale tends to get smaller and increase in amplitude when observing at shorter wavelengths. The continuum emission (S_ν) over a large range in frequency (ν) can be described by a simple power law of the form:

$$S_\nu(\nu_0) \propto \nu^{-\alpha}, \tag{1.2}$$

Were α is the spectral index and normally ranges between 0 and 1. Many AGN emit thermal FIR emission from hot dust (Haas et al., 1998) on top of the non-thermal continuum emission.

The most powerful AGN are classified as quasars. They normally consist of an optical point source in the centre, which is accompanied by two bright radio jets. The optical emission comes from a small region around the SMBH, making the quasars look like a star in optical imaging. Radio loud AGN can dominate the radio emission from a galaxy, outshining the radio emission caused by supernova remnants. It is therefore difficult to estimate the star formation in a galaxy with an AGN when only using radio data.

There is a remarkable close correlation between the mass of the SMBH and the absolute magnitude or the velocity dispersion of the bulge of the host galaxy (Magorrian et al., 1998). This "Magorrian relation" shows that there is a strong co-evolution between galaxies and their SMBH.

1.1.3 The interstellar and intergalactic medium

The space between stars is not empty but filled with gas and dust particles. The space density of these dust and gas particles variate heavily for different locations within the galaxy. Interstellar dust mainly consists of irregular particles with sizes ranging from a few molecules up to 1.0 μm. This dust forms in cool atmospheres in the dying phase of low mass stars and in the gas ejected from supernovae. These particles grow in the interstellar medium when atoms and molecules, typically made of graphites and silicates, accrete together. The dust particles can be destroyed by high-energy radiation and from supernova shocks (Barlow and Silk, 1977). The lifetime of dust particles depend on supernova rates and the dust destruction efficiencies and is estimated to be around 5×10^8 year (Jones et al., 1994).

Cool clouds of dust and gas have a strong influence on the shape of a galaxy SED as they absorb and scatter the incoming energetic radiation. The cool, canonical dust ($T \sim 40$ K) within a galaxy significantly absorbs the UV light from massive stars. Due to this absorption the cloud warms up and starts to radiate black body radiation at temperatures of several tens of Kelvin. This dust radiation peaks at around 70-100 μm, and can dominate the radiation output from a galaxy with lots of ongoing star formation. Due to the absorption in the UV and optical, a correction factor needs to be applied to find the star formation rate (SFR) of a galaxy when using only UV data. This correction factor depends on the total dust content of the galaxy and the distribution of the dust, and is therefore largely unknown. Radio emission is free from dust extinction and does not need a correction factor to calculate the star formation in the absence of an AGN.

Hot dust ($T \sim 150$ K) traces compact star-forming regions, or the emission arising from a dusty torus around a SMBH accretion disk. The radiation from these hot clouds is emitted around at 20 μm, in the mid-infrared. This emission from star-forming regions contains radiation from heavier dust grain particles, most commonly the Polycyclic Aromatic Hydrocarbons (PAHs, Lagache et al., 2004). No PAHs features are found around AGN as energetic photons destroy the PAH grains. Dust at kpc scales nearby a SMBH can potentially be warmed by the AGN to similar temperatures to the canonical dust clouds

heated by bright stars. These AGN heated clouds can therefore leave a comparable signal to star formation, which can cause over-estimates of the SFRs in dusty galaxies with a very bright quasar ($L_{\mathrm{X(1-10keV)}} \gtrsim 10^{43.5}$, Symeonidis et al., 2016; Symeonidis, 2017).

Neutral gas around star-forming regions absorbs most radiation with wavelengths shorter than 912 Å. This Lyman limit arises from the energy an electron in the ground state of a hydrogen atom needs to escape and therefore more energetic radiation will cause an ionisation of the hydrogen atom. A large break in the observed galaxy SED is caused by this feature if the galaxy is very bright at wavelengths around 912 Å. This wavelength lies in the UV and as described in Section 1.1.1 this is primarily the case for galaxies with large amount of massive stars and therefore a high SFR. Vast numbers of galaxies have been found with this large break in the spectrum. The technique to find galaxies with such a break is called the Lyman-break technique and has been very successful in finding the most distant galaxies (e.g. Bouwens et al., 2004; Oesch et al., 2012). The Balmer break at 3646 Å can be used in a similar way, but is less strong and harder to observe from Earth due to the opaqueness of our atmosphere in the infrared.

As newly ionized cool gas recombines, it begins to radiate at specific wavelengths, which emerge from the energy radiated when an excited electron drops to a lower energy level. The ionisation of the gas mainly happens by stars more massive than 20 $M_{\odot}$ and therefore the recombination lines probe the star formation in the last $\sim 10^7$ year. The most commonly used Hydrogen lines to measure the star formation are Hα (transition from the third to the second energy level) and Lyman-α (transition from the second to the first energy level).

Especially Lyman-α can then still be absorbed by dust. Weaker lines such as Paschen-α can be used as the optical/UV lines are absorbed, but this line is too weak to detect in very distant galaxies. These newly formed HII regions also radiate in the radio due to free-free emission. This free-free emission is proportional to the production of Lyman continuum photons (e.g. Condon, 1992).

The space around galaxies is not empty, but consists of the intergalactic medium (IGM). This IGM contains the bulk of the matter in our Universe. The baryonic matter in the IGM chiefly consists of ionized hydrogen (HII) and can be described as a plasma with equal numbers of protons and electrons. Temperatures in the IGM are very high and are of order 10^6 K. For a review about the IGM see McQuinn (2016). Hydrogen is ionized in the current cosmic epoch, but was neutral before being heated by radiation from the first stars and AGN in the early Universe.

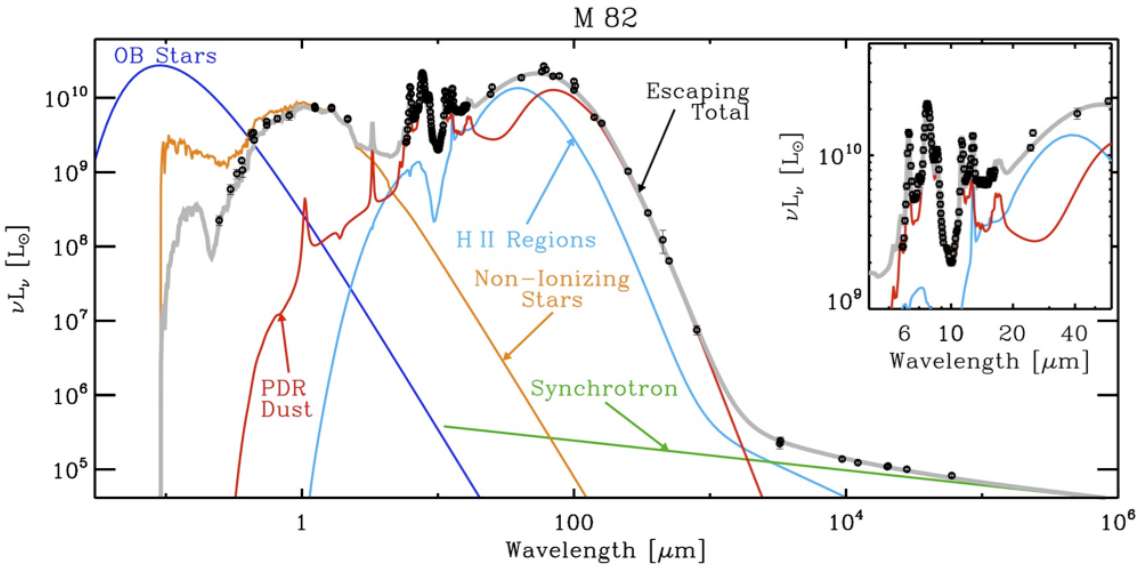

Figure 1.1: A complete SED picture of M82 from Galliano et al. (2011); Davies et al. (2017). M82 does not host a bright AGN. The SED of the light escaping M82 is shown in grey, the individual component are labelled in the figure and described in Section 1.1. This picture makes it clear that many different observations are needed to get a full understanding of the underlying galaxy.

The time between the formation of the first stars and the end of this ionization is called the epoch of reionization. This period roughly ends 1 Gyr after the formation of the Universe. During this period large clouds of neutral Hydrogen (HI) exist throughout the intergalactic medium. These gas clouds effectively scatter energetic radiation, causing large absorption features at the location of hydrogen absorption lines in the observed SED of quasars that we observe from this epoch. When the light travels through several clouds this causes an almost complete extinction of photons with a wavelength shorter than Lyman-α, the so called Gunn-Peterson effect (Gunn and Peterson, 1965). This effect faded away when the Universe was fully ionized and we can only measure it for very distant quasars.

As a summary of all the described components of a galaxy we show the complete SED of M82 in Figure 1.1. This figure demonstrates the way in which the different components described above contribute towards a real galaxy SED, which for M82 peaks at FIR wavelengths.

1.1.4 Galaxy shapes and environment

The above picture shows the different processes which determine the shape of a galaxy SED. For local galaxies it is possible to detect the different components contributing to this total SED independently, but for more distant galaxies it is not (yet) possible to observe most of these components separately. From the local Universe we can learn that star forming regions tend to lie in the outer parts of the galaxy where the inner part typically hosts a halo of older stars.

With optical and NIR surveys the morphology of many different galaxies can be estimated. With these surveys it was shown that galaxies have many different kind of shapes. Elliptical galaxies appear with (nearly) elliptical contours of surface brightnesses, and have no clearly defined structure. Elliptical galaxies are detected with a wide range of ellipticities, $0 < \epsilon \lesssim 0.7$, and tend to have a red optical colour. Spiral galaxies have a (blue) disk with spiral arms and a central halo of older stars, and tend to be less massive than ellipticals. The spiral type galaxies tend to have more ongoing star formation than more massive elliptically shaped galaxies. As a consequence the 4000 Å break is primarily visible in elliptical galaxies and is much weaker in galaxies which have spiral arms. The extinction due to the interstellar medium of elliptical galaxies is lower than in spiral galaxies, due to a lower amount of interstellar matter, which partly explains the lower star formation. Traditionally elliptical galaxies are referred to as early-type galaxies and spiral galaxies as late-type galaxies.

For several decades there has been substantial evidence that the environment influences galaxy properties such as shape and colour (Dressler, 1980). In the nearby Universe the red elliptically shaped galaxies tend to lie in the centre of clusters, where the blue star-forming spiral shaped galaxies tend to lie in the field. When galaxies are located in clusters they are more likely to have lower star formation, indicating that environment influences the quenching of galaxies (e.g. Wetzel et al., 2013). In the high redshift Universe it is not fully clear if this density-star formation relations holds or reverses (Elbaz et al., 2007). Another example of environmental influence on star formation is when two galaxies are undergoing a major merger. This merger causes an enhancement of star formation for gas-rich galaxies.

1.1.5 Observing from Earth

All the above features are described at the rest-frame wavelength of the galaxy, but due to the expansion of the Universe (Hubble, 1929) the emission will look redder (due to the

Doppler effect) and fainter when observed from earth:

$$S_\nu(\nu_0) = \frac{(1+z)L_\nu([1+z]\nu_0)}{4\pi D_{\rm L}^2}. \tag{1.3}$$

Where S_ν is the flux, ν_0 is the observed frequency, z the redshift and $D_{\rm L}$ the luminosity distance towards the galaxy. It is shown form Equation 1.3 that when we observe from earth at a fixed wavelength, we will probe rest-frame emission from a different wavelength according to the galaxy's redshift. It is therefore crucial to know the galaxy redshift in order to understand the underlying SED and galaxy properties.

The complexity of a galaxy SED makes it important to observe a galaxy at as many wavelengths as possible to get a coherent picture of the different components in the galaxy. Understanding the origin of all the different wavelength components from the cosmic background (all galaxies and inter galactic medium combined) has led to a partial understanding of galaxy populations and evolution. Ideally, the full understanding of galaxy evolution would need observations about all events, ranging from the formation of the first stars, to observations in the local Universe where we can see a large variety in mass, colour, shapes and clustering properties of galaxies.

1.1.6 The Herschel Extragalactic Legacy Project

The aim of the Herschel Extragalactic Legacy Project (HELP, Oliver et al. in preparation) is to collect multi-wavelength data over 1300 deg^2 of extragalactic sky observed by the *Herschel* extragalactic survey projects: *H*-ATLAS (Eales et al., 2010) and HerMES (Oliver et al., 2012). The data will be homogenised and made available to the astronomical community via a database interface. HELP will add value to the data in various ways, including providing selection functions and estimates of key physical parameters. The data set will enable users to probe the evolution of galaxies across cosmic time and is intended to be easily accessible for the astronomical community. HELP will provide i.e. master-lists of cross matched photometry, photometric redshifts, far-infrared flux densities, full galaxy SEDs, star formation rates and masses. The aim is to provide a census of the galaxy population in the distant Universe, along with their distribution throughout the 3-dimensional space.

The future of astronomy lies in finding the best possible way in using the combined information over all those different wavelength bands. In this thesis we primarily focus on the far-infrared (FIR) emission of galaxies, and we use many other wavelength bands to help us with this mission.

1.2 Far-infrared astronomy

When stars form from collapsing clouds of dust and gas, not all the material is used to form the star. This means that the newly formed stars will be embedded by the dust clouds in which they form. The infrared light from these stars will pass through the dust clouds, but the optical and especially the UV light from young stars will be absorbed by the dust (Calzetti et al., 1994). The blue and UV light is absorbed and scattered as the wavelength of this light is of comparable and smaller size as the dust particles. This absorption causes the cloud to heat up and to start emitting thermal radiation in the FIR.

The total integrated output from this thermal emission is strongly connected with the ongoing star formation in the galaxy. This results in a simple relation (Kennicutt, 1998b) between the star formation rate (SFR) and the infrared luminosity ($L_{\rm IR}$):

$$SFR \propto L_{\rm IR}. \tag{1.4}$$

The infrared luminosity of a galaxy is a crucial probe of the SFR, as it does not suffer from absorption like other SFR-indicators such as Hα and UV radiation. There are different attenuation laws which describe the level of attenuation from dust at different wavelengths. These laws mostly agree about the extinction in the UV but can have large discrepancies in the optical and NIR (Buat et al., 2017).

The total emission we receive from the extragalactic galaxies in the infrared makes up the Cosmic Infrared Background (CIB). This Background light in the infrared forms roughly 50 per cent of the total extragalactic background light (e.g. Hauser and Dwek, 2001; Inoue et al., 2013). Hence roughly half the UV+optical light is absorbed and re-emitted by dust clouds over the history of the Universe. Due to the link with star formation (Equation 1.4) this CIB is closely related to the total star formation history of the Universe. By observing at the FIR wavelengths we are able to characterise this total star formation history (Burgarella et al., 2013). It is crucial to observe the infrared part of the spectrum as otherwise the total SFR-density of the Universe will be vastly underestimated, see Figure 1.2 taken from Madau and Dickinson (2014).

The observed spectrum of the CIB is a complex function of the luminosity, space density and evolution of individual galaxies in combination with the formation history of dust. As the CIB is emitted from individual sources there are large fluctuations for the measured CIB on galactic and galaxy cluster scales, but the CIB is largely isotropic when measured over larger scales ($\gg 1$ deg^2).

Water vapour in our own atmosphere causes the sky to be opaque in the infrared and

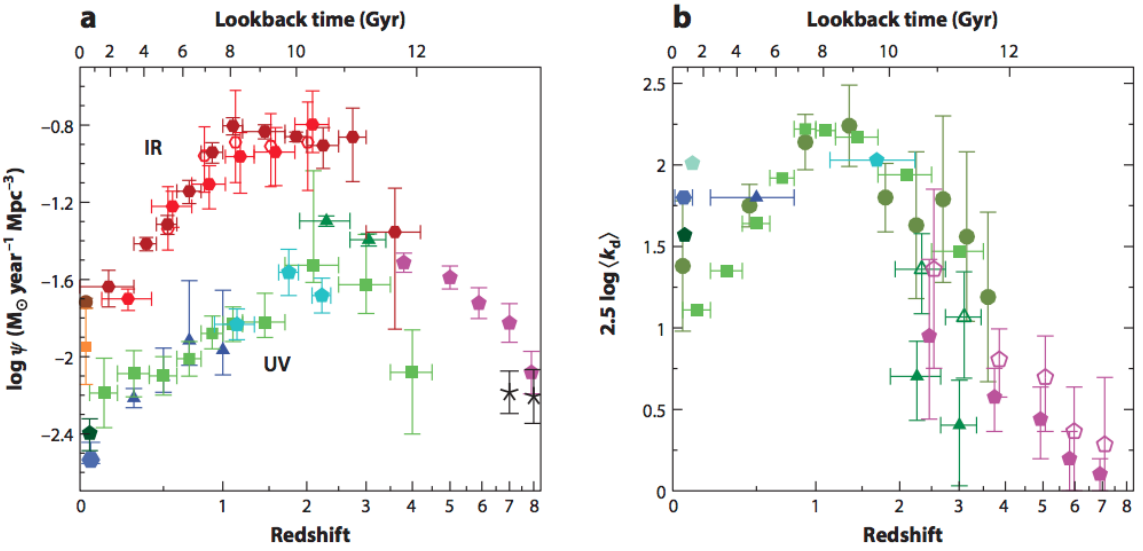

Figure 1.2: The SFRD (plot a) from Madau and Dickinson (2014) as measured in the FIR and in the UV (uncorrected for dust attenuation). On the right (plot b) the total dust attenuation in magnitude as a function of redshift. At redshift $\lesssim 3$ the extinction in the UV is larger that one magnitude and the total SFRD will be heavily underestimated if only uncorrected UV data was used.

therefore very difficult to observe at wavelengths 10-1000 μm. To get around this problem, the telescopes have to be built in very dry (high) locations or preferably in space. Another problem arises from the detectors used to observe FIR radiation, the so called bolometers. These bolometers have a relatively low sensitivity compared to CCDs used to observe the optical light.

A bolometer consists of an absorbing element, which is heated up by the infrared radiation above the temperature of a thermal reservoir, which is connected to the absorbing material with a weak thermal link. Due to the increase in temperature of the absorbing element there will be less resistance and the voltage over the system changes. This change in voltage is measured and translated into the energy from radiation observed by the bolometer.

Another technical challenge is that the temperature of the telescope and instrument contribute to the flux measurement of the bolometer and so measuring a zero flux level is non-trivial. To reduce this effect, and increase sensitivity of the bolometer, the instrument can be cryogenically cooled down and ideally placed outside of the Earth's atmosphere.

The peak wavelength of the FIR emission for individual galaxies lies around 70-100 μm, which is a factor $\sim$100 larger than the optical. As a result of the the Rayleigh criterion

(Equation 1.5) this longer wavelength (λ) reduces the angular resolution (θ) of FIR telescopes compared to optical telescopes with the same diameter (D):

$$\theta = 1.22\frac{\lambda}{D}. \tag{1.5}$$

Due the opaqueness of our atmosphere at these wavelengths it is also not possible to build a very large ground based telescope to compensate for this lack of resolution, as can been done in the radio (e.g. Nan et al., 2011). This lack of resolution provides an extra challenge in observing at FIR wavelengths.

1.2.1 A selection of historical infrared observatories

Infrared radiation was discovered in 1800 with the discovery of infrared radiation emitted by the Sun (Herschel, 1800). This detection was made with the use of a thermometer located at the end of a prism where only light redder than the optical is diffracted. The rise in temperature of the thermometer was explained by invisible light with a longer wavelength than optical light. It took until the development of the bolometer in 1878 and the usages of cryogenically cooled systems to cool the bolometers in the early 1960s, before infrared astronomy really took off (Low, 1961). The thermal cooling is crucial as otherwise the thermal radiation of the telescope itself will be detected by the bolometers. The first generation of cooled bolometers led to the discovery that our own atmosphere contains large amounts of thermal radiation at 10 μm. The temperatures and infrared radiation of solar system objects and nearby stars were also quantified (Low et al., 1970).

The first telescope to classify the extragalactic dust of nearby galaxies, the Infrared Astronomical Satellite (IRAS, Neugebauer et al., 1984), launched in 1983 and surveyed the whole sky at 12, 25, 60 and 100 μm. The majority of IRAS selected galaxies had infrared luminosities in excess of 10^{11} $L_{\odot}$, the so called luminous Infrared galaxies (LIRGS). Some of the IRAS detected galaxies were even brighter and had infrared luminosities in excess of 10^{12} $L_{\odot}$ (ultraluminous infrared galaxies, ULIRGs). Those extremely bright galaxies were found to be rare in the local Universe.

These very high infrared luminosities come from dust heated by intense starburst or AGN activity. The optical and UV light from those galaxies is largely absorbed, making some of these LIRGS very faint at these short wavelengths. The brightest part of those IRAS discovered galaxies tend to be gas rich major mergers (Sanders and Mirabel, 1996). The IRAS observations showed how important the role of dust is for the shape of the SED of a galaxy. IRAS however did not have an accurate way of measuring the thermal radiation

from the telescope itself and so could not accurately determine the zero point needed to measure the CIB. The Far Infrared Absolute Spectrophotometer (FIRAS) onboard of the Cosmic Background Explorer (COBE, Puget et al., 1996) did have a cold external calibrator to make absolute measurements and was therefore able to measure accurate limits for the CIB (Fixsen et al., 1998; Lagache et al., 1999). This total CIB measurement indicated that bright dusty star forming galaxies should be more common in the more distant Universe.

The main mission of COBE was to quantify the CMB, which is observed as an almost perfect blackbody peaking around 1.9 mm (2.7 K). The peak of the CIB is longward of most observed FIR emission from extragalactic sources. To accurately probe the CMB it is necessary to observe over a larger range in wavelengths to find the temperature of the blackbody. Variations in the blackbody peak occur for different regions of the sky and are of on order $\delta T/T \sim 10^{-5}$ (Planck Collaboration, 2016) and much smaller than the fluctuations caused by very bright (lensed) foreground galaxies and proto-clusters. This property makes it relatively easy to use large area CMB surveys to find foreground extremely bright FIR emitting galaxies and to remove them from the CMB signal (Bennett et al., 2003; Carlstrom et al., 2011).

The first instrument which was efficient in finding high-redshift ($z > 0.3$) dusty star forming galaxies (DSFGs) was the Submillimeter Common User Bolometric Array (SCUBA, Holland et al., 1999) in 1997. The deep field surveys undertaken with this camera discovered thousands of these distant DSFGs (e.g. Smail et al., 1997). SCUBA was especially sensitive at 850 μm which has a beam size of ∼15 arcsec. This large beam size made it difficult to identify optical counterparts, as there will potentially be several galaxies detected within the FWHM of the 850 μm detection and the real counterpart might be obscured by dust within the galaxy. Due to the lack of optical counterpart it was difficult to obtain the redshift for these distant dusty galaxies. These high redshift DSFGs were not typically associated with mergers as in the local Universe. For a complete overview on past and current facilities which have observed at FIR wavelengths see Casey et al. (2014).

1.2.2 The negative *K*-correction

Observations at $\gg 100$ μm are successful in finding higher redshift galaxies due to the so called negative K-correction. The K-correction is the correction applied to the galaxy flux to convert from observed-frame to rest-frame. At wavelengths $\gg 100$ μm we are observing

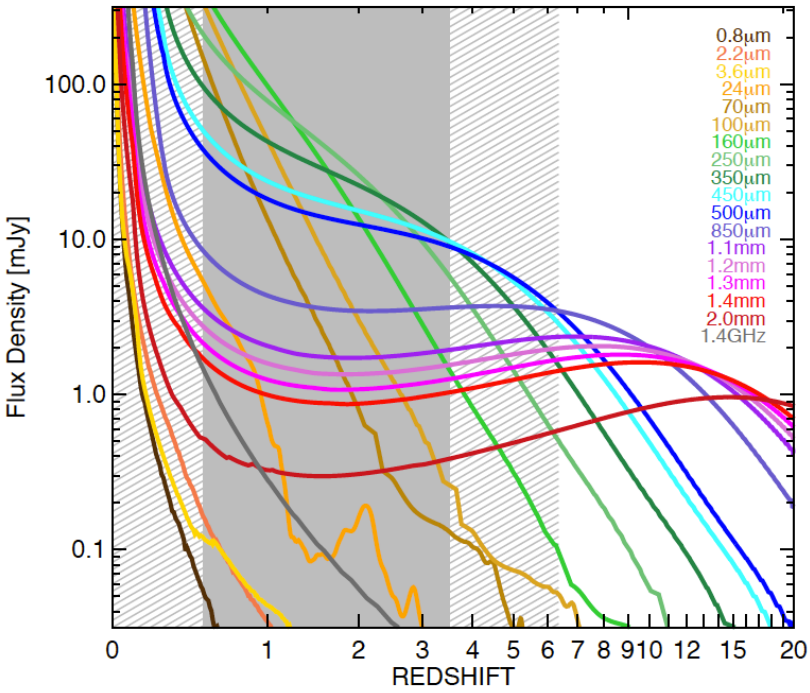

Figure 1.3: A visualisation of the observed flux density for a DSFG placed over a large range of different redshifts, visualized by Casey et al. (2014). The FIR luminosity of the DSFG is $10^{12.5}$L$_\odot$. At wavelengths $\gtrsim$ 850 μm a DSFG can appear brighter if it is located father away.

past the peak of the FIR emission in the Rayleigh-Jeans part of the spectrum. But this peak is redshifted towards the observed band for high-redshift galaxies, causing the galaxy to look relatively bright compared with what you would expect from naively looking at the luminosity distance towards the galaxy. The K-correction is strong enough at wavelengths around 1 mm to let galaxies appear brighter if they are located farther away from us, this very strong K-correction is referred to as the very negative K-correction.

A visualisation of the flux density for the same galaxy, placed over a large range of different redshifts is shown in Figure 1.3. It is visible from the figure that the flux density very quickly drops off if a galaxy is located at higher and higher redshifts. Wavelength bands which observe at $\gtrsim$ 350 μm are an exception to this and for observations performed at $\gtrsim$ 850 μm it is even possible that galaxies will appear brighter if they are located at high redshift.

The redshifts of distant DSFGs are difficult to find as due to the high obscuration it is not always possible to find an optical counterpart. Higher resolution mid-infrared or radio data can be used as a bridge between the optical and the FIR emission to determine

the counterpart. An unambiguous way to determine the redshift of a distant DSFG is by matching observed emission lines with known rest frame emission lines in the (sub-)mm regime. The first mm spectroscopic redshift of a high-redshift dust obscured galaxy was obtained using EMIR at IRAM in 2009 by detecting the CO(3-2) and CO(5-4) line (Weiß et al., 2009a). Recently the Atacama Large Millimeter Array (ALMA) has been very successful in detecting CO and CII lines for large numbers of distant galaxies (e.g. Vieira et al., 2013).

Redshift obtained without spectral data, but with broad and narrow band continuum detections are called Photometric redshifts. This method relies on an assumed rest-frame shape of the galaxy SED. Photometric redshifts can be obtained by using only FIR data. The problem with this method is that the peak and shape of the FIR emission is not fixed and varies for different types of galaxies. Determining the rest-frame SED shape is therefore not good enough to calculate accurate photometric redshifts, unlike optical data where by finding distinct features such as the 4000 Å break provide a precise solution. Both a higher redshift and a colder temperature make the SED look red and it can therefore be difficult to distinguish between a cold, low redshift galaxy and a hot higher redshift galaxy. Knowing the range of temperatures for DSFGs is crucial in determining more accurate photometric redshifts due to the very large degeneracy between temperature and redshift. This degeneracy leads to photometric redshift accuracy which can be a factor of a hundred larger than the accuracy obtained with very well sampled optical and NIR data. Even though there is a large uncertainty, it is still possible to select likely high-redshift candidates over large areas of the sky using this method.

1.3 Observations with *Herschel*

Observations of a large part of the extragalactic sky were made by *Herschel* over the period of 2009-2013. The primary mirror of *Herschel* had a diameter of 3.5 m, which made the collecting mirror a factor of $\gtrsim 5$ larger than its FIR predecessors and larger then any other space-based telescope. *Herschel* was cooled by liquid helium to reduce the thermal radiation from the instruments. The observations from *Herschel* were taken from the Earth-Sun Lagrangian point 2 and the telescope was therefore located farther away from Earth than Earth orbiting satellites. This more distant location reduces the impact of the Earth's infrared radiation but also made potential repairs or re-filling of helium impossible.

The continuum observations were done by two instruments: the Photodetector Array

Camera & Spectrometer (PACS, Poglitsch et al., 2010) and the Spectral and Photometric Imaging Receiver (SPIRE, Griffin et al., 2010). The PACS instrument observed at 70, 100 and 160 μm respectively, and probed the peak of the FIR emission for galaxies with $z \lesssim 1$. For higher redshift galaxies the peak of the FIR emission is observed by the 250, 350 and 500 μm bands from SPIRE.

The three SPIRE filters observed simultaneously and have a $\lambda/\Delta\lambda \sim 3$. The SPIRE instrument uses feedhorn-coupled bolometers for detections and is cooled to 0.3 K. The three hexagonal arrays of bolometers contain 43, 88 and 139 detectors, respectively. When observing with the SPIRE instrument *Herschel* uses scan mapping with a field of view of 4 $\times$ 8 arcmin to fully sample the sky. The first data product which can be obtained from SPIRE are calibrated timelines for individual bolometers, these timelines can then be turned into a map. The instrumental noise in these SPIRE maps is approximately Gaussian (Smith et al., 2017).

The full width half maximum (FWHM) for the SPIRE bands is $\sim$18, 25 and 36 arcsec, respectively. The SPIRE beams are well described by 2-D Gaussians. This large beam size makes confusion (Nguyen et al., 2010) in SPIRE bands a major concern. Confusion noise is caused by unknown sources near the target source, making it impossible to distinguish exactly what percentage of the measured flux density is caused by which of the underlying galaxies. The confusion noise in the three SPIRE bands have comparable values of 6-7 mJy per beam. The SPIRE 500 μm beam is much larger than the SPIRE 250 μm beam, indicating that there are less sources with a large contribution to the confusion noise at 500 μm than at 250 μm. This effect is even stronger at even longer wavelengths where at 850 μm the confusion noise drops below 1 mJy for a comparable beam size as the SPIRE 250 μm (Geach et al., 2017).

There are several methods to get around the problem of confusion noise. The easiest method is to only select for galaxies which have a flux density which largely exceeds the confusion noise. The problem with this method is that it completely ignores the fainter and more abundant population (see Chapter 2) and this method can select rare alignments from several galaxies (see Chapter 3). A second commonly used method is stacking, which does not give information about an individual galaxy but can tell us the mean of the population. Prior information about the positions of the galaxies is needed to obtain a stacking result and one has to be very careful in stacking on low resolution maps to correct for correlated sources, the mean subtraction and double counting (Section 1.4; Chapter 4; Viero et al., 2013a). The latest method to measure FIR flux densities is

to use prior based source extraction. A full Bayesian approach in combination with prior information from deep high-resolution data can be used to find accurate flux densities of galaxies which are not detected in the FIR. This method can distribute the observed flux density over the underlying galaxy population (Hurley et al., 2017). The drawback of this method is that it is computationally expensive and is largely dependent on the availability of prior information.

1.4 Stacking

Throughout Chapter 2 and 4 we use stacking to obtain the mean *Herschel* SPIRE fluxes for groups of optical/NIR detected galaxies. Basic stacking takes all the positions from a certain type of galaxies detected at one wavelength and uses these positions to add/stack the images together in another wavelength band where some of those galaxies are not detected. By adding this data together the instrumental noise reduces with $\sqrt{N}$, with N the number of stacked galaxies. This method makes it possible to gain a stacking signal and mean flux density from previously undetected galaxies. It is a mistake to stack sources on a background subtracted map, in this case a large list of random positions will obtain a positive significant signal as some of the random positions will randomly align with galaxies. This effect can be neglectable in stacking on high-resolution optical maps, but is problematic in the highly confused maps at FIR wavelengths. The simple solution for this problem is to mean-subtract the map, which means that a random list of positions will obtain zero flux and a list of undetected galaxies will get this zero flux plus the total flux density from those sources.

In the highly confused SPIRE maps, another problem arises due to the large beam. Galaxies are positively correlated with each other (Totsuji and Kihara, 1969), which means that there is a higher probability to find a galaxy nearby another galaxy than on a random position on the sky. In the optical this is not a major problem for stacking, as the stacking galaxy list will appear separately from the correlated galaxies. For the SPIRE maps these correlated sources can be located within the same beam as the stacking galaxy, causing an overestimate of the stacked galaxies flux density (Béthermin et al., 2010).

A solution to this problem is to stack the correlated galaxies simultaneously (Kurczynski and Gawiser, 2010; Viero et al., 2013a). An example of such a code is `SIMSTACK` (Viero et al., 2013a) where the sources are divided over several catalogues to create synthetic maps which are fitted simultaneously (Figure 1.4). In this case The SPIRE flux will be divided over the sources in those catalogues. `SIMSTACK` will still add the flux density of

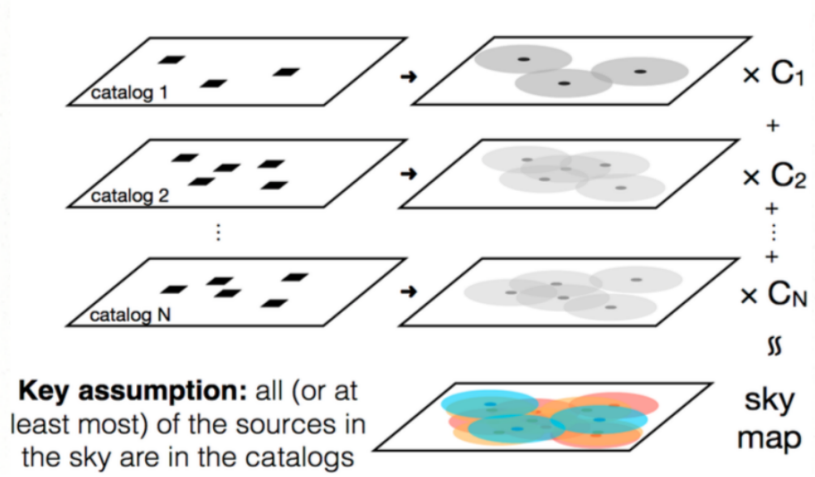

Figure 1.4: Simultaneously fitting of synthetic source maps with `SIMSTACK` (Viero et al., 2013a). The N catalogues are divided over N synthetic maps and convolved with the SPIRE beam. Those maps are then simultaneously fitted to the real map. The flux density from correlated not stacked sources will be added to the flux density of the stacked sources. `SIMSTACK` therefore performs better if most of the galaxies on the sky are in the prior catalogues.

correlated galaxies which are not in the catalogues and are within the SPIRE beam of a catalogued galaxy, to sources within the catalogues.

Incompleteness can also bias the stacking results. In stacking it is assumed that the background from the stacked sources is equal to the average background of the sky. However, in deep optical/NIR surveys, it is not possible to detect a faint galaxy near a very bright galaxy. Therefore the list of faint galaxies is incomplete, and the locations of the incomplete galaxies are correlated to bright areas of the sky. When the faint optical galaxies are stacked on the mean subtracted SPIRE maps than a negative flux density can be detected for the stacked galaxies (Heinis et al., 2013). In this situation the background is not fully sampled, as bright regions in the optical are avoided. The absence of these bright background sources causes the background of the faint galaxies to be negative. This biases the flux density of the stacked galaxies low.

1.5 Thesis summary

With this thesis we aim to gain a better understanding of which galaxies contribute to the CIB their dependence on environment and redshift. We investigate this question by looking at all the detected galaxies in the 2 deg^2 COSMOS field (Scoville et al., 2007a). The

galaxies in the COSMOS field have excellent multi-wavelength data in the optical and NIR and therefore have very accurate stellar masses and photometric redshifts (Ilbert et al., 2013). We only pick galaxies outside of optically masked areas and with a photometric redshift between 0.1 and 3.2. We picked this limit because the COSMOS field is too small to get a statistical and representative sample at $z < 0.1$, and for $z > 3.2$ the photometric redshifts become inaccurate and the galaxy sample becomes heavily incomplete. We picked the COSMOS field due to the availability of very accurate and deep ancillary data and due to the relatively large size of the field. This data allows us to measure the accurate location of the galaxies in 3-d space.

To measure this 3-d position we divide the COSMOS catalogue into redshift slices and smoothed the density in those slices with an adaptive kernel. We take every galaxy into account while making our redshift slices, giving the galaxies a weight according to their probability of lying within any given slice. The positions of every galaxy from the COSMOS catalogue is used for a stacking analysis on the SPIRE maps to calculate the mean SPIRE flux densities for a galaxy with a given mass and redshift. We use this result to calculate the main sequence of star forming galaxies with the star formation derived from the FIR. This main-sequence is the apparent relation between stellar mass and SFR for star-forming galaxies and it is not clear how this sequence depends on environment. We use the local density of the main-sequence galaxies to divide them over different prior lists for stacking. When those prior lists are simultaneously stacked, the offset from the global main-sequence can be found for different environments. With this result, we show how the SFRs of star forming galaxies are correlated with local environment of the galaxy and how it evolves over redshift. We furthermore calculate the star formation rate density over cosmic time and its dependency on environment. The results from this research topic are described in detail in Chapter 2 and are published in Duivenvoorden et al. (2016).

To find extremely rare sources (with a density > 1 deg^{-2}), one must use fields a lot larger than COSMOS. We used the available red SPIRE source catalogue (Asboth et al., 2016) in the 274 deg^2 HeLMS field to select 188 bright 500 μm riser ($S_{500} > S_{350} > S_{250}$) galaxies and observe them at 850 μm with SCUBA-2. With the additional SCUBA-2 data we are now able to probe the peak of the FIR emission. Those red SPIRE sources are expected to lie around $z \sim 4$ and difficult to detect in shallow large field optical/NIR surveys as they are very distant and dust obscured. The SFRs and evolution of those distant bright objects is still an outstanding question in astronomy as their SFRs are predicted to be very high because the DSFGs are directly detected over the instrumental

and confusion noise over such a long luminosity distance. We perform SED fits for this sample to determine the redshifts and SFRs. The mean redshift of the sample is 3.6 and the SFRs exceed 10^3 $M_{\odot}yr^{-1}$

We compare the observed number density of galaxies with galaxy simulations and our own simulated mock catalogues. We use a novel way to incorporate instrumental and correlated confusion noise in those comparisons. The incorporation of noise is crucial for these comparisons with simulations. With these noise added simulations we find that the observed number counts are consistent with the phenomenological galaxy evolution models. This sample of galaxies is very interesting as they are too rare to be detected in deep (narrow) optical or radio surveys and they are too faint (obscured) to detect with large area optical surveys. For this reason, SPIRE is the ideal instrument to find and select those extreme sources. We also estimate the star formation rate density of such galaxies and we found that one of our SFRs is contaminated by FIR emission from a quasar. There is a statistically significant excess of WISE-1 and SDSS sources near our red galaxies, giving a strong indication that lensing may explain some of the apparently extreme objects. The results from this research topic are described in detail in Chapter 3 and are published in Duivenvoorden et al. (2018).

With the projects mentioned above we aim to explain the populations which contribute to the CIB. The third and final project of this thesis aims to calculate new bounds to the CIB and to see which (future) large area galaxy surveys are ideal in selecting the galaxies which contribute most to the CIB. We again use the COSMOS field to preform our analysis but this time we use the deeper updated COSMOS2015 catalogue (Laigle et al., 2016) to obtain separate r, K_s, 3.6 μm, 24 μm, 100 μm, 250 μm, 850 μm and 21 cm prior catalogues for stacking. We developed an improved version of `SIMSTACK` (Viero et al., 2013a), which now simultaneously fits the galaxies, the system background and the leakage of flux from galaxies located in masked areas.

With our novel map fitting algorithm, we fit all galaxies detected at r, K_s, 3.6 μm in the 1.38 deg^2 deep and unmasked areas to calculate the total CIB. The total CIB found is 17.5 ± 1.8, 6.8 ± 0.6 and 3.2 ± 0.2 nWm^2 sr^1 at 250, 350 and 500μm, respectively. These results indicate that future large area surveys like the Large Synoptic Survey Telescope (LSST) survey are likely to resolve the whole population responsible for the CIB at 250 μm $\leq \lambda \leq$ 500 μm. The results from this research topic are described in Chapter 4. We will complete this thesis with a summary of the results of the three chapters and our final conclusions can be found in Chapter 5.

1.6 Other work

Besides the work described in this thesis I have provided photometric redshifts and SCUBA-2 flux densities for Oteo et al. (2017a) and provided comments for the following papers for which I am a co-author: Viero et al. (2015); Hurley et al. (2017); Donevski et al. (2017).

Viero et al. (2015) uses `SIMSTACK` to calculate the CIB from K_s selected galaxies and their faint companion galaxies in the COSMOS field. The SPIRE maps are smoothed with a 300 arcsec FWHM Gaussian kernel to capture the contribution from the faint undetected companion galaxies. The total values of the CIB obtained are consistent with results from FIRAS indicating that the CIB is built up by galaxies with K_s magnitude < 23.4 and their fainter companions.

Hurley et al. (2017) developed a novel prior-based source extraction tool to deblend the *Herschel* SPIRE images called XID+. With this algorithm it is possible to divide the flux density in the SPIRE maps over a prior list of previously detected galaxies from higher resolution surveys in a full Bayesian way. XID+ provides the full posterior probability of galaxy photometry for all the objects in the prior catalogue. The code is tested on simulated SPIRE maps in the COSMOS field and outperforms the prior-based source extraction tool `DESPHOT` in flux accuracy and flux uncertainty accuracy.

Donevski et al. (2017) described the detection of 133 500 μm riser galaxies in the 55 deg^2 Herschel Virgo Cluster Survey using the selection criteria of $S_{500} > S_{350} > S_{250}$, $S_{250} > 13.2$ mJy and $S_{500} > 30$ mJy. In this paper it is shown that noise and strong lensing have an important impact on measured counts and redshift distribution of red SPIRE galaxies. The medium redshift of the detected DSFGs is 4.3 and the brightest galaxy inside the beam contributes on average 75 per cent and 64 per cent to the total single-dish flux density measured at 250 μm and 500 μm.

Oteo et al. (2017a) uses high spatial resolution (~ 0.12 arcsec) ALMA 870 μm detection of ultrared DSFGs to calculate their shapes and SFRs. Some of the DSFGs have total obscured SFRs exceeding 4 000 $M_\odot yr^{-1}$ even after correcting for lensing. This luminous infrared sample had a large variety of morphologies ranging from compact sources to extended disks. The average size ($\sigma_{\rm FWHM}$) of the galaxies is 1.5 ± 0.4 kpc, which is considerably smaller than local DSFGs. With the help of the ALMA data we are able to probe the birth of the high-mass tail of the current day red sequence of galaxies.

Chapter 2

HELP: star formation as a function of galaxy environment with Herschel

2.1 Abstract of chapter 2

The Herschel Extragalactic Legacy Project (HELP) brings together a vast range of data from many astronomical observatories. Its main focus is on the Herschel data, which maps dust-obscured star formation over 1300 deg^2. With this unprecedented combination of data sets, it is possible to investigate how the star formation versus stellar mass relation (main sequence) of star-forming galaxies depends on environment. In this pilot study, we explore this question within $0.1 < z < 3.2$ using data in the COSMOS field. We estimate the local environment from a smoothed galaxy density field using the full photometric redshift probability distribution. We estimate star formation rates by stacking the SPIRE data from the Herschel Multi-tiered Extragalactic Survey. Our analysis rules out the hypothesis that the main sequence for star-forming systems is independent of environment at $1.5 < z < 2$, while a simple model in which the mean specific star formation rate declines with increasing environmental density gives a better description. However, we cannot exclude a simple hypothesis in which the main sequence for star-forming systems is independent of environment at $z < 1.5$ and $z > 2$. We also estimate the evolution of the star formation rate density in the COSMOS field, and our results are consistent with previous measurements at $z < 1.5$ and $z > 2$ but we find a $1.4^{+0.3}_{-0.2}$ times higher peak value of the star formation rate density at $z \sim 1.9$.

2.2 Introduction of chapter 2

Galaxies are found in different environments, from rich clusters, to small groups, to isolated galaxies residing in cosmic voids. For several decades, there has been substantial evidence that the environment influences galaxy properties, such as star formation rate (SFR), morphology and colour (e.g. Dressler, 1980). The environment has been found to influence the timing of the quenching of star formation (e.g. Wetzel et al., 2013), though the onset of star formation is not necessarily caused by environment (e.g. Rettura et al., 2011). This quenching leads to a decline in the fraction of actively star-forming galaxies in clusters from $\sim$ 20 per cent at z $\sim$ 0.4 to almost zero in the local Universe (e.g. Butcher and Oemler, 1984; Haines et al., 2013).

There are several ways to probe the SFR of a galaxy. For a young stellar population, the radiation is dominated by the UV light emitted from massive stars. Due to the short lifetime of these stars, this emitted power is a good indicator for star formation. However, not all emitted UV light escapes the galaxy. In the presence of dust, a significant percentage of this light is absorbed and reradiated at mid- and far-infrared (FIR) wavelengths. The total FIR luminosity is therefore a function of the amount of obscured UV light, and provides another method to measure the SFR (e.g. Kennicutt, 1998b; Madau and Dickinson, 2014).

Low-redshift galaxies in dense environments are redder on average than field galaxies (e.g. Kauffmann et al., 2004; Koyama et al., 2013; Scoville et al., 2013). This can be partly explained by a higher dust content of galaxies or a lower SFR of individual systems. Although these relations are well established at low redshift, it is still open to debate whether the trends stop, or may even be reversed at higher redshift (e.g. Elbaz et al., 2007; Tonnesen and Cen, 2014).

The environment is not the only parameter that influences the evolution of galaxies. Both internal and external effects determine how much gas is available for forming stars, as the internal gas supply gets replenished by accretion of cold gas from the environment (e.g. Dekel et al., 2009). The availability of this cold gas has a significant influence on the SFR of galaxies (e.g. Santini et al., 2014).

To distinguish between environment and internal influences, we need to characterize them simultaneously. Recent studies indicate that quenching is driven more by the internal properties of a galaxy than by the environment (e.g. Hahn et al., 2015). However, the fractional role of the internal and external processes in galaxy quenching may depend on, e.g., redshift and stellar mass of galaxies (e.g. Peng et al., 2010; Sobral et al., 2011; Darvish

et al., 2016). We note that separating the internal and external effects can be difficult because they seem to be strongly connected with each other (De Lucia et al., 2012).

Another example of the importance of internal galaxy properties on galaxy evolution is the strong relation, between SFR and stellar mass for star-forming galaxies: termed the main-sequence (MS, Brinchmann et al., 2004). The MS has been found in both the local Universe and at higher redshifts (e.g. Noeske et al., 2007; Sobral et al., 2014; Delvecchio et al., 2015; Lehnert et al., 2015). A trend is seen for galaxies on the MS, where the more massive a star-forming galaxy is, the higher the star formation rate becomes. In relative terms, the specific star formation rate (sSFR, the star formation rate per unit stellar mass) appears to drop for higher mass galaxies: galaxies with higher total stellar mass are redder and have relatively less star formation per unit mass. The MS seems to be in place out to z $>$ 2.5 (Whitaker et al., 2012). However, the specific details of the MS, such as slope and dispersion, vary between different studies (e.g. Speagle et al., 2014). Moreover, the sSFR of galaxies on the MS evolves with redshift as roughly $(1+z)^3$ out to redshift of 2-3 (Oliver et al., 2010a; Lehnert et al., 2015; Johnston et al., 2015; Pannella et al., 2015).

Whether or not the normalisation of the MS depends on environment is still under discussion. Ricciardelli et al. (2014) found that the MS is constant for void, void-shell, and reference galaxies at $z < 0.12$. Tyler et al. (2013, 2014) found no difference between the MS in clusters and in the field. Paccagnella et al. (2016) found a similar result, but also found a population of galaxies with reduced SFR (departing from the MS) within the virial radius of the cluster at $z \sim 0.1$.

It has been argued that higher density environments only reduce the fraction of galaxies that are star-forming and do not seem to have a major effect on the average SFR of star-forming galaxies (e.g. Peng et al., 2010; Wijesinghe et al., 2012; Darvish et al., 2014, 2016). However, at low redshift, von der Linden et al. (2010, $z < 0.1$) and Haines et al. (2013, $0.15 < z < 0.3$) found a reduction of the SFR of star-forming cluster galaxies, compared to their counterparts in the field. Furthermore Scudder et al. (2012a) found an enhanced MS in isolated compact groups, but compact groups embedded in larger systems do not have this enhanced SFR.

At intermediate redshift ($0.4 \leq z \leq 0.8$) Vulcani et al. (2010) found that the SFR of cluster star-forming galaxies was a factor of 1.5 lower than in the field. This result is in agreement with Patel et al. (2011) at $0.6 < z < 0.9$. However, Lin et al. (2014) did not find evidence (out to $z \sim 0.8$) for an environmental dependence of the MS, although they did find a significant reduction of the sSFR by 17 per cent in cluster environments

($M_{\rm halo} > 10^{14}{\rm M}_{\odot}$). At z $\sim$ 0.5, Darvish et al. (2015a) also showed that [OII] EW (a measure of sSFR) versus stellar mass relation is independent of environment (filament versus field), indicating the environmental invariance of the MS. Furthermore Darvish et al. (2014) showed the environmental (filament, cluster, field) independence of the MS in the COSMOS field (Scoville et al., 2007a) at z $\sim$ 0.84.

At higher redshift ($z \sim 1.5$) Koyama et al. (2014) found no direct evidence for an environmental dependence of the MS for Hα emitters. Furthermore, Koyama et al. (2013) found that the difference between the field and cluster MS is less than 0.2 dex in redshifts smaller than ~ 2 based on Hα emitters.

The dependence of the MS on the large scale environment is still under discussion, however a clear correlation seems to exist between SFR and paired galaxies. Melnyk et al. (2015) found that paired massive ($\log(M_*/{\rm M}_{\odot}) > 11.5$) galaxies have higher SFR than isolated galaxies, and this same result was found for lower mass galaxies with the galaxy pairs in the Sloan Digital Sky Survey (e.g. Ellison et al., 2010; Scudder et al., 2012b) and for major-merger pairs in *Herschel* (Cao et al., 2016).

No consensus has yet been reached on how the MS depends on environment or redshift. This is partially because the aforementioned methods differ in how they select the galaxies, how they estimate star formation, and how they measure environment. The selection of which method to use to determine the environment can cause differences in which galaxies are selected to be in a certain density regime, and therefore different results (Muldrew et al., 2012).

To accurately probe the normalisation of the MS, it is necessary to measure the SFR in a wide range of different environments over cosmic time. For the SFR we use the FIR data from the Herschel Multi-tiered Extragalactic Survey (HerMES; Oliver et al., 2012). In order to probe the environment and the stellar mass, we exploit the rich multi-wavelength data and volume of the COSMOS field.

The Herschel Extra-galactic Legacy Project (HELP; Vaccari (2015), Oliver et al. 2016 in preparation) aims to collate and homogenize observations from many astronomical observatories to provide an integrated data set covering a wide range of wavelengths from the radio to the UV. The key focus of the HELP project is the data from the extra-galactic surveys from ESA's *Herschel* mission (Pilbratt et al., 2010), covering over 1300 deg^2. HELP will add value to these data in various ways, including providing selection functions and estimates of key physical parameters. The data set will enable users to probe the evolution of galaxies across cosmic time and is intended to be easily accessible

for the astronomical community. The aim is to provide a census of the galaxy population in the distant Universe, along with their distribution throughout the 3-dimensional space.

Another key feature of HELP will be the generation of galaxy density maps. In this paper, we apply our chosen methodology for measuring density fields to publicly available data in the COSMOS field to explore the environmental dependence of star formation as probed by *Herschel*.

The format of this paper is as follows. We describe the data we use in Section 2.3. We describe our methods of determining the environment of the galaxy (Section 2.4.2), our stacking analysis (Section 2.4.3) and how we obtained SFRs (Section 2.4.4). The results are described in Section 2.5. The discussion and conclusions can be found in Sections 2.6 and 2.7. We use a standard flat cosmology with $\Omega_M = 0.3$ and $H_0 = 70$ km s^{-1}Mpc^{-1}.

2.3 Data

2.3.1 The HerMES survey

We use the SPIRE data (Griffin et al., 2010) from the HerMES (Oliver et al., 2012) survey to compute the SFRs of our sample of galaxies. We use all 250 μm, 350 μm and 500 μm SPIRE bands in the COSMOS field from the second data release, DR2 (5σ depth of 15.9, 13.3, 19.1 mJy; at 250, 350 and 500 μm, respectively, Viero et al., 2015). The HerMES (and in future also the HELP) data can be obtained from the HeDAM database[1].

One of the challenges at the longer wavelengths probed by SPIRE is extragalactic confusion (e.g. Nguyen et al., 2010), whereby many sources detectable with higher resolution shorter wavelength imaging are located within a single SPIRE beam, and therefore appear as one SPIRE source. The SPIRE FWHM for 250, 350 and 500 μm is 18.1, 25.5, and 36.6 arcsec, respectively (Griffin et al., 2010; Viero et al., 2015). To estimate the SPIRE flux density for individual galaxies we need to exploit prior information of the position, mass and redshift of the galaxies. We use a stacking method to obtain these flux density estimates, with a method that will be addressed in Section 2.4.3.

2.3.2 Multi wavelength catalogue

Photometric redshifts for our sample are obtained from the COSMOS UltraVISTA K_s-band selected catalogue (Ilbert et al., 2013; McCracken et al., 2012). The catalogue contains 30 bands ranging from UV to NIR in broad, intermediate and narrow bands, and

[1] hedam.lam.fr

contains 220 000 galaxies. The photometric redshifts were obtained using the `Le_Phare` code (Ilbert et al., 2006) and calibrated against spectroscopic redshifts. Due to the large range in wavelength, the availability of intermediate bandwidth photometric filters and the good quality of the data, the estimated redshifts are very accurate. For $z < 1.5$, Ilbert et al. (2013) obtained a precision of $\sigma_{\Delta z/(1+z)} = 0.008$ at $i^+ < 22.5$ (< 1 per cent catastrophic outliers) and even for faint ($i^+ \simeq 24$) sources the accuracy is better than 3 per cent. At higher redshift ($1.5 < z < 4$) the precision is given by $\sigma_{\Delta z/(1+z)} \approx 0.03$ (Ilbert et al., 2013). Furthermore the photometric redshifts are characterised by their full probability distribution function (PDF).

Stellar masses are derived from the SED using the Stellar Population Synthesis model of Bruzual and Charlot (2003) in combination with the Chabrier (2003) initial mass function. The stellar masses are model dependent and can vary by 0.1-0.15 dex depending on the model. The sample of star-forming galaxies is complete above a stellar mass of $\sim 10^8$ $M_\odot$ at $z = 0.2$ and or $\sim 10^{10}$ $M_\odot$ at $z = 3.0$.

We treat the star-forming and the quiescent galaxies differently, as we expect that their FIR properties to be quite distinct. To discriminate we use the indicator from Ilbert et al. (2013). This indicator is based on a rest-frame colour selection: galaxies with $M_{\rm NUV} - M_r > 3(M_r - M_J) + 1$ and $M_{\rm NUV} - M_r > 3.1$ are considered to be quiescent (Figure 2.1). This colour selection was chosen instead of a U-V versus V-J selection because of the larger dynamical range. The NUV rest-frame can also be sampled by optical data while the U band falls out of this wavelength range at $z > 2$. Furthermore, the NUV-r seems to be a better indicator of current SF activity (e.g. Martin et al., 2007; Ilbert et al., 2013).

Because we only use the colour-colour selection we do not segregate starburst galaxies (galaxies that lie above the MS). This means that our average SFR estimates for the MS will be enhanced by 12.1 per cent relative to other methods which exclude the starburst galaxies from their sample (Sargent et al., 2012). This 12 per cent represents the increase in the mean SFR changing from a single log-normal distribution for the MS only to a MS+starburst distribution as described by two offset log-normals (Sargent et al., 2012).

2.4 METHOD

2.4.1 Sample selection

Many methods have previously been used to probe the environment of galaxies. The most reliable methods of determining if a galaxy is located in a cluster, has close companions

or resides in a dense environment rely on the use of spectroscopic redshifts. However, spectroscopy is time-consuming to obtain and is not practical for large numbers of galaxies over a large luminosity and redshift range, which are needed to exploit the full potential of HELP.

To avoid this problem, we use photometric redshifts. The main disadvantage of photometric redshifts is that they are not accurate enough to associate a given galaxy with a given structure; the physical scale associated with the uncertainty in photometric redshift is normally much larger than the size of a galaxy cluster. However, for a large galaxy sample we can statistically infer that galaxies found in dense regions according to their photometric redshifts will also be in dense environments in real space (Lai et al., 2016).

Several methods have been developed to extract the environmental density of galaxies using their spatial distribution. Some of the most commonly used methods are the Nth nearest neighbour method (N divided by the area containing N neighbours), galaxy counts in a circular (adaptive) kernel, and the Voronoi tessellation method (e.g. Muldrew et al., 2012; Scoville et al., 2013).

The redshift range we used to make maps of the density of galaxies was selected carefully to optimise the accuracy of the density map. For lower redshifts the volume of the COSMOS field is too small to be useful, and does not accurately probe a range of environments. On the other hand, at higher redshift the photometric redshifts become more uncertain and the number densities decrease, so we restrict ourselves to the range $0.1 < z < 3.2$ (Darvish et al., 2015b). The typical photometric redshift error increases with magnitude, so we only consider galaxies with $K_{\rm sAB} < 24$. We made this magnitude cut to use all available galaxies with accurate redshifts. However, by making this cut we only select relatively bright galaxies in the mass range for which we are incomplete. This can result in an overestimation of the mean SFR for low mass galaxies because we do not detect galaxies with a low SFR. Note that we cannot see this effect in Figure A.1 because the galaxies are weighted according to their mass, leading to a very small contribution of the few galaxies below the mass limit. Furthermore, we only consider those galaxies outside the optically masked areas defined by Ilbert et al. (2013).

To obtain sufficiently large samples, while exploring the evolution across time and environment, we divide galaxies into bins of redshift and density. We defined nine bins in environment and five in redshift so that each subset would contain approximately 11 per cent of the actively star-forming galaxies at that redshift. This yields > 1400 active star-forming galaxies in every bin (Table 2.1).

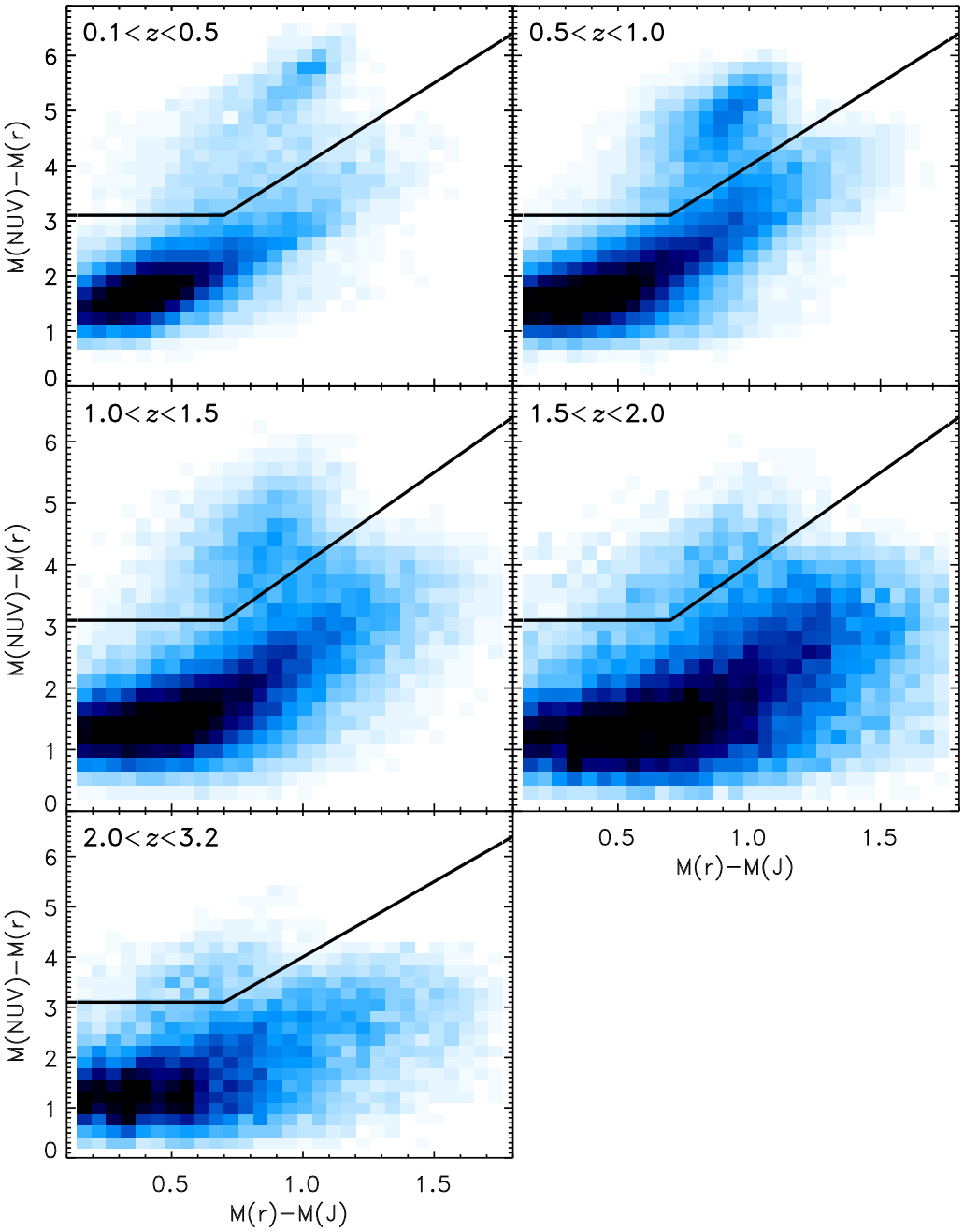

Figure 2.1: The colour selection used to separate the star-forming and quiescent galaxies. Galaxies with $M_{\rm NUV} - M_r > 3(M_r - M_J) + 1$ and $M_{\rm NUV} - M_r > 3.1$ are considered to be quiescent.

In Section 2.4.2 we describe how we obtained the environmental information for our sample of galaxies, and in Section 2.4.3 we describe our method to assign flux densities to the galaxies with the use of stacking.

2.4.2 Density estimates

The density maps are constructed using the adaptive Gaussian kernel procedure from Darvish et al. (2015b). This method uses a Gaussian kernel (with an adaptive width) to smooth the map, and therefore gives an estimate for the density at the scale of the kernel width. This choice of method was made on consideration of tables 3 and 4 of Darvish et al. (2015b), where the kernel method performed best in simulations. Another advantage of the kernel method is its simplicity and the intuitive way in which the weights are assigned to a galaxy. We adopt the same adaptive kernel size, angular position cut, magnitude selection and overlap between redshift slices as used by Darvish et al. (2015b). However, we make some changes in the application of weights and the edge corrections.

Our method is as follows:

- We construct a series of redshift slices starting at $z = 0.1$ and with a width ($\delta z = 2\Delta z_{\rm med}$), where $\Delta z_{\rm med}$ is the median of the photo-z uncertainty of galaxies within that redshift slice. Each redshift slice starts in the middle of the previous slice. For galaxies without a second peak in the PDF (with a probability bigger than 5 per cent for the second peak) we make a Gaussian assumption for the shape of the PDF (Darvish et al., 2015b).

- Every galaxy is distributed between all slices according to the PDF (Burton et al., 2013). If a galaxy has a probability of 60 per cent to be in slice a and 20 per cent to be in slice b then the weight (w) in slice a will be 0.6 and for slice b will be 0.2. In Darvish et al. (2015b), a galaxy can influence the density maps in adjacent slices since slices are overlapped.

- Within a slice the local density ($\hat{\Sigma}_i$) at a galaxy position ($\bar{r}_i$) is determined by a weighted adaptive kernel estimator with a global width h of 0.5 Mpc, following Darvish et al. (2015b):

$$\hat{\Sigma}_i = \frac{1}{\sum_{j=1,j\neq i}^{N} w_j} \sum_{j=1,j\neq i}^{N} w_i K(\bar{r}_i, \bar{r}_j, h), \tag{2.1}$$

$$K(\bar{r}_i, \bar{r}_j, h) = \frac{1}{2\pi h^2} \exp\left(\frac{-|\bar{r}_i - \bar{r}_j|^2}{2h^2}\right), \tag{2.2}$$

where $\bar{r}_j$ is the position of a galaxy with weight w_j. Rather than adopting a uniform value for h over the whole field, the local kernel width changes adaptively in accordance with the density of galaxies, with smaller kernel values in more crowded regions:

$$h_i = 0.5\text{Mpc}\left(G/\hat{\Sigma}(\bar{r}_i)\right)^{0.5}, \tag{2.3}$$

where $\hat{\Sigma}(\bar{r}_i)$ is the galaxy density at position $\bar{r}_i$ calculated with $h = 0.5$ Mpc and G is the geometric mean of all $\hat{\Sigma}(\bar{r}_i)$. The density field ($\Sigma(\bar{r})$) is then obtained by

$$\Sigma(\bar{r}) = \frac{1}{\sum_{i=1}^{N} w_i} \sum_{i=1}^{N} w_i K(\bar{r}, \bar{r}_i, h_i), \tag{2.4}$$

with $\bar{r} = (x, y)$ is the location in our 2D grid map.

- As a convenient, dimensionless, measure of the galaxy environment, we define the over-density for a galaxy at position $\bar{r}$ by the density at that position in the map divided by the median density of every position in the slice:

$$1 + \delta = \frac{\Sigma(\bar{r})}{\text{median}\left(\Sigma(\bar{r})\right)}. \tag{2.5}$$

- For scientific analysis, Darvish et al. (2015b) discarded those galaxies that were close to the edge or masked areas. We correct for the underestimation of densities near edges and masked areas using a different method. We create 40 mock maps in which the galaxies within a given redshift slice are given angular coordinates of galaxies selected randomly from all redshift slices. We divide the observed density field by the average of the mock density field. To avoid errors introduced by large corrections in the proximity of heavily masked regions, we exclude all areas in which the density in the mock map is less than half the mean. With this method we can still use galaxies relatively near the edge without introducing spurious low-density environments (see Figure 2.2).

Our density maps optimally exploit the redshift PDF information for a smoothing kernel that is adaptively smoothed in the transverse direction, but is convolved with a discrete, top-hat kernel in the radial direction. In future work for HELP we will amend the method to provide an adaptive kernel in 3D.

Having determined the density field, we can then assign a density to each galaxy. This assigned density is the measurement of the density at the angular position of the galaxy in the redshift slice where the photo-z PDF is highest.

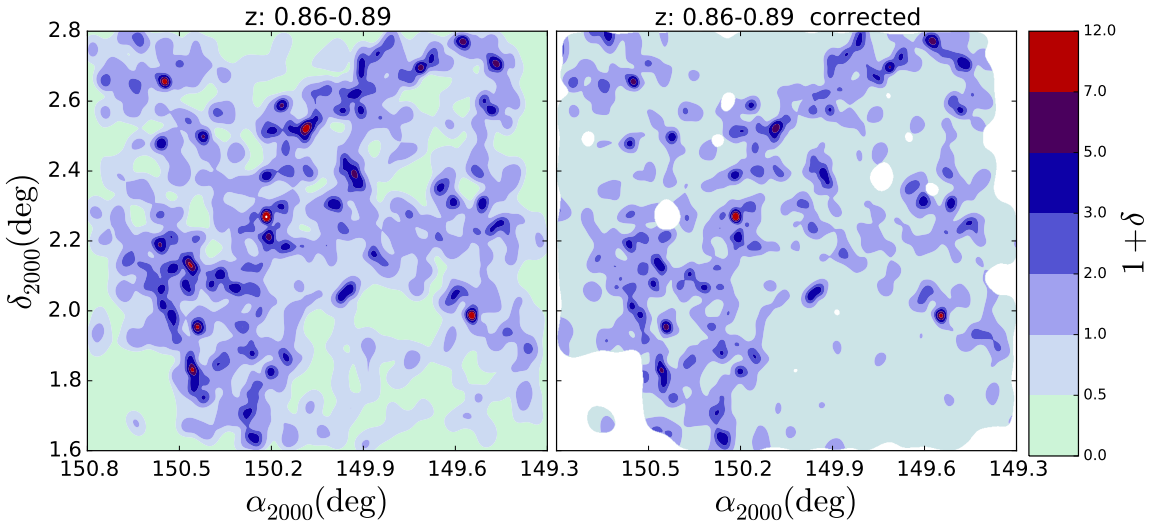

Figure 2.2: One of the redshift slices in the COSMOS field. On the left we show the density map, using essentially the method of Darvish et al. (2015b), with slight modifications of the original method. On the right we show the same map but divided by the average of 40 mock maps. Regions where the mock map has a density less that half of the mean density in the slice are not taken into account (white areas).

Since the absolute density and the over-density field evolve significantly with time through gravitational instability, we define the environment with reference to the surface density percentiles. In each redshift bin, we compute the density percentiles using every redshift slice within that redshift bin. We use these percentiles to create nine density bins, and we assign galaxies to the density bin appropriate to their density (Table 2.1). To some extent, the environments defined by density percentiles are fixed with cosmic time, i.e. galaxies in the densest 5 per cent of the Universe today are expected to have been in the densest 5 per cent regions at an earlier time.

2.4.3 SIMSTACK

Our aim is to measure the average star formation activity of galaxies aggregated by redshift and environment, while taking into account variations across bins, e.g. in the empirical relation between star formation and stellar mass – the "main-sequence". To do this we use a flux stacking technique, with a weighting scheme to account for these known variations. We are using a stacking technique to get around the confusion problem: for one individual galaxy we cannot say what the contribution from non-correlated background sources is, but the mean contribution for a random stacked sample goes to zero in a mean subtracted map.

Density percentile	Redshift ranges									
	0.1<z<0.5		0.5<z<1.0		1.0<z<1.5		1.5<z<2.0		2.0<z<3.2	
	$N_{\rm gal}$,	$f_{\rm sf}$	$N_{\rm gal}$,	$f_{\rm sf}$	$N_{\rm gal}$,	$f_{\rm sf}$	$N_{\rm gal}$,	$f_{\rm sf}$	$N_{\rm gal}$,	$f_{\rm sf}$
0 – 40	4148	0.91	8353	0.91	7505	0.90	5756	0.95	3493	0.95
40 – 55	3037	0.91	6471	0.90	5612	0.90	3528	0.94	2870	0.95
55 – 65	2751	0.92	5480	0.89	4739	0.90	2869	0.94	2384	0.95
65 – 75	3292	0.89	6981	0.88	5666	0.90	3368	0.95	2952	0.95
75 – 85	4292	0.89	9247	0.87	7086	0.90	3995	0.95	3607	0.95
85 – 90	2770	0.86	5694	0.86	4342	0.89	2358	0.94	2213	0.95
90 – 95	3587	0.85	7274	0.84	5040	0.89	2688	0.94	2509	0.96
95 – 97.5	2401	0.82	4581	0.83	3057	0.89	1614	0.93	1489	0.96
97.5 – 100	4048	0.66	7168	0.76	3952	0.87	2051	0.93	1726	0.97
all	30 326	0.85	61 249	0.86	46 999	0.90	28 277	0.94	23 243	0.95

Table 2.1: Number of galaxies ($N_{\rm gal}$) in the percentile bins we use for stacking, and the star-forming fraction ($f_{\rm sf}$) Every bin of star-forming galaxies contains over 1400 galaxies, leading to a reliable stacked signal. The density percentile bins where chosen to approximately obtain the same number of galaxy in every density percentile bin, but for comparison we fixed the density percentile bins over redshift. Due to this combination there is a slight variation in the number of galaxies per density bin.

We use SIMSTACK (Viero et al., 2013a) as our stacking tool. SIMSTACK simultaneously estimates the average flux density for a number of samples of galaxies, modelling the SPIRE map by assuming that all galaxies in this sample to have the same flux density. Viero et al. (2013a) segregated galaxies according to their stellar mass and redshift, and characterised how the FIR emission depended on these parameters.

The SIMSTACK algorithm has been used and tested by several papers (Alberts et al., 2014; Banerji et al., 2015; Béthermin et al., 2015; Viero et al., 2015; Webb et al., 2015; Noble et al., 2016). It works optimally for large samples of galaxies which are expected to have a similar flux density.

Even in our highest redshift bin, we have over 23 000 galaxies simultaneously fitted by SIMSTACK, so random foreground and background sources will not affect our results.

In Table 2.1, we list the number of galaxies in each redshift bin used in our stack. We ran SIMSTACK simultaneously on the star-forming and quiescent sample to avoid overestimating the SFR in dense environments due to confusion with nearby quiescent sources. Because SIMSTACK simultaneously fits all galaxies, it will give reliable values for the stack in both the field and for cluster galaxies. Only galaxies below the detection limit (in $K_{\rm s}$) and correlated with our target sample can affect the result. This effect should be larger in the clusters, but we expect these "non detected galaxies" to have low SFR (and low flux density in the SPIRE bands) and therefore they should not change our results very much. If they have any effect it would be to increase our estimates of the SFR in dense environments.

To account for the known internal variation within the bins we model the relationship between the FIR emission, stellar mass and the redshift of the galaxies. Since we are interested in relative measurements of SFR (in different environments) we do this by using weights in the stacking code. Essentially, these weights scale the contribution of each galaxy in the flux stack to what would be emitted by a reference galaxy at the centre of the redshift bin and with a reference stellar mass, see Section 2.4.3 for more detail.

Redshift weighting

Within each redshift bin, there is a distribution of redshifts. The nearby ones will appear to be brighter, without having intrinsically higher luminosity or SFR. We correct for this effect following Oliver et al. (2010a). We weight the galaxies by w_d, which comes from the square of the luminosity distance (D_L) relative to that of the middle of the redshift bin ($z_{\rm ref}$):

$$w_d = \left(\frac{D_{\rm L}(z_{\rm ref})}{D_{\rm L}(z)} \right)^2 . \tag{2.6}$$

Another adjustment originates from the K correction, the SPIRE flux densities sample different parts of the rest-frame spectrum (I_λ) for galaxies at different redshifts. We estimate the weight (w_k) for the K correction for an observed frequency (ν_0) and luminosity (L_ν) to be the ratio of the rest-frame flux density for an object at redshift z to that of the value at the middle of the bin:

$$w_k = \frac{1+z}{1+z_{\rm ref}} \frac{L_\nu([1+z]\nu_0)}{L_\nu([1+z_{\rm ref}]\nu_0)}. \tag{2.7}$$

We use template SEDs provided by Berta et al. (2013), which fits the median SED in the FIR (with at least seven FIR bands) for different spectral types of galaxies. As a first approximation, we use the spiral galaxy template for the star-forming systems, and the elliptical template for the quiescent galaxies. Later this formed the basis for an iteration described at the end of Section 2.4.3.

Another weight (w_e) arises from the known evolution in the MS with roughly $(1+z)^\gamma$; that is if a galaxy has a higher redshift we expect a higher flux density due to relatively higher star formation:

$$w_e = \left(\frac{1+z}{1+z_{\rm ref}} \right)^\gamma . \tag{2.8}$$

Here we initially used $\gamma = 3$, and again this was the basis for an iteration. The overall effect of all these corrections is summarised in Table 2.2. Since all of the corrections depend on redshift, we combine them to obtain a redshift dependent combined weight (w_z) for every galaxy in the stack:

$$w_z = w_d \times w_k \times w_e. \tag{2.9}$$

Mass weighting

To characterise the stellar mass dependence of the FIR emission, we follow the procedure explained by Viero et al. (2013a). We bin galaxies according to mass, redshift and galaxy type. We need several mass bins to obtain a good fit for the MS. For the star-forming galaxies we select the mass bins to contain either a total stellar mass of $10^{14}{\rm M}_\odot$ and a minimum of 100 galaxies, or $10^{15}{\rm M}_\odot$ and 50 galaxies. These mass bins were chosen so that each yield a clear detection of the stacked results in the SPIRE maps, and in the case that the slope of the MS is 1 these bins will all have approximately the same total signal. The quiescent galaxies are all placed in one bin.

Redshift bin	Weighting				
	$\langle w_k^2 \rangle$			$\langle w_e^2 \rangle$	$\langle w_d^2 \rangle$
	250 μm	350 μm	500 μm		
0.1 – 0.5	0.040	0.067	0.099	0.038	3.552
0.5 – 1.0	0.015	0.042	0.077	0.039	0.313
1.0 – 1.5	0.002	0.016	0.038	0.024	0.094
1.5 – 2.0	0.000	0.006	0.018	0.016	0.046
2.0 – 3.2	0.000	0.012	0.035	0.037	0.125

Table 2.2: Mean square deviation of the redshift-dependent weights. Each weight, w, normalises galaxies at different redshifts to a reference point at the centre of the bin. Columns 2 to 4 show the weight that arises from the change in observed SED due to the K correction. The fifth column shows the weight for the evolution of the MS over time. The last column shows the weight for the luminosity distance. For this table no distinction is made between galaxies in different environments.

From this set of stacked results, we can fit a mass versus (redshift corrected) SPIRE flux density relation. This relation can be seen as a MS (Elbaz et al., 2011) though with the redshift-corrected (w_z, Equation 2.9) FIR flux density as a proxy for SFR. We exploit the fact that the integrated FIR flux density is expected to be proportional to the SFR, therefore we can use the model normally used to fit the MS:

$$\log \mathrm{SFR} \propto \log S_{\mathrm{SPIRE}} = \alpha \log(M) + \beta. \tag{2.10}$$

Here S_{SPIRE} is the measured flux density with `SIMSTACK`. We fit the parameters α and β, constraining the slope, α, to be the same for the three bands. The results are shown in Figure A.1. This enables us to apply a weight in comparison with a galaxy of reference stellar mass, $\mathrm{M_{ref}}$:

$$w_{\mathrm{mass}} = \frac{10^{\alpha \log(M)+\beta}}{10^{\alpha \log(M_{\mathrm{ref}})+\beta}} = 10^{\alpha \log(M/M_{\mathrm{ref}})}. \tag{2.11}$$

We set M_{ref} to a stellar mass of $10^{10}\mathrm{M}_{\odot}$, so that the stacked results give us the average flux density of a star-forming $10^{10}\mathrm{M}_{\odot}$ stellar mass galaxy at the middle of the redshift bin. We also use this slope α for the quiescent bin.

Having determined the weighting factors, we can use `SIMSTACK` to compute the mean, normalised SPIRE flux densities, aggregated in bins of redshift and environment. Our procedure also allows us to normalise the known variations with redshift and stellar mass to the centre of each redshift bin and for this reference stellar mass.

Our results are independent of choice of $M_{\rm ref}$. If we had selected a different $M_{\rm ref}$ then $w_{\rm mass}$ would change for every galaxy accordingly, and the output of `SIMSTACK` would be the flux density of the new $M_{\rm ref}$ (we fit all the galaxies at the same time given the weights calculated in equation 2.9 and 2.11). The underlying assumption for this is that all the galaxies follow the same slope in the Mass versus SFR plane (α, equation 2.10), at a certain redshift. With `SIMSTACK` we find the normalisation of this line at $M_{\rm ref}$ and it is this normalization that we track in different environments.

In total we had four runs with `SIMSTACK`. The first run was with the parameters described above, from which we got a first estimate for our best SED template, α and γ. For the second run we used these best values as input for our weights (equations 2.9 and 2.10). A third run was used to optimise the results for the fourth and final run, Section 2.4.4.

2.4.4 SFR estimation

Having determined the mean, normalised SPIRE flux densities in each SPIRE band, we estimate a total integrated FIR luminosity (and hence SFR) for each redhift and density bin.

We find the best fit SED through a least-squares fit from the library of Berta et al. (2013) to the mean normalised flux densities in the three SPIRE bands. The SPIRE bands probe the peak of the SED for intermediate redshifts and this gives us the most accurate SED normalisation. PACS data (Poglitsch et al., 2010) could be added and would probe the peak of the FIR emission better in our lowest redshift bin; however, due to differences in the map-making procedure (i.e. the non linear map making in PACS), and higher noise in the PACS data, we choose not to include these data in our analysis to avoid introducing biases into the sample (Lutz et al., 2011).

Different SEDs are allowed for star-forming galaxies and passive galaxies and for different redshift slices. However, we use the same template for different stellar mass bins and environments at the same redshift. The best templates for every redshift bin are listed in Table A.1.

With this SED template, we compute the total FIR luminosity $L_{\rm FIR}$ integrated over the rest-frame spectrum (L_ν) between 8 μm and 1000 μm. This process is performed iteratively with the weighting processes in Section 2.4.3, i.e. applying the K-correction using the optimum template.

We then compute the SFR from $L_{\rm FIR}$, using the following calibration (Rowan-Robinson

et al., 1997, 2008; Oliver et al., 2010a)[2];

$$\frac{L_{\rm FIR}}{\rm L_\odot} = 0.51 \times 10^{10} \frac{\rm SFR}{\rm M_\odot yr^{-1}}. \tag{2.12}$$

Here the fraction of ultraviolet energy absorbed by dust has been assumed to be $\epsilon = 2/3$. Because we are stacking, we use a fixed value of ϵ, but ideally we would need this value for every galaxy. The HELP project will eventually assist in obtaining more information about the variation of ϵ, but that is beyond the scope of this paper.

2.5 RESULTS

2.5.1 SFR in different environments

Our resulting SFR for the reference stellar mass in different environments and different redshifts are shown in Figure 2.3. We test our results against a constant MS for all environments and a toy model for which we fit a straight line to the SFR versus percentile density. A fit to the evolution of this reference SFR (i.e. a normalisation of the main-sequence) yields $(1+z)^{2.4}$; this evolutionary rate was used to iteratively re-calculate the weights, w_e, used in Section 2.4.3.

We construct the error bars (σ_{tot}) as a quadrature sum of the jackknife error (σ_{jk}), which covers the random errors associated with the sample variations within a bin) and the error (σ_z) from re-sampling our redshifts from the PDF (which covers the systematic errors from the uncertainty in the redshift of each galaxy):

$$\sigma_{tot}^2 = \sigma_{JK}^2 + \sigma_z^2. \tag{2.13}$$

From Figure 2.3 we can see that there is no dramatic trend in the reference SFR as a function of environment at any epoch. Because our reference SFR has scaled every galaxy to the MS this indicates that the MS is roughly the same in every environment. However we can confirm that the SFR for star-forming system increases over cosmic time with roughly $(1+z)^{2.4}$.

An additional subtle trend is worth noticing. In the range $0.1 < z < 2$ there appears to be a slight decline in SFR towards higher densities. We quantified this by calculating the reduced χ^2 for a declining toy model. This toy model (red dashed line in Figure 2.3) has a lower reduced χ^2 in all of our redshift bins, indicating a lower MS in dense

[2]This calibration is based on a Salpeter (1955) IMF, to convert to other mass functions we refer to Madau and Dickinson (2014) and Rowan-Robinson et al. (1997) for conversion factors.

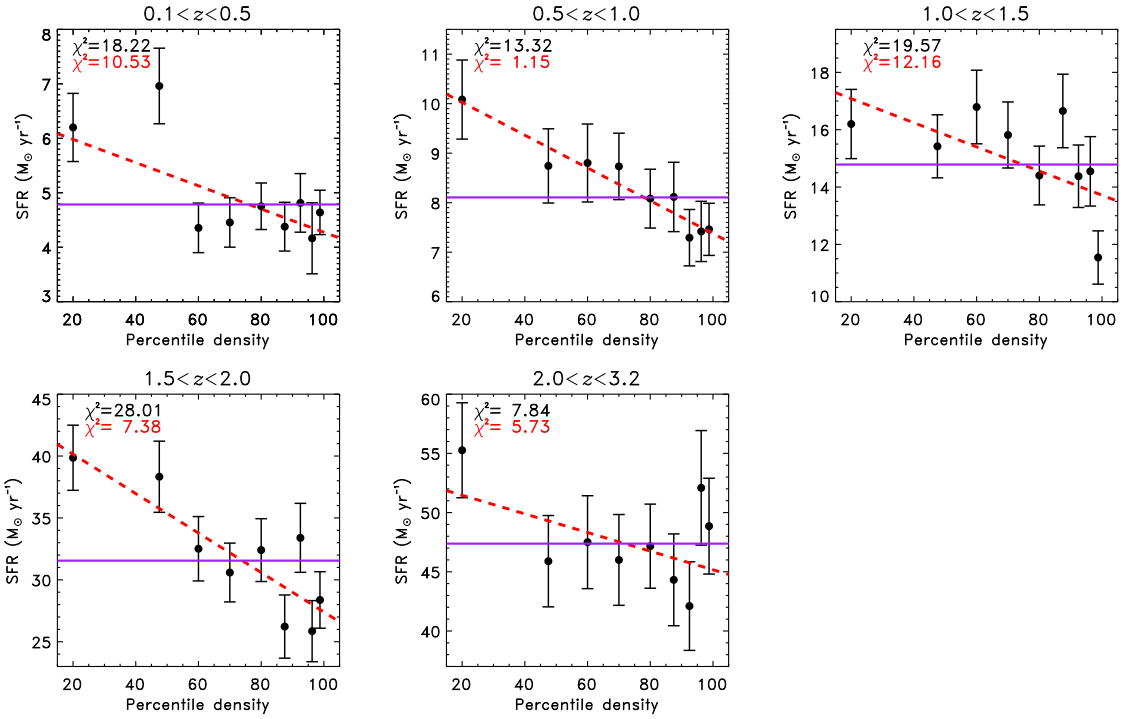

Figure 2.3: SFR of a $10^{10}M_{\odot}$ stellar mass star forming galaxy in the COSMOS field versus environment density for different redshift bins. $10^{10}M_{\odot}$ is the used $M_{\rm ref}$ in Equation 2.11, and is the normalisation of the MS with slope α at the given density percentile. The black symbols represent the weighed mean of the calculated SFR of the three SPIRE bands (Figure A.2). The purple line represents the average value, the value of the SFR which should arise from a constant MS over different environments. In the top left corner, the χ^2 value for an environmental-independent star formation (8 degrees of freedom, $N_{\rm dof}$) is noted in black. It is clear that the star formation rate increases at higher redshift (the mean SFR is significantly higher in every higher redshift band). At intermediate redshift ($0.1 < z < 2$) a simple toy model (the line with the lowest χ^2 in dashed red, 7 degrees of freedom) of a declining MS over environment seems to be a better fit (has a lower $\frac{\chi^2}{N_{\rm dof})}$). In the redshift range $1.5 < z < 2$ this toy model has a reduced χ^2 around one (indicating a good model), where the purple line has a $\frac{\chi^2}{N_{\rm dof})} > 3$ indicating that we can exclude this model for this redshift range. This effect is small (though marginally significant in a statistical sense), and both models (red and purple) are well within the intrinsic scatter of the SFRs in the MS.

environments. This is in agreement with Vulcani et al. (2010) and Patel et al. (2011) who found a lower SFR for star-forming galaxies in cluster environments. Similarly Allen et al. (2015) found that the mean observed F814W−F160W colours for star-forming cluster galaxies at $z \sim 2.1$ are 20 per cent ($3.6\,\sigma$) redder (indicating a lower SFR) than for field galaxies at the same masses, indicating a suppressed MS. Note that in Figure 2.3 we have not included the systematic error on the SFR, because the effect of taking the wrong SED template is to move all data points up or down together. We have omitted this error for our comparisons of different regions (see Appendix B for more detail about the error analysis).

In the redshift range $1.5 < z < 2$ the declining toy model has a reduced χ^2 close to one, indicating a good fit, where the environment independent model has a reduced χ^2 greater than three. We conclude that our data at $1.5 < z < 2$ is inconsistent with the hypothesis of an environmental independent MS with significance at level of 1 per cent, measured using p-value. However, this is a small effect and all our data falls well within the 0.2 dex intrinsic scatter of the SFRs in the MS. In the other redshift bins we cannot exclude the simple hypothesis.

We can also use the stacked, normalised, SFRs to assign an estimated SFR to every galaxy (taking into account its stellar mass and the weights applied). With this SFR for each galaxy we can produce estimates for the SFR-density in the COSMOS field.

2.5.2 Cosmic variance

Figure 2.3 does not include the effect of "cosmic variance", i.e., the possibility that our measurements in the COSMOS field, may not be representative of the Universe as a whole[3]. We consider this to be an uncertainty only in the environmental metric, i.e. that the characterisation of the SFR for a population is unaffected by cosmic variance but that the density percentile ascribed to that population is.

Our primary environmental metric is the percentile of the density field. This is based on the over-density estimate, δ, and so we consider the uncertainty in this in the following way:

The fractional error in over-density, δ, for dark-matter halos, or galaxy populations in a finite volume, is determined by the statistics of the density field and is the normal "cosmic-variance" metric. The "cosmic-variance" depends on the geometry of the field

[3]We use the term "cosmic variance" here, as is common in the galaxy cluster literature, although we appreciate the phrase is also used to refer to uncertainties due to the finite size of the observable Universe, and therefore some prefer "sampling variance" for uncertainties for a finite field size.

Redshift bin	Effect of cosmic variance in $(1+\delta)$
0.1 – 0.5	13.1–14.5 per cent
0.5 – 1.0	7.2– 8.1 per cent
1.0 – 1.5	6.0–7.5 per cent
1.5 – 2.0	5.9–7.8 per cent
2.0 – 3.2	5.0–10.0 per cent

Table 2.3: Cosmic variance quantified in percentage error on $1+\delta$ over our redshift bins. The two values in the second column represent the cosmic variance for the lowest and highest density region respectively.

and the clustering strength or "bias" of the population under consideration. Moster et al. (2011) provide a tool, `getcv`, for calculating this variance using a halo occupation model to characterise the galaxy bias and clustering as a function of redshift and stellar mass. Our populations are segregated by local environment rather than stellar mass, and so we cannot use this tool directly. Instead we approximate it by assuming that bias follows the rarity of the samples under-consideration, e.g. if we take the galaxies in the top 11 per cent of dense environments we assume that they will have the same bias (and thus cosmic variance) as the 11 per cent most massive galaxies (as in abundance matching). Using the same stellar mass function as Ilbert et al. (2013) then allows us to estimate the stellar mass of galaxies with the same abundance.

To map this uncertainty in over-density to an uncertainty in percentile density is less straightforward. We take a conservative approach, assuming that the uncertainty in percentile is compounded by the uncertainty in the mean density of the COSMOS field as a whole. Again we use the code *getcv* to determine cosmic variance for dark matter halos in our redshift bin, which can be translated to the uncertainty on the mean density of the field.

Combining the variance estimates on the density for certain type of galaxy in quadrature with the variance on the mean density provides us with an estimate of the effect of cosmic variance on our galaxy bins (see Table 2.3).

This effect could be represented as a horizontal error bar in Figure 2.3. However, it should be kept in mind that this is a systematic effect and not a measurement error. The values in Table 2.3 suggest that if we had carried out the same analysis on a different part of the sky, we would have found different values of $1+\delta$ for the galaxies. If one wishes to compare our absolute results with those from a different field this effect should be taken

into account. However, the density estimates for our individual galaxies originate from the same field, and so the relative environmental ranking should be unaffected by cosmic variance, for this reason we did not plot this error bar in Figure 2.3.

An example of the effect of cosmic variance in the COSMOS field is the $z = 0.73$ large scale structure found by Guzzo et al. (2007). The effect of such a structure is that the mean density of that particular redshift slice increases. Therefore the overdensities assigned to the galaxies in that redshift slice will be slightly lower than the overdensity we assign to a galaxy in a similar environment in another redshift slice.

2.5.3 SFR density

With our estimates of individual galaxy SFRs we can calculate the SFR density (for galaxies with stellar mass $> 10^8 M_\odot$) of the COSMOS field, and we plot this in Figure 2.4. We correct for incompleteness by using the mass function of Ilbert et al. (2013) to calculate the number (and the mass) of galaxies which we do not observe. With our estimate for the MS we can assign a SFR to these galaxies and add this to the observed SFR density.

We estimate errors in these SFR densities using jackknife samples over the map combined in quadrature with errors from the mass function correction (Ilbert et al., 2013) and an estimate of the systematic error in the template fitting. The full error analysis is discussed in Appendix B.

Our SFRD results follow the curve of Madau and Dickinson (2014), with only a difference in the peak which is higher by a factor of $1.4^{+0.3}_{-0.2}$. This result is in agreement with recent SFRD estimates from the FIR, using 500 μm detected sources (Rowan-Robinson et al., 2016).

We can also use the same SFRs and arrange the galaxies over the density regions to obtain SFR density estimates for different density environments over cosmic time (Figure 2.5). With this analysis, we cannot see a significant difference in the evolution of the SFR density for different environments. From our highest to lowest density sample we find a 73, 79 and 86 per cent decline in the SFRD.

This result is in slight tension with Guglielmo et al. (2015) who found a steeper decline in the SFRD for cluster galaxies than for field galaxies. Guglielmo et al. (2015) used local cluster/field galaxies and probed the SFRD(z) by constructing the SFR-history of these samples. We look at the total instantaneous SFR as a function of cosmic time and environment. These two different ways to determine the SFR could lead to different results (e.g. Shamshiri et al., 2015).

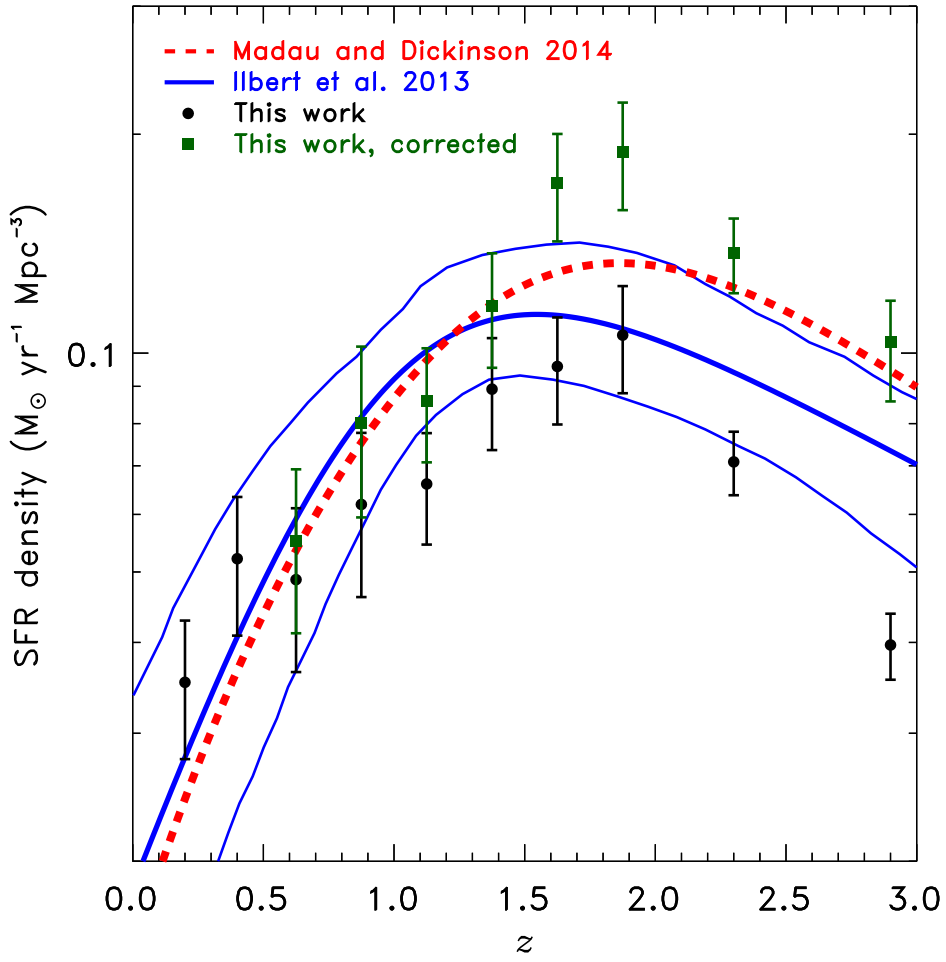

Figure 2.4: SFR density for galaxies with stellar mass $> 10^8$ $M_\odot$ as function of redshift (black symbols); error bars include variance in the bias from choosing different templates, as well as the jackknife errors over the map. The green squares represent our completeness-corrected sample (and include the uncertainty associated with this correction). For comparison the results from Madau and Dickinson (2014) and Ilbert et al. (2013) are shown in red (dotted) and blue respectively. The results from Ilbert et al. (2013) are converted to a Salpeter IMF using the conversion constant from Madau and Dickinson (2014).

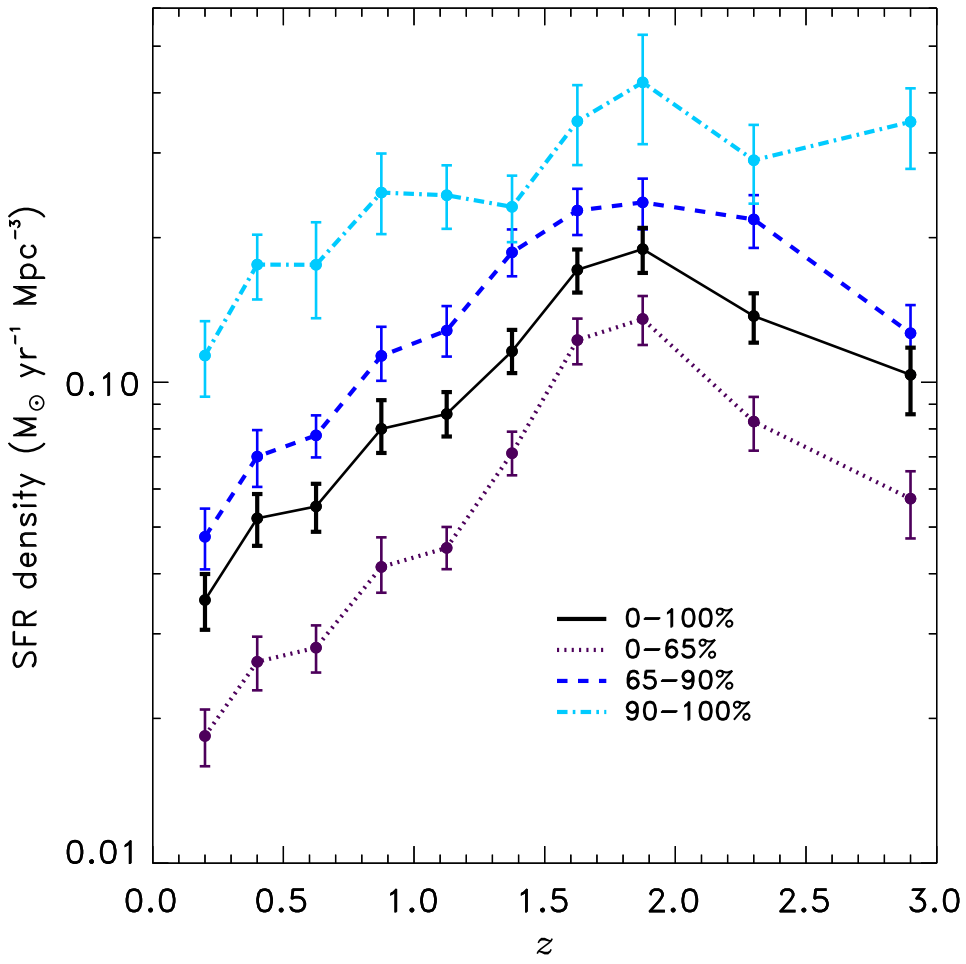

Figure 2.5: SFR density for four different percentile density regions as a function of redshift. The volume used to calculate the density is the volume of the percentile region, not the total volume of the field. There are no significant differences in the evolutionary trends of the four sub-samples. This figure also shows that although galaxies corresponding to the highest density sample themselves might have a lower star formation per unit mass, this population of galaxies still has a higher star formation per unit volume than the low density sample at every redshift. All data points have been corrected for incompleteness, but the bias in the templates is not taken into account here.

2.6 Discussion

It is interesting to explore possible explanations for the weak evidence that the typical SFR might be lower in denser environments, particularly in the range $1.5 < z < 2$. This lower MS was previously found at redshifts lower than 1 (e.g. Vulcani et al., 2010; Patel et al., 2011; Paccagnella et al., 2016). This result may be spurious if the photometric redshift errors are significantly larger for the more extreme star-forming systems (i.e. those with higher sSFR) at higher redshift, scattering them out of overdense regions. But if real, this could be very interesting. These redshifts correspond to the epoch of the peak of star formation activity and it is possible that we are actually witnessing the transition from star-forming to quiescent galaxies. At $z > 2$ the densest regions appear to follow the same star formation relation as lower densities. However, below $z < 2$ those star-forming galaxies might be expected to fall into the cluster and star formation begins to shut down. During the first part of this process these galaxies will still be classified as "star-forming", but the star formation rate is reduced relative to the stellar mass, lowering the average. This explanation would fit with results that show that *Herschel* maps exhibit strong clustering, compatible with halo models in which star formation at $z \sim 2$ occurs in rich groups (Viero et al., 2013b).

It is important to remember that the subtle, but statistical significant differences we find in the MS over different environments is smaller than the intrinsic scatter (of 0.2 dex) of the SFR in the MS. Our results come from a mean stack which includes starburst galaxies, i.e. galaxies off the MS. These small environmental effects may come from MS galaxies or starburst galaxies. At low redshift starburst are merger driven and more prominent in intermediate and less dense environments (e.g. Scudder et al., 2012b; Madau and Dickinson, 2014). However at higher redshift the clustering of Herschel sources (Cooray et al., 2010) and maps (Amblard et al., 2011; Viero et al., 2013b) indicate that galaxies with high SFR are found in denser environments.

At $z < 1.5$ and $z > 2.0$ we cannot formally exclude a hypothesis that the star formation rate verses stellar mass relation (i.e. the "main-sequence") is the same for every environment. That hypothesis has been supported by other observations, although it is somewhat surprising theoretically, implying that environmental effects can change the relative proportion of galaxies that are star-forming or passive, but not the average SFR of the star-forming galaxies themselves (e.g. Peng et al., 2010). This implies that the environmental effects result in a rapid truncation of star formation (Darvish et al., 2016).

This tantalising result raises several questions, which are beyond the scope of this

paper. For example, can we confirm this weak trend with better statistics including other fields with less cosmic variance, and where we can see a broader range of environments? Does our result depend on how we classify galaxies to be star-forming or quiescent? How do our results depend on the accuracy of the photometric redshifts, both within COSMOS and extending to regions with poorer phot-z estimate? This shows the exciting opportunities that will come from exploiting the whole HELP data set, which will enable such analysis using multi-wavelength data over several fields.

2.7 Conclusions of chapter 2

We have undertaken an investigation of the dust-obscured star formation activity as a function of environment and redshift. We constructed a galaxy density field using an adaptive kernel smoothing and exploiting the full photometric redshift probability distribution function from the deep optical, NIR and IRAC data in the COSMOS field. We characterised the density fields in terms of percentiles to facilitate comparisons between redshifts. We employed a "stacking" technique to estimate the normalisation of the "main-sequence" (i.e. the correlation between the SFR and stellar mass). This techniques fits the Herschel SPIRE data from HerMES to all galaxies with photometric redshifts and stellar masses in the same redshift bin simultaniously.

A simple model in which the mean specific star formation rate for star-forming galaxies declines with increasing environmental density gives a better description at $0.1 < z < 2$ and is significantly better at $1.5 < z < 2.0$ with a reduced $\chi^2 \sim 1$ (q.v. $\chi^2 \sim 3$ for constant normalisation). At $z < 1.5$ and $z > 2.0$ we cannot exclude a simple hypothesis in which the main-sequence for actively star-forming systems is independent of environment over the range. We also estimate the evolution of the universally averaged star formation rate density in the COSMOS field and we find similarly strong evolution to previous studies though with a $1.4^{+0.3}_{-0.2}$ times higher peak value of the star formation rate density at $z \sim 1.9$. When deconstructing the contributions to this evolution by density percentiles we do not see any significant differences in the shape of the evolution and note that the higher density regions of the Universe contribute more to the cosmic star formation history despite having a lower specific star formation rate.

This works demonstrates the power of the *Herschel* SPIRE data when coupled with high-resolution data sets and demonstrates methodology that we will build upon to extend these studies to rarer higher density regions when exploiting the full 1300 deg^2 of data from the Herschel Extragalactic Legacy Project, HELP.

Chapter 3

Red, redder, reddest: SCUBA-2 imaging of colour-selected *Herschel* sources

3.1 Abstract of chapter 3

High-redshift, luminous, dusty star-forming galaxies (DSFGs) constrain the extremity of galaxy formation theories. The most extreme are discovered through follow-up on candidates in large area surveys. Here we present extensive 850 μm SCUBA-2 follow-up observations of 188 red DSFG candidates from the *Herschel* Multitiered Extragalactic Survey (HerMES) Large Mode Survey, covering 274 deg^2. We detected 87 per cent with a signal-to-noise ratio > 3 at 850 μm. We introduce a new method for incorporating the confusion noise in our spectral energy distribution fitting by sampling correlated flux density fluctuations from a confusion limited map. The new 850 μm data provide a better constraint on the photometric redshifts of the candidates, with photometric redshift errors decreasing from $\sigma_z/(1+z) \approx 0.21$ to 0.15. Comparison spectroscopic redshifts also found little bias ($\langle(z - z_{\rm spec})/(1 + z_{\rm spec})\rangle = 0.08$). The mean photometric redshift is found to be 3.6 with a dispersion of 0.4 and we identify 21 DSFGs with a high probability of lying at $z > 4$. After simulating our selection effects we find number counts are consistent with phenomenological galaxy evolution models. There is a statistically significant excess of *WISE*-1 and SDSS sources near our red galaxies, giving a strong indication that lensing may explain some of the apparently extreme objects. Nevertheless, our sample includes examples of galaxies with the highest star formation rates in the Universe ($\gg 10^3$ M$_\odot$yr^{-1}).

3.2 Introduction of chapter 3

Over the last few decades, great progress has been made in understanding the star formation history of the Universe (see e.g. review by Madau and Dickinson 2014). It has become apparent that observing at UV and optical wavelengths is insufficient as a large fraction of the star formation is obscured, resulting in dusty star-forming galaxies (DSFGs; see e.g reviews by Lonsdale et al. 1984; Cesarsky et al. 1996; Smail et al. 1997; Burgarella et al. 2013; Casey et al. 2014). The most extreme forms of obscured star formation at high redshift still pose serious challenges to galaxy evolution models (e.g. Baugh et al., 2005; Lacey et al., 2010; Narayanan et al., 2010; Hayward et al., 2013; Béthermin et al., 2017). The discovery and characterization of the rarest and most extreme galaxies (star formation rates, SFR, $\gg 10^3$ $M_\odot yr^{-1}$, number densities $\ll 10^{-4}\,Mpc^{-3}$, Gruppioni et al. 2013) is thus an important goal, but requires large volume surveys at long wavelengths.

This is now possible with deep large-area surveys ($\gg 10$ deg^2) at far-infrared (FIR) and sub-mm wavelengths with e.g. the South Pole Telescope (SPT; Carlstrom et al., 2011) and the *Herschel Space Observatory* (Pilbratt et al., 2010).

Follow-up of SPT sources has been very successful in finding high-redshift DSFGs (Vieira et al., 2013; Weiß et al., 2013; Strandet et al., 2016, 2017). The SPT source selection at a wavelength of 1.4 mm has however a broader redshift distribution than *Herschel* detected sources (Greve et al., 2012)

Herschel surveys cover a huge area $\sim 1300\,\mathrm{deg}^2$ (the largest being HerMES Oliver et al. 2012 and *H*-ATLAS Eales et al. 2010) and while most detections are associated with $z \sim 1-2$ starburst galaxies (e.g. Casey et al. 2012a; Casey et al. 2012b) it has been clearly demonstrated that selecting those with red colours is extremely efficient for identifying a tail extending towards higher redshift ($z > 4$) (Cox et al., 2011; Riechers et al., 2013; Dowell et al., 2014; Asboth et al., 2016; Ivison et al., 2016; Riechers et al., 2017; Donevski et al., 2017; Zavala et al., 2018). The challenge now is using these very large *Herschel* surveys to find and systematically study, large, homogeneous samples of rare, extremely luminous, $z > 4$ sources.

Asboth et al. (2016) probed this high-redshift population in the largest *Herschel* Multitiered Extragalactic Survey (HerMES) field, the HerMES Large Mode Survey (HeLMS, covering approximately 300 deg^2) by selecting all bright "500 μm riser" ($S_{500} > S_{350} > S_{250}$) DSFGs candidates. This sample was selected over an area a factor of 13 times larger than previous 500 μm riser HerMES surveys (Dowell et al., 2014). The number of sources that fulfilled these criteria (477) is an order of magnitude higher than predicted by galaxy

evolution models (Béthermin et al., 2011, 2012; Dowell et al., 2014)

Another large 600 deg^2 red DSFGs search in the H-ATLAS survey (Ivison et al., 2016) used a 3.5σ (30 mJy) detection threshold at S_{500} in combination with $S_{500}/S_{250} \geq 1.5$ and $S_{500}/S_{350} \geq 0.85$ colour selection criteria to obtain a sample of 7961 candidate high-redshift DSFGs. After a visual inspection (Ivison et al., 2016) a sub-sample of 109 DSFGs, candidates were selected for follow-up at longer wavelengths with SCUBA-2 or LABOCA.

All these red sources are candidates for high-luminosity sources. Some, particularly those with a flux density at $S_{500} > 100$ mJy, are likely to be strongly gravitationally lensed (Negrello et al., 2010; Conley et al., 2011; Nayyeri et al., 2016; Negrello et al., 2017) others may be blends (e.g. Scudder et al., 2016). Nevertheless, they are extremely interesting because, those that are not lensed, blended, or otherwise boosted may represent the most active galaxies in cosmic history.

In this work, we present a follow-up study of 188 of the brightest 200 ($S_{500} > 63$ mJy), of the 477 Asboth et al. (2016) objects using SCUBA-2 (Holland et al., 2013) on the James Clerk Maxwell Telescope (JCMT). With the addition of the S_{850} data provided by SCUBA-2 we have a better constraint on both the FIR luminosities and the redshifts of these DSFGs and prepare the way for high-resolution follow-up.

With our sample of 188 galaxies observed by SCUBA-2 we roughly double the number of 500 μm riser galaxies possessing longer submm wavelength data.

The format of this paper is as follows. We describe the data in Section 3.3. We describe our methods for determining the photometric redshifts, FIR luminosities and SFRs in Section 3.4. The results are described in Section 3.5, and the discussion and conclusions in Sections 3.6 and 3.7, respectively. We use a standard flat cosmology with $\Omega_{\rm M} = 0.3$ and $H_0 = 70$ km s^{-1}Mpc^{-1}.

3.3 Data

3.3.1 Selecting high-redshift dusty galaxies in HeLMS

We use the red HeLMS sample identified in Asboth et al. (2016) and below follows a short summary of their selection. The area mapped by HeLMS is a 300 deg^2 equatorial field which is part of the HerMES project. The observations were performed using the SPIRE instrument (Griffin et al., 2010) on board the *Herschel Space Observatory*. Some parts of the HeLMS field were masked. Edge effects, along with a "seagull-shaped" region of strong Galactic cirrus were removed, leaving a useful area of 274 deg^2.

Sources were detected using a map-based search method described in Asboth et al. (2016), similar to what was used in Dowell et al. (2014), instead of sources from the HerMES catalogue derived directly from the 250 μm map (Clarke et al. in preparation). For a description of how the sources were selected and the exact spatial filters adopted we refer the reader to Asboth et al. (2016), but we give a brief description here for completeness.

The SPIRE 250, 350, 500 μm maps are created with the same pixel size (6 arcsec) and (for source detection only) smoothed to the same resolution using an optimal filter for easy comparison between wavebands (Chapin et al., 2011). The local background is removed by smoothing the maps with a 2D median boxcar filter on 3 arcmin scales to remove any cirrus contamination. The filters are also applied to the error map to find the typical instrumental noise in the smoothed map. The 1σ instrumental noise values are 7.56, 6.33 and 7.77 mJy, in the 250, 350, and 500 μm SPIRE bands.

The confusion noise ($\sigma_{\rm conf}$) in the SPIRE map is caused by sources which emit at all three SPIRE wavelengths. This causes the confusion noise to be correlated between wavelengths. This information is used to construct a difference map (D) from the SPIRE 500 μm (M_{500}) and SPIRE 250 μm (M_{250}) maps with a reduced confusion limit (Dowell et al., 2014);

$$D = \sqrt{1-k^2}M_{500} - kM_{250} \tag{3.1}$$

with a k value of 0.392 to maximize the $D/\sigma_{\rm conf}$. This D-map has a confusion noise of 3.50 mJy, which is much lower than in the three smoothed SPIRE bands (13.66, 11.21, 6.98 mJy at 250, 350 and 500 μm, respectively).

The bright peaks in the D-map are selected with a 4σ cut-off at 34 mJy. At these positions the SPIRE flux densities are determined from the (higher resolution) nominal resolution map while taking into account the positional uncertainty of 6 arcsec (as measured with simulations in Asboth et al. 2016). From these flux densities a catalogue of $S_{500} > S_{350} > S_{250}$ sources is created. There is no requirement for a detection in both 250 and 350 μm, in order to avoid biasing the selection against the reddest objects.

The smoothed and raw images are compared with each other within a 30 $\times$ 30 arcsec region around each source to find cosmic rays. All candidate sources with $S_{\rm raw} - S_{\rm smooth} > 5\sigma_{\rm raw}$ are removed. The final catalogue is selected to have $S_{500} > 52$ mJy in order to minimize the effect of faint cosmic rays which are not found by the described technique. All 17 sources with radio fluxes in excess of 1 mJy are removed using the the 21 cm radio catalogues from the NRAO VLA Sky Survey (NVSS, Becker et al., 1995) and the Radio Sky at Twenty-cm (FIRST) survey (Condon et al., 1998) to avoid contamination

by flat spectrum quasars at $z < 1$. The rejection of NVSS/FIRST sources means that we potentially miss some genuine red sources that are lensed by radio-loud galaxies (Haas et al., 2014; Leung and Riechers, 2016). The final Asboth et al. (2016) catalogue contains a total of 477 sources.

3.3.2 SCUBA-2

We selected the 200 brightest galaxies i.e. $S_{500} > 63$ mJy, of the 477 Asboth et al. (2016) sources, and we observed a random sub-set of 188 of them for 15 min each using the `DAISY` pattern with the SCUBA-2 camera at the JCMT (Holland et al., 2013). The observations were taken in semester 15B between 2015 July 31 and 2015 November 15 with an opacity at 225GHz between 0.05 and 0.12.

Our integration times were based on the previous observations of 28 red objects from Dowell et al. (2014) with almost identical selection criteria as our sample. Those observations were 12.5 min `DAISY` observations and 27 out of the 28 where detected. Using the S_{850}/S_{500} colour distribution from these data to simulate the 850 μm fluxes of the HeLMS sample we estimated that a 1σ $\mathrm{rms}_{850} = 4.5$mJy would detect 70 per cent of our targets at $>3\sigma$.

We explored several data reduction methods including the data reduction used for the SCUBA-2 Cosmology Legacy Survey (S2CLS; Geach et al., 2017), and the quick pipeline reduction using `REDUCE SCAN FAINT POINT SOURCES`. We found that the "zero-mask" (Holland et al., 2017) data reduction used in Ivison et al. (2016) provided us with the highest signal-to-noise values and a rms_{850} ranging between 3.2 and 6.4 mJy with a mean of 4.3 mJy where the S2CLS method reaches an average rms_{850} of 4.9 mJy. The flux densities obtained with the zero-mask method are on average 2.6±4.0 mJy higher than the S2CLS method. We decided to use the zero-mask data reduction technique for all our observations because of its effectiveness in suppressing large-scale noise (Ivison et al., 2016; Holland et al., 2017).

The zero-mask data reduction uses the Dynamic Iterative Map Maker within the `SMURF` package (Chapin et al., 2013). This algorithm assumes that the image is free of significant emission except for a 60 arcsec diameter region centred on our target. Since the positions of our targets are in the centres of our `DAISY` observations this algorithm is very effective in suppressing large-scale noise. This has an advantage over the S2CLS pipeline (Geach et al., 2017), which can make no prior assumptions about the positions of the targets. The maps are generated with 1 arcsec × 1 arcsec pixels.

We use the same data reduction technique for the SCUBA-2 flux calibrators to get accurate flux conversion factors (FCF). These FCFs, ranging between 658 and 777 Jy pW^{-1} beam^{-1}, are used to convert our reduced image to units of Jy beam^{-1}. The FCFs are expected to be accurate to within 5 per cent (Dempsey et al., 2013).

Our prior positions are derived from the *Herschel* data and have a typical positional uncertainty (σ_H) of 6 arcsec (Asboth et al., 2016). Another positional uncertainty arises from the JCMT 2-3 arcsec rms pointing accuracy (σ_J). We combine both uncertainties to obtain the final positional uncertainty (σ_p):

$$\sigma_p = \sqrt{\sigma_H^2 + \sigma_J^2}. \tag{3.2}$$

We apply our source extraction by taking the flux density of the brightest pixel within a 20 arcsec radius of our prior position in the beam convolved image. This 20 arcsec radius corresponds roughly to the $3\sigma_p$ positional uncertainty of our prior source in the SCUBA-2 map. We obtained an average noise level of 4.3 mJy for our point source extraction.

For the purpose of analysis we divide our sample into three sub-groups with fairly arbitrary signal-to-noise ratio boundaries. Group 1 contains objects that have a clear detection, $S_{850} \geq 5\sigma$. Group 2 consists of detections between $3\sigma \leq S_{850} < 5\sigma$. Finally, Group 3 are galaxies for which we do not have a clear detection, $S_{850} < 3\sigma$. (Due to the large uncertainty in position we are unable to obtain a significant detection in the stacked signal for the Group 3 galaxies.) The three groups contain 64, 99 and 25 objects respectively.

As we are considering SCUBA-2 measurements of *Herschel* detected galaxies we are concerned about the accuracy of the flux measurement, rather than the reality of a catalogued source (as we would be with a blank field survey). Nevertheless we would expect random noise fluctuations and confusion noise from galaxies not associated with our original target. Furthermore we are using the brightest pixel, so our flux measurements are biased high (Coppin et al., 2008). We quantify this bias using the simulation shown in Figure 3.1. This simulation takes all deep S2CLS fields as the "truth".

We add noise to the S2CLS maps by adding extra Gaussian noise to reach a total noise of $\sigma = 4.3$ mJy, similar to those of our observations, we call this new maps the noise-added map. We then add positional errors to the S2CLS catalogue with a mean of zero and a standard deviation of 7 arcsec to the S2CLS positions to simulate the positional uncertainty of our DSFGs. We then apply our photometric measurement at the original S2CLS position and compare with the original S2CLS flux. We repeat this process five times to get the results from different random noise simulations.

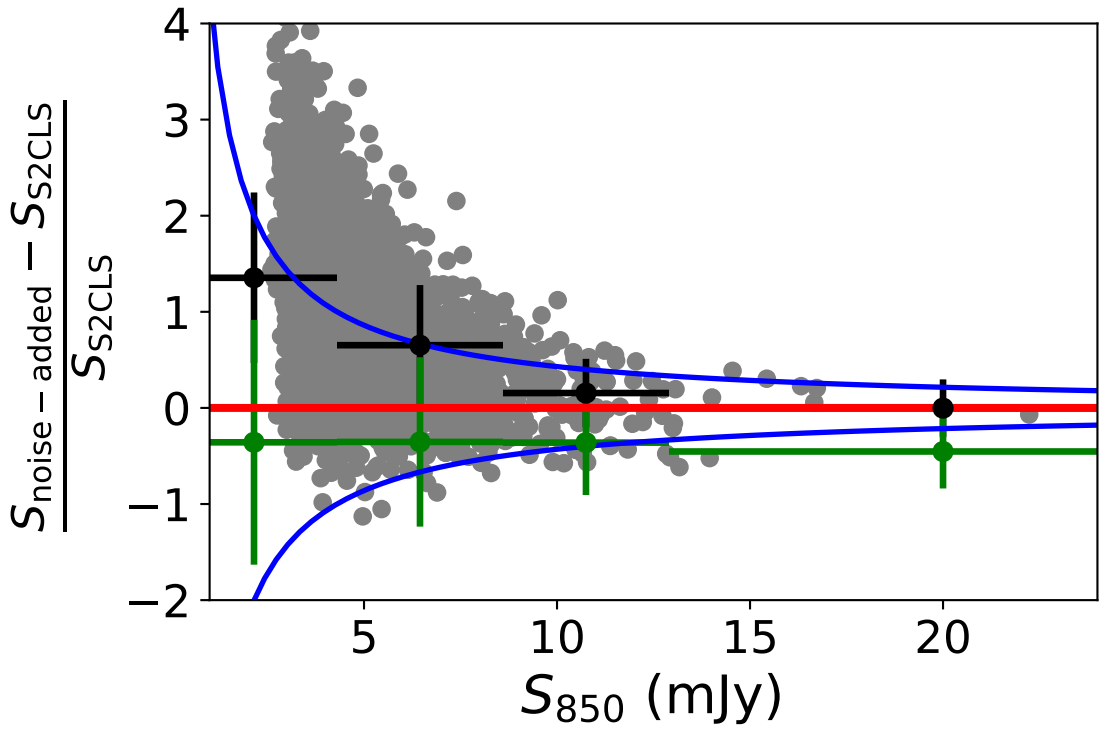

Figure 3.1: Simulation of our photometric errors and biases. S2CLS maps and catalogues are taken to be the truth and the noise-added fluxes are generated by adding Gaussian noise to mimic our observations ($\sigma = 4.3\,\mathrm{mJy}$). Flux densities are measured by taking the highest flux density within a 20 arcsec radius from the new S2CLS source position. The new S2CLS positions are generated by adding a random positional error of $\sigma = 7$ arcsec to it, which is comparable with the positional error of our data. The fractional difference between the (S2CLS) 850 μm flux density "truth" and the measured 850 μm flux density are plotted as function of the S2CLS flux density for all sources in grey, the black points show the mean of this measured fraction and the green points show the mean for a nearest pixel source extraction. The red line indicates zero offset and the blue lines indicate 1σ (4.3 mJy) bounds.

The comparison shows that for sources with S_{850} below 13 mJy (3σ) we are (on average) overestimating the flux density, but this overestimation is on average lower than 4.3 mJy (1σ). We also tested the sources extraction method of picking the nearest pixel to our prior positions and find that this method underestimates the flux density significantly for sources with $S_{850} > 13$ mJy. We decided to use our brightest pixel sources extraction because we expect that a significant percentage of our sources will lie above $S_{850} > 13$ mJy given that $S_{500} > 63$ mJy.

3.3.3 Ancillary data

It is unlikely that our high-redshift galaxy sample will be directly detected in any shallow large-field surveys at optical/NIR wavelengths which are not likely to contain $z > 1$ galaxies without an AGN (Section 3.5.2). However, low-redshift galaxies can significantly magnify a higher redshift source behind them via gravitational lensing.

Therefore it is possible to identify a lens using the available low-redshift galaxies from the *Wide-field Infrared Survey Explorer* (Wright et al., 2010, *WISE*) and the Sloan Digital Sky Survey (York et al., 2000, SDSS). We examined the SDSS images for possible contamination from large extended nearby galaxies and we found none. However, we do find several SDSS galaxies nearby and within the FWHM area of the SPIRE beam. Due to the large SPIRE/SCUBA-2 beam it will not be possible to unambiguously identify which of the several galaxies within the beam is potentially lensing the DSFG or is the optical/NIR counterpart of the DSFG.

For all our sources (excluding HELMS_RED_80 and HELMS_RED_421, see AGN Section 3.5.2) we find a total of 400 *WISE* detected sources (Cutri and et al., 2013) within a 20 arcsec radius. Of those sources only one is detected ($> 5\sigma$) in *WISE*-4 and this source is located 19.8 arcsec away from the SPIRE detection, additionally we find four *WISE*-3 detections ($> 5\sigma$) near other sources which are all located >11.2 arcsec away from the SPIRE detection. For the numerous detections in the *WISE*-1 band it is not clear if the *WISE* source is a random aligned nearby galaxy, associated with our source, is an AGN or is lensing the background DSFG. We therefore did not use *WISE* data in our SED fit. We can, however, study the statistical excess of galaxies nearby to our sources (Wang et al., 2011), where we only use *WISE*-1 sources as all but two *WISE*-2 galaxies are detected in *WISE*-1. We use SDSS DR9 (Ahn et al., 2012) and the Cutri and et al. (2013) *WISE* catalogue to select all detected galaxies near the line of sight of our targets (see Section 3.6.1).

Strong gravitational lensing, with a lensing magnification factor (μ) larger than 2, could provide an explanation for our high flux densities. Wide field *Herschel* surveys show that galaxies with a flux density at $S_{500} > 100$ mJy are likely to be strongly gravitationally lensed (Negrello et al., 2010; Conley et al., 2011; Nayyeri et al., 2016; Negrello et al., 2017). This $S_{500} > 100$ mJy limit comes from the steep slope in the FIR luminosity function, which causes intrinsically luminous ($S_{500} > 100$ mJy) sources to be extremely rare. Our sample of 500 μm riser galaxies contains nine galaxies with $S_{500} > 100$ mJy, of which we expect ≥ 80 per cent to be strongly lensed (Negrello et al., 2010; Wardlow et al., 2013). The probability that a DSFG is strongly lensed declines for $S_{500} < 100$ mJy, but for galaxies around 70 mJy at S_{500} there is still a significant ($\sim$20 per cent) chance that they are lensed (Bussmann et al., 2015; Nayyeri et al., 2016).

Other follow-up programs have observed part of our sample:

- Four of the sources (HELMS_RED_3, HELMS_RED_4, HELMS_RED_6 and HELMS_RED_7) were observed at the CSO using MUSIC (Sayers et al., 2014) at four wavelengths, 2.09, 1.4, 1.1 and 0.92 mm. The resulting flux densities can be found in section 6.2 and table 4 of Asboth et al. (2016).

- Two sources (HELMS_RED_4, HELMS_RED_31) have spectroscopic follow up with the Atacama Large Millimeter Array (ALMA). The resulting spectra can be found in Asboth et al. (2016). The redshift of HELMS_RED_4 is 5.162 and the redshift of HELMS_RED_31 is 3.798 or 4.997 depending on the line detection being the CO(5-4) or the CO(4-3) line.

- Two sources (HELMS_RED_1, HELMS_RED_2) have spectroscopic follow up by the Combined Array for Research in Millimeter-wave Astronomy (CARMA). The detected redshifts are 4.163 and 4.373, respectively (Riechers et al. in preparation, Leung et al. in preparation).

- Five sources (HELMS_RED_1, 2, 4, 10, 13) have been observed with the Submillimeter Array (SMA), and will be discussed in detail in Greenslade et al., in preparation.

- Two sources (HELMS_RED_1, 3) are detected in the Atacama Cosmology Telescope (ACT) equatorial survey (Su et al., 2017). The measured flux densities at 148, 218 and 278 GHz are 12.49$\pm$1.74, 35.11$\pm$2.62, and 72.32$\pm$6.26 mJy for HELMS_RED_1 and 6.14$\pm$1.76, 19.50$\pm$2.56, and 35.32$\pm$6.24 mJy for HELMS_RED_3.

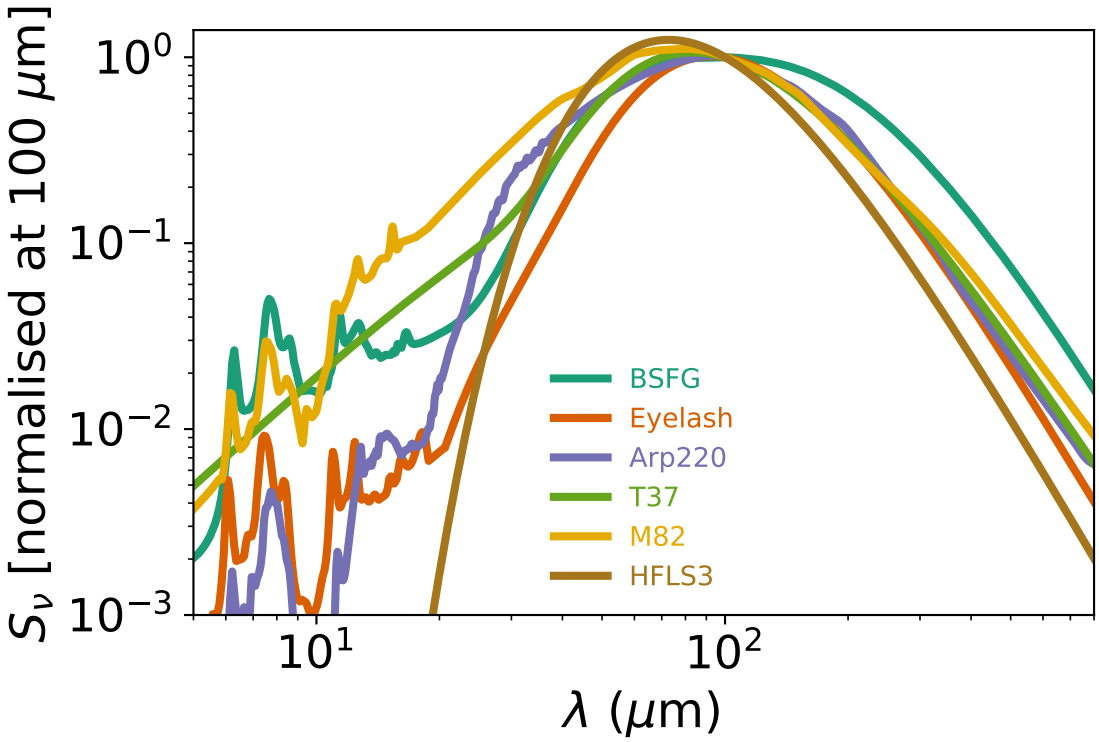

Figure 3.2: The six spectral energy distribution templates SEDs that we use in our photometric redshift fitting process. These are broad star-forming – BSFG derived by Berta et al. (2013), cosmic Eyelash, and three warm starburst galaxies M82, Arp220 (Polletta et al., 2007) and HFLS3 (Riechers et al., 2013).

- Twelve sources (HELMS_RED_3, 4, 7, 10, 19, 23, 31, 68, 69, 82, 118, 270) have 870 μm continuum observations from ALMA (Oteo et al., 2017a).

MUSIC and ACT provide even more data points in the Rayleigh-Jeans part of the spectrum. These additional long wavelength data will improve our SED-fitting process. The spectroscopic redshifts from CARMA and ALMA will be used to help validate our SED-fitting process and to confirm that our selection process does indeed pre-select high-redshift galaxies. We use the preliminary SMA results to get accurate information about the source positions and to determine if any sources are blended.

3.4 Modeling the DSFGs

3.4.1 SED fitting for photometric redshifts

Fits to the FIR/submm spectral energy distributions (SED) to obtain photometric redshifts and integrated properties are performed using the `EAZY` code (Brammer et al., 2008)

using a sample of representative FIR/submm templates (e.g. Aretxaga et al., 2003).

The FIR peak of luminous infrared galaxies ($L_{\rm IR} > 10^{10}{\rm L}_{\odot}$) can be, crudely, characterized by cool dust with average temperatures in the 25-45 K range (e.g. Soifer et al., 1984; Klaas et al., 1997). The lack of strong features means it is difficult to distinguish between either very cold dust or high-redshift galaxies using only SPIRE photometry. The addition of the S_{850} data enables us to estimate the peak of the FIR emission, and therefore able to place far tighter constraints on the redshift (Section 3.4.3). However, since temperature and redshift are degenerate the choice of templates is a critical factor in photometric redshift estimation and so our templates have been carefully chosen to cover a broad range of temperatures.

Our six templates consist of the broad star-forming galaxy (BSFG) derived by Berta et al. (2013), cosmic Eyelash and three warm starburst galaxies M82, Arp220 (Polletta et al., 2007) and HFLS3 (Riechers et al., 2013). However, these templates have a gap at an effective temperature 37 K so we create an extra SED template from a modified blackbody (MBB) with a temperature of 37 K, a dust emissivity index (β) of 1.5 and a MIR power-law component (α) of 2.0 (Casey, 2012). These templates are illustrated in Figure 3.2. With EAZY we fit all possible linear combinations of our templates set.

In Figure 3.3 we show the colour-colour plot of our observations. We overlay the redshift tracks from our sample of SED templates. Our template set thus contains a wide range of representative DSFGs over a large redshift range. We can exclude very cold ($T \sim 20$ K) galaxies at $z \lesssim 1.7$ as they would not be a 500 μm riser. Such galaxies at higher redshift could potentially contaminate our sample. But this type of galaxies are very rare between $0.1 < z < 2.0$ (Symeonidis et al., 2013). Such a cold galaxy would furthermore have a higher S_{850}/S_{500} colour than any of our measured S_{850}/S_{500} colours at $z > 2.5$.

We only use broad-band FIR data, and we neglect the contribution of emission lines. At redshifts of $z \sim 4$ FIR lines have a ~ 6 per cent effect at 250 μm, however, they have a negligible effect at 350, and 500 μm; at 850 μm they have a ~ 1 per cent contribution at $z \sim 4$ though this rises to ~ 8 per cent at $z \sim 5$ (Smail et al., 2011).

We adjust EAZY to allow for 10 per cent systematic error for the data. This 10 per cent incorporates both the 5 per cent error in the FCF for SCUBA-2 and our use of a different algorithm to reduce the data for SCUBA-2 and SPIRE. The advantage of using this extra 10 per cent systematic error is that it dominates unrealistically small statistical errors for very bright ($> 10\sigma$) sources.

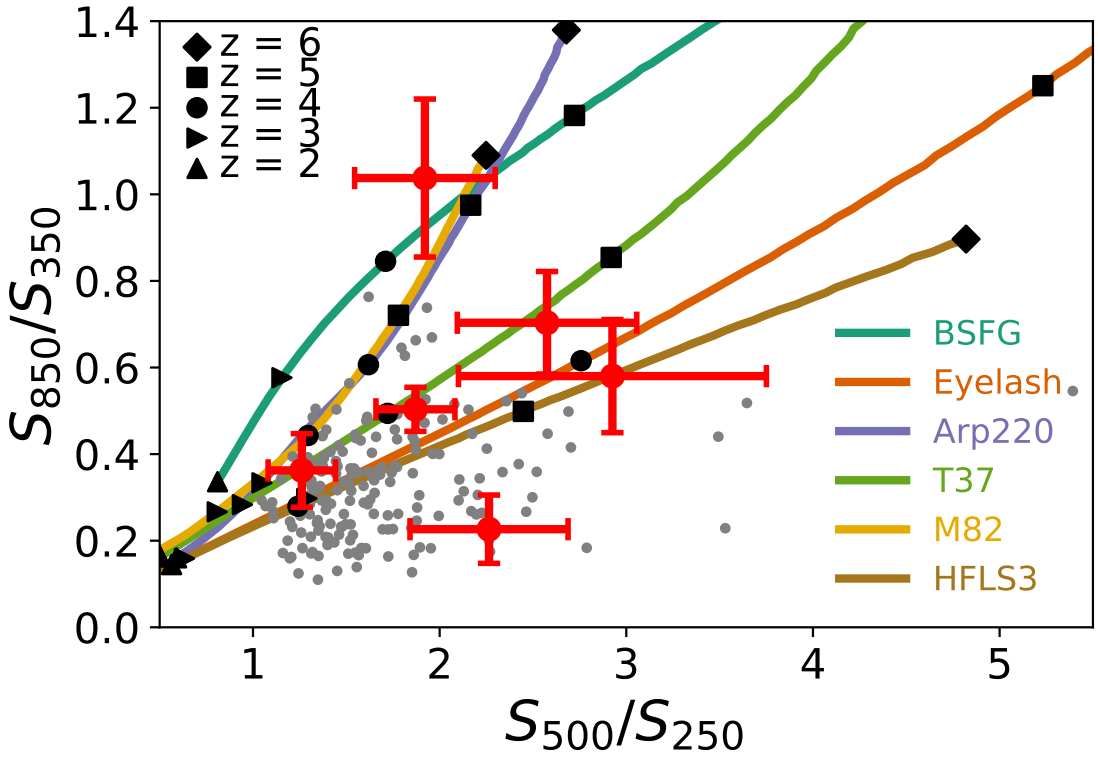

Figure 3.3: Colour-colour plot of our sample of DSFGs in grey, with a sub-set of points with representative error bars in red. The coloured lines show the redshift tracks of our SED templates. The crossing of such a line indicates that for a certain colour there are degenerate solutions for the photo-z estimates. The black shapes indicate the colour of a SED template at the indicated redshift. The data points significantly below the HFLS3 line could only be sampled by a non-physical template narrower than a blackbody. The presence of the DSFGs in this part of the diagram indicates flux boosting in either S_{350} or S_{500} (see Section 3.6).

In Section 3.4.4 we directly compare our method with other methods, other template choices and with spectroscopic redshifts.

3.4.2 Noise estimates

The SPIRE and SCUBA-2 maps contain both confusion and instrumental noise. Both have to be included in the SED fitting to ensure that the errors on fitted parameters, e.g. photometric redshift are assigned the appropriate errors. The confused background in the SPIRE band is caused by coincident sources; these contribute in all three wavelength bands. The instrumental noise can be assumed to be uncorrelated and included straightforwardly in the χ^2 calculations within `EAZY`. However, to incorporate the confusion noise we need to consider that this is correlated noise.

The confusion noise at S_{850} from SCUBA-2 is significantly lower than the confusion in the SPIRE bands (1 mJy versus $\sim$ 6-7 mJy; Geach et al., 2017; Nguyen et al., 2010) due to the smaller beams size of SCUBA-2 and lower number counts. The SCUBA-2 confusion noise is subdominant to the instrumental noise we obtained in the images. We can therefore safely neglect the effects of confusion in our SCUBA-2 flux density estimates. We can simulate possible values for the SPIRE contribution in the following way.

In a confusion limited map, where the instrumental noise is negligible compared with the confusion noise, the fluctuations in that map can be considered to be caused by confusion noise alone. We can randomly sample such a confusion limited map at the same position in all three bands drawing a 3-tuple of flux density values that represent the confusion noise. These samples automatically include the correlation between the bands[1].

The HELMS field is not confusion limited so we sample the confusion limited COSMOS (Scoville et al., 2007b) field. COSMOS has a 1σ instrumental noise < 2.5 mJy, though small, this residual instrumental noise means we will slightly overestimate the confusion noise values. We perturb the 3-tuple flux of each object in our catalogue by one of the sample 3-tuples drawn from COSMOS. We then run `EAZY` on the perturbed catalogue. We do this simulation exercise 1000 times (however, due to the finite size of the field these are not independent).

We average the redshift probability distribution function (PDF) over all simulation runs to obtain the final PDF for each galaxy. The results of 1000 runs for a single representative galaxy are shown in Figure 3.4. The resulting PDF is slightly broader than the

[1] An alternative, would be to estimate the covariance matrix between the maps, and synthesize correlated flux density values from this assuming Gaussian fluctuations. However, by sampling directly from the map we skip this step and get a more direct model of the correlated confusion noise

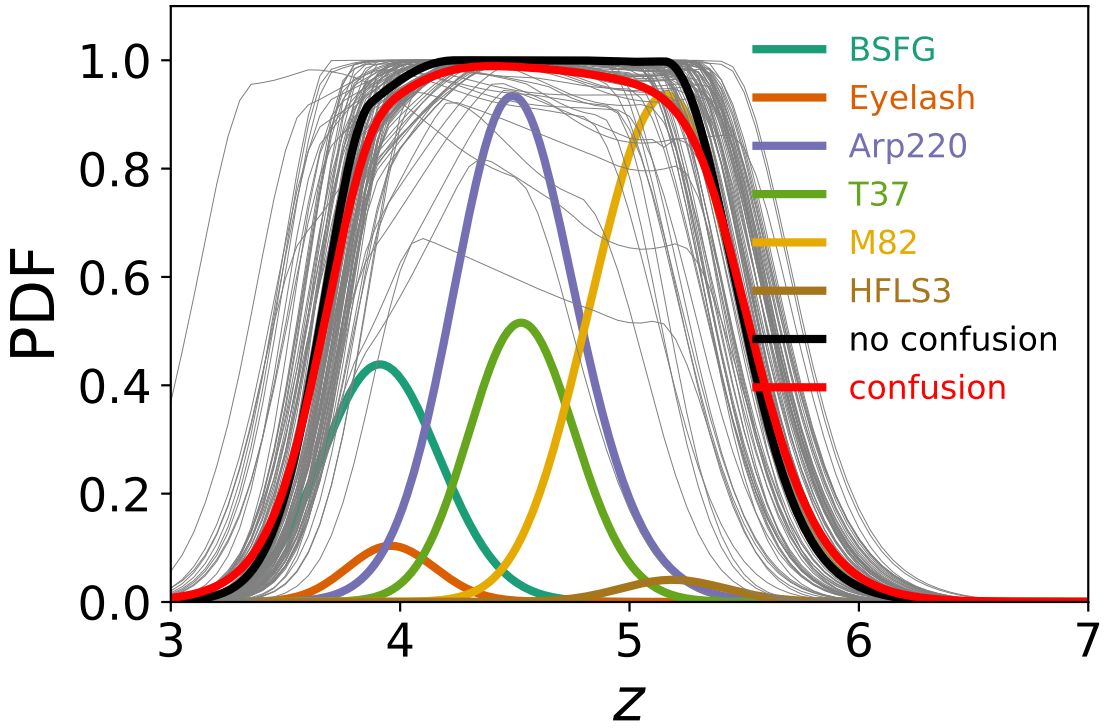

Figure 3.4: Redshift PDF for a single galaxy, illustrating the contribution from different galaxy templates. Each grey line represent the PDF from a single run with `EAZY`, perturbed by one particular sample of the confusion noise. The red line represents the average of the 1000 EAZY runs and the black line is the result from the traditional method without confusion noise. The coloured lines show the contribution to the PDF from each galaxy template used.

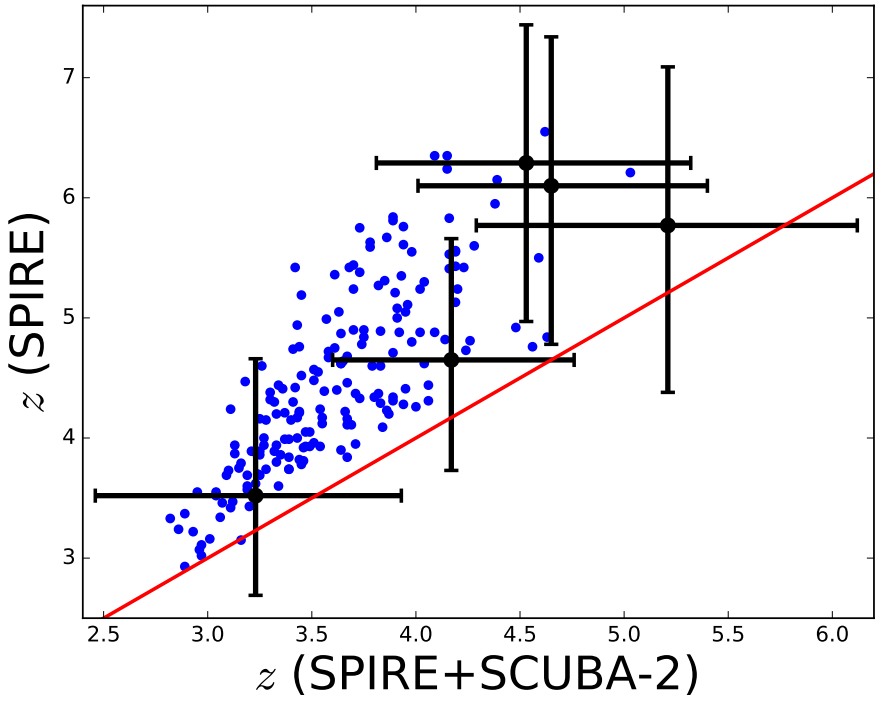

Figure 3.5: Redshift estimates from our SED fits using SPIRE photometry only verses those where we include SCUBA-2 data. All points in blue, and in black a subset of representative error bars. The average uncertainty for the SPIRE-only data set is larger, $\sigma_z/(1+z) = 0.21$, than the uncertainty with the additional SCUBA-2 data $\sigma_z/(1+z) = 0.15$. It is also clear that the SPIRE-only SED fits overestimate the redshift due to the lack of constraints on the peak of the FIR emission.

PDF from the traditional method of not using the confusion noise. This effect would be larger if the noise in HeLMS had been dominated by confusion noise.

In Figure 3.5, we show the improvement in photometric redshift by adding the longer wavelength SCUBA-2 data. The average uncertainty (calculated from the variance of the estimated PDF from EAZY) when we only use the SPIRE flux densities is larger, $\sigma_z/(1+z) = 0.21$, than the uncertainty with the additional SCUBA-2 data $\sigma_z/(1+z) = 0.15$. This figure also shows that we overestimate the photometric redshift when we only use the SPIRE data.

3.4.3 Physical parameters

Using `EAZY` we obtain the full PDF and the best-fitting SED template for every galaxy. With this template we compute the total infrared luminosity, $L_{\rm IR}$. The FIR luminosity is defined as the integral over the rest-frame spectrum between 8 and 1000 μm, i.e. $L_{\rm IR} =$

$\int_{8\mu m}^{1000\mu m} L_\nu \, d\nu$. In practice we lack a good measurement of the flux in the rest frame mid-infrared (MIR) from 8 to 30 μm. We therefore integrate between 30 and 1000 μm and use a correction factor for the potentially large amounts of missed flux in the MIR. We calculate the correction factor from the average fraction of the FIR luminosity contained in the MIR regime for five of our six templates. We exclude the HFLS3 template for this measurement due to a lack of constraints in the MIR. We obtain a correction factor of 1.17 and we multiply our measured integral by this factor to obtain the resulting $L_{\rm IR}$. We also obtain an error on $L_{\rm IR}$ using both the errors on our flux density estimates and the scatter from our 1000 `EAZY` runs.

The negative K-correction (for galaxies measured at longer wavelengths than the peak of their SED) counteracts (to some extent) the dimming with distance, and so these galaxies are relatively constant in brightness (e.g. Casey et al., 2014). Therefore our estimates of $L_{\rm IR}$ can be tightly constrained even with a large uncertainty in the redshift.

Our $L_{\rm IR}$ can be translated into SFR estimates using Kennicutt (1998a) for a Salpeter IMF

$$\frac{\rm SFR}{\rm M_\odot yr^{-1}} = 1.96 \times 10^{-10} \frac{L_{\rm IR}}{\rm L_\odot}. \tag{3.3}$$

Here the fraction of ultraviolet energy absorbed by dust has been assumed to be $\epsilon = 0.88$, for which we have no constraint. Our estimates for the SFR would be the same if we had used the Rowan-Robinson et al. (1997) calibration factor with a $\epsilon = 2/3$. We assume no gravitational lensing (Section 3.6.1) and no contamination by AGN (Section 3.5.2) in our calculation of the SFR. The resulting SFRs should be multiplied by a factor 0.63 or 0.67 if assuming a Chabrier or Krupa IMF (Madau and Dickinson, 2014).

Our final catalogue is presented in Appendix C, where we list the positions, flux densities, redshifts and $L_{\rm IR}$ of all our galaxies observed with SCUBA-2.

3.4.4 Testing the photometric redshifts

Ivison et al. (2016) made a similar assumption with the selection of their templates, and tested their photometric redshift code against 25 red high-redshift DSFGs with spectroscopic redshift. Their photometric redshifts where found by finding the lowest χ^2 value for their set of three templates. The main difference between our method is that `EAZY` not only fits the provided templates but also any linear combination of those templates. The results from Ivison et al. (2016) show only a small offset in $(z_{\rm phot} - z_{\rm spec})/(1 + z_{\rm spec}) = -0.03$ with a scatter of 0.14.

We compare our photometric redshift method (z_{EAZY}) directly with Ivison et al.

(2016), by running our code on their sample. We obtain a mean (μ) offset in $(z_{\rm EAZY} - z_{\rm Ivison})/(1 + z_{\rm EAZY})$ of 0.11 and a median ($\mu_{1/2}$) offset of 0.12. We note that this offset is smaller than the mean estimated error in our redshift ($\langle\sigma_z/(1 + z_{\rm EAZY})\rangle = 0.15$).

The main difference between our method and that of Ivison et al. (2016) is that they tested a set of siz templates individually with a sample of available spectroscopic redshifts, and discarded the ones with the poorest fit in $(z_{\rm Ivison} - z_{\rm spec})/(1+z_{\rm spec})$. Two of the poorest fitting templates in their analysis were the Arp 220 and HFLS3, which are on the "blue" end of the range of FIR SEDs. If we discard our "blue" templates (M82, HFLS3 and Arp 220) we find that our photometric redshift estimates are very close to the Ivison et al. (2016) estimates ($\mu = 0.024$ and $\mu_{1/2} = 0.035$). However, we keep these "blue" templates in our analysis, to ensure conservative errors, noting that `EAZY` produces a full redshift PDF using all our templates (and all linear combinations of them) simultaneously.

We can see how our results would change if we made a different choice of templates. Strandet et al. (2016) used a Monte Carlo method to sample a range of MBB from Greve et al. (2012) with dust temperature parameter sampled from a Gaussian with mean and standard deviation 39 ± 10 K. We use a similar full MCMC approach to fit using the FITIR module of the INTERROGATOR[2] code (Wilkins et al. in preparation). With this method we can specify prior information about all free parameters. We consider both the MBB parametrization of Greve et al. (2012) (which has two free parameters, the temperature T, and the emissivity β) and the parametrization of Casey (2012) (which has three free parameters: the temperature, emissivity β, and the slope of the near-IR power-law α). For the Greve et al. (2012) parametrization we fix the emissivity $\beta = 2.0$ and consider three different priors on the temperature T: fixed to $T = 40$ K, a normal distribution centred at $T = 39$ K with $\sigma = 10$ K, and a uniform prior $T/{\rm K} = [20, 40]$. For the Casey (2012) we assume uniform prior on the temperature of $T/{\rm K} = [20, 60]$ and consider cases where both α and β are fixed (to 2.0 and 1.5 respectively) and where they have a uniform prior: $\beta = [1, 2]$ and $\alpha = [1., 2.5]$.

The results are shown in Table 3.1 where we compare the output of each different template set to our chosen templates when applied to our sample. We compute a number of comparison statistics, the mean offset ($\mu = \frac{z - z_{\rm this\ work}}{1+z_{\rm this\ work}}$), the rms scatter in μ (σ) and the χ^2 in comparison with our three spectroscopic redshifts. For the normal distributed ($T = 39$ K) method we find a $\mu = -0.056$ and a $\chi^2 = 1.35$, for the uniform prior ($T/{\rm K} = [20, 40]$) μ is -0.011 and the $\chi^2 = 0.67$ and for the single temperature model we find a $\chi^2 = 54$.

[2] http://users.sussex.ac.uk/~sw376/Interrogator/

Method	This work	Gaussian (39±10 K)	Uniform (20-60 K)	Delta (40 K)	Casey (20-60 K)	Casey wide (20-60 K)
$\langle z \rangle$	3.60 ± 0.43	3.34 ± 0.37	3.54 ± 0.40	3.24 ± 0.32	4.46 ± 0.54	4.79 ± 0.51
$\langle z_{\rm h} - z_{\rm l} \rangle/2$	0.67	1.04	1.16	0.32	2.03	1.80
μ	0	-0.056	-0.011	-0.078	0.187	0.260
σ	0	0.034	0.041	0.027	0.043	0.033
χ^2	3.07	1.35	0.67	53.6	0.35	0.62

Table 3.1: Comparison of templates for photometric redshift accuracy. Mean photometric redshift, 1σ error, mean difference (μ) with the photometric redshift used in this work in $\frac{z - z_{\rm this\ work}}{1+z_{\rm this\ work}}$ and, the rms scatter (σ) in μ as function of different photometric redshift methods. The last row shows the sum of the χ^2 in comparison with the three spectroscopic redshifts of our sample. The Gaussian (39±10 K) model produces comparable results compared to our method, but slightly overestimates the error bar size. The delta model is insufficient in fitting photometric redshifts, and the uniform models vastly overestimate the error bar size.

From these results we can see that the Gaussian prior produces very similar results as our method, and that the flat 20-60 K prior models are consistent with the spectroscopic redshifts, but overestimate the size of the error bars ($\chi^2 \ll 1$). The single temperature model is insufficient in fitting photometric redshifts.

The ultimate test is the comparison against spectroscopic redshifts. We obtain a good total χ^2 of 3.07 for our three spectroscopic redshifts. But due to the limited number of spectroscopic redshifts in our sample we also use the SPT detected DSFGs which fulfil our colour selection criteria (Weiß et al., 2013; Strandet et al., 2016, 2017), HFLS3 and the *H*-atlas 500 μm risers Fudamoto et al. (2017). The results are shown in Figure 3.6. We estimate a bias of $\langle (z - z_{\rm spec})/(1 + z_{\rm spec}) \rangle = 0.08$ with a rms of 0.19 and a reduced χ^2 of 1.4. The rms scatter in the bias (0.19), our average uncertainty per galaxy ($\sigma_z/(1+z) = 0.15$) and $\langle |z - z_{\rm spec}|/(1 + z_{\rm spec}) \rangle = 0.17$ all have comparable values.

There is a visible trend in Figure 3.6 that $(z - z_{\rm spec})/(1 + z_{\rm spec})$ is decreasing with redshift, the reduced χ^2 for linear decreasing model is 0.9 compared to 1.4 for the non-evolving model. This result indicates that we underestimate the redshift of high-redshift galaxies due to a rising dust temperature of our spectroscopic sample towards higher redshift (Ivison et al., 2016). However, this same result could also arise from selection effects, where a warm HFLS3 type galaxy would not have made our selection criteria at $z < 4.6$ as it would not be a 500 μm riser (Figure 3.7). Another possible explanation for this trend is that higher redshift galaxies need to be brighter to fulfil our flux density selection criteria, and these brighter galaxies tend to be warmer (e.g. Symeonidis et al.,

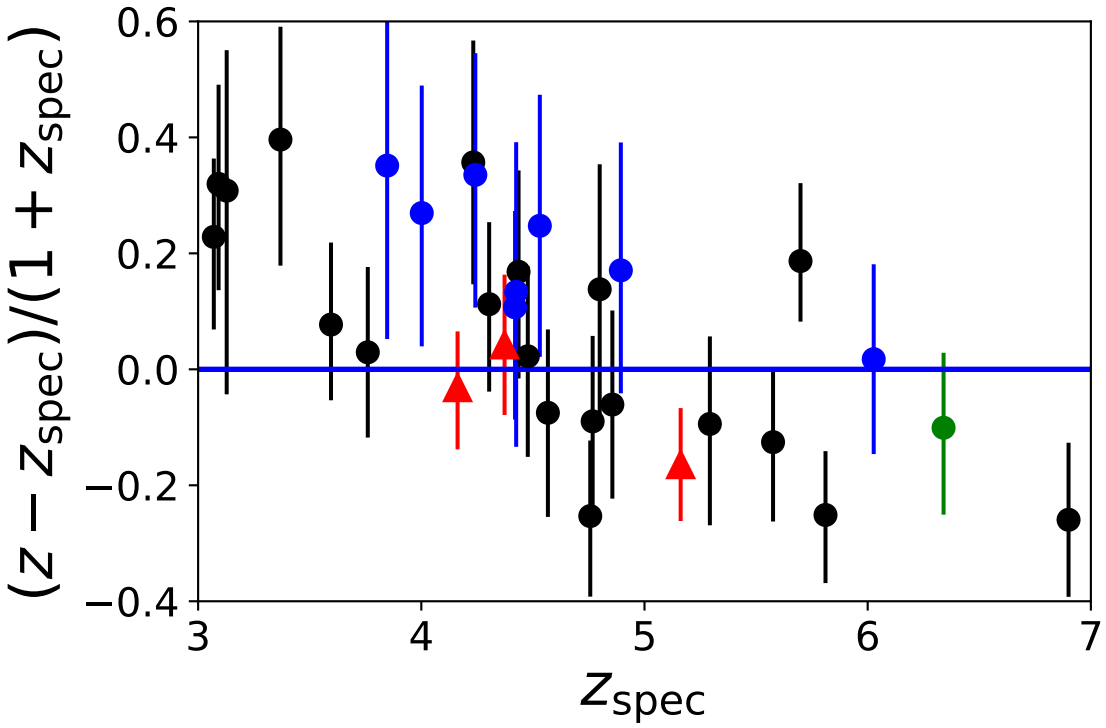

Figure 3.6: Comparison with available 500μm riser spectroscopic redshifts at $z > 3$. In green we show HFLS3, in black the SPT sample and in blue the H-atlas sample (Weiß et al., 2013; Strandet et al., 2016, 2017; Fudamoto et al., 2017) and in red the spectroscopic redshifts for our sample. We obtain an offset $\langle (z - z_{\rm spec})/(1 + z_{\rm spec}) \rangle = 0.08$ with a rms of 0.19 and a average χ^2 per galaxy of 1.4.

2013; Kirkpatrick et al., 2017).

Any fitting methods with a range of temperatures and no explicit prior on the temperatures is effectively assigning a uniform prior to the temperatures. This is what our method does as do most photometric redshift fitting methods. In the low signal-to-noise regime the prior has a stronger influence on the posterior and so there will be a trend to fit mid-range temperatures rather than high or low temperatures. This naturally tempers the extremes of redshifts distributions based on the best redshift. However, the redshift PDFs are a reasonable representation of the information available.

3.5 Results

3.5.1 Statistical properties

In Figure 3.7 we show the SFR vs redshift distribution of our sources. Our sources have a median redshift of 3.6 $\pm$0.4 and a median SFR (uncorrected for flux boosting[3] or the possible presence of gravitational lensing) of $5.2 \pm 1.9 \times 10^3$ $M_{\odot}yr^{-1}$. All our galaxies could be classified as distant hyper-luminous infrared galaxies (HyLIRGS), i.e. with $L_{\rm IR}$ exceeding 10^{13} $L_{\odot}$ and a mean $L_{\rm IR}$ of 2.7 $\times 10^{13}$ $L_{\odot}$.

We find that 31.4$\pm$4.7 per cent lie between redshifts of 4 and 6. This finding is consistent with Ivison et al. (2016) who found 33 $\pm$ 6 per cent of their sample to lie within this redshift range. The inferred space density (ρ_{obs}) in this redshift range is 1.1×10^{-8} Mpc^{-3}. Due to the predicted short lifetime for the starburst ($t_{\rm burst}$) phase we need to apply a duty-cycle correction to the observed space density to infer the actual underlying space density (ρ) for these type of galaxies

$$\rho = t_{obs}/t_{\rm burst} \times \rho_{obs}, \tag{3.4}$$

were t_{obs} is the time between $4 < z < 6$. For $t_{\rm burst}$ we assume 100 Myr, which is in agreement with their expected gas depletion times (Ivison et al., 2011; Bothwell et al., 2013). The final inferred space density estimate is thus 7×10^{-8} Mpc^{-3}. The assumption of 100 Myr is the same as used by Ivison et al. (2016) and while longer time-scales (0.5-1.0 Gyr) have been postulated (e.g. Lapi et al., 2014; Aversa et al., 2015) these would result in an even lower space density.

[3]Due to noise the measured flux densities are scattered around the true flux densities. When measuring these flux densities just above a detection threshold it is more likely that galaxies with a positive contribution form the noise are detected, as those with a negative contribution will fall below the threshold. It is also the case that there are more faint than bright sources, therefore more faint sources scatter towards higher flux densities than bright sources scatter towards fainter flux densities.

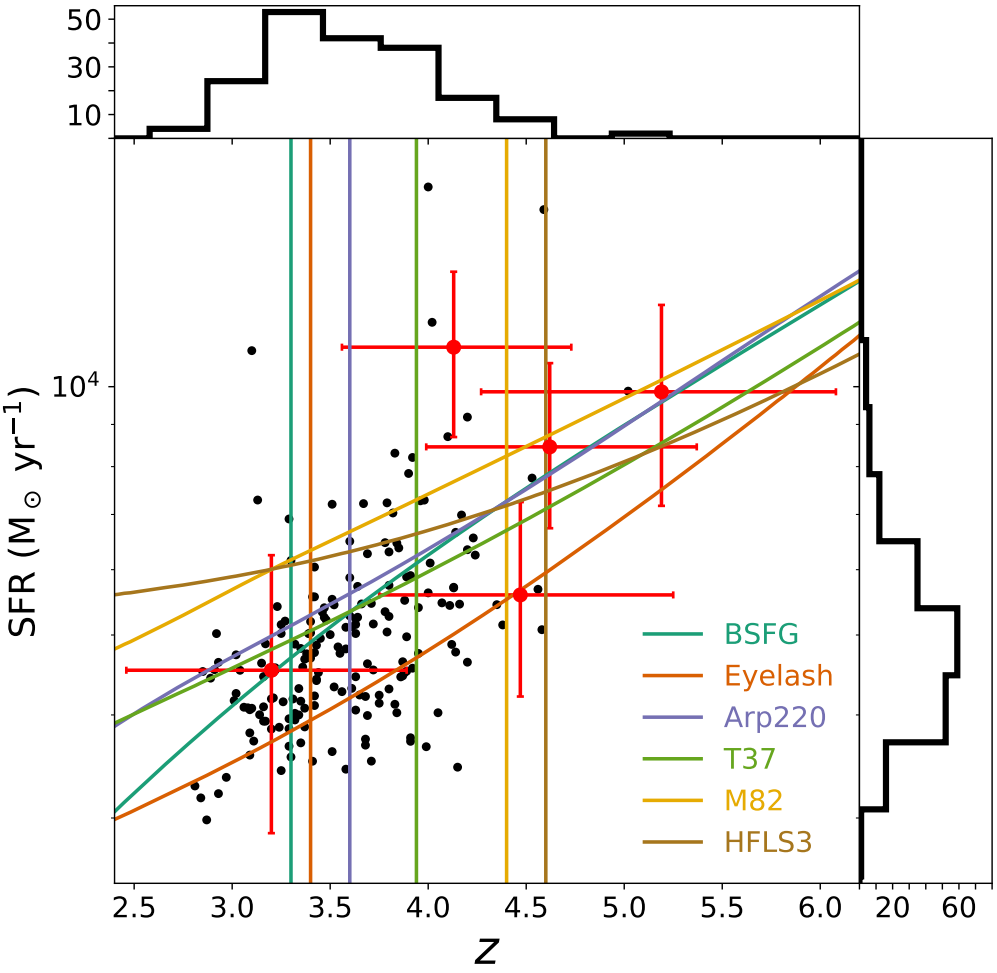

Figure 3.7: SFR versus redshift for our 188 targets. Red represents a set of representative error bars. There are several objects which have a strong indication to lie at very high redshifts, but the bulk of our sample is expected to lie around z≈3-4. The coloured lines represent the lower redshift limits for 500 μm riser galaxies and SFR tracks for our range of SED templates.

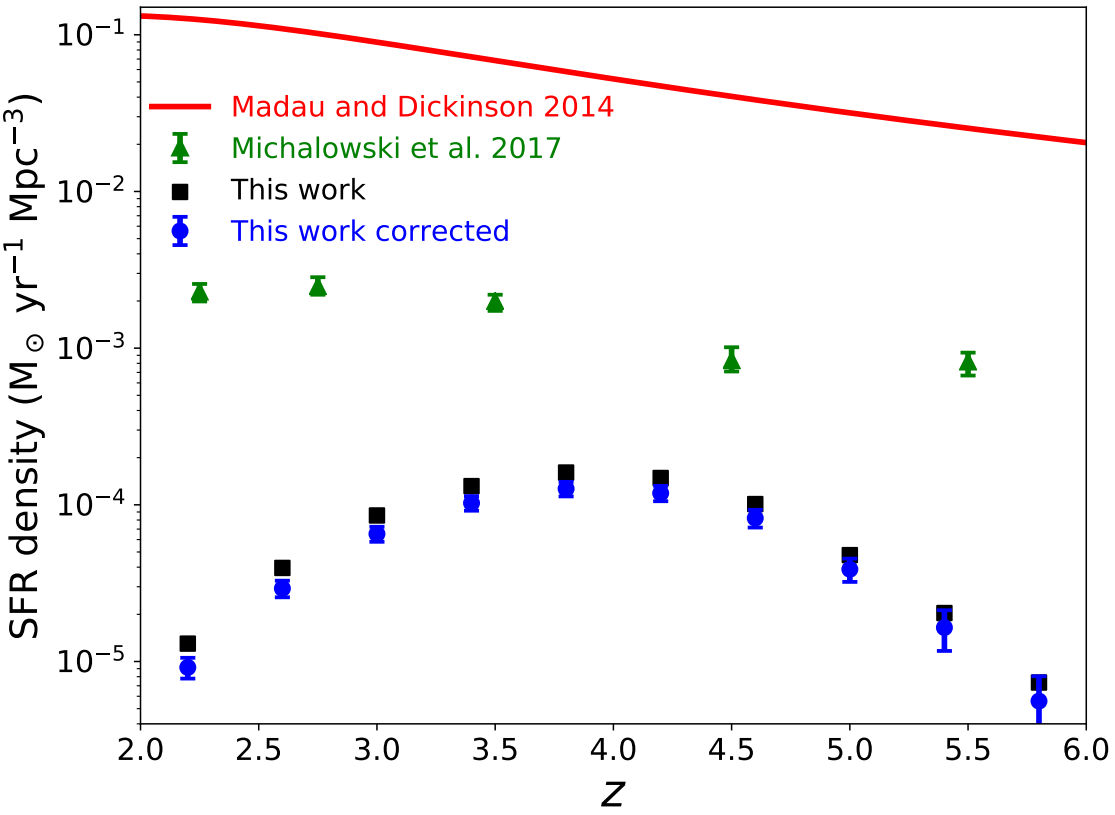

Figure 3.8: SFR density of sources with $S_{500} > 63$ mJy and $S_{500} > S_{350} > S_{250}$ in the HeLMS field in black squares, using the full redshift PDF. In blue is the corrected contribution of those sources, where contamination from AGN is removed and we corrected for flux boosting (see Section 3.5.2 and 3.5.1). The red line is the Madau and Dickinson (2014) SFRD estimates for all sources in the Universe. The green triangles are the Michałowski et al. (2017) measurements of DSFGs with SFR > 300 M$_\odot$ yr^{-1} from two blank S2CLS fields. The maximum contribution to the total SFRD is 0.3 per cent at $z \simeq 4.2$.

The primary difference between the Ivison et al. (2016) sample and our sample is that Ivison et al. (2016) used a $S_{500} > 30$ mJy selection where we use a $S_{500} > 63$ mJy sample. Therefore our sample has a space density of about a factor of 10 lower than the Ivison et al. (2016) estimate of 6×10^{-7} Mpc^{-3}.

We use our sample to calculate the SFRD for bright 500 μm risers in the SPIRE bands as shown in Figure 3.7. The contribution to the overall SFRD is below 1 per cent at any redshift. For comparison we also show the SFRD results from the S2CLS $S_{850} \geq 4$ mJy selected sources, which is complete for galaxies with an SFR > 300 M$_\odot$ yr^{-1} (Michałowski et al., 2017). The Michałowski et al. (2017) result comes from 2 deg^2 blank fields, which observe the more common population of DSFGs and contribute more to the overall SFRD

at any epoch.

Luminosity function

The SPIRE sources luminosity function and its evolution to z $\sim$ 4 has been reported in Gruppioni et al. (2013). We can use this luminosity function as a basis to predict the number of galaxies we expect in our sample. To get an accurate estimate for our incompleteness we need to know the relative distribution of different galaxy types at these high luminosities and redshifts. The intrinsic colours of different galaxy types can be used to determine whether or not they fulfil our selection criteria as a function of redshift.

Due to the lack of information on the distribution of galaxy types at high redshift we have to extrapolate what we know about the distribution of SED shapes at lower redshift and luminosity to the redshifts and luminosities of our sample. We do this using the results from Symeonidis et al. (2013), who measured the correlation between average dust temperatures and infrared luminosities. They characterized the rising dust temperature with luminosity for a sample of $10^{11} < L_{\rm IR}/{\rm L}_{\odot} < 10^{12.7}$ galaxies, and , to provide a simple phenomenological characterization of this, we apply a linear fit in temperature versus $\log L_{\rm IR}$ to predict the average temperature for $L_{\rm IR}/{\rm L}_{\odot} \geq 10^{12.5}$ galaxies. We also use the average value for the variance in the temperature for $L_{\rm IR}/{\rm L}_{\odot} > 10^{12}$ galaxies.

Using this temperature-luminosity-redshift distribution we draw 200 galaxies at every redshift between 1.5 and 8 ($\Delta z = 0.1$) and luminosities between $10^{12.5} < L_{\rm IR} < 10^{15.0}$ ($\Delta \log L_{\rm IR} = 0.1$) and then each galaxy is assigned a temperature drawn from a Gaussian with mean from the temperature-luminosity and a sigma of 6 K. This produces a mock catalogue of 325 000 galaxies, for which we have mock T, z, and $L_{\rm IR}$ values. We use the Casey (2012) MBB to calculate the expected flux densities at SPIRE and SCUBA-2 wavelengths for each galaxy. The upper limit of $L_{\rm IR} = 10^{15.0}$ is used for practical reasons to simplify the drawing of a random luminosity. It was not intended to indicate a realistic physical limit. However, the number density is dropping off very steeply at high luminosity so exactly where this cut is made makes little difference to the outcome.

We add Gaussian noise with a mean of zero and a sigma of the mean instrumental error of our observations to simulate the variations caused by instrumental noise. On top of the Gaussian noise we also draw a correlated confusion noise estimate for every source using the COSMOS map (see Section 3.4.2), and we add this correlated confusion to our mock observed flux density estimates. Our novel way of adding the correlated confusion noise is crucial as it partly conserves the colour of the source. The standard deviation of

the confusion noise we added is 6.7, 7.1 and 6.8 mJy at 250, 350 and 500 μm, respectively and together with the instrumental noise of order 7 mJy this leads to 1σ fluctuations of $\sim$10 mJy. It will therefore not be uncommon that sources of order 30 mJy at 500 μm will be boosted to the selection criteria of 63 mJy due to the noise and the steepness of luminosity function.

We multiply the fraction of mock galaxies in every luminosity and redshift bin which fulfil our selection criteria by the expected space density for such galaxies (Gruppioni et al., 2013) to obtain the number of galaxies we would expect in the HeLMS field. This results in a total sample of $\sim 260^{+180}_{-100}$ galaxies in our mock catalogue over an area of 274 deg^2. This is mildly larger than, but consistent with, the 200 galaxies we observed in the HeLMS field. The error bars are based on the large error on the normalization of the luminosity function (Gruppioni et al., 2013). We do acknowledge that the consistency is partly due to the large error bars in this normalization.

We make an additional 10 mock catalogues where we modify the mean temperature in the relations of Symeonidis et al. (2013) to measure the effect of the average temperature of DSFGs on the observed number counts. In Table 3.2 we show the total number counts as function of (mean) temperature. It is clear that the number of observed galaxies is a strong function of temperature and it is therefore important to get a better understanding of the distribution of galaxy types at high redshift to fully understand the number counts.

In Figure 3.9 we show the resulting S_{500} and S_{850} number counts for our mock catalogues shown in Table 3.2. Our mock catalogue is consistent at S_{500} but overpredicts the number of bright sources at S_{850}, even when we raise the temperature of our mock catalogues with 5 K we keep overpredicting the number of sources at $S_{850} > 50$ mJy.

We use our mock model as input for `EAZY` to predict the observed luminosity function using our method. On top of the 200 galaxies we have already drawn at every redshift and luminosity bin we draw an additional 100 galaxies for every very bright bin ($L_{\rm IR}/{\rm L}_\odot > 10^{13.5}$), an additional 300 galaxies for the $10^{13.1} < L_{\rm IR}/{\rm L}_\odot < 10^{13.5}$ bins and an additional 500 galaxies for the $L_{\rm IR}/{\rm L}_\odot < 10^{13.1}$ bins. these extra galaxies lead to a total mock size to test the luminosity function of 630 500 galaxies. These extra galaxies give us extra statistics on the lower end of the luminosity function, where galaxies are intrinsically not bright enough to be detected with our detection method but might be very occasionally scattered up by noise. In Figure 3.10, we compare the predicted luminosity with the calculated luminosities for our galaxies.

From Figure 3.10, we can see that the simulated galaxies are scattered up in luminosity

Model	Number count
Observed	200 ± 14
Béthermin et al. (2017)	172 ± 18
Symeonidis et al. (2013)	262^{+184}_{-103}
T + 5 K	54^{+38}_{-21}
T + 4 K	76^{+54}_{-30}
T + 3 K	85^{+61}_{-34}
T + 2 K	117^{+83}_{-46}
T + 1 K	170^{+121}_{-57}
T − 1 K	330^{+234}_{-130}
T − 2 K	373^{+264}_{-147}
T − 3 K	493^{+349}_{-194}
T − 4 K	611^{+433}_{-241}
T − 5 K	842^{+597}_{-332}

Table 3.2: Red number counts from observations, from Béthermin et al. (2017) and from our mock catalogue based on Gruppioni et al. (2013) and Symeonidis et al. (2013). We created additional mock catalogues with different average temperatures to show the dependence on temperature for the predicted number counts. Error bars on the mock catalogue come from the error in the normalization of the Gruppioni et al. (2013) luminosity function, our observations error bars come from poison statistics. With the current large error bar sizes we can only exclude (difference $> 3\sigma$) the T+5 K model.

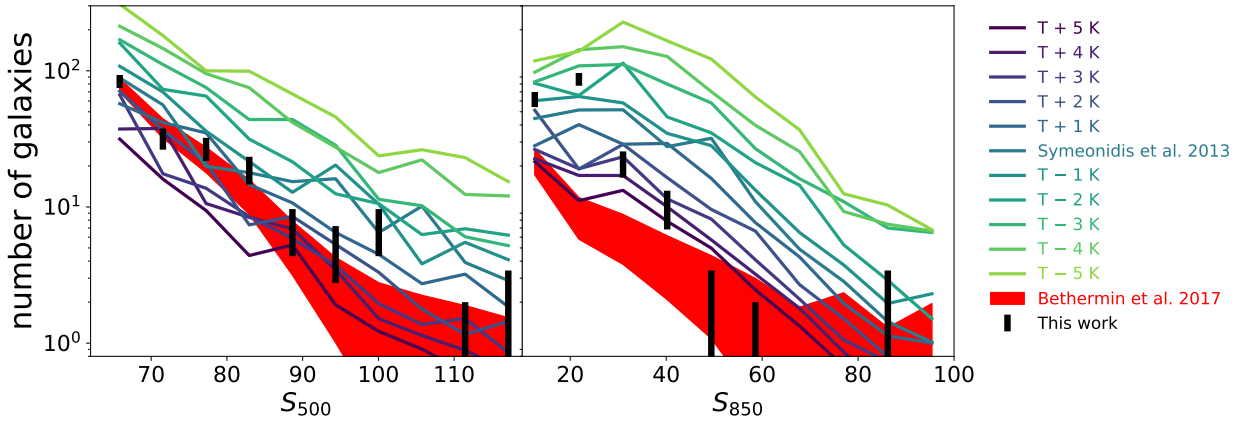

Figure 3.9: Number of galaxies which fulfil our selection criteria as function of 500 μm flux density on the left and as function of 850 μm on the right in black with Poisson error bars. In red the number of galaxies from the SIDES model (Béthermin et al., 2017) in combination with observational errors. The coloured lines represent the number of galaxies we expect from the Gruppioni et al. (2013) luminosity function in combination with the nominal mean temperature, and variations on that mean temperature from Symeonidis et al. (2013).

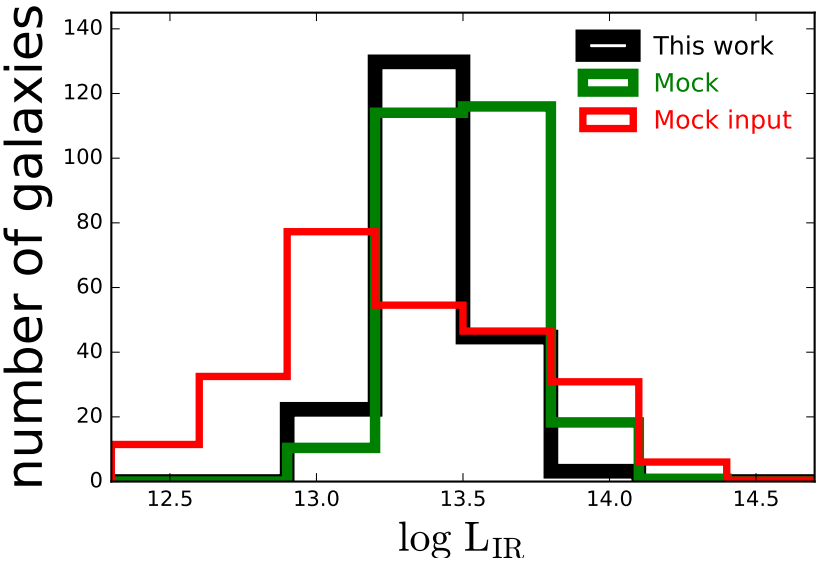

Figure 3.10: Luminosity histogram of 500 μm riser galaxies in the HeLMS field in black. In green we show the output from our pipeline for the mock catalogue obtained from sampling galaxies from the Gruppioni et al. (2013) luminosity function and adding observational uncertainties to them. In red, we show the input luminosities for the mock sample shown in green.

due to confusion and instrumental noise. This is a flux boosting effect, well-known in sub-mm surveys (e.g. Coppin et al., 2005, 2006). From our mock catalogue we derive that 61 per cent of the mock galaxies which observational properties fulfil our selection criteria are intrinsically not bright enough and are scattered up due to confusion and instrumental noise. We use the average boosting factor (difference between input and output Luminosity of our Mock) to correct our SRFD in Figure 3.8.

Comparison with simulations

The Simulated Infrared Dusty Extragalactic Sky (`SIDES`, Béthermin et al., 2017) includes a 274 deg^2 simulation to match the size of the HeLMS field. The size of the model and its capability to simulate the observed FIR and submillimetre flux densities makes it ideal for comparison with our observations.

The main `SIDES` model predicts the FIR and submillimetre emission in a 2 deg^2 light cone, which simulates clustering by using abundance matching to populate dark matter haloes with galaxies according to their star formation evolution model. This model is accurate in describing the number counts at 350 and 500 μm. This 2 deg^2 light cone is not a large enough volume to get accurate predictions for our rare sources. Béthermin et al. (2017) tackled this problem by producing the 274 deg^2 simulation to predict number counts for much rarer (brighter) sources but this larger simulation does not contain any clustering estimates.

The number of sources in the 274 deg^2 `SIDES` model which fulfil the Asboth et al. (2016) criteria is 22, and all are strongly lensed. This number goes down to 11 in the case we use our $S_{500} > 63$ mJy cut on top of the Asboth et al. (2016) criteria. These numbers are an order of magnitude lower that the bright red sources found in the HeLMS field.

Those results do not account for the effect of flux boosting by both instrumental and confusion noise. Béthermin et al. (2017) calculated this effect of flux boosting by adding random (Gaussian) instrumental and confusion noise to the fluxes. This increased the number count to 114 sources which fulfil the Asboth et al. (2016) criteria and 35 sources when we add $S_{500} > 63$ mJy constraint. The 2 deg^2 `SIDES` model was used to calculate the effect of clustering on these number counts. They found that the confusion which arises from clustering increases the number of red sources by a factor of $1.7^{+1.9}_{-0.9}$. This leaves them with an estimate of 229^{+258}_{-121} sources which is within 1σ of the 477 sources found in Asboth et al. (2016). This boosting factor of $1.7^{+1.9}_{-0.9}$ is however not high enough to boost the 35 sources in the 274 deg^2 `SIDES` model to the 200 sources found in the HeLMS field.

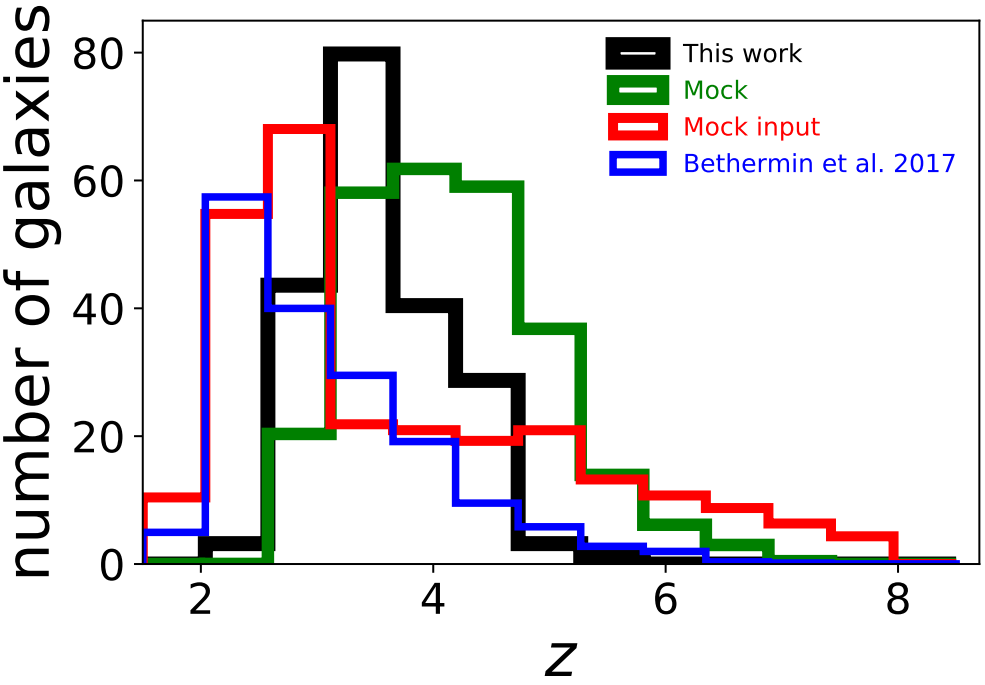

Figure 3.11: Redshift distributions of our observations (black), the mock (green) catalogue, the mock input (red) and the Béthermin et al. (2017) model (blue).

Our method of drawing correlated confusion noise estimates provides us with a different way of using the 274 deg^2 SIDES model to predict the number of sources in the HeLMS field. We do this by adding both random Gaussian instrumental noise, and our correlated confusion noise estimates to the SIDES 274 deg^2 catalogue. This noise increases the number of sources from 11 to 172±18 (where the noise only accounts for different sets of random numbers and Poisson noise, and does not account for any other uncertainties in the SIDES model), which is very close to 200 sources which were detected with our selection criteria (see Table 3.2 and Figure 3.9).

Seventeen per cent of these 172 sources are strongly lensed and the mean redshift is 3.1 ± 0.9. Figure 3.11 shows the full redshift distribution of our data compared with the SIDES model and our mock catalogue.

From Figure 3.11 we can see that the redshift distribution of the mock has a larger tail to higher redshifts than our observations. We test if there is any significant net bias we calculate the mean of the observed mock and input mock redshifts, we calculate the error on this mean using jack-knife samples. We find a different value for the mean redshift (4.17 ± 0.04 q.v. 3.69 ± 0.08), which is smaller than the rms of the refshifts of 0.6, but nevertheless statistically significant. Flux boosting can happen at every wavelength band but because of our 500 μm riser selection we are biased towards selecting galaxies which

are boosted at 500 μm. These selected galaxies look therefore redder than they truly are, which results in a overestimate of the redshift. This argument mainly holds for galaxies which are intrinsically not red or bright enough to fulfil our selection criteria. For all galaxies we see the same trend as in Figure 3.6, where our redshifts are overestimated at high redshift and under estimated at low redshifts. As we stated in more detail in Section 3.4.4 this trend is partly due to selection effects and due to the prior pushing us towards mean and not "extreme" redshift estimates.

The 274 deg^2 `SIDES` model model has a comparable high-redshift tail, but this model peaks at lower redshift, causing the mean redshift to be lower (3.1 ± 0.07 q.v. 3.6 ± 0.04 from our observations).

3.5.2 SDSS and *WISE* quasars

We cross-matched the 188 galaxies with the SDSS quasar catalogue (Pâris et al., 2017) and found two matches within 20 arcsec. We test the chance on a random alignment with an SDSS quasar by taking 50 000 random positions in the HeLMS field and see how many of these random positions match with an SDSS quasar within a 20 arcsec radius. The number of matches is 127, leading to a probability of 0.25 per cent that there is a random alignment within 20 arcsec. Using this statistics we would expect that there is a 38 per cent chance that at least one of our object is randomly aligned with an SDSS quasar and there is a probability of 8 per cent for at least two alignments.

HELMS_RED_80 is located 3 arcsec from SDSS_J005036.93+014449.1 which has a redshift of 3.4351 ± 0.0003. Our estimated photometric redshift is $3.65^{+0.65}_{-0.7}$, which is within 1σ agreement with the quasars spectroscopic redshift. The quasar is furthermore detected in *WISE*-1, *WISE*-2 and *WISE*-3. We use the intrinsic quasar SED derived in Symeonidis et al. (2016) in combination with the *WISE* magnitudes to calculate the AGN contribution to the FIR luminosity. This contribution is estimated at $\log(L_{FIR}) = 12.97^{+0.11}_{-0.12}$ and is a factor of ~ 3 lower that our measured luminosity. We thus conclude that it is likely that HELMS_RED_80 is associated with SDSS_J005036.93+014449.1 and that the quasar contaminates our SFR estimate.

HELMS_RED_421 is located 12 arcsec away from SDSS_J000127.11-010603.1 which has a redshift of 1.934 ± 0.001. Our estimated photometric redshift is $2.95^{+0.7}_{-0.8}$, which is in 1.3σ tension with the quasars spectroscopic redshift. The separation of 12 arcsec is furthermore in 2σ tension with our positions. The quasar is not detected in any *WISE* bands, but there is a nearby (z = 0.163) SDSS galaxy 9.0 arcsec away from our SPIRE

detection which is detected in all four *WISE* bands $> 5\sigma$ (WISE_J000127.76-010607.5). Furthermore, WISE_J000126.74-010612.2 is located 9.6 arcsec away and is detected in *WISE*-1 and *WISE*-2 and WISE_J000127.44-010626.6 is located 12.4 arcsec away and has besides a *WISE*-1 and *WISE*-2 detection a 3.3σ detection in *WISE*-3. The location of our SPIRE source lies in the middles between those four *WISE*/SDSS sources, indicating that this source is likely contaminated by several of those galaxies. We tested the probabilistic de-blender XID+ (Hurley et al., 2017) using the default flat uniform flux prior (as used for the HELP data base, Vaccari, 2016, Oliver et al., in preparation) to disentangle the SPIRE flux densities over the four sources. XID+ with a uniform flux prior, assigns the flux evenly among them as they are all located at roughly the same distance from the centre of the SPIRE emission. We note XID+ can be run with more sophisticated priors, using both SED and redshift information, however this requires thorough analysis and so we leave the nature of this SPIRE detection for future work.

HELMS_RED_421 may be associated with SDSS_J000127.11-010603.1 but would be consistent with a spurious coincidence. The percentage of the FIR luminosity which is caused by the (potential) quasars is a function of the AGN luminosity (Rosario et al., 2012; Symeonidis et al., 2016; Symeonidis, 2017), which we do not know. We therefore exclude the source from our final corrected SFRD.

3.5.3 Sub-mm interferometry

We use the high-resolution SMA data, the ALMA and the CARMA redshifts to more closely examine the properties of the subset of galaxies possessing this information. The images and SED fits of the six galaxies with interferometry data are shown in Figure 3.12. We now discuss the sources individually below:

- HELMS_RED_1: The photometric redshift of $4.0^{+0.55}_{-0.52}$ is consistent with the spectroscopic redshift of 4.163 which is obtained with CO(4-3) and CO(5-4) line detections (Riechers et al. in preparation). The 500 μm flux density of 192 mJy suggests that the object is lensed (e.g. Negrello et al., 2017). This source was also detected with ACT with flux densities of 12.49 ± 1.74, 35.11 ± 2.62 mJy and 72.32 ± 6.26 mJy at 148 (2.0), 218 (1.4) and 278 (1.1) GHz (mm), respectively. Our best-fitting SED predicts flux densities of 7, 24 and 47 mJy at those frequencies, which are considerably lower. The SMA flux density at 1.1 mm is 28.6 ± 2.3 mJy, which is less than half that of the ACT value at 278 GHz which is observed at a similar wavelength but with a much larger beam. The predicted 1.1 mm flux density from our best-fitting SED is 46.6

mJy. The nearest *WISE*-1 or SDSS source near to the SMA position is 15.6 arcsec away. The SMA position is 3.9 arcsec away from the SCUBA-2 position.

- HELMS_RED_2: The photometric redshift of $4.6^{+0.67}_{-0.65}$ is consistent with the spectroscopic redshift of 4.373, which is obtained with CO(4-3) and CO(5-4) line detections (Riechers et al. in preparation). The 500 μm flux density of 132 mJy means the object is likely to be lensed. The SMA flux density is 33.9 ± 2.25 and the predicted 1.1 mm flux density from our best-fitting SED is 53.9 mJy. The nearest *WISE*-1 or SDSS object near the SMA position is 2.0 arcsec away, the location of the source is J005258.53+061317.5 and has a *WISE*-1 AB magnitude of 17.5 ± 0.2. The SMA position is 2.0 arcsec away from the SCUBA-2 position.

- HELMS_RED_4: The photometric redshift of $4.15^{+0.60}_{-0.57}$ is in 1.7σ tension with the spectroscopic redshift of 5.162, which is obtained with CO(5-4) and CO(6-5) line detections (Asboth et al., 2016). The 500 μm flux density of 116 mJy makes the object likely to be lensed. The SMA flux density is 21.3 ± 1.9 mJy and the predicted flux density at 1.1 mm from our best-fitting SED is 29.8 mJy. The nearest *WISE*-1 or SDSS object near the SMA position is 1.0 arcsec away, the location of the source is J002220.73-015520.2 and has a *WISE*-1 AB magnitude of 17.4 ± 0.2. The SMA position is 1.5 arcsec away from the SCUBA-2 position.

- HELMS_RED_10: The photometric redshift is $4.6^{+0.75}_{-0.63}$. The SMA flux density of 13.3 ± 2.8 and the predicted 1.1 mm flux density from our best-fitting SED is 24.5 mJy. The nearest *WISE*-1 or SDSS object near the SMA position is 8.7 arcsec away. The SMA observations are not centred on the SCUBA-2 position and the brightest peak is 4.7σ. The SMA position is 13.4 arcsec away from the SCUBA-2 position. It is unclear if the SMA sources is the same source as our SPIRE/SCUBA-2 detection more detail of this sources will be provided in Greenslade et al. (in preparation).

- HELMS_RED_13: Our photometric redshift of $3.3^{+0.62}_{-0.64}$. The SMA flux density is 11.5 ± 1.8 mJy and the predicted flux density at 1.1 mm from our best-fitting SED is 19 mJy. The nearest *WISE*-1 or SDSS object near the SMA position is 3.6 arcsec away. The SMA position is 2.9 arcsec away from the SCUBA-2 position.

- HELMS_RED_31: This object has a single line detection which might be either the CO(5-4) or the CO(4-3) transition (Asboth et al., 2016) suggesting a redshift of 3.798 or 4.997. The photometric redshift of $4.15^{+0.76}_{-0.73}$ is consistent with the lower

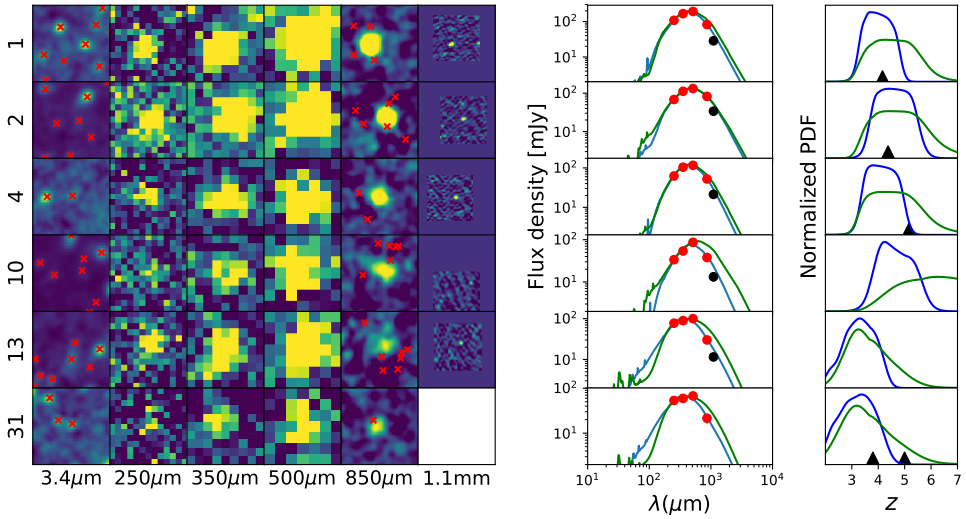

Figure 3.12: *WISE*-1 (3.4 μm), SPIRE (250, 350, 500 μm), SCUBA-2 (850 μm) and SMA (1.1 mm) 70 arcsec $\times$ 70 arcsec cut-outs of bright S_{850} sources in the HeLMS field with ancillary sub-mm interferometry data. The wavelength of each image is noted on the bottom of the plot in μm and the source ID (see Appendix C) on the left. The second on the right shows the best-fitting SED in blue, the best-fitting SED using only SPIRE in green, and the flux density from SPIRE and SCUBA-2 in red. The right-hand panel shows the redshift PDF of our sample in blue, and the PDF if we exclude the SCUBA-2 data in green (showing the improvement in constraining the redshift by including longer wavelength data). The black triangles show the spectroscopic redshifts derived from ALMA and CARMA, where the two black triangles for HELMS_RED_31 show the redshift in the case the line detection is the CO(5-4) or the CO(4-3) line. The red crosses on top of the *WISE* bands show 5σ source detections in *WISE*-1. On top of the SCUBA-2 image we overlay all SDSS-detected galaxies in red.

redshift from and in a small (1.1σ) tension with $z = 4.997$. The nearest *WISE*-1 or SDSS source is 4 arcsec away from the SCUBA-2 position.

3.5.4 Extreme sources

We isolate a subset of potentially high-redshift extremely bright galaxies. This subset consists of galaxies which have a clear detection with SCUBA-2 ($S_{850} \geq 5\sigma$) as well as a redshift PDF which has 50 per cent of its probability at $z > 4$. In total we find 21 galaxies fulfilling those conditions, which includes HELMS_RED_2 , 4, 10 and 31. Figure 3.13 shows the *WISE*-1, SPIRE and SCUBA-2 cut-outs of these sources, excluding the ones we already discussed in Section 3.5.3.

These sources might contain some of the highest redshift DSFGs ever detected. Therefore this catalogue provides a high priority sample for spectroscopic follow-up with ALMA. High-resolution follow up observations are also required for accurately determining the blending fraction (see Section 3.6.1) for these types of sources.

Our candidate with the highest chance of being a z $\geq$ 6 galaxy is HELMS_RED_69. Its redshift is estimated to be $5.19^{+0.89}_{-0.92}$ and 19 per cent of its redshift PDF lies above a redshift of 6. Another remarkable feature of HELMS_RED_69 is that its 500 μm flux density is 1.5 times higher than that of HFLS3. There is a possibility that this source has been lensed by a foreground galaxy as we find an SDSS counterpart at a distance of 3.0 arcsec.

3.6 Discussion

3.6.1 Blending and Lensing

Due to the relatively large beam of the 500 μm data there is a high probability that in many cases some parts of the measured flux density comes from randomly aligned galaxies or companion galaxies of the main source (confusion; Nguyen et al., 2010).

ALMA observations (Hodge et al., 2013; Karim et al., 2013) of bright LABOCA (S_{870} > 12 mJy) sources in the 0.25 deg^2 LESS survey (Weiß et al., 2009b) showed that these sources contain emission from several fainter sources with an upper limit of 9 mJy per source, in later work this fraction of sources breaking up is found to be less significant (Simpson et al., 2015). This indicates that there might be a maximum SFR for DSFGs of 10^3 M$_\odot$ yr^{-1} (Chabrier IMF). Bussmann et al. (2015) found that 20 out of 29 bright SPIRE sources (S_{500} = 52-134 mJy) break down into multiple ALMA sources, and of the nine isolated sources five have a magnification factor larger than five. Simpson et al. (2015) found that 61^{+19}_{-15} per cent of their sample of bright galaxies (median $S_{850}\pm$ 0.4 mJy) consist of a blend of two or more sources in the ALMA maps. Their sample was selected to be representative of the bright end of the 1 deg^2 deep 850 μm S2CLS field. The brightest detection with ALMA had a flux density of 12.9 $\pm$ 0.6 mJy and is considerably brighter than the sources observed in Karim et al. (2013). Michałowski et al. (2017) found that bright DSFGs found in SCUBA-2 blank fields (around 10 mJy) typically have a second component of about 1-2 mJy. Furthermore, they found that the bright end of the source counts is hardly affected by replacing from SCUBA-2 flux densities with those from

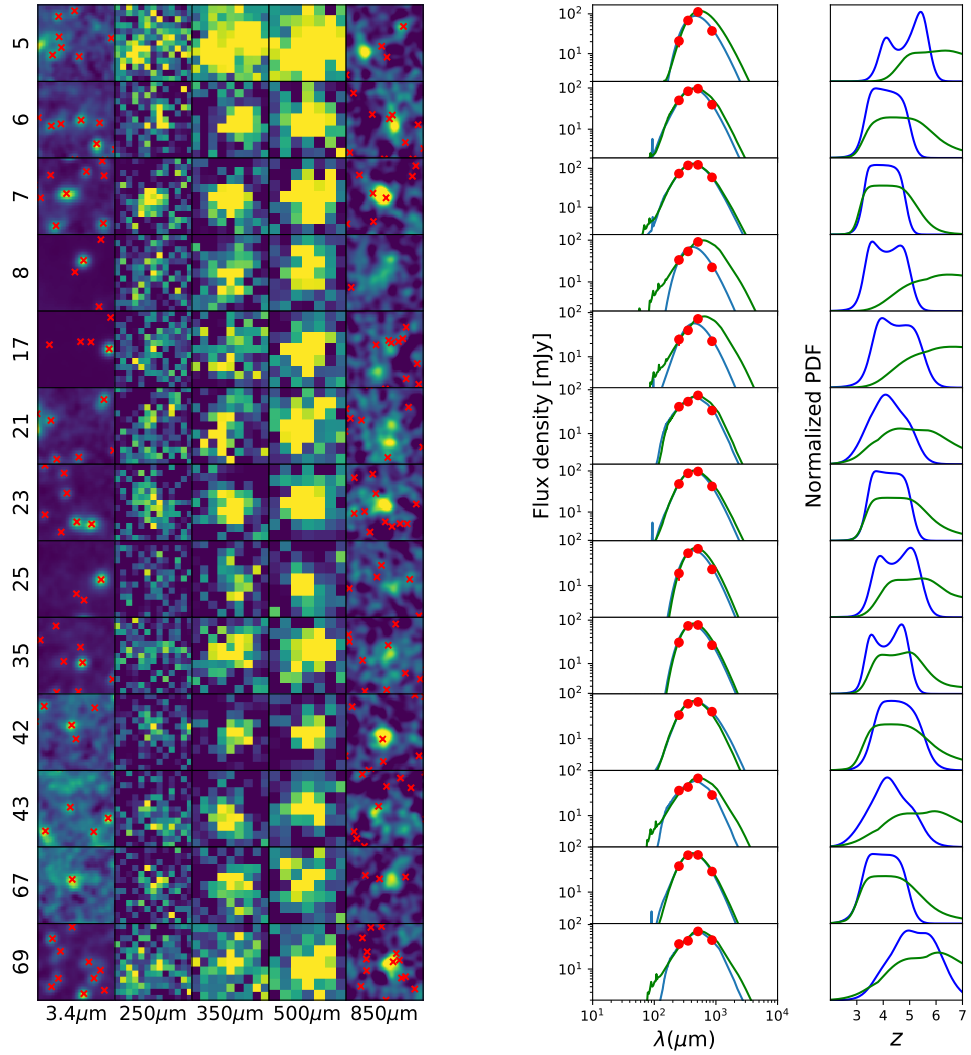

Figure 3.13: *WISE*-1 (3.4 μm), SPIRE (250, 350, 500 μm) and SCUBA-2 (850 μm) 70 arcsec $\times$ 70 arcsec cut-outs of bright S_{850} sources in the HeLMS field. The wavelength of each image is noted on the bottom of the plot in μm and the source ID (see Appendix C) on the left. The second on the right shows the best-fitting SED in blue, the best-fitting SED using only SPIRE in green and the flux density from SPIRE and SCUBA-2 in red. The right-hand panel shows the redshift PDF of our sample in blue, and the PDF if we exclude the SCUBA-2 data in green (showing the improvement in constraining the redshift by including longer wavelength data). The red crosses on top of the *WISE* bands show 5σ source detections in *WISE*-1. We overlay all SDSS-detected galaxies in red over the SCUBA-2 images.

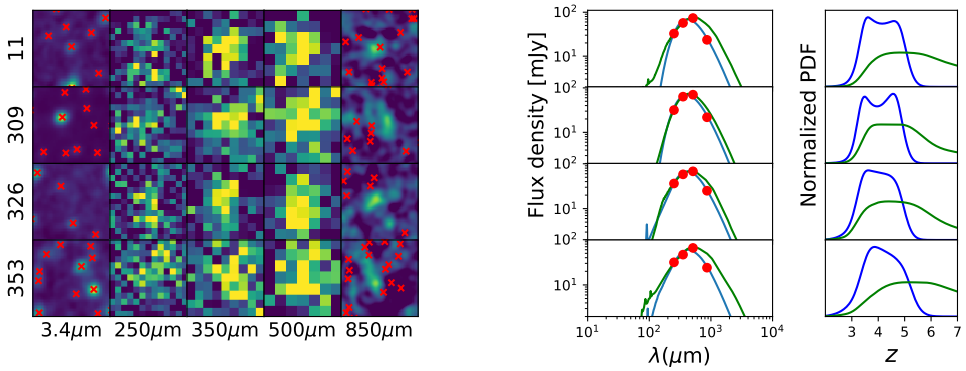

Figure 3.13: (Continued)

ALMA. The survey was taken over an area of 2 deg^2.

The bright end of the Karim et al. (2013), Simpson et al. (2015) and Michałowski et al. (2017) sources are fainter than 20 mJy, and are thus much fainter than our Group 1 galaxies. Hence, it would be interesting to see if our brightest sources are also characterized by having a second component of about 1-2 mJy or a 61^{+19}_{-15} per cent blending fraction.

Prior-based source extraction (XID+ Hurley et al., 2017) to investigate multiplicities of bright *Herschel* sources at 250 μm in the COSMOS field show that the brightest component contributes roughly 40 per cent of the source flux density (Scudder et al., 2016).

The multiplicity due to blending seen in these studies is a potential concern. Blending of objects at the same redshift will not seriously impact on the redshift determination, although we will determine the luminosity and star formation of the combined system, rather than a single object. Blending of two (or more) objects at different redshifts will produce composite SEDs which are likely to elicit an intermediate redshift estimate. We derive from our mock observations that $\sim$ 60 per cent of our detected galaxies are likely to be scattered up to our selection criteria due to flux boosting partly caused by blending with foreground objects. Some of those boosting factors are as large as 0.5 dex, but can be explained by instrumental and confusion noise. An example of such a large effect might be HELMS_RED_421 where the SPIRE position is in the middle of three *WISE* sources and an SDSS detected quasar. Similar results were found in Donevski et al. (2017), where $\sim$40 per cent of selected 500 μm riser galaxies in a simulated map would intrinsically not have made their selection criteria of $S_{250} > 13.2$ mJy and $S_{500} > 30$ mJy.

The advantage with our sample is that we probed a much wider field, over 100 times wider than COSMOS and S2CLS and more than 1000 times bigger than the area targeted by the ALMA observations of the LESS field. Our sample is therefore expected to be comprised of a much rarer and more luminous and less confused population of sources.

However, a proper investigation of the blending of these objects is deferred until we are able to obtain high-resolution data of a significant sub-set.

HFLS3 has an observed flux density of 35.4±0.9 mJy at 850 μm (Robson et al., 2014), which is comparable to our Group 1 galaxies. Riechers et al. (2013) found that HFLS3 is only marginally magnified by a factor of 1.2-1.5 by a foreground lens. This magnification factor was updated by Cooray et al. (2014) to a factor of 2.2 ± 0.3, which yields an SFR of 1320 $M_{\odot}$ yr^{-1}.

Another explanation for the high SFRs in our sample is that the galaxies might be lensed (Zavala et al., 2018). We do not expect to detect weak lensing from high-redshift lenses or even unambiguous confirmation of large magnifications from nearby lenses from our current data. We can however asses the likely incidence of lensing statistically by looking at the density of *WISE*-1 and SDSS sources near our SCUBA-2 detections. For this we use our Group 1 galaxies which have $> 5\sigma$ SCUBA-2 detections. For this group we can use the SCUBA-2 positions with a statistical positional accuracy of $\sigma_{pos} = 0.6 \times \frac{\mathrm{FWHM}}{S/N}$ (Ivison et al., 2007) which is of the order of 2 arcsec, which is comparable with the JCMT pointing accuracy of 2-3 arcsec. We combine these two uncertainties ($\sigma_u^2 = \sigma_{pos}^2 + \sigma_{JCMT}^2$) and assume that either the optical/NIR counterpart or the lens should lie within a $\approx 2\sigma_u$ $\approx$ 7 arcsec annulus around our source position.

We use this 7 arcsec aperture to count the number of 5σ *WISE*-1 detected objects near our Group 1 sources and find that 53 per cent have a nearby *WISE* galaxy. We calculate the significance of this number by using the same aperture at 64 (same number as Group 1 galaxies) random positions in the HeLMS field 1000 times. With these 1000 runs we can calculate both the expectation value and the 84.1, 97.8 and 99.9 percentiles.

In Figure 3.14 we show our results for our 7 arcsec aperture and several larger apertures. It is clear that there is a significant overdensity of *WISE*-1 sources near our Group 1 galaxies. The total space density of *WISE*-1 sources is a factor of 3 higher, which is a strong indication that part of this sample is lensed (Wang et al., 2011). We perform the same measurement on a $S_{500} > 100$ mJy subset and find that seven of the nine sources have a *WISE*-1 counterpart within the 7 arcsec annulus. This leads to an even higher *WISE*-1 space density compared to our Group 1 sample, but due to the low number of galaxies this is less significant than our Group 1 overdensity. González-Nuevo et al. (2014) found a similar result by cross-correlating SDSS and GAMA $0.2 \leq z \leq 0.6$ galaxies with $S_{350} \geq 30$ mJy *H*-ATLAS sources. They found a $> 10\sigma$ spatial correlation, which for non-overlapping redshift distributions can be explained by weak gravitation lensing, where the

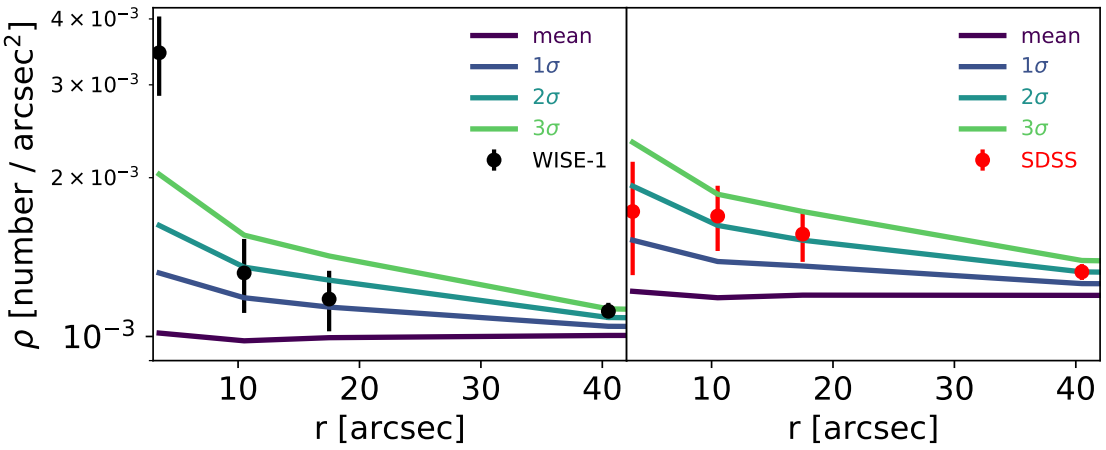

Figure 3.14: Surface density of *WISE*-1 sources (left, black) and SDSS galaxies (right, red). There is a significant increase in low-redshift sources (possible lenses) near our targets in comparison with average number counts (solid lines). The higher number density near our targets can be caused by an overlap of the redshift distribution of optical/NIR sources and sub-mm sources and/or a signature of foreground lensing.

weak regime has a lensing factor smaller than 2.

We do, however, wish to stress that this is a statistical measurement, and we lack accurate enough positions and morphologies for our DSFGs to do a proper lensing analysis to yield a magnification estimate. Furthermore, we lack sufficiently deep optival data to find potential lenses at z $>$ 0.5. For our estimates of the $L_{\rm IR}$ and SFR we do not take this significant foreground source detection into account.

An overlap between the redshift distribution of *WISE*-1 sources and 500 μm risers could provide another explanation for the excess *WISE*-1 sources seen near our high-redshift DSFGs. Ménard et al. (2013) used the cross-correlation between SDSS quasars and *WISE* sources to recover the redshift distribution of WISE sources. They found that there is a potential sub-sample of *WISE* sources with a redshifts $>$ 2, indicating that it is possible that our high-redshift sample could be detected in *WISE*. However, their red *WISE* sources with z $>$ 2 are at least 1.2 magnitudes brighter in the *WISE*-2 band than in *WISE*-1 and several orders of magnitude brighter in the *WISE*-3 band.

We find that 34 of our 64 Group 1 galaxies have at least one *WISE*-1 source within the 7 arcsec aperture. Of these 33 closest *WISE* sources, only 2 have a *WISE*-2 magnitude 1.2 brighter than *WISE*-1. The remaining 31 are either undetected in *WISE*-2 (and we would have detected them if they were 1.2 magnitude brighter than in *WISE*-1) or they have a *WISE*-2 magnitude that is not bright enough to fall in the red sample. The non-red

WISE sources have a mean redshift of 0.5 and are very unlikely to have a redshift above 1.5 Ménard et al. (2013).

High-resolution follow-up is required to properly assess the incidence of lensing and to resolve any blending issues and determine the merging, interacting or stable disc-like morphologies of the systems (e.g. Dye et al., 2017; Oteo et al., 2017b, Leung et al. in preperation). The high-resolution 870 μm ALMA continuum observations of 11 of our DSFGs show that 7 of them show disturbed morphologies, indicating strong lensing (Oteo et al., 2017a). These results show that lensing can explain some of the extremely high flux densities but also shows that some sources are not strongly lensed and do have extreme SFRs ($\gg 10^3$ $M_\odot yr^{-1}$). For a full description of the ALMA data and the morphology of the sources see Oteo et al. (2017a).

3.6.2 Space density

Ivison et al. (2016) compared their space density of DSFGs at $4 < z < 6$ to the space density of *UVJ* selected massive galaxies at $3.4 < z < 4.2$ (Straatman et al., 2014) which are predicted to form their stellar mass around redshift 5. Straatman et al. (2014) found a space density for massive $M_{\rm stars} > 10^{11} M_\odot$ quiescent galaxies of 4×10^{-6} Mpc^{-3}, which is an order of magnitude higher than Ivison et al. (2016) and 2 orders of magnitude higher than our results of 7×10^{-8} Mpc^{-3}.

We can therefore make a similar conclusion to that of Ivison et al. (2016) for *H*-ATLAS ($S_{500} > 30$ mJy), i.e. that the HeLMS ($S_{500} > 63$ mJy) red sample cannot account for the massive quiescent galaxies found at $z \sim 3-4$. This can be confirmed by our measured SFRs (5000 $M_\odot yr^{-1}$), which for a t_{burst} of 100 Myr generate a higher stellar mass of $M_{\rm stars} \sim 5 \times 10^{11} M_\odot$ than the (Straatman et al., 2014) sample. This suggests that part of our sample might go through a short phase ($\ll$100 Myr) of extremely high star formation, or is lensed, or is more massive (and thus rarer) than the population probed by Straatman et al. (2014).

3.7 Conclusions of chapter 3

We have observed 188 high-redshift, dusty, star-forming galaxy candidates with the SCUBA-2 camera at the JCMT. The sample had been selected to be very red and bright at *Herschel* SPIRE wavelengths and was taken from the 274 deg^2 HerMES HeLMS field. We achieve a 1σ rms depth of $S_{850\mu m}$ =4.3 mJy and detected 87 per cent of our candidates with S/N >3.

We developed a new method of incorporating correlated confusion noise into our SED fitting procedure.

We applied `EAZY` with a range of galaxy templates to determine the full redshift PDF. The addition of the longer wavelength 850μm data improves our photometric redshifts which are systematically lower than with SPIRE data alone and reduces the estimated uncertainties from $\sigma_z/(1+z) \approx 0.25$ to 0.19. Our photometric redshifts are consistent with the four spectroscopic redshifts available in our sample.

With this final PDF we compute the redshift, FIR luminosity and SFRs of our sample. From these we computed the SFRD and showed that the population of 500 μm risers with $S_{500} > 63$ mJy contribute less than 1 per cent of the total SFRD at any epoch. The number density of 500 μm risers is consistent with a model extrapolated from the Gruppioni et al. (2013) FIR luminosity function and with the Béthermin et al. (2017) empirical model, contradicting previous tensions with physically motivated models. Consistency with the models arises from our novel way in adding both confusion and instrumental noise were $\sim$60 per cent of the galaxies are predicted to be scattered up to our selection criteria due to flux boosting.

The excess number of *WISE*-1 sources near our DSFGs gives a strong indication that some of our sample may be lensed or that there is a surprising overlap with the redshift distribution of *WISE*-1 sources.

High-resolution SMA observations of five of our sources reveal that two of the sources have a *WISE*-1 source at the same position. In all cases the SMA flux density at 1.1 mm is lower than predicted from our best-fitting SED.

We identify a subset of 21 excellent very high-redshift DSFGs candidates, of which two are already identified as z>4 DSFGs. This group is clearly detected by SCUBA-2 with a high probability that they lie above a redshift of 4. These 21 galaxies would be ideal targets for interferometric imaging and spectroscopy to get a better understanding of these high-redshift objects with extreme ($\gg 1000$ $M_\odot yr^{-1}$) star formation.

Observing the high-redshift, dust-obscured Universe remains an important challenge for current day astronomy. Interferometry has the resolution and sensitivity to answer our questions about the SFR and nature of these obscured galaxies. With telescopes like ALMA it is still impractical to cover a large enough area of the sky to find a representative population of extreme star-forming sources. With our new catalogue we now possess an ideal target list for high-resolution and spectroscopic follow up.

Chapter 4

Have we seen all the galaxies that comprise the cosmic infrared background at 250 μm $\leq \lambda \leq$ 500 μm?

4.1 Abstract of chapter 4

The cosmic infrared background (CIB) provides a fundamental observational constraint on the star-formation history of galaxies over cosmic history. We calculate the contributions to the CIB in the 250–500 μm range originating from the faintest catalogued galaxies. The CIB contributions are estimated by using a novel map fitting technique on the *Herschel* SPIRE maps at the positions of galaxies catalogued in the COSMOS field over a large range in wavelengths, namely r, K_s, 3.6 μm, 24 μm, 100 μm, 250 μm, 850 μm and 3 GHz. At these depths, subtle systematic effects in the stacking method arise. We have developed an improved version of `SIMSTACK`, which now simultaneously fits the galaxies, the system background and the leakage of flux from galaxies located in masked areas. We also correct for a new "over-fitting" effect. We determine how the contribution to the CIB depends on galaxy selection band and magnitude. We find high contributions to the CIB with the deep r ($m_\mathrm{AB} \leq 26.5$), K_s ($m_\mathrm{AB} \leq 24.0$) and 3.6 μm ($m_\mathrm{AB} \leq 25.5$) catalogues. We combine these three deep catalogues and find a total CIB contributions of 10.5 $\pm$ 1.2, 6.7 $\pm$ 0.7 and 3.1 $\pm$ 0.3 nWm^{-2}sr^{-1} at 250, 350 and 500 μm, respectively. Our CIB estimates are consistent with recent phenomenological models and consistent with (though much more precise than) the diffuse total measured by FIRAS. Our results raise the interest-

ing prospect that the CIB contribution from known galaxies has converged. Our results provide an important benchmark for future modelling of star-forming galaxy populations and prior-based modelling of confused *Herschel* data. These results indicate that future large-area surveys like those with the Large Synoptic Survey Telescope are likely to resolve a substantial fraction of the population responsible for the CIB at $250\,\mu\mathrm{m} \leq \lambda \leq 500\,\mu\mathrm{m}$.

4.2 Introduction of section 4

The diffuse extragalactic cosmic infrared background (CIB, e.g., Puget et al., 1996) is caused by the re-radiation of absorbed UV and optical light emitted by young stars and active galactic nuclei (AGN). This thermal re-radiation contributes approximately half of the radiation we receive from extragalactic sources (e.g. Hauser and Dwek, 2001; Hill et al., 2018). It is therefore important to understand which sources are responsible for this CIB, as they are the likely contributors to the star-formation rate density of the Universe (e.g. Madau and Dickinson, 2014).

The aim of the paper is to measure the contribution of galaxies in different catalogues to the CIB. The result can be used as a practical indicator of what depth of data is needed to detect a significant fraction of the star-forming populations that cause the CIB, which is part of the aim of future generation large area surveys like Large Synoptic Survey Telescope (LSST; Ivezic et al., 2008). We can furthermore use the results to give new and more accurate lower limits for the *total* CIB. These more accurate limits can be used to constrain galaxy evolution models.

The Far Infrared Absolute Spectrophotometer (FIRAS) instrument aboard the Cosmic Background Explorer (*COBE*; Puget et al., 1996) was designed to measure the cosmic microwave background spectrum and deviations from it, including the CIB (Fixsen et al., 1998; Lagache et al., 1999). FIRAS was able to measure the total CIB due to the presence of a cold external calibrator, a facility that more recent space based telescopes like the *Herschel Space Observatory* (Pilbratt et al., 2010) and *Spitzer* (Werner et al., 2004) lacked. Due to the absence of this absolute measurement and a high thermal background from the warm telescope, the *Herschel* maps all have their means subtracted. To measure the total flux in the *Herschel* maps we therefore need to sum up the flux density of the individual sources contributing to these maps (Dole et al., 2006).

Relatively few extragalactic sources are directly detected with *Herschel*, with the integrated flux density of those galaxies being a factor of about 7 lower that the total radiation received as the CIB (Oliver et al., 2010b). Recent work in deblending the *Herschel* maps

(Hurley et al., 2017) reveals that it is possible to assign the flux density in the confused (e.g. Nguyen et al., 2010) *Herschel* SPIRE (Griffin et al., 2010) maps to sources that are detected in higher resolution optical/NIR images. The question now arises: what depth of data do we need to effectively deblend these images?

To calculate new bounds for the CIB we will use a novel map fitting analysis based on `SIMSTACK` (Viero et al., 2013a) applied to the *Herschel* SPIRE (Griffin et al., 2010) maps in the COSMOS field (Scoville et al., 2007a). This field contains very deep catalogues in various wavelength bands and is therefore ideal for creating deep prior lists. In the near future, large area surveys will obtain data with the COSMOS depths over areas $\gg$ 100 deg^2 which could be used to find the optical/NIR counterparts of dusty star-forming galaxies over larger areas of the sky observed by *Herschel*.

The paper is structured as follows. In Section 4.3 we introduce the different sets of prior catalogues we use for our map fitting. In Section 4.4 we explain our map fitting method and we test our method in Section 4.4.1. Our results are described in Section 4.5 and discussed in Section 4.6. Our conclusions can be found in Section 4.7.

4.3 Data

4.3.1 HELP database

Most of the data described below will be part of the *Herschel* Extragalactic Legacy Project (HELP, Oliver et al. in prep.) database. HELP aims to collate and homogenize observations from many astronomical observatories to provide an integrated data set covering a wide range of wavelengths from the radio to the UV. The key focus of the HELP project is the data from the extragalactic surveys from ESA's *Herschel* mission, covering over 1300 deg^2. HELP will add value to these data in various ways, including providing selection functions and estimates of key physical parameters. The data set will enable users to probe the evolution of galaxies across cosmic time and is intended to be easily accessible for the astronomical community. The aim is to provide a census of the galaxy population in the distant Universe, along with their distribution throughout three-dimensional space.

4.3.2 Prior catalogues

For the optical/NIR data sets we use the Laigle et al. (2016) COSMOS2015 catalogue. From this catalogue we retrieve the r-band data, which were observed with the SUBARU Suprime-Cam as part of the COSMOS-20 project (Taniguchi et al., 2007, 2015). The

r-band data have a 3σ depth of $m_{\rm AB} = 26.5$ in a 3 arcsec aperture. We use the un-flagged regions in the optical bands inside the COSMOS 2 deg^2 field, which leaves us with a total useful area of 1.77 deg^2 for the r-band (Laigle et al., 2016). We only select galaxies with a `SExtractor` flag of 3 or lower (Bertin and Arnouts, 1996). With this flag we remove saturated or corrupted objects. We do keep neighbouring galaxies which could potentially bias each others magnitudes (an effect we discuss below).

The VIRCAM instrument on the VISTA telescope was used to obtain the $K_{\rm s}$-band data as part of the UltraVISTA survey (McCracken et al., 2012). Several ultra-deep stripes were observed, which cover a total area of 0.62 deg^2 (Laigle et al., 2016). We will use both the deep and ultra-deep K_s data, but we use the 3σ depth of the deep data ($m_{\rm AB}$ = 24.0 in a 3 arcsec aperture) as a cut-off for the whole catalogue. The total area with deep or ultra-deep $K_{\rm s}$-band data covers 1.38 deg^2 inside the COSMOS 2 deg^2 field (after excluding masked regions).

IRAC channel-1 (3.6 μm) observations consist of the first two-thirds of the SPLASH COSMOS data set, together with S-COSMOS (Sanders et al., 2007) and smaller IRAC surveys in the COSMOS filed (Capak et al. in prep.). The 3σ depth cut-off for IRAC channel 1 is $m_{\rm AB} = 25.5$, and the area covered is 1.77 deg^2 (after removing masked regions).

We use the new COSMOS catalogues, as they contain deeper NIR and IR data from UltraVISTA and SPLASH than in previous catalogues. The optical/NIR photometry is obtained using dual-image mode using `SExtractor`, which is highly effective in finding and selecting galaxies. Due to the new data depth and the dual-image strategy, the galaxy samples are highly complete (Laigle et al., 2016), with a stellar mass limit for star-forming galaxies of 10^{10} M$_\odot$ at $z < 2.75$ and 6×10^{10} M$_\odot$ at $z < 4.8$. Viero et al. (2015) used the Muzzin et al. (2013) catalogue to obtain the prior K-selected ($m_{\rm AB} = 23.4$) catalogue for stacking. However the Muzzin et al. (2013) catalogue only has 115 000 such galaxies within a 1.62 deg^2 area where the Laigle et al. (2016) catalogue contains 149,000 galaxies with $m_{\rm AB} \leq 23.4$ over an area of 1.38 deg^2, and a total of 200,000 detected galaxies with $K_{\rm s} < 24.0$. We therefore expect that the percentage of the CIB that we can resolve will be higher than that in Viero et al. (2015) due to the much higher completeness.

In the mid-infrared we use the MIPS 24 μm data obtained by Le Floc'h et al. (2009). We select objects with $S_{24} > 80$ μJy ($m_{\rm AB} < 19.1$) and that have S/N > 3. The total area observed with the MIPS instrument is 2.27 deg^2.

The PACS (Poglitsch et al., 2010) 100 μm data in COSMOS was observed as part of the PEP survey (Lutz et al., 2011). The PACS catalogue contains 7443 sources with S/N

> 3 and $m_{\rm AB} \leq 14.8$, spanning an area of 2.1 deg^2.

SPIRE (Griffin et al., 2010) data were obtained as part of the HerMES survey 4th data release (Oliver et al., 2012) and covers an area of 4.9 deg^2. We use the xID250 catalogues, which use the 250 μm `starfinder` detections as prior information for the positions. We only select sources with S/N > 5 (where N is instrumental noise only, the S/N for using both confusion and instrumental noise is around 1.2).

We use the SCUBA-2 (850 μm) data observed as part of S2CLS (Geach et al., 2017). The catalogue produced by S2CLS contains 719 sources detected with S/N > 3 within the 1.3 deg^2 observed with an RMS below 2 mJy beam^{-1}.

The VLA 3 GHz data (Smolčić et al., 2017) covers an area of 3.1 deg^2, where a median rms of 2.3 μJy beam^{-1} is reached in the central 2 deg^2 COSMOS area. We use 5.5σ detected sources ($m_{\rm AB} \leq 21.4$) in the central 2 deg^2 COSMOS area for our prior list.

We furthermore test our method in different fields to obtain an estimate of the effect of cosmic variance. We picked the SERVS IRAC channel 1 catalogues (Mauduit et al., 2012) in the ELAIS-N1 and CDFS-SWIRE fields to perform this test. The depth of the SERVS catalogues is $m_{\rm AB} = 23.1$ and therefore two orders of magnitude shallower that the COSMOS SPLASH sample. For those two fields we use the star masks provided by HELP to remove sources in our catalogue contaminated by stars or bright galaxies.

4.3.3 Maps for fitting

We use the SMAP (Levenson et al., 2010; Viero et al., 2013b) SPIRE maps described in Viero et al. (2015) for our map fitting analysis. These maps have a pixel scale of 4 arcsec, which is smaller than the standard HerMES maps, which have a pixel scale of 6, 8.33 and 12 arcsec at 250, 350 and 500 μm, respectively. The SPIRE maps are all mean-subtracted.

We use the 250, 350 and 500 μm SPIRE maps in the COSMOS field for our main analysis and we use the maps in the ELAIS-N1 and CDFS-SWIRE fields to check our method against cosmic variance. For ELAIS-N1 and CDFS-SWIRE fields we use the nominal pixel size maps. Absolute calibration in SPIRE has a 5 per cent calibration uncertainty (Griffin et al., 2010).

4.3.4 Previous CIB estimates

We have collated a number of previous estimates for the CIB to compare with our results (Table 4.1). Fixsen et al. (1998) measured the the CIB from FIRAS measurements by removing foreground emission from interplanetary and Galactic interstellar dust. Lagache

Work	250 μm	350 μm	500 μm
Fixsen et al. (1998)*	10.4 ± 2.3	5.4 ± 1.6	2.6 ± 0.6
Lagache et al. (1999)*	11.8 ± 2.9	6.4 ± 1.6	2.7 ± 0.7
Marsden et al. (2009)†	8.60 ± 0.59	4.93 ± 0.43	2.27 ± 0.20
Zemcov et al. (2013)$^+$	$8.3^{+1.4}_{-0.8}$		
Cai et al. (2013)	12.4	7.9	3.7
Viero et al. (2015)†	9.82 ± 0.78	5.77 ± 0.43	2.32 ± 0.19
Lacey et al. (2016)	7.4	4.8	2.3
Béthermin et al. (2017)	11.2	6.4	2.7

Table 4.1: The total CIB at the SPIRE wavelengths as measured by FIRAS*, stacking†, lensing$^+$ and simulations.

et al. (1999) obtained a different estimate of the CIB with the same FIRAS measurements, which differ from each other by around 25 per cent, but are still consistent within error bars. The FIRAS-derived values are systematics dominated, where the main systematic uncertainty is the removal of the Galaxy. Higher resolution observations with *Herschel* are not sensitive for this large scale Galactic emission.

Another method to measure the CIB is by adding (stacking) the flux density for all known galaxies in the Universe. This method can potentially miss (if it exist) a diffuse part of the CIB outside our own galaxy. But the main problem with this method is that stacking in the highly confused SPIRE maps is non trivial (see Section 4.4) and that it potentially misses the flux density of galaxies which are not detected. Therefore these measurements (Marsden et al., 2009; Viero et al., 2015) are technically an underestimate of the total CIB.

We use the simulated COSMOS map and catalogue adopted in Hurley et al. (2017) to calculate a model-based estimate for the CIB. This mock catalogue was created using the Durham semi-analytic model (`GALFORM`; Cowley et al., 2015; Lacey et al., 2016), which realistically simulates clustering and optical magnitudes. This optical catalogue is than used as input for the radiative transfer code `GRASIL` (Silva et al., 1998) to obtain $\lambda_{\rm rest} > 70\,\mu$m flux density estimates. These values are lower than (and at 250 μm in more than 1σ tension with) either results from FIRAS. On the other hand, the Béthermin et al. (2017) simulation (which we are going to use for the testing of our method) and the Cai et al. (2013) simulation contains a higher flux density at the SPIRE wavelengths, which in both cases are in line with the FIRAS methods.

4.4 Method

We use an improved stacking analysis to measure the contribution to the CIB originating from galaxies detected in different catalogues. Stacking is equivalent to determining the covariance between a catalogue and a map (Marsden et al., 2009). In traditional stacking a list of prior positions is used to add the map at those position on the sky together. The noise in this "stacked" image will go down with $\sqrt{N}$, with N the number of stacked positions.

Normal stacking overestimates the flux density in maps which are clustered and confused, as it will add the flux density from correlated sources to the galaxies in the stacking sample. To get around this problem `SIMSTACK` (Viero et al., 2013a) was developed, which measures this covariance between the map and a catalogue by simultaneously fitting all the known sources in the map.

Traditionally `SIMSTACK` creates images with delta functions at the positions of galaxies in the prior catalogue. These images are convolved with the instrument PSF. This results in a linear model for every pixel (j) in the map (M) with the mean flux (S_α) for galaxies in each list, α, as a free parameter:

$$M^j = S_1 C_1^j + ... + S_n C_n^j, \tag{4.1}$$

where C_α^j is the beam-convolved mean-subtracted image of the sources in list α, at pixel j. This method should provide an unbiased estimate of the mean fluxes of the populations.

There are, however, two problems with the traditional `SIMSTACK`, it does not fit the background nor does it consider signal arising from sources located in masked areas. These masked areas are regions on the sky where there are no observations for the prior catalogue or regions where these data are corrupted. The corrupted areas mainly arise due to the saturation of pixels by nearby bright galaxies or stars. No galaxies are detected in these masked areas, and therefore we should not take them into account for our map fitting.

The masked regions provided by Laigle et al. (2016) have a higher mean signal than non masked regions in the SPIRE map due to the presence of bright nearby sources. A naive application of SIMSTACK on a mean-zero map would thus underestimate mean fluxes, even leading to negative flux densities.

To solve these two problems we adjusted the `SIMSTACK` code to fit a foreground layer[1] (F) and leakage from flux from masked areas (S_L) simultaneously with the pointing-matrix

[1] We use foreground for the diffuse component, which consist of the emission from the telescope, Galactic emission and the emission from galaxies which are not correlated with the galaxies in our prior catalogues. This layer also incorporates the mean subtraction of the SPIRE maps.

created in Equation 4.1. As we are now fitting for a background there is no more need to mean subtract the beam convolved number of sources (N_α^j) in a layer. The equation we are solving in this work is therefore:

$$M^j = S_1 N_1^j + ... + S_n N_n^j + S_L N_L^j + F, \tag{4.2}$$

where the constant foreground, F, is not a function of pixel j.

We recreate the SPIRE maps with holes on the positions of masked areas in the prior catalogue. In these holes we mask the SPIRE pixels and these pixels are therefore not used in the fitting process. Not using these areas is crucial, since otherwise flux from sources within those areas will be added to the foreground estimation and to nearby galaxies outside of the mask.

Areas masked because they have not been observed or because of saturation due to bright stars should have a comparable value for the SPIRE intensity as non-masked areas. However, the areas masked due to saturation from bright galaxies will have (on average) a brighter mean SPIRE intensity.

We do not use our map fitter in those masked areas, but due to the large SPIRE beam, there is still flux from those masked sources within the fitted regions. This excess flux will be put into the foreground layer (or to galaxies near the masked area), which causes an overestimate of the foreground over the whole field and an underestimate of the prior galaxies flux densities. We therefore added the extra layer (Equation 4.2) to our fitting process, this being the convolution of the masked pixels with the SPIRE beam (N_L^j). We provide a more detailed explanation when we describe the use of simulations in the next section.

4.4.1 Tests on simulations

We use the 2 deg^2 SIDES model simulation (Béthermin et al., 2017) to test our method. The SIDES simulation populates the halos in a dark-matter light cone with galaxies. For each galaxy a star-formation rate and hence spectral energy distribution is assigned and a gravitational lensing factor is also calculated. From this simulation the observed flux densities are calculated between 24 μm and 1.3 mm. We create our own 4 arcsec pixel SPIRE maps from the catalogue provided by Béthermin et al. (2017). We make these maps by smoothing the sources with a Gaussian PSF having a FWHM of 17.6, 23.9 and 35.2 arcsec for 250, 350 and 500 μm, respectively. We then add Gaussian pixel noise with σ = 5.7, 7.6, 13.4 mJy, comparable to the values for the instrumental noise in the observations. These simulated SPIRE maps contain clustering, instrumental noise, and

confusion noise, which makes them ideal to test our map fitting analysis. For the prior lists we divide the sources into magnitude bins ($\Delta_{\rm magnitude} = 0.4$) using the observed MIPS (24 μm) magnitudes. We use all 10^6 galaxies in the 2 deg^2 with 24 μm magnitudes < 26.4, these galaxies contribute more than 99 per cent of the CIB in this model.

To test our map fitting algorithm we create the SPIRE maps from the Béthermin et al. (2017) sources in several different ways: including or excluding the effects of clustering; instrumental noise; and confusion. These variants test how our method performs in different simulations and estimates corrections for systematic effects. For the simulated maps we know that the foreground is zero. Due to the lack of a foreground we can test if our code works in the absence of this foreground layer; however, the real SPIRE maps will have a non-zero foreground and we therefore need to use the foreground layer for the real maps.

For the first series of tests we assign every source a random position in the map to avoid spatial correlations. In the first example we assign the mean flux density of the galaxies in a magnitude bin to every source within that bin. For this map our layer model (Equation 4.2) is perfect as our model is able to exactly describe the flux en every position in the map. Therefore, we obtain a $\chi^2 = 0$ without noise and a $\chi^2/N_{\rm pix} \sim 1$ when instrumental noise is included. These results are unaffected if the foreground is allowed to vary. The next tests are the same, but instead of the mean flux we use the actual flux density of each source. In this case we do not have a perfect model and we obtain a reduced $\chi^2/N_{\rm pix} \sim 0.3$ in the absence of instrumental noise. The scatter of the source flux within a list could thus be seen as an additional "modelling noise". The results for 250 μm are shown in Figure 4.1, and we obtain the correct (within 2.5 per cent) shape for the total flux density for galaxies as function of magnitude. The total estimate for the CIB is correct to within 1 per cent. This results shows that our fitting routine works well in the absence of correlated sources.

For the second series of tests we use the actual positions of the sources from the simulation, which means that the galaxies in different lists are correlated. Otherwise, we run the same set of tests as in the previous series. We are able to correctly probe the mean flux densities of galaxy populations, but with two important exceptions (see Figure 4.2).

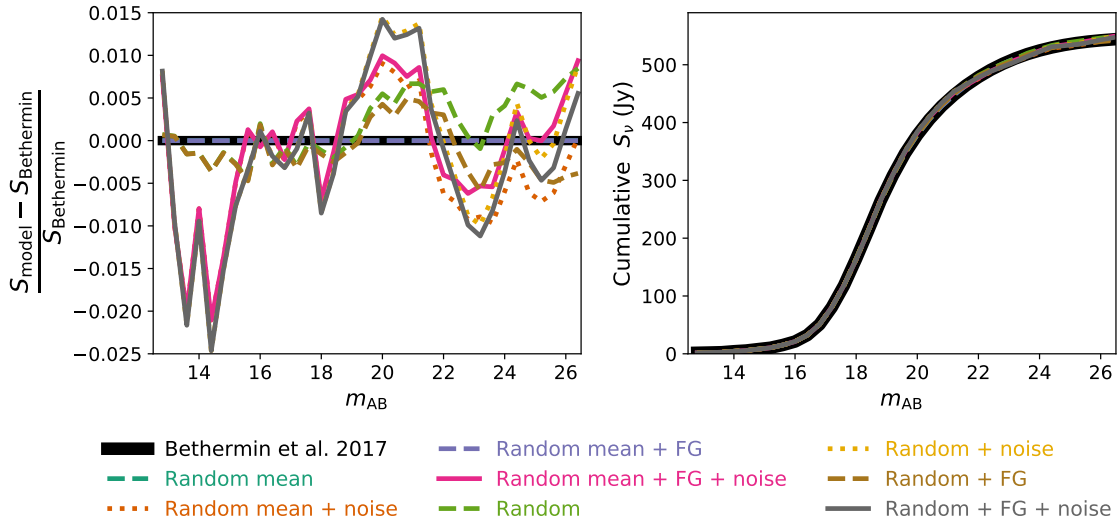

Figure 4.1: Testing our map fitting method at 250 μm for unclustered sources. In black is the "truth" from the simulation. On the left we show the offset from the true answer and on the right the cumulative flux density as function of magnitude. In all tests the sources have random Poisson-distributed (uncorrelated) positions. Here "Mean" indicates that the mean flux density of a population is used to create the map, "noise" indicates that instrumental noise is added, and "FG" indicates that we simultaneously fit for a foreground. For all models we are able to calculate the total CIB within 1 per cent accuracy.

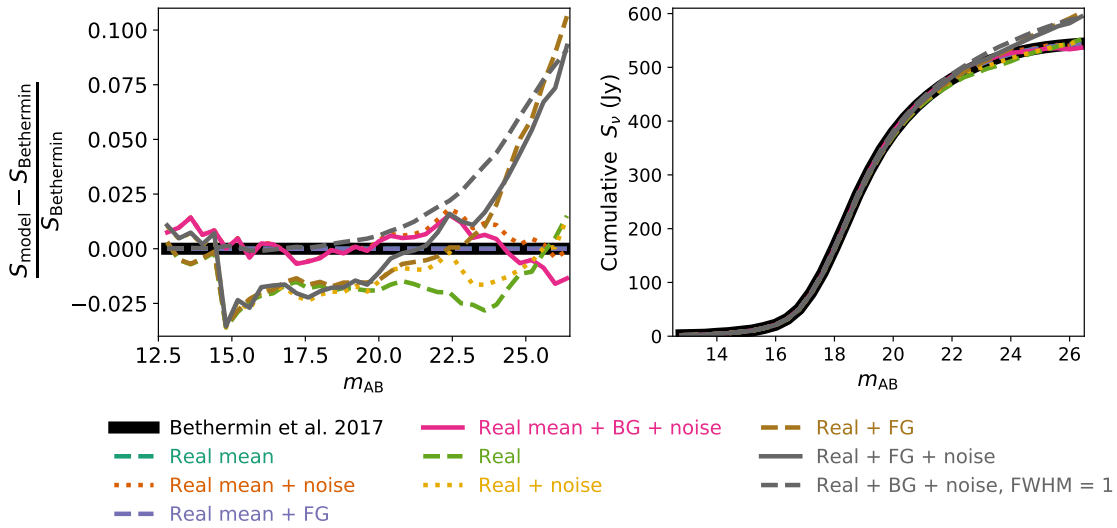

Figure 4.2: Testing our map fitting method at 250 μm for clustered sources. The labels are the same as in Figure 4.1, but in all these test the sources have the real (correlated) positions. We overestimate the flux density for faint sources when we allow the foreground to vary. This overestimation also occurs when we create the map with a very small beam (FWHM = 1 arcsec).

These cases are where we overestimate the flux density of faint ($m_{\rm AB} > 20$) galaxies when we allow the foreground to vary while using the individual source flux densities, both with and without noise.[2]

With a fixed foreground we do not obtain this overestimate. In this case there is finite amount of flux density available in the map and we cannot interchange flux between galaxies and a foreground. However for the real maps we do not know the value for this foreground and we have to fit for it (while we can set it to zero for the simulations). This overestimate when we fit the foreground simultaneously is potentially worrying, as it could cause an overestimate of the CIB in the real observations.

The overestimate is primarily caused by very faint sources. We therefore perform a test where we add another three layers of faint sources, between a magnitude of 26.4 and 27.6. These additional 170 000 galaxies contribute only about 0.5 per cent to the CIB. The results for this run are shown in Figure 4.3. This new model leads to an even larger overestimate (13 per cent) of the CIB in the simulations.

[2]We performed another test in this series using a FWHM of 1 arcsec to create the map, so that only galaxies within the same pixel are likely to bias each others flux densities. In this case we still obtain the same overestimate as in the nominal resolution (17.6 arcsec) map.

An over-fitting problem

A potential cause for this overestimate is "over-fitting", where the faint sources fit the noise, instead of being assigned a low flux. The results from our FWHM = 1 arcsec test show that this is primarily caused by brighter galaxies in the same pixel, with which the flux density could be exchanged between those galaxies and the foreground.

We run another test where we created a new map where we add 0.3 mJy to all faint galaxies with a $m_{\rm AB} > 23.2$ to see if this over-fitting effect is flux depended. With this simulation the overestimate reduces to ∼1 per cent. For this test the fit of galaxies that are located father away from another galaxy will dominate over this flux exchange between nearby sources on the sky. This flux exchange between galaxies and the foreground is still there when we bin our galaxies randomly instead of binning the galaxies according to their magnitude.

We perform a test to see if we can eliminate this over-fitting effect by removing all sources within a 4 arcsec radius of a brighter source. With this test we obtain the correct estimate for the CIB (Figure 4.3). By removing these sources we obtain a more realistic comparison with the real data, where we would not find multiple sources within a few arcsec due to resolution effects. However, when we make this radius too large then we will *under*estimate the CIB due to the missing sources; we show this by removing all sources within 10 arcsec of a brighter source (Figure 4.3). The removal of sources on the sub-arcsecond scale removes both random line-of-sight alignments and galaxies that are located very near each other and are undergoing a merger; these types of sources might be observed as one in the real observations, making this potential over-fitting less of a problem for the real observations.

This overestimate can be explained as follows. Correlated galaxies are more likely to appear near each other on the sky. As both populations of galaxies are fitted simultaneously with our code this should not be a problem. However, if a galaxy population (A) is correlated with a population (B) *and* this correlation is enhanced around bright galaxies from population A, then galaxies from B can be assigned the residual (positive) flux density from A.

We can illustrate our explanation in a simpler form (see Figure 4.4). We make a map containing four sources in layer A and add three correlated sources in layer B. We assume we can always obtain an optimal estimate of the mean flux of sources in A (e.g. because they are significantly brighter or more numerous than the B sources). The four A (A_1, A_2, A_3 and A_4) galaxies have flux densities of 1.3, 0.7,1.0 and 1.0 mJy, respectively,

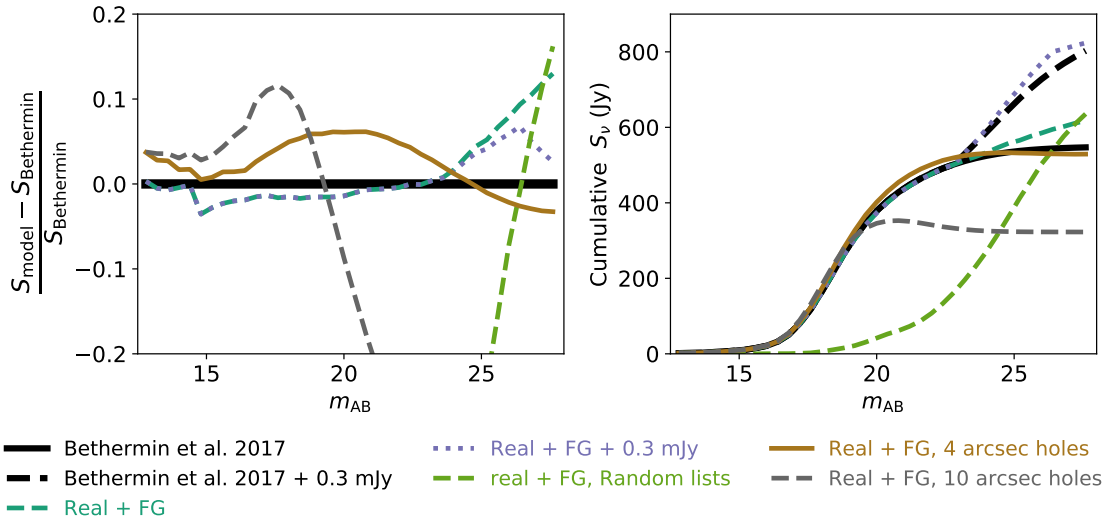

Figure 4.3: Testing our map fitting method at 250 μm for deeper simulated data. In black is the "truth" from the simulation. On the left we show the offset from the true answer and on the right the cumulative flux density as function of magnitude. In all tests the sources have the real (correlated) positions. "+0.3 mJy" indicates that we add 0.3 mJy to faint sources ($m_{\rm AB} > 23.2$), "random lists" indicates that we binned the galaxies randomly, and "holes" indicate that we removed faint sources within the hole radius from a brighter source. We overestimate the CIB when we fit for the foreground, but this overestimation is diminished when we add 0.3 mJy to faint sources or when we only allow for a maximum of one galaxy within a 4 arcsec radius. When we bin our galaxies randomly we obtain the same estimate for the CIB as if binned the galaxies according to magnitude.

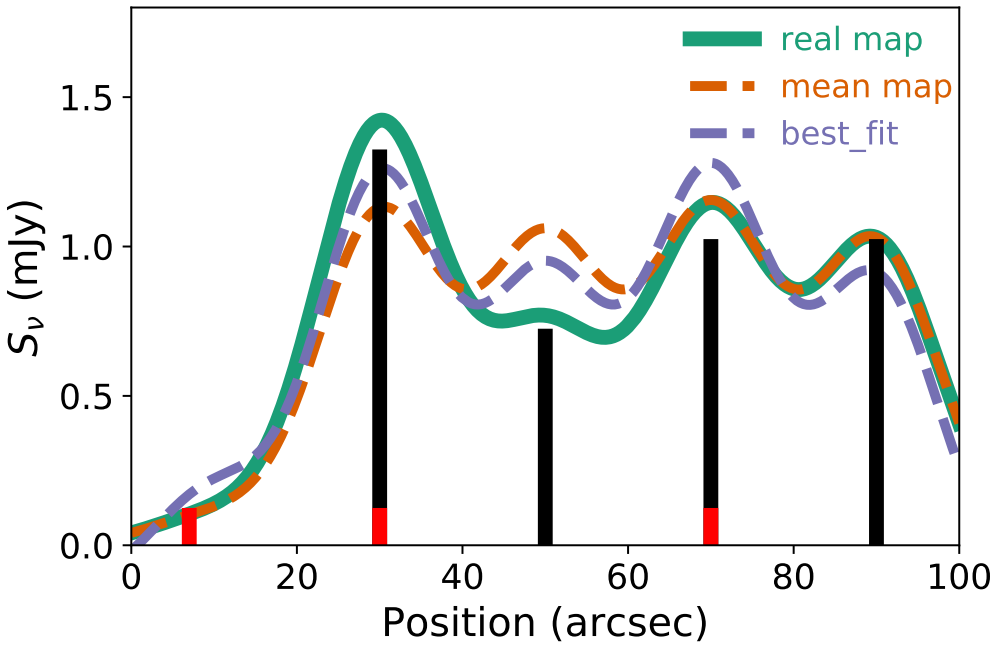

Figure 4.4: An example of an overestimation of the flux density in a 1-D 250 μm map (green). This map contains two populations of sources (A, black and B, red). The sources in layer B are faint (0.1 mJy) and correlated with the sources in list A, with a higher correlation for bright A sources. The purple line shows the best fit of our model and the orange line contains the mean flux of the populations, the result we are looking for.

with a mean of 1 mJy. Since we have the optimal mean then we have residuals of 0.3, -0.3, 0.0 and 0.0 mJy at the four positions of A in the map. The mean of the residuals is zero and the foreground fit will therefore be zero, the correct answer. We now add the three correlated B sources (all 0.1 mJy) at the location of the sources A_1 and A_3 and one at a random position. After subtracting the (optimal) mean of A, the residual flux densities in the map at the position of the B sources are 0.1, 0.4 and 0.1 mJy. The B layer will fit for the mean and obtain 0.2 mJy as an average. The total residuals, after subtracting layer B, for our five source locations is -0.3 mJy. This results in a negative foreground fit (Figure 4.4). It is important to note that this over-fitting would not happen if B were equally correlated with faint and bright A sources. This over-fitting is also reduced if there are many locations of B sources that are not near an A source, as the fit to B will be dominated by the uncorrelated sources.

Comparison with SIMSTACK

The real observations have masked areas on the sky and we simulate this by: (a) removing the outermost 8 arcsec from the three simulated SPIRE maps; (b) by removing 30 arcsec radius circles around all 392 MIPS sources with $m_{\rm AB} < 16$; and (c) by removing 392 random 30 arcsec radius circles from the map. The bright sources are removed as an examples of saturation by nearby bright galaxies, with the random circles are removed as examples of bright stars, which are not correlated with the galaxies and do not radiate significantly at SPIRE wavelengths.

All sources within those masked areas are removed from our prior list, and we do not fit the map at those positions. After the removal of masked areas we mean-subtract the map. Due to the large SPIRE beam, there is still flux from sources in the masked areas within the fitted regions of the map. We fit for this flux by adding one extra layer, being the convolution of all the masked pixels with the SPIRE beam. We now have a simulated map that incorporates instrumental noise and correlated confusion noise, with our prior catalogues contain selection effects from saturation by stars (the random circles) and from nearby bright galaxies (circles around bright sources). We test our algorithm at all three SPIRE wavelengths in Figure 4.5 and we compare our results with the basic SIMSTACK results.

Our method outperforms traditional SIMSTACK. When we only stack the bright end of the sources or if we make 4 arcsec holes around our prior sources (removing the over-fitting effect) we obtain the correct CIB within 5 per cent. The traditional SIMSTACK method underestimates the total CIB. This underestimation is mainly due to the negative flux density assigned to faint sources, because the mean subtraction of the maps also takes the brighter masked areas into account.

Most papers using SIMSTACK bin the galaxies according to redshift. We test our code and SIMSTACK in Figure 4.6 with this redshift slicing, where we fit the redshift slices separately from each other. We can see that our code performs very well for galaxies within a $\Delta = 0.5$ redshift slice, where SIMSTACK underestimates the total CIB. This underestimation only arises for very faint sources that are normally not present in the prior catalogues. This suggests that previous results from SIMSTACK are not likely to be incorrect, but that our algorithm is required when a very high (> 90 per cent) fraction of the CIB is resolved by the prior catalogue.

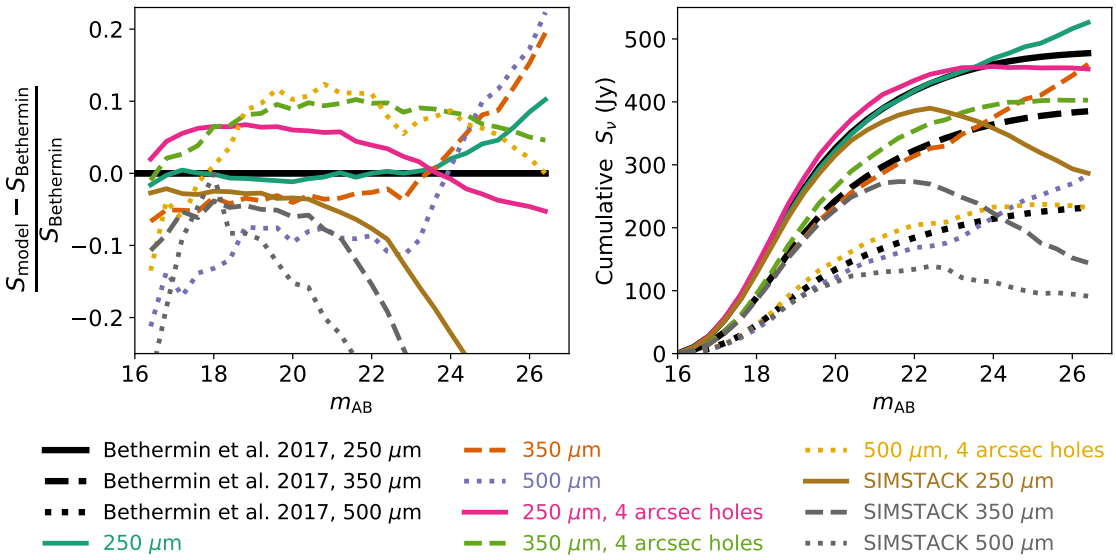

Figure 4.5: Testing our map fitting method at 250 (solid), 350 (dashed) and 500 μm (dots). In black is the "truth" from the simulation. On the left we show the offset from the true answer and on the right the cumulative flux density as function of magnitude. "SIMSTACK" indicates that we did not use our map fitting algorithm, but that we used the basic SIMSTACK. We overestimate the flux density when we fit all the sources in the simulation, due to the effect visualized in Figure 4.4, and we obtain the correct CIB (within 5 per cent) when we remove galaxies within 4 arcsec of a brighter galaxy. Traditional SIMSTACK underestimates the CIB substantially when (almost) all sources in the map are fitted simultaneously.

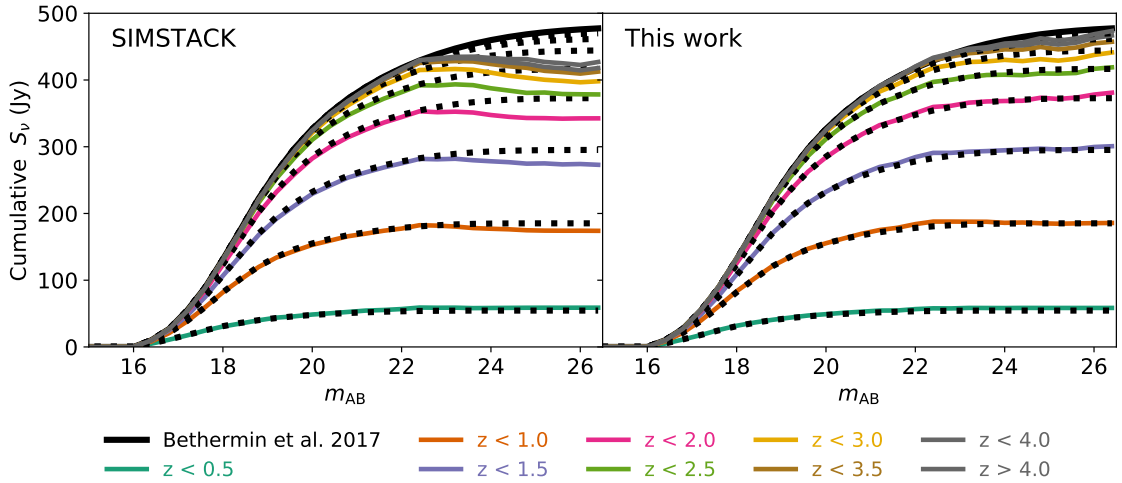

Figure 4.6: Comparison between SIMSTACK and our map fitting method when we use the redshift of the galaxies. In solid black is the "truth" from the simulation, and the black dots show the true answer for each redshift range. On the left we fit the redshift slices with `SIMSTACK`, which underpredicts the flux density for faint galaxies. On the right we use our new map fitting algorithm.

Incompleteness around bright galaxies

Our simulated catalogues are complete, while the observed prior catalogues in the optical/NIR suffer from incompleteness, as we cannot detect galaxies that are below a detection limit or located within a few arcseconds of another galaxy. We simulate this effect in Figure 4.6, where we remove all galaxies with a brighter galaxy within 2 arcsec on the sky. In this case we dramatically underestimate the flux densities for faint galaxies and obtain negative flux densities for $m_{\rm AB} < 22$ galaxies. This same effect was found by Heinis et al. (2013) and is a general problem in stacking.

When a prior list is stacked on, what is found is the total flux density of all the prior sources plus that of correlated coincident sources. Stacking should be done on a mean-subtracted map, so the mean flux from random alignments is zero, leading to a total stacking signal equal to the total flux of the prior sample. However, when the stacking sample is incomplete for faint objects that are coincident (but not necessarily correlated) with bright objects, a bias occurs. This results in there being a lower probability of finding a randomly aligned bright source at the location of the stacking sample, leading to a foreground of the stack that is lower than the average foreground of the field. For a mean-subtracted map this lower-than-average foreground will be negative, leading to a underestimate for the stacking signal. If the total flux density from the stacked galaxies is

less than this negative foreground, then a negative stacking signal can be measured (Heinis et al., 2013).

We do not see this effect when we fit all sources (Figure 4.5, 4 arcsec holes model) as in this case all the brighter galaxies are fitted simultaneously, leading to a foreground estimate for which the bright sources are taken into account. When we slice in redshifts these bright foreground galaxies are not fitted simultaneously but are just part of the foreground, and when we do not detect faint sources near them on the sky there is a correlation between faint parts in the foreground and the source layer, leading to an underestimate of the source flux density. When we fit all the galaxies simultaneously we do not have the effect described in Heinis et al. (2013). We therefore choose to fit all lists of galaxies simultaneously, even if redshift information is available.

4.4.2 Final method

The step by step description of our map fitting procedure is as follows.

i Every prior catalogue is binned by AB magnitude with bins ranging from 12.0 to 26.8, with a bin size of 0.4.

ii The sources within a bin are used to construct a synthetic δ-function map (+1 for pixels with a source and 0 at locations where there is no source). These maps are convolved with the SPIRE PSFs to produce as a fitting-matrix with dimensions M x N where M is number of pixels in SPIRE map and N is number of bins.

iii We use the mask provided along with the prior catalogues to re-create the SPIRE maps, with holes at locations where the prior catalogue does not have good data.

iv We add two extra layers to our fitting-matrix: one layer models the foreground and is a uniform map i.e. 1 for every pixel; the second layer is the mask convolved with the SPIRE PSF. This second layer fits the leakage of flux from sources into the map from masked regions.

v The fitting-matrix is used to simultaneously fit all layers using our improved version of `SIMSTACK`. The layers are fit on all three SPIRE maps independently using Equation 4.2.

vi We re-run our map fitting algorithm five times with a different bootstrap sample to calculate the errors by calculating the standard deviation from these five measure-

ments. These bootstrap samples come from random re-sampling of the pixels in the map which we use for the fit.

vii The obtained mean flux density per magnitude bin is multiplied by the number of sources within the bin to obtain the cumulative flux density as a function of the prior source magnitude (i.e. there is no incompleteness correction).

viii We calculate the error bars as the quadratic sum of Poisson errors, bootstrap errors and the SPIRE calibration uncertainty.

ix We make another run with our code, where we allow a maximum of one galaxy within a 4 arcsec radius, to estimate the effects of potential over-fitting, as described in Section 4.4.1.

x We use the flux densities derived from the main run with the error bars calculated in the second to last step to define our upper limit; for the lower limit we use the result from the 4 arcsec holes run, minus our error bar.

We cannot formally exclude the possibility that we are over-fitting our real maps in the same way that we over-fit the SIDES simulation. However the maximum source density we fit on the real SPIRE maps is $250\,000\,\mathrm{deg}^{-2}$, while we fit $500\,000\,\mathrm{deg}^{-2}$ for our simulated maps. The over-fitting only affects the faintest of those simulated galaxies, which are (potentially) not detected in the real surveys.

The problem of over-fitting only arises if faint galaxies are not only correlated with brighter galaxies (brighter in the flux density of the prior catalogue), but also have a higher correlation with the bright end (in the SPIRE map) than with sources that are fainter in the SPIRE maps. An example would be a merger that enhances star formation and therefore SPIRE flux. To determine the magnitude of this effect we need to know the real SPIRE flux densities of the sources, which is what we are trying to find. We do, however, believe that the effect will be smaller than in the SIDES simulation, due to the lower number counts and incompleteness of faint companion galaxies near bright galaxies in the real data. For the SIDES simulation the over-fitting effects cancel out when we remove all faint sources within 4 arcsec of a brighter source. We therefore perform an additional fit where we remove faint sources in a similar way to obtain a conservative underestimate of the flux density contained in those sources.

We expect our map fitting estimates to be correct to within 5 per cent, as shown in Section 4.4.1. This is comparable with the SPIRE calibration uncertainty and the uncertainty calculated from the bootstrap sampling.

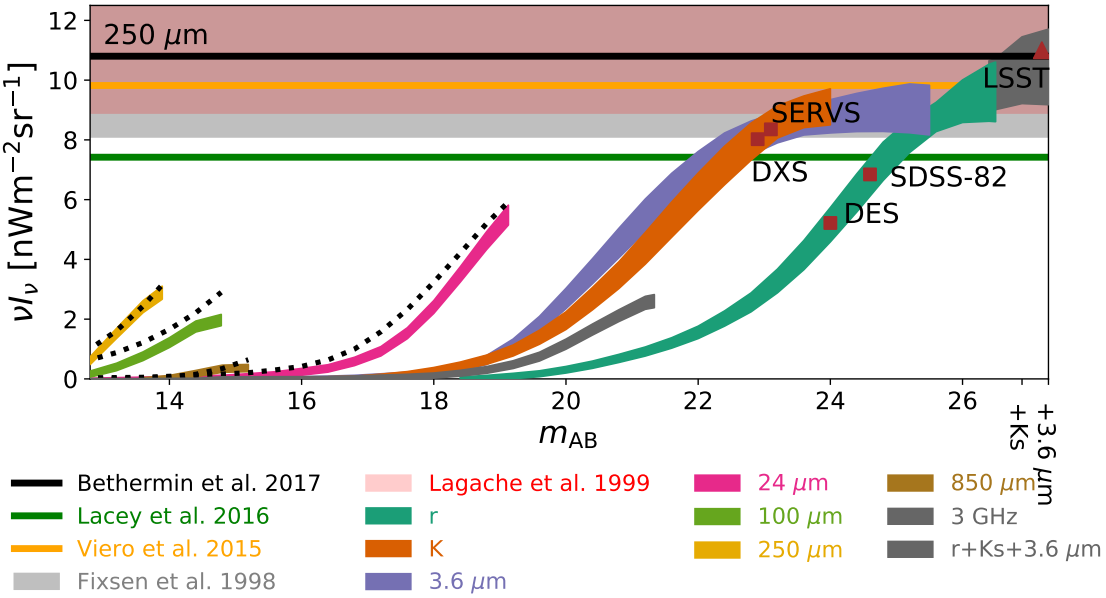

Figure 4.7: Cumulative measured CIB at 250 μm as a function of prior source apparent AB magnitude. Brown squares show the depth of several current and future large area surveys, with the solid lines show the total CIB as calculated from simulations or previous measurements with SPIRE. The grey and pink shaded areas show the CIB ($\pm 1\sigma$) estimated using FIRAS. The black dotted lines contain the estimates for the CIB from the SIDES simulation contained within FIR prior catalogues. For the r-band catalogue we add the 5σ K_s-band and 3.6 μm detected sources as two extra layers to obtain an estimate for the total CIB.

4.5 Results

The results of our map fitting method for 250 μm are shown in Figure 4.7. The best prior catalogues, which reach the highest fraction of the CIB, are the deep optical/NIR surveys. In all these three bands we reach a cumulative flux density that is higher than the 1σ lower bounds of the CIB measured by Fixsen et al. (1998). With the deep optical/NIR data sets we obtain a very high fraction of the CIB, with our r-band stack resolving 9.6 $\pm$ 1.0 nW m^{-2} sr^{-1} (at m_{AB} = 26.5) which is consistent with the FIRAS results. We combine the r-band data with 5σ detected K_s-band and 3.6 μm detected sources to obtain an estimate of the total CIB of 10.5 $\pm$ 1.2 nW m^{-2} sr^{-1}; for this measurements we only use the area (1.38 deg^2) with uncorrupted deep K_s-band data. Our estimates of the CIB are consistent with the total CIB predicted in the SIDES simulation and the total stacked values from Viero et al. (2015).

The results for 350 μm are shown in Figure 4.8 and those for 500 μm are shown in

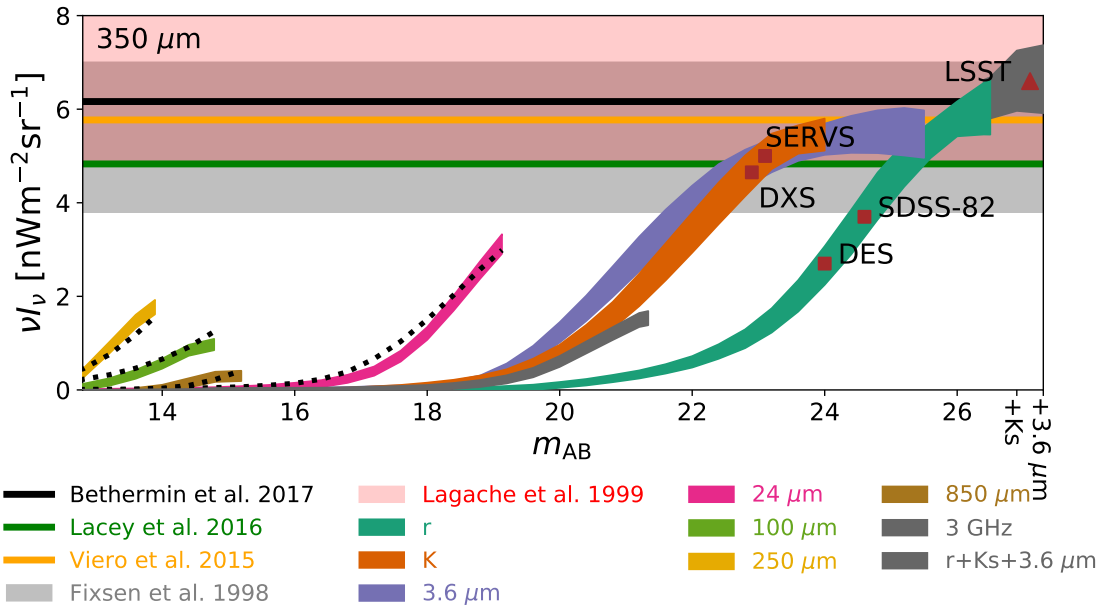

Figure 4.8: Cumulative measured CIB at 350 μm as function of prior source AB magnitude. The labels are the same as in Figure 4.7.

Figure 4.9. At 350 μm we resolve consistent values of the CIB as those measured by FIRAS and Viero et al. (2015) and simulated by Béthermin et al. (2017). The total CIB we find is 6.7 $\pm$ 0.7 nWm^{-2}sr^{-1}, with the combination of r, K_s and 3.6 μm data. For 500 μm we find a total CIB of 3.1 $\pm$ 0.3 nWm^{-2}sr^{-1}, which is higher than (but consistent within 1σ with) most previous measurements.

We partly calculated the effects of cosmic variance by using our bootstrap samples and our Poisson error bars. To robustly test the effect of this sampling variance we run our code with IRAC 3.6 μm priors on the 2.4 deg^2 ELAIS-N1 (EN1) and the 4.8 deg^2 CDFS-SWIRE (CDFS) field. We also re-run the code for the COSMOS IRAC data, where we make a cut at $m_{\rm AB} = 21.0$ for all three fields, so that the three fields have similar depths. The results are shown in Figure 4.10.

The difference between the three fields lies mainly in the masking of the IRAC catalogues. The EN1 and CDFS field use the HELP star masks (HELP masks just define the "holes" from bright stars, not the artefact regions), while the COSMOS field uses a more detailed mask where bright galaxies are more likely to get masked due to saturation of the very deep data.

The difference in number densities between the three fields is shown in Figure 4.11. It is clear that the number of bright galaxies is much higher in the shallower EN1 and CDFS fields. At the faint end the number of galaxies detected in COSMOS is higher, since it is

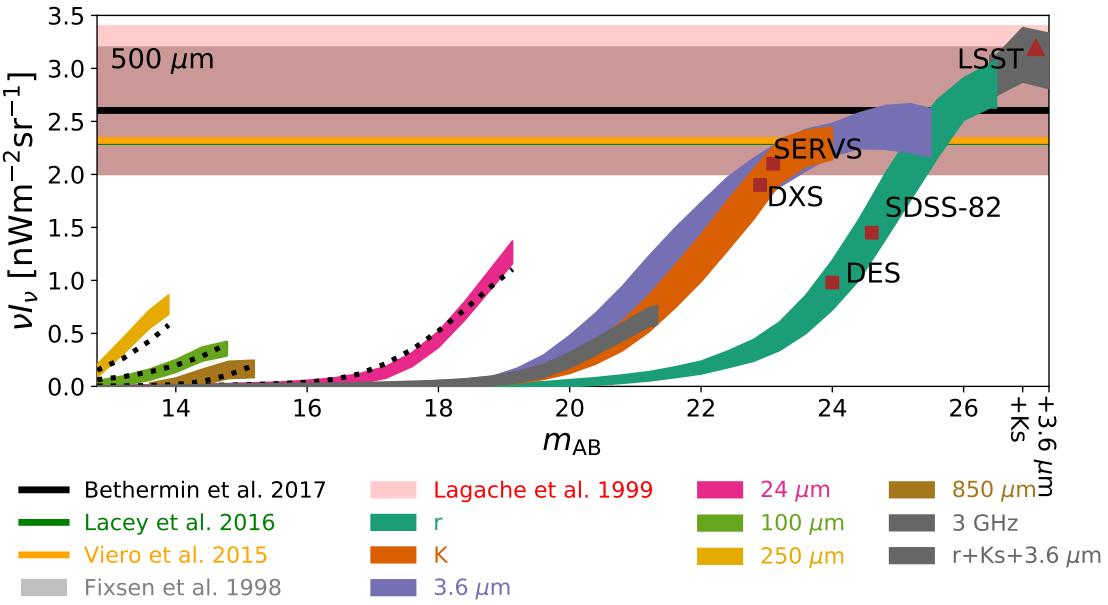

Figure 4.9: Cumulative measured CIB at 500 μm as function of prior source AB magnitude. The labels are the same as in Figure 4.7.

more complete due to the higher depth. It is also possible that some of the bright objects in the EN1 and CDFS fields are blends of fainter sources, which would have been detected as separate galaxies with the prior-based source extraction code used in COSMOS. This can both explain the excess of bright sources and the lack of faint sources compared to the COSMOS field. These effects of those different number counts can explain the differences in estimated CIB (Figure 4.10). Even though the measured CIB is different in the three fields they are still consistent within each others' 1σ error bars.

4.6 Discussion

In Figure 4.7 we also indicate the depth of existing and future large area surveys. Current and ongoing large area r-band surveys, such as the 5 000 deg^2 Dark Energy Survey (DES, The Dark Energy Survey Collaboration, 2005) and the 300 deg2 SDSS stripe 82 (Jiang et al., 2014) will detect galaxies responsible for about 50 per cent of the CIB at 250 μm over these large areas (Figure 4.7). This area and depth will later be exceeded by the 18,000 deg^2 LSST survey (Ivezic et al., 2008). The r-band depth (27.5) of LSST will be deeper than COSMOS over a huge area and will probe almost all the galaxies responsible for the CIB. It is important to note there likely exists a population of highly obscured (dusty) galaxies at high redshift which even LSST likely not see, but will only be visible in small area observations by ALMA and possibly JWST. Wide area K-band and IRAC

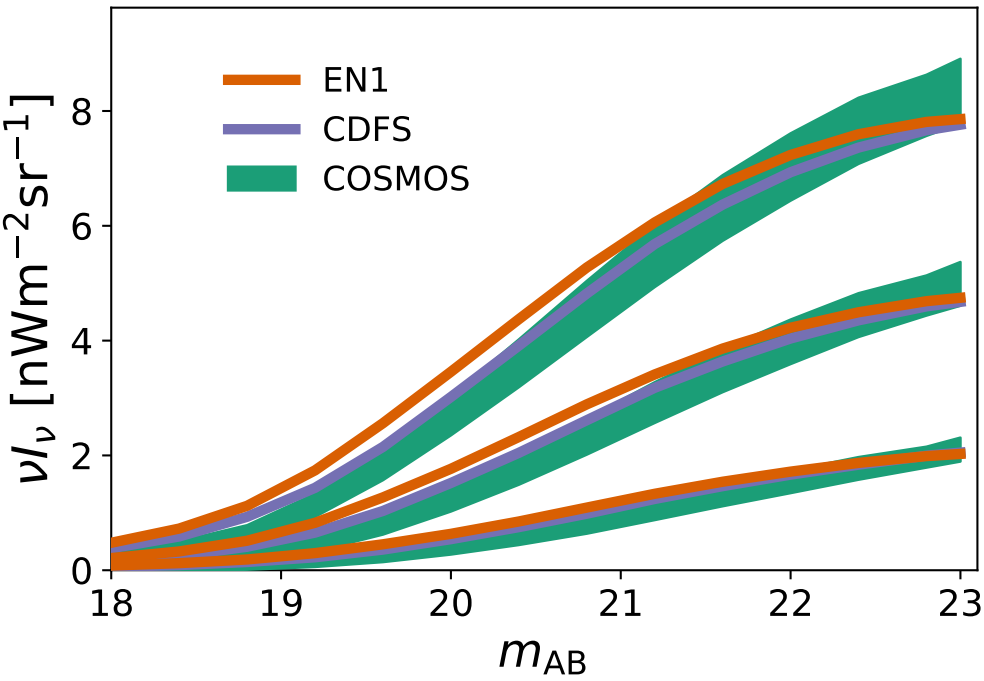

Figure 4.10: Cumulative CIB at SPIRE wavelengths as a function of IRAC 3.6 μm AB magnitude for the EN1, CDFS and COSMOS fields. The top three lines are the measurements at 250 μm, the middle three are measured at 350 μm and the bottom lines are measured at 500 μm. We only plot the $\pm 1\sigma$ error region for the COSMOS field for clarity (the error bars for the other two fields have similar sizes). The contribution to the CIB from bright galaxies is higher (but not significantly) in the EN1 and CDFS fields. However, once faint galaxies are included the total contribution to the CIB is higher in the COSMOS field. The differences between the fields is caused by a combination of different masking in IRAC and sampling variance.

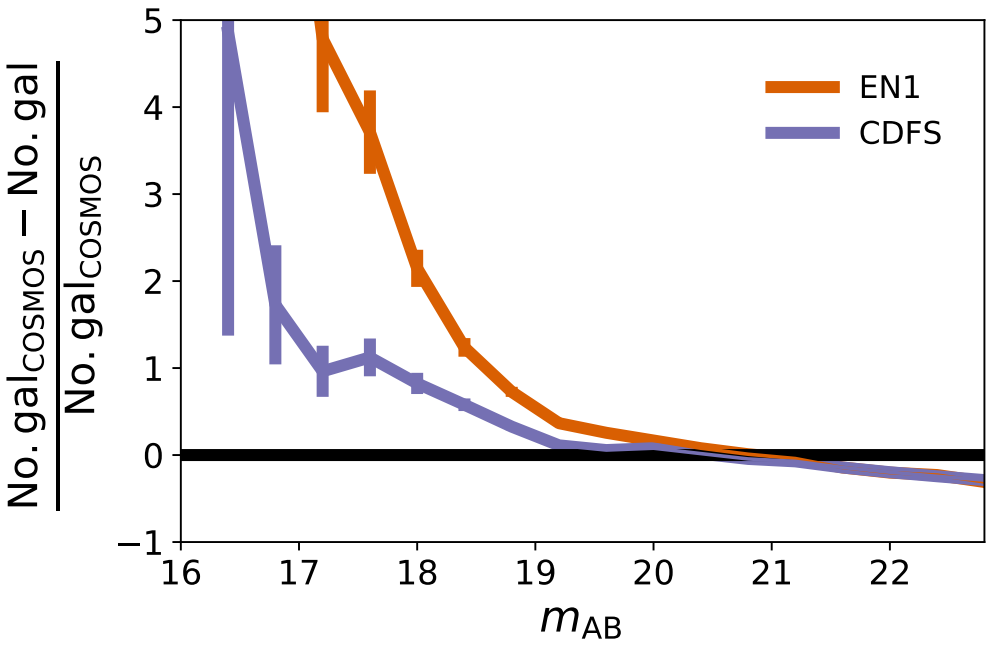

Figure 4.11: Fractional difference in the number density of IRAC channel-1-detected objects in the EN1 and CDFS fields with the COSMOS field. Poisson error bars are plotted here. The deep COSMOS field has a lower number of bright detected objects and a higher number of faint objects than the larger and shallower fields.

surveys, such as the 35 deg^2 DXS (Lawrence et al., 2007) and the 18 deg^2 SERVS survey (Mauduit et al., 2012) detect over 75 per cent of the CIB at 250 μm (Figure 4.7).

For the total CIB we do not stack on the location of undetected galaxies, which causes an underestimation of the CIB. For galaxies physically nearby our stacked galaxies this will not be a problem, since the flux density will be added to the companion galaxy (Viero et al., 2015). The missed galaxies are faint at r, K_{s} and 3.6 μm and are therefore intrinsically very faint or are located at high redshift, which makes it more likely that our 500 μm CIB estimate is biased low compared to the shorter wavelength estimates. However, our new determination of the CIB amplitude are higher than most others and provide new lower bounds for the total CIB.

The absolute FIRAS CIB estimates from Fixsen et al. (1998) and Lagache et al. (1999) differ by around 25 per cent, and can be considered as an estimate of the systematic uncertainty. These measurements differ in the way the Galactic foreground emission is removed, which provides the main uncertainty in the FIRAS based CIB measurement (Lagache et al., 1999). *Herschel* SPIRE maps have a dramatically better resolution than FIRAS (10s of arcsec vs. several degrees) and it is therefore possible to remove large scale (few arcmin) Galactic foreground emission. Furthermore, the COSMOS field used in this

work lies outside the area of the sky which has high contributions from our own Galaxy. By using the SPIRE data we removed the largest uncertainty in the CIB detection.

4.7 Conclusions of chapter 4

In this paper we have developed a novel map fitting algorithm based on `SIMSTACK` to find the contribution to the CIB from different populations of galaxies. Our code simultaneously stacks all the sources while fitting for the foreground and leakage from masked areas. We tested our code against realistic simulations, which incorporate clustering, confusion noise, instrumental noise and incompleteness effects. Our algorithm outperforms previous stacking algorithms, especially when prior catalogues contain the sources responsible for producing most of the total flux density in the map.

We tested our code thoroughly in Section 4.4.1, and our code performs well in confused maps and with prior catalogues that suffer from incompleteness effects. By testing our method we found a particular kind of bias in stacking/map fitting which can potentially overestimate the total values of the CIB measured. However, these effects are removed in the SIDES simulation by allowing a maximum of one galaxy within a 4 arcsec radius. We used this approach to recalculate the CIB, finding values that are marginally lower due to the missing sources and the biasing effect. We make the assumption that this effect is smaller in the real data than in the SIDES simulation, since the real data have a lower source density and will miss companion galaxies used to fit the residuals of bright nearby galaxies. Because this effect is smaller in the real data, then our error bars form a conservative lower bound.

We propose a previously undetected bias in stacking/map fitting that could arise when two different lists of prior sources are stacked or fitted simultaneously. In this case the bright excess of the sources in the first list is fitted by the sources of the second list, leading to an overestimate. This bias is different than the bias discussed in Heinis et al. (2013), which is due to incompleteness, and also different from the bias in stacking due to confusion (Viero et al., 2013a).

We used a large range of different prior catalogues in the COSMOS field (r, K_s, 3.6 μm, 24 μm, 100 μm, 250 μm, 850 μm and 3 GHz) and divided them up into magnitude bins. Using these bins we measured the total contribution to the CIB as a function of prior source magnitude. We found that compared to the other catalogues the deep ($m_\mathrm{AB} = 26.5$) r-band data resolves the highest fraction of the total CIB at SPIRE wavelengths.

We add 5σ detected galaxies in either K_s or 3.6 μm to the r-band stack to calculate

the total CIB in the maps. Our measurement on the total CIB is 10.5 ± 1.2, 6.7 ± 0.7 and 3.1 ± 0.3 $\mathrm{nWm^{-2}sr^{-1}}$ at 250, 350 and 500 μm, respectively. The new CIB estimate are consistent with the previous absolute measurements determined using FIRAS data. Our measurements provide new constraints on simulations that aim to predict the FIR flux from galaxies.

Chapter 5

Conclusions and summary of results

5.1 Summary of results

We constructed density maps in the COSMOS field. To create these density maps we used a method based on Darvish et al. (2015b). For our method we made redshift slices between $0.1 < z < 3.2$ where we gave every galaxy a weight according to the full redshift PDF. We smoothed these maps with an adaptive kernel and used the final density maps to divide all the galaxies over percentile bins in the density.

The main sequence for star forming galaxies was measured with a stacking method in the FIR using SPIRE data. We confirmed that the MS has higher SFRs at increasing redshifts. We used our percentile densities to calculate the different offsets of the MS for different environment. `SIMSTACK` was adapted for this method, where we stack the whole MS in a percentile density bin in one stacking bin using a weighting scheme based on the global MS at the given redshift. We found that the MS is lower in denser environments, however this is only significant in the redshift range $1.5 < z < 2.0$.

The measured MS was used to calculate the SFRD over the full COSMOS field and we corrected this SFRD for non-detected galaxies. Our estimate of the SFRD is higher than measured from the optical and UV for the same set of galaxies (Ilbert et al., 2013). Our estimates of the SFRD are close to the review values of Madau and Dickinson (2014).

We calculated the SFRD for different percentile density regions in the Universe and found that the highest density regions have a higher SFRD. This statement holds even in the local universe where many galaxies in the high density environment tend to be red and dead.

We selected 188 bright ($S_{500} > 63$ mJy) 500 μm riser DSFGs for observations with SCUBA-2. The reduction of the SCUBA-2 data was preformed using the zero-mask technique (Holland et al., 2017). The flux destinies at 850 μm were obtained by selecting the brightest pixel within 20 arsec of our prior positions. Using the deep S2CLS data (Geach et al., 2017) we showed that using the nearest pixel would have biased the measured flux densities low. Some of the colours of our DSFGs show high S_{500}/S_{250} colour to S_{850}/S_{350} colour ratios, leading to a narrow SED which can only be fitted by a un-physical function narrower than a perfect blackbody.

To get an estimate for the correlated confusion noise we sampled the deep SPIRE COSMOS map. This map has very low instrumental noise, therefore the fluctuations in the map can be explained by the confusion noise alone. Accurate estimates for the correlated confusion noise can than be sampled by using the flux densities at the same positions at all three SPIRE band.

We modelled the SEDs of our sample of DSFGs using `EAZY` and a set of 6 different well sampled infrared SEDs. The obtained mean redshift is 3.6 ± 0.4 and the SFRs of the DSFGs are extremely high, exceeding 10^3 $M_{\odot}yr^{-1}$. We show that photometric redshift for 500 μm riser galaxies are over-estimated if no data in the Rayleigh-Jeans part of the spectrum is used. With the use of the 850 μm data our photometric redshift error reduces to $\sigma_z/(1+z) = 0.15$. We tested our method against spectroscopic redshift and found that we underestimate the redshift for high redshift sources ($z > 5$) and over-estimate the redshift for lower redshift sources ($z < 4$). This result can be explained by a higher temperature for high-redshift sources, and the selection criteria of not selecting cold low redshift sources, as they would not be 500 μm risers.

Our sample of 500 μm riser galaxies contribute less than 0.3 per cent of the SFRD at any epoch and can therefore not be a main contributor to the CIB. When we test our observed number counts against phenomenological galaxy evolution models and mock catalogues we find that these models underestimate the number of bright 500 μm. However, when we add instrumental and correlated confusion noise to the simulations we are able to explain the observed number counts with our mock catalogues and the simulation from (Béthermin et al., 2017). From our mock catalogues we have derived that ∼60 per cent of our observed galaxies are boosted by noise to fulfil our selection criteria. We identified 21 DFSGs with a high probability to lie at $z > 4$. And we found that the estimated SFR for HELMS_RED_80 is for ∼30 per cent contaminated by a quasar.

SMA data for five galaxies shows that two sources have a WISE detection and there

is also an aces of WISE-1 and SDSS detected galaxies near our target DSFGs, indicating that part of our sample is lensed or that some of our sources can be detected with the shallow WISE survey.

We developed an improved version of the stacking algorithm `SIMSTACK`, which simultaneously fits for the system background and the leakage of flux from galaxies located in masked areas in the prior catalogues. This new map fitting algorithm outperforms the old `SIMSTACK` when almost all sources which produce the CIB are fitted simultaneously. We discovered a new stacking bias in the case that two prior catalogues are correlated and this correlation is stronger with either the bright or faint part of those catalogues. When the correlation is stronger for the brighter sources, then the excess of flux density is fitted by the correlated catalogues, causing an overestimate of the total flux density for the stacked sources. We demonstrated this bias in the SIDES simulation and corrected for this bias by removing sources with a brighter galaxy within 4 arcsec. We expect this bias to be smaller in the real data, due to the lower amount of detected sources.

The code was used on the SPIRE COSMOS maps with deep prior r, $K_{\rm s}$, 3.6 μm, 24 μm, 100 μm, 250 μm, 850 μm and 3 GHz catalogues. We obtained the CIB resolved from the stacked sources and we calculated new bounds for the total CIB using a combination of the r, $K_{\rm s}$ and 3.6 μm catalogues. We find a total CIB of 17.5 ± 1.8, 6.8 ± 0.6 and 3.2 ± 0.2 nWm^{2}sr^{-1} at 250, 350 and 500 μm. We tested our map fitting code on shallower EN1 and CDFS fields and found no evidence that cosmic variance would significantly change our results.

Our measured CIB at 250 μm is consistent with the recent SIDES simulation but is significantly higher than the diffuse "total" measured by FIRAS. At 350 μm and 500 μm we find CIB values which are consistent with, though much more precise than, the measurements done with FIRAS. With our results we indicate that future large area surveys as LSST are likely to resolve a substantial fraction of the population responsible for the CIB at $250\,\mu{\rm m} \leq \lambda \leq 500\,\mu{\rm m}$.

5.1.1 Future work

In the near future the full HELP database will be available. With this data we will be able to measure the dependence on environment of the MS over much larger areas. Due to the extra data it will be possible to separate galaxies over a larger number of different bins for stacking. An option for these new stacking bins is to divide the galaxies up into stellar mass, environment and redshift bins. With these results it would be possible to find the

masses of the galaxies which cause the MS to be different in certain environments.

Spectroscopic follow up of our red SPIRE galaxies will help us determine the nature of such sources. This will help us confirming (or disproving) the claim that 60 per cent of our sample is boosted by noise to our selection criteria. Deep continuum data of the objects will help with determining the stellar masses and lensing factor of the galaxies. With this information it is possible to see if some of the galaxies have an extremely high specific star formation rate.

Our new map fitting algorithm can easily be used when new deep large area surveys come available in the area of HELP. With these new surveys an even more accurate bound on the CIB can be calculated. Our new bounds on the CIB can be used to constrain models and simulations which predict the FIR flux densities of galaxies.

Bibliography

Abbott, B. P., Abbott, R., Abbott, T. D., Abernathy, M. R., and Acernese, F. e. a. (2016). Observation of Gravitational Waves from a Binary Black Hole Merger. *Physical Review Letters*, 116(6):061102. 1

Abbott, B. P., Abbott, R., Abbott, T. D., Acernese, F., and Ackley, K. e. a. (2017). GW170817: Observation of Gravitational Waves from a Binary Neutron Star Inspiral. *Physical Review Letters*, 119(16):161101. 1

Ahn, C. P., Alexandroff, R., Allende Prieto, C., Anderson, S. F., and Anderton, T. e. a. (2012). The Ninth Data Release of the Sloan Digital Sky Survey: First Spectroscopic Data from the SDSS-III Baryon Oscillation Spectroscopic Survey. ApJS, 203:21. 54

Alberts, S., Pope, A., Brodwin, M., Atlee, D. W., and Lin, Y.-T. e. a. (2014). The evolution of dust-obscured star formation activity in galaxy clusters relative to the field over the last 9 billion years. MNRAS, 437:437–457. 34

Allen, R. J., Kacprzak, G. G., Spitler, L. R., Glazebrook, K., and Labbé, I. e. a. (2015). The Differential Size Growth of Field and Cluster Galaxies at z = 2.1 Using the ZFOURGE Survey. ApJ, 806:3. 40

Amblard, A., Cooray, A., Serra, P., Altieri, B., and Arumugam, V. e. a. (2011). Sub-millimetre galaxies reside in dark matter haloes with masses greater than $3{\times}10^{11}$ solar masses. Nature, 470:510–512. 45

Aretxaga, I., Hughes, D. H., Chapin, E. L., Gaztañaga, E., Dunlop, J. S., and Ivison, R. J. (2003). Breaking the 'redshift deadlock'- II. The redshift distribution for the submillimetre population of galaxies. MNRAS, 342:759–801. 57

Asboth, V., Conley, A., Sayers, J., Béthermin, M., and Chapman, S. C. e. a. (2016). HerMES: a search for high-redshift dusty galaxies in the HerMES Large Mode Survey

- catalogue, number counts and early results. MNRAS, 462:1989–2000. 19, 48, 49, 50, 51, 52, 55, 73, 77

Aversa, R., Lapi, A., de Zotti, G., Shankar, F., and Danese, L. (2015). Black Hole and Galaxy Coevolution from Continuity Equation and Abundance Matching. ApJ, 810:74. 66

Banerji, M., McMahon, R. G., Willott, C. J., Geach, J. E., and Harrison, C. M. e. a. (2015). Cold dust emission from X-ray AGN in the SCUBA-2 Cosmology Legacy Survey: dependence on luminosity, obscuration and AGN activity. MNRAS, 454:419–438. 34

Barlow, M. J. and Silk, J. (1977). Sputtering in interstellar shocks - A model for heavy element depletion. ApJ, 211:L83–L87. 5

Baugh, C. M., Lacey, C. G., Frenk, C. S., Granato, G. L., and Silva, L. e. a. (2005). Can the faint submillimetre galaxies be explained in the Λ cold dark matter model? MNRAS, 356:1191–1200. 48

Becker, R. H., White, R. L., and Helfand, D. J. (1995). The FIRST Survey: Faint Images of the Radio Sky at Twenty Centimeters. ApJ, 450:559. 50

Bennett, C. L., Hill, R. S., Hinshaw, G., Nolta, M. R., and Odegard, N. e. a. (2003). First-Year Wilkinson Microwave Anisotropy Probe (WMAP) Observations: Foreground Emission. ApJS, 148:97–117. 13

Berta, S., Lutz, D., Santini, P., Wuyts, S., and Rosario, D. e. a. (2013). Panchromatic spectral energy distributions of Herschel sources. A&A, 551:A100. 35, 37, 56, 57, 139

Bertin, E. and Arnouts, S. (1996). SExtractor: Software for source extraction. A&AS, 117:393–404. 89

Béthermin, M., Daddi, E., Magdis, G., Lagos, C., and Sargent, M. e. a. (2015). Evolution of the dust emission of massive galaxies up to z = 4 and constraints on their dominant mode of star formation. A&A, 573:A113. 34

Béthermin, M., Daddi, E., Magdis, G., Sargent, M. T., and Hezaveh, Y. e. a. (2012). A Unified Empirical Model for Infrared Galaxy Counts Based on the Observed Physical Evolution of Distant Galaxies. ApJ, 757:L23. 49

Béthermin, M., Dole, H., Cousin, M., and Bavouzet, N. (2010). Submillimeter number counts at 250 μm, 350 μm and 500 μm in BLAST data. A&A, 516:A43. 17

Béthermin, M., Dole, H., Lagache, G., Le Borgne, D., and Penin, A. (2011). Modeling the evolution of infrared galaxies: a parametric backward evolution model. A&A, 529:A4. 49

Béthermin, M., Wu, H.-Y., Lagache, G., Davidzon, I., and Ponthieu, N. e. a. (2017). The impact of clustering and angular resolution on far-infrared and millimeter continuum observations. A&A, 607:A89. 48, 71, 72, 73, 74, 85, 91, 93, 94, 106, 113

Bothwell, M. S., Smail, I., Chapman, S. C., Genzel, R., and Ivison, R. J. e. a. (2013). A survey of molecular gas in luminous sub-millimetre galaxies. MNRAS, 429:3047–3067. 66

Bouwens, R. J., Thompson, R. I., Illingworth, G. D., Franx, M., and van Dokkum, P. G. e. a. (2004). Galaxies at z˜7-8: z_{850}-Dropouts in the Hubble Ultra Deep Field. ApJ, 616:L79–L82. 6

Brammer, G. B., van Dokkum, P. G., and Coppi, P. (2008). EAZY: A Fast, Public Photometric Redshift Code. ApJ, 686:1503–1513. 56

Brinchmann, J., Charlot, S., White, S. D. M., Tremonti, C., Kauffmann, G., Heckman, T., and Brinkmann, J. (2004). The physical properties of star-forming galaxies in the low-redshift Universe. MNRAS, 351:1151–1179. 24

Bruzual, G. and Charlot, S. (2003). Stellar population synthesis at the resolution of 2003. MNRAS, 344:1000–1028. 27

Buat, V., Oi, N., Burgarella, D., Malek, K., and Matsuhara, H. e. a. (2017). Nep-Akari Evolution with Redshift of Dust Attenuation in 8 #13211 Selected Galaxies. *Publication of Korean Astronomical Society*, 32:257–261. 10

Burgarella, D., Buat, V., Gruppioni, C., Cucciati, O., and Heinis, S. e. a. (2013). Herschel PEP/HerMES: the redshift evolution ($0 \leq z \leq 4$) of dust attenuation and of the total (UV+IR) star formation rate density. A&A, 554:A70. 10, 48

Burton, C. S., Jarvis, M. J., Smith, D. J. B., Bonfield, D. G., and Hardcastle, M. J. e. a. (2013). Herschel-ATLAS/GAMA: the environmental density of far-infrared bright galaxies at $z \leq 0.5$. MNRAS, 433:771–786. 30

Bussmann, R. S., Riechers, D., Fialkov, A., Scudder, J., and Hayward, C. C. e. a. (2015). HerMES: ALMA Imaging of Herschel-selected Dusty Star-forming Galaxies. ApJ, 812:43. 55, 79

Butcher, H. and Oemler, Jr., A. (1984). The evolution of galaxies in clusters. V - A study of populations since Z approximately equal to 0.5. ApJ, 285:426–438. 23

Cai, Z.-Y., Lapi, A., Xia, J.-Q., and De Zotti, G. e. a. (2013). A Hybrid Model for the Evolution of Galaxies and Active Galactic Nuclei in the Infrared. ApJ, 768:21. 91

Calzetti, D., Kinney, A. L., and Storchi-Bergmann, T. (1994). Dust extinction of the stellar continua in starburst galaxies: The ultraviolet and optical extinction law. ApJ, 429:582–601. 10

Cao, C., Xu, C. K., Domingue, D., Buat, V., and Cheng, Y.-W. e. a. (2016). Herschel Observations of Major Merger Pairs at z = 0: Dust Mass and Star Formation. ApJS, 222:16. 25

Carlstrom, J. E., Ade, P. A. R., Aird, K. A., Benson, B. A., and Bleem, L. E. e. a. (2011). The 10 Meter South Pole Telescope. PASP, 123:568. 13, 48

Casey, C. M. (2012). Far-infrared spectral energy distribution fitting for galaxies near and far. MNRAS, 425:3094–3103. 57, 63, 69

Casey, C. M., Berta, S., Béthermin, M., Bock, J., and Bridge, C. e. a. (2012a). A Population of z >2 Far-infrared Herschel-SPIRE-selected Starbursts. ApJ, 761:139. 48

Casey, C. M., Berta, S., Béthermin, M., Bock, J., and Bridge, C. e. a. (2012b). A Redshift Survey of Herschel Far-infrared Selected Starbursts and Implications for Obscured Star Formation. ApJ, 761:140. 48

Casey, C. M., Narayanan, D., and Cooray, A. (2014). Dusty star-forming galaxies at high redshift. Phys. Rep., 541:45–161. 13, 14, 48, 62

Cesarsky, C. J., Abergel, A., Agnese, P., Altieri, B., and Augueres, J. L. e. a. (1996). ISOCAM in flight. A&A, 315:L32–L37. 48

Chabrier, G. (2003). Galactic Stellar and Substellar Initial Mass Function. PASP, 115:763–795. 2, 27

Chapin, E. L., Berry, D. S., Gibb, A. G., Jenness, T., and Scott, D. e. a. (2013). SCUBA-2: iterative map-making with the Sub-Millimetre User Reduction Facility. MNRAS, 430:2545–2573. 51

Chapin, E. L., Chapman, S. C., Coppin, K. E., Devlin, M. J., and Dunlop, J. S. e. a. (2011). A joint analysis of BLAST 250-500 μm and LABOCA 870 μm observations in the Extended Chandra Deep Field-South. MNRAS, 411:505–549. 50

Condon, J. J. (1992). Radio emission from normal galaxies. ARA&A, 30:575–611. 6

Condon, J. J., Cotton, W. D., Greisen, E. W., Yin, Q. F., and Perley, R. A. e. a. (1998). The NRAO VLA Sky Survey. AJ, 115:1693–1716. 50

Conley, A., Cooray, A., Vieira, J. D., González Solares, E. A., and Kim, S. e. a. (2011). Discovery of a Multiply Lensed Submillimeter Galaxy in Early HerMES Herschel/SPIRE Data. ApJ, 732:L35. 49, 55

Cooray, A., Amblard, A., Wang, L., Arumugam, V., and Auld, R. e. a. (2010). HerMES: Halo occupation number and bias properties of dusty galaxies from angular clustering measurements. A&A, 518:L22. 45

Cooray, A., Calanog, J., Wardlow, J. L., Bock, J., and Bridge, C. e. a. (2014). HerMES: The Rest-frame UV Emission and a Lensing Model for the z = 6.34 Luminous Dusty Starburst Galaxy HFLS3. ApJ, 790:40. 82

Coppin, K., Chapin, E. L., Mortier, A. M. J., Scott, S. E., and Borys, C. e. a. (2006). The SCUBA Half-Degree Extragalactic Survey - II. Submillimetre maps, catalogue and number counts. MNRAS, 372:1621–1652. 73

Coppin, K., Halpern, M., Scott, D., Borys, C., and Chapman, S. (2005). An 850-μm SCUBA map of the Groth Strip and reliable source extraction. MNRAS, 357:1022–1028. 73

Coppin, K., Halpern, M., Scott, D., Borys, C., and Dunlop, J. e. a. (2008). The SCUBA HAlf Degree Extragalactic Survey - VI. 350-μm mapping of submillimetre galaxies. MNRAS, 384:1597–1610. 52

Cowley, W. I., Lacey, C. G., Baugh, C. M., and Cole, S. (2015). Simulated observations of sub-millimetre galaxies: the impact of single-dish resolution and field variance. MNRAS, 446:1784–1798. 91

Cox, P., Krips, M., Neri, R., Omont, A., and Güsten, R. e. a. (2011). Gas and Dust in a Submillimeter Galaxy at z = 4.24 from the Herschel Atlas. ApJ, 740:63. 48

Cutri, R. M. and et al. (2013). VizieR Online Data Catalog: AllWISE Data Release (Cutri+ 2013). *VizieR Online Data Catalog*, 2328. 54

Darvish, B., Mobasher, B., Sobral, D., Hemmati, S., Nayyeri, H., and Shivaei, I. (2015a). Spectroscopic Study of Star-forming Galaxies in Filaments and the Field at z ˜ 0.5: Evidence for Environmental Dependence of Electron Density. ApJ, 814:84. 25

Darvish, B., Mobasher, B., Sobral, D., Rettura, A., Scoville, N., Faisst, A., and Capak, P. (2016). The Effects of the Local Environment and Stellar Mass on Galaxy Quenching to z ˜ 3. ApJ, 825:113. 23, 24, 45

Darvish, B., Mobasher, B., Sobral, D., Scoville, N., and Aragon-Calvo, M. (2015b). A Comparative Study of Density Field Estimation for Galaxies: New Insights into the Evolution of Galaxies with Environment in COSMOS out to z˜3. ApJ, 805:121. 28, 30, 31, 32, 112

Darvish, B., Sobral, D., Mobasher, B., Scoville, N. Z., Best, P., Sales, L. V., and Smail, I. (2014). Cosmic Web and Star Formation Activity in Galaxies at z ˜ 1. ApJ, 796:51. 24, 25

Davies, J. I., Baes, M., Bianchi, S., Jones, A., and Madden, S. e. a. (2017). DustPedia: A Definitive Study of Cosmic Dust in the Local Universe. PASP, 129(4):044102. 7

De Lucia, G., Weinmann, S., Poggianti, B. M., Aragón-Salamanca, A., and Zaritsky, D. (2012). The environmental history of group and cluster galaxies in a Λ cold dark matter universe. MNRAS, 423:1277–1292. 24

Dekel, A., Sari, R., and Ceverino, D. (2009). Formation of Massive Galaxies at High Redshift: Cold Streams, Clumpy Disks, and Compact Spheroids. ApJ, 703:785–801. 23

Delvecchio, I., Lutz, D., Berta, S., Rosario, D. J., and Zamorani, G. e. a. (2015). Mapping the average AGN accretion rate in the SFR-M_* plane for Herschel-selected galaxies at $0 < z \leq 2.5$. MNRAS, 449:373–389. 24

Dempsey, J. T., Friberg, P., Jenness, T., Tilanus, R. P. J., and Thomas, H. S. e. a. (2013). SCUBA-2: on-sky calibration using submillimetre standard sources. MNRAS, 430:2534–2544. 52

Dole, H., Lagache, G., Puget, J.-L., Caputi, K. I., and Fernández-Conde, N. e. a. (2006). The cosmic infrared background resolved by Spitzer. Contributions of mid-infrared galaxies to the far-infrared background. A&A, 451:417–429. 87

Donevski, D., Buat, V., Boone, F., Pappalardo, C., and Bethermin, M. e. a. (2017). Towards a census of high-redshift dusty galaxies with *Herschel*: A selection of "500 μm-risers". *ArXiv e-prints*. 21, 48, 81

Dowell, C. D., Conley, A., Glenn, J., Arumugam, V., and Asboth, V. e. a. (2014). HerMES: Candidate High-redshift Galaxies Discovered with Herschel/SPIRE. ApJ, 780:75. 48, 49, 50, 51

Dressler, A. (1980). Galaxy morphology in rich clusters - Implications for the formation and evolution of galaxies. ApJ, 236:351–365. 8, 23

Duivenvoorden, S., Oliver, S., Buat, V., Darvish, B., and Efstathiou, A. e. a. (2016). HELP: star formation as a function of galaxy environment with Herschel. MNRAS, 462:277–289. 19

Duivenvoorden, S., Oliver, S., Scudder, J. M., Greenslade, J., and Riechers, D. A. e. a. (2018). Red, redder, reddest: SCUBA-2 imaging of colour-selected Herschel sources. MNRAS. 20

Dye, S., Furlanetto, C., Dunne, L., Eales, S. A., and Negrello, M. e. a. (2017). Modelling high resolution ALMA observations of strongly lensed highly star forming galaxies detected by Herschel. *ArXiv e-prints*. 84

Eales, S., Dunne, L., Clements, D., Cooray, A., and De Zotti, G. e. a. (2010). The Herschel ATLAS. PASP, 122:499. 9, 48

Elbaz, D., Daddi, E., Le Borgne, D., Dickinson, M., and Alexander, D. M. e. a. (2007). The reversal of the star formation-density relation in the distant universe. A&A, 468:33–48. 8, 23

Elbaz, D., Dickinson, M., Hwang, H. S., Díaz-Santos, T., and Magdis, G. e. a. (2011). GOODS-Herschel: an infrared main sequence for star-forming galaxies. A&A, 533:A119. 36

Ellison, S. L., Patton, D. R., Simard, L., McConnachie, A. W., Baldry, I. K., and Mendel, J. T. (2010). Galaxy pairs in the Sloan Digital Sky Survey - II. The effect of environment on interactions. MNRAS, 407:1514–1528. 25

Fabian, A. C. (2012). Observational Evidence of Active Galactic Nuclei Feedback. ARA&A, 50:455–489. 4

Filippenko, A. V. (1997). Optical Spectra of Supernovae. ARA&A, 35:309–355. 3

Fixsen, D. J., Dwek, E., Mather, J. C., Bennett, C. L., and Shafer, R. A. (1998). The Spectrum of the Extragalactic Far-Infrared Background from the COBE FIRAS Observations. ApJ, 508:123–128. 13, 87, 90, 91, 105, 109

Fudamoto, Y., Ivison, R. J., Oteo, I., Krips, M., and Zhang, Z.-Y. e. a. (2017). The most distant, luminous, dusty star-forming galaxies: redshifts from NOEMA and ALMA spectral scans. MNRAS, 472:2028–2041. 64, 65

Galliano, F., Hony, S., Bernard, J.-P., Bot, C., Madden, S. C., Roman-Duval, J., Galametz, M., Li, A., Meixner, M., Engelbracht, C. W., Lebouteiller, V., Misselt, K., Montiel, E., Panuzzo, P., Reach, W. T., and Skibba, R. (2011). Non-standard grain properties, dark gas reservoir, and extended submillimeter excess, probed by Herschel in the Large Magellanic Cloud. A&A, 536:A88. 7

Geach, J. E., Dunlop, J. S., Halpern, M., Smail, I., and van der Werf, P. e. a. (2017). The SCUBA-2 Cosmology Legacy Survey: 850 μm maps, catalogues and number counts. MNRAS, 465:1789–1806. 16, 51, 59, 90, 113

González-Nuevo, J., Lapi, A., Negrello, M., Danese, L., and De Zotti, G. e. a. (2014). Herschel-ATLAS/GAMA: SDSS cross-correlation induced by weak lensing. MNRAS, 442:2680–2690. 82

Greve, T. R., Vieira, J. D., Weiß, A., Aguirre, J. E., and Aird, K. A. e. a. (2012). Submillimeter Observations of Millimeter Bright Galaxies Discovered by the South Pole Telescope. ApJ, 756:101. 48, 63

Griffin, M. J., Abergel, A., Abreu, A., Ade, P. A. R., and André, P. e. a. (2010). The Herschel-SPIRE instrument and its in-flight performance. A&A, 518:L3. 16, 26, 49, 88, 90

Gruppioni, C., Pozzi, F., Rodighiero, G., Delvecchio, I., and Berta, S. e. a. (2013). The Herschel PEP/HerMES luminosity function - I. Probing the evolution of PACS selected Galaxies to z $\simeq$ 4. MNRAS, 432:23–52. 48, 69, 70, 71, 72, 85

Guglielmo, V., Poggianti, B. M., Moretti, A., Fritz, J., and Calvi, R. e. a. (2015). The star formation history of galaxies: the role of galaxy mass, morphology and environment. MNRAS, 450:2749–2763. 42

Gunn, J. E. and Peterson, B. A. (1965). On the Density of Neutral Hydrogen in Intergalactic Space. ApJ, 142:1633–1641. 7

Guzzo, L., Cassata, P., Finoguenov, A., Massey, R., and Scoville, N. Z. e. a. (2007). The Cosmic Evolution Survey (COSMOS): A Large-Scale Structure at z=0.73 and the Relation of Galaxy Morphologies to Local Environment. ApJS, 172:254–269. 42

Haas, M., Chini, R., Meisenheimer, K., Stickel, M., and Lemke, D. e. a. (1998). On the Far-Infrared Emission of Quasars. ApJ, 503:L109–L113. 4

Haas, M., Leipski, C., Barthel, P., Wilkes, B. J., and Vegetti, S. e. a. (2014). 3C 220.3: A Radio Galaxy Lensing a Submillimeter Galaxy. ApJ, 790:46. 51

Hahn, C., Blanton, M. R., Moustakas, J., Coil, A. L., and Cool, R. J. e. a. (2015). PRIMUS: Effects of Galaxy Environment on the Quiescent Fraction Evolution at z <0.8. ApJ, 806:162. 23

Haines, C. P., Pereira, M. J., Smith, G. P., Egami, E., and Sanderson, A. J. R. e. a. (2013). LoCuSS: The Steady Decline and Slow Quenching of Star Formation in Cluster Galaxies over the Last Four Billion Years. ApJ, 775:126. 23, 24

Hauser, M. G. and Dwek, E. (2001). The Cosmic Infrared Background: Measurements and Implications. ARA&A, 39:249–307. 10, 87

Hayward, C. C., Behroozi, P. S., Somerville, R. S., Primack, J. R., Moreno, J., and Wechsler, R. H. (2013). Spatially unassociated galaxies contribute significantly to the blended submillimetre galaxy population: predictions for follow-up observations of ALMA sources. MNRAS, 434:2572–2581. 48

Heinis, S., Buat, V., Béthermin, M., Aussel, H., and Bock, J. e. a. (2013). HERMES: unveiling obscured star formation - the far-infrared luminosity function of ultraviolet-selected galaxies at z $\sim$ 1.5. MNRAS, 429:1113–1132. 18, 102, 103, 110

Herschel, W. (1800). Experiments on the Refrangibility of the Invisible Rays of the Sun. By William Herschel, LL. D. F. R. S. *Philosophical Transactions of the Royal Society of London Series I*, 90:284–292. 12

Hill, R., Masui, K. W., and Scott, D. (2018). The Spectrum of the Universe. *ArXiv e-prints*. 87

Hodge, J. A., Karim, A., Smail, I., Swinbank, A. M., and Walter, F. e. a. (2013). An ALMA Survey of Submillimeter Galaxies in the Extended Chandra Deep Field South: Source Catalog and Multiplicity. ApJ, 768:91. 79

Holland, W. S., Bintley, D., Chapin, E. L., Chrysostomou, A., and Davis, G. R. e. a. (2013). SCUBA-2: the 10 000 pixel bolometer camera on the James Clerk Maxwell Telescope. MNRAS, 430:2513–2533. 49, 51

Holland, W. S., Matthews, B. C., Kennedy, G. M., Greaves, J. S., and Wyatt, M. C. e. a. (2017). SONS: The JCMT legacy survey of debris discs in the submillimetre. MNRAS, 470:3606–3663. 51, 113

Holland, W. S., Robson, E. I., Gear, W. K., Cunningham, C. R., and Lightfoot, J. F. e. a. (1999). SCUBA: a common-user submillimetre camera operating on the James Clerk Maxwell Telescope. MNRAS, 303:659–672. 13

Hubble, E. (1929). A Relation between Distance and Radial Velocity among Extra-Galactic Nebulae. *Proceedings of the National Academy of Science*, 15:168–173. 8

Hurley, P. D., Oliver, S., Betancourt, M., Clarke, C., and Cowley, W. I. e. a. (2017). HELP: XID+, the probabilistic de-blender for Herschel SPIRE maps. MNRAS, 464:885–896. 17, 21, 76, 81, 88, 91

Ilbert, O., Arnouts, S., McCracken, H. J., Bolzonella, M., and Bertin, E. e. a. (2006). Accurate photometric redshifts for the CFHT legacy survey calibrated using the VIMOS VLT deep survey. A&A, 457:841–856. 27

Ilbert, O., McCracken, H. J., Le Fèvre, O., Capak, P., and Dunlop, J. e. a. (2013). Mass assembly in quiescent and star-forming galaxies since z $\simeq$ 4 from UltraVISTA. A&A, 556:A55. 19, 26, 27, 28, 41, 42, 43, 112, 142

Inoue, Y., Inoue, S., Kobayashi, M. A. R., Makiya, R., Niino, Y., and Totani, T. (2013). Extragalactic Background Light from Hierarchical Galaxy Formation: Gamma-Ray Attenuation up to the Epoch of Cosmic Reionization and the First Stars. ApJ, 768:197. 10

Ivezic, Z., Tyson, J. A., Abel, B., Acosta, E., Allsman, R., and the LSST Collaboration (2008). LSST: from Science Drivers to Reference Design and Anticipated Data Products. *ArXiv e-prints*. 87, 107

Ivison, R. J., Greve, T. R., Dunlop, J. S., Peacock, J. A., and Egami, E. e. a. (2007). The SCUBA HAlf Degree Extragalactic Survey - III. Identification of radio and mid-infrared counterparts to submillimetre galaxies. MNRAS, 380:199–228. 82

Ivison, R. J., Lewis, A. J. R., Weiss, A., Arumugam, V., and Simpson, J. M. e. a. (2016). The Space Density of Luminous Dusty Star-forming Galaxies at z >4: SCUBA-2 and LABOCA Imaging of Ultrared Galaxies from Herschel-ATLAS. ApJ, 832:78. 48, 49, 51, 62, 63, 64, 66, 68, 84

Ivison, R. J., Papadopoulos, P. P., Smail, I., Greve, T. R., and Thomson, A. P. e. a. (2011). Tracing the molecular gas in distant submillimetre galaxies via CO(1-0) imaging with the Expanded Very Large Array. MNRAS, 412:1913–1925. 66

Jiang, L., Fan, X., Bian, F., McGreer, I. D., and Strauss, M. A. e. a. (2014). The Sloan Digital Sky Survey Stripe 82 Imaging Data: Depth-optimized Co-adds over 300 deg^2 in Five Filters. ApJS, 213:12. 107

John, T. L. (1988). Continuous absorption by the negative hydrogen ion reconsidered. A&A, 193:189–192. 2

Johnston, R., Vaccari, M., Jarvis, M., Smith, M., Giovannoli, E., Häußler, B., and Prescott, M. (2015). The evolving relation between star formation rate and stellar mass in the VIDEO survey since z = 3. MNRAS, 453:2540–2557. 24

Jones, A. P., Tielens, A. G. G. M., Hollenbach, D. J., and McKee, C. F. (1994). Grain destruction in shocks in the interstellar medium. ApJ, 433:797–810. 5

Karim, A., Swinbank, A. M., Hodge, J. A., Smail, I. R., and Walter, F. e. a. (2013). An ALMA survey of submillimetre galaxies in the Extended Chandra Deep Field South: high-resolution 870 μm source counts. MNRAS, 432:2–9. 79, 81

Kauffmann, G., White, S. D. M., Heckman, T. M., Ménard, B., Brinchmann, J., Charlot, S., Tremonti, C., and Brinkmann, J. (2004). The environmental dependence of the relations between stellar mass, structure, star formation and nuclear activity in galaxies. MNRAS, 353:713–731. 23

Kennicutt, Jr., R. C. (1998a). Star Formation in Galaxies Along the Hubble Sequence. ARA&A, 36:189–232. 62

Kennicutt, Jr., R. C. (1998b). The Global Schmidt Law in Star-forming Galaxies. ApJ, 498:541–552. 3, 10, 23

Kirkpatrick, A., Pope, A., Sajina, A., Dale, D. A., and Díaz-Santos, T. e. a. (2017). A Controlled Study of Cold Dust Content in Galaxies from z = 0-2. ApJ, 843:71. 66

Klaas, U., Haas, M., Heinrichsen, I., and Schulz, B. (1997). Infrared spectral energy distributions of the interacting galaxies ARP 244, NGC 6240, and ARP 220. A&A, 325:L21–L24. 57

Koyama, Y., Kodama, T., Tadaki, K.-i., Hayashi, M., Tanaka, I., and Shimakawa, R. (2014). The Environmental Impacts on the Star Formation Main Sequence: An Hα Study of the Newly Discovered Rich Cluster at z = 1.52. ApJ, 789:18. 25

Koyama, Y., Smail, I., Kurk, J., Geach, J. E., and Sobral, D. e. a. (2013). On the evolution and environmental dependence of the star formation rate versus stellar mass relation since z ˜ 2. MNRAS, 434:423–436. 23, 25

Kroupa, P. (2001). On the variation of the initial mass function. MNRAS, 322:231–246. 2

Kurczynski, P. and Gawiser, E. (2010). A Simultaneous Stacking and Deblending Algorithm for Astronomical Images. AJ, 139:1592–1599. 17

Lacey, C. G., Baugh, C. M., Frenk, C. S., Benson, A. J., and Bower, R. G. e. a. (2016). A unified multiwavelength model of galaxy formation. MNRAS, 462:3854–3911. 91

Lacey, C. G., Baugh, C. M., Frenk, C. S., Benson, A. J., and Orsi, A. e. a. (2010). Predictions for Herschel from Λ-cold dark matter: unveiling the cosmic star formation history. MNRAS, 405:2–28. 48

Lagache, G., Abergel, A., Boulanger, F., Désert, F. X., and Puget, J.-L. (1999). First detection of the warm ionised medium dust emission. Implication for the cosmic far-infrared background. A&A, 344:322–332. 13, 87, 90, 91, 109

Lagache, G., Dole, H., Puget, J.-L., Pérez-González, P. G., and Le Floc'h, E. e. a. (2004). Polycyclic Aromatic Hydrocarbon Contribution to the Infrared Output Energy of the Universe at z ˜= 2. ApJS, 154:112–117. 5

Lai, C.-C., Lin, L., Jian, H.-Y., Chiueh, T.-H., and Merson, A. e. a. (2016). Can We Detect the Color-Density Relation with Photometric Redshifts? ApJ, 825:40. 28

Laigle, C., McCracken, H. J., Ilbert, O., Hsieh, B. C., and Davidzon, I. e. a. (2016). The COSMOS2015 Catalog: Exploring the 1 <z <6 Universe with Half a Million Galaxies. ApJS, 224:24. 20, 88, 89, 92

Lapi, A., Raimundo, S., Aversa, R., Cai, Z.-Y., and Negrello, M. e. a. (2014). The Coevolution of Supermassive Black Holes and Massive Galaxies at High Redshift. ApJ, 782:69. 66

Lawrence, A., Warren, S. J., Almaini, O., Edge, A. C., and Hambly, N. C. e. a. (2007). The UKIRT Infrared Deep Sky Survey (UKIDSS). MNRAS, 379:1599–1617. 109

Le Floc'h, E., Aussel, H., Ilbert, O., Riguccini, L., and Frayer, D. T. e. a. (2009). Deep Spitzer 24 μm COSMOS Imaging. I. The Evolution of Luminous Dusty Galaxies Confronting the Models. ApJ, 703:222–239. 89

Lehnert, M. D., van Driel, W., Le Tiran, L., Di Matteo, P., and Haywood, M. (2015). On the cosmic evolution of the specific star formation rate. A&A, 577:A112. 24

Leung, T. K. D. and Riechers, D. A. (2016). A Massive Molecular Gas Reservoir in the Z = 2.221 Type-2 Quasar Host Galaxy SMM J0939+8315 Lensed by the Radio Galaxy 3C220.3. ApJ, 818:196. 51

Levenson, L., Marsden, G., Zemcov, M., Amblard, A., and Blain, A. e. a. (2010). HerMES: SPIRE Science Demonstration Phase maps. MNRAS, 409:83–91. 90

Lin, L., Jian, H.-Y., Foucaud, S., Norberg, P., and Bower, R. G. e. a. (2014). The Pan-STARRS1 Medium-Deep Survey: The Role of Galaxy Group Environment in the Star Formation Rate versus Stellar Mass Relation and Quiescent Fraction out to z ˜ 0.8. ApJ, 782:33. 24

Lonsdale, C. J., Persson, S. E., and Matthews, K. (1984). Infrared observations of interacting/merging galaxies. ApJ, 287:95–107. 48

Low, F. J. (1961). Low-Temperature Germanium Bolometer. *Journal of the Optical Society of America (1917-1983)*, 51:1300–1304. 12

Low, F. J., Johnson, H. L., Kleinmann, D. E., Latham, A. S., and Geisel, S. L. (1970). Photometric and Spectroscopic Observations of Infrared Stars. ApJ, 160:531. 12

Lutz, D., Poglitsch, A., Altieri, B., Andreani, P., and Aussel, H. e. a. (2011). PACS Evolutionary Probe (PEP) - A Herschel key program. A&A, 532:A90. 37, 89

Madau, P. and Dickinson, M. (2014). Cosmic Star-Formation History. ARA&A, 52:415–486. 10, 11, 23, 38, 42, 43, 45, 48, 62, 68, 87, 112

Magorrian, J., Tremaine, S., Richstone, D., Bender, R., and Bower, G. e. a. (1998). The Demography of Massive Dark Objects in Galaxy Centers. AJ, 115:2285–2305. 5

Marsden, G., Ade, P. A. R., Bock, J. J., Chapin, E. L., and Devlin, M. J. e. a. (2009). BLAST: Resolving the Cosmic Submillimeter Background. ApJ, 707:1729–1739. 91, 92

Martin, D. C., Wyder, T. K., Schiminovich, D., Barlow, T. A., and Forster, K. e. a. (2007). The UV-Optical Galaxy Color-Magnitude Diagram. III. Constraints on Evolution from the Blue to the Red Sequence. ApJS, 173:342–356. 27

Mauduit, J.-C., Lacy, M., Farrah, D., Surace, J. A., and Jarvis, M. e. a. (2012). The Spitzer Extragalactic Representative Volume Survey (SERVS): Survey Definition and Goals. PASP, 124:714. 90, 109

McCracken, H. J., Milvang-Jensen, B., Dunlop, J., Franx, M., and Fynbo, J. P. U. e. a. (2012). UltraVISTA: a new ultra-deep near-infrared survey in COSMOS. A&A, 544:A156. 26, 89

McQuinn, M. (2016). The Evolution of the Intergalactic Medium. ARA&A, 54:313–362. 6

Melnyk, O., Karachentseva, V., and Karachentsev, I. (2015). Star formation rates in isolated galaxies selected from the Two-Micron All-Sky Survey. MNRAS, 451:1482–1495. 25

Ménard, B., Scranton, R., Schmidt, S., Morrison, C., and Jeong, D. e. a. (2013). Clustering-based redshift estimation: method and application to data. *ArXiv e-prints*. 83, 84

Michałowski, M. J., Dunlop, J. S., Koprowski, M. P., Cirasuolo, M., and Geach, J. E. e. a. (2017). The SCUBA-2 Cosmology Legacy Survey: the nature of bright submm galaxies from 2 deg^2 of 850-μm imaging. MNRAS, 469:492–515. 68, 79, 81

Moster, B. P., Somerville, R. S., Newman, J. A., and Rix, H.-W. (2011). A Cosmic Variance Cookbook. ApJ, 731:113. 41

Muldrew, S. I., Croton, D. J., Skibba, R. A., Pearce, F. R., and Ann, H. B. e. a. (2012). Measures of galaxy environment - I. What is 'environment'? MNRAS, 419:2670–2682. 25, 28

Muzzin, A., Marchesini, D., Stefanon, M., Franx, M., and Milvang-Jensen, B. e. a. (2013). A Public K_s -selected Catalog in the COSMOS/ULTRAVISTA Field: Photometry, Photometric Redshifts, and Stellar Population Parameters. ApJS, 206:8. 89

Nan, R., Li, D., Jin, C., Wang, Q., Zhu, L., Zhu, W., Zhang, H., Yue, Y., and Qian, L. (2011). The Five-Hundred Aperture Spherical Radio Telescope (fast) Project. *International Journal of Modern Physics D*, 20:989–1024. 12

Narayanan, D., Hayward, C. C., Cox, T. J., Hernquist, L., and Jonsson, P. e. a. (2010). The formation of high-redshift submillimetre galaxies. MNRAS, 401:1613–1619. 48

Nayyeri, H., Keele, M., Cooray, A., Riechers, D. A., and Ivison, R. J. e. a. (2016). Candidate Gravitationally Lensed Dusty Star-forming Galaxies in the Herschel Wide Area Surveys. ApJ, 823:17. 49, 55

Negrello, M., Amber, S., Amvrosiadis, A., Cai, Z.-Y., and Lapi, A. e. a. (2017). The Herschel-ATLAS: a sample of 500 μm-selected lensed galaxies over 600 deg^2. MNRAS, 465:3558–3580. 49, 55, 76

Negrello, M., Hopwood, R., De Zotti, G., Cooray, A., and Verma, A. e. a. (2010). The Detection of a Population of Submillimeter-Bright, Strongly Lensed Galaxies. *Science*, 330:800. 49, 55

Neugebauer, G., Habing, H. J., van Duinen, R., Aumann, H. H., and Baud, B. e. a. (1984). The Infrared Astronomical Satellite (IRAS) mission. ApJ, 278:L1–L6. 12

Nguyen, H. T., Schulz, B., Levenson, L., Amblard, A., and Arumugam, V. e. a. (2010). HerMES: The SPIRE confusion limit. A&A, 518:L5. 16, 26, 59, 79, 88

Noble, A. G., Webb, T. M. A., Yee, H. K. C., Muzzin, A., and Wilson, G. e. a. (2016). The Phase Space of z˜1.2 SpARCS Clusters: Using Herschel to Probe Dust Temperature as a Function of Environment and Accretion History. ApJ, 816:48. 34

Noeske, K. G., Weiner, B. J., Faber, S. M., Papovich, C., and Koo, D. C. e. a. (2007). Star Formation in AEGIS Field Galaxies since z=1.1: The Dominance of Gradually Declining Star Formation, and the Main Sequence of Star-forming Galaxies. ApJ, 660:L43–L46. 24

Oesch, P. A., Bouwens, R. J., Illingworth, G. D., Labbé, I., and Trenti, M. e. a. (2012). Expanded Search for z ˜ 10 Galaxies from HUDF09, ERS, and CANDELS Data: Evidence for Accelerated Evolution at z >8? ApJ, 745:110. 6

Oliver, S., Frost, M., Farrah, D., Gonzalez-Solares, E., and Shupe, D. L. e. a. (2010a). Specific star formation and the relation to stellar mass from 0 <z <2 as seen in the far-infrared at 70 and 160 μm. MNRAS, 405:2279–2294. 24, 34, 38

Oliver, S. J., Bock, J., Altieri, B., Amblard, A., and Arumugam, V. e. a. (2012). The Herschel Multi-tiered Extragalactic Survey: HerMES. MNRAS, 424:1614–1635. 9, 25, 26, 48, 90

Oliver, S. J., Wang, L., Smith, A. J., Altieri, B., and Amblard, A. e. a. (2010b). HerMES: SPIRE galaxy number counts at 250, 350, and 500 μm. A&A, 518:L21. 87

Oteo, I., Ivison, R. J., Negrello, M., Smail, I., and Pérez-Fournon, I. e. a. (2017a). Witnessing the birth of the red sequence: the physical scale and morphology of dust emission in hyper-luminous starbursts in the early Universe. *ArXiv e-prints*. 21, 56, 84

Oteo, I., Zwaan, M. A., Ivison, R. J., Smail, I., and Biggs, A. D. (2017b). ALMACAL II: Extreme Star Formation Rate Densities in Dusty Starbursts Revealed by ALMA 20 mas Resolution Imaging. ApJ, 837:182. 84

Paccagnella, A., Vulcani, B., Poggianti, B. M., Moretti, A., and Fritz, J. e. a. (2016). Slow Quenching of Star Formation in OMEGAWINGS Clusters: Galaxies in Transition in the Local Universe. ApJ, 816:L25. 24, 45

Pannella, M., Elbaz, D., Daddi, E., Dickinson, M., and Hwang, H. S. e. a. (2015). GOODS-Herschel: Star Formation, Dust Attenuation, and the FIR-radio Correlation on the Main Sequence of Star-forming Galaxies up to z $\simeq$4. ApJ, 807:141. 24

Pâris, I., Petitjean, P., Ross, N. P., Myers, A. D., and Aubourg, É. e. a. (2017). The Sloan Digital Sky Survey Quasar Catalog: Twelfth data release. A&A, 597:A79. 75

Patel, S. G., Kelson, D. D., Holden, B. P., Franx, M., and Illingworth, G. D. (2011). The Star-formation-rate-Density Relation at 0.6 <z <0.9 and the Role of Star-forming Galaxies. ApJ, 735:53. 24, 40, 45

Peng, Y.-j., Lilly, S. J., Kovač, K., Bolzonella, M., and Pozzetti, L. e. a. (2010). Mass and Environment as Drivers of Galaxy Evolution in SDSS and zCOSMOS and the Origin of the Schechter Function. ApJ, 721:193–221. 23, 24, 45

Penzias, A. A. and Wilson, R. W. (1965). A Measurement of Excess Antenna Temperature at 4080 Mc/s. ApJ, 142:419–421. 4

Pilbratt, G. L., Riedinger, J. R., Passvogel, T., Crone, G., and Doyle, D. e. a. (2010). Herschel Space Observatory. An ESA facility for far-infrared and submillimetre astronomy. A&A, 518:L1. 25, 48, 87

Planck Collaboration (2016). Planck 2015 results. XIII. Cosmological parameters. A&A, 594:A13. 13

Poglitsch, A., Waelkens, C., Geis, N., Feuchtgruber, H., and Vandenbussche, B. e. a. (2010). The Photodetector Array Camera and Spectrometer (PACS) on the Herschel Space Observatory. A&A, 518:L2. 16, 37, 89

Polletta, M., Tajer, M., Maraschi, L., Trinchieri, G., and Lonsdale, C. J. e. a. (2007). Spectral Energy Distributions of Hard X-Ray Selected Active Galactic Nuclei in the XMM-Newton Medium Deep Survey. ApJ, 663:81–102. 56, 57

Puget, J.-L., Abergel, A., Bernard, J.-P., Boulanger, F., and Burton, W. B. e. a. (1996). Tentative detection of a cosmic far-infrared background with COBE. A&A, 308:L5. 13, 87

Rettura, A., Mei, S., Stanford, S. A., Raichoor, A., and Moran, S. e. a. (2011). Early-type Galaxies at z ˜ 1.3. III. On the Dependence of Formation Epochs and Star Formation Histories on Stellar Mass and Environment. ApJ, 732:94. 23

Reynolds, S. P. (2008). Supernova Remnants at High Energy. ARA&A, 46:89–126. 3

Ricciardelli, E., Cava, A., Varela, J., and Quilis, V. (2014). The star formation activity in cosmic voids. MNRAS, 445:4045–4054. 24

Riechers, D. A., Bradford, C. M., Clements, D. L., Dowell, C. D., and Pérez-Fournon, I. e. a. (2013). A dust-obscured massive maximum-starburst galaxy at a redshift of 6.34. Nature, 496:329–333. 48, 56, 57, 82

Riechers, D. A., Leung, T. K. D., Ivison, R. J., Pérez-Fournon, I., and Lewis, A. J. R. e. a. (2017). Rise of the Titans: A Dusty, Hyper-luminous 870 μm Riser Galaxy at z ˜ 6. ApJ, 850:1. 48

Robson, E. I., Ivison, R. J., Smail, I., Holland, W. S., and Geach, J. E. e. a. (2014). Imaging the Environment of a z = 6.3 Submillimeter Galaxy with SCUBA-2. ApJ, 793:11. 82

Rosario, D. J., Santini, P., Lutz, D., Shao, L., and Maiolino, R. e. a. (2012). The mean star formation rate of X-ray selected active galaxies and its evolution from z ˜ 2.5: results from PEP-Herschel. A&A, 545:A45. 76

Rowan-Robinson, M., Babbedge, T., Oliver, S., Trichas, M., and Berta, S. e. a. (2008). Photometric redshifts in the SWIRE Survey. MNRAS, 386:697–714. 38

Rowan-Robinson, M., Mann, R. G., Oliver, S. J., Efstathiou, A., and Eaton, N. e. a. (1997). Observations of the Hubble Deep Field with the Infrared Space Observatory - V. Spectral energy distributions, starburst models and star formation history. MNRAS, 289:490–496. 37, 38, 62

Rowan-Robinson, M., Oliver, S., Wang, L., Farrah, D., and Clements, D. L. e. a. (2016). The star formation rate density from z = 1 to 6. MNRAS, 461:1100–1111. 42

Salpeter, E. E. (1955). The Luminosity Function and Stellar Evolution. ApJ, 121:161. 2, 38

Sanders, D. B. and Mirabel, I. F. (1996). Luminous Infrared Galaxies. ARA&A, 34:749. 12

Sanders, D. B., Salvato, M., Aussel, H., Ilbert, O., and Scoville, N. e. a. (2007). S-COSMOS: The Spitzer Legacy Survey of the Hubble Space Telescope ACS 2 deg^2 COSMOS Field I: Survey Strategy and First Analysis. ApJS, 172:86–98. 89

Santini, P., Maiolino, R., Magnelli, B., Lutz, D., and Lamastra, A. e. a. (2014). The evolution of the dust and gas content in galaxies. A&A, 562:A30. 23

Sargent, M. T., Béthermin, M., Daddi, E., and Elbaz, D. (2012). The Contribution of Starbursts and Normal Galaxies to Infrared Luminosity Functions at z <2. ApJ, 747:L31. 27

Sayers, J., Bockstiegel, C., Brugger, S., Czakon, N. G., and Day, P. K. e. a. (2014). The status of MUSIC: the multiwavelength sub-millimeter inductance camera. In *Millimeter, Submillimeter, and Far-Infrared Detectors and Instrumentation for Astronomy VII*, volume 9153 of Proc. SPIE, page 915304. 55

Scoville, N., Arnouts, S., Aussel, H., Benson, A., and Bongiorno, A. e. a. (2013). Evolution of Galaxies and Their Environments at z = 0.1-3 in COSMOS. ApJS, 206:3. 23, 28

Scoville, N., Aussel, H., Benson, A., Blain, A., and Calzetti, D. e. a. (2007a). Large Structures and Galaxy Evolution in COSMOS at z <1.1. ApJS, 172:150–181. 18, 25, 88

Scoville, N., Aussel, H., Brusa, M., Capak, P., and Carollo, C. M. e. a. (2007b). The Cosmic Evolution Survey (COSMOS): Overview. ApJS, 172:1–8. 59

Scudder, J. M., Ellison, S. L., and Mendel, J. T. (2012a). The dependence of galaxy group star formation rates and metallicities on large-scale environment. MNRAS, 423:2690–2704. 24

Scudder, J. M., Ellison, S. L., Torrey, P., Patton, D. R., and Mendel, J. T. (2012b). Galaxy pairs in the Sloan Digital Sky Survey - V. Tracing changes in star formation rate and metallicity out to separations of 80 kpc. MNRAS, 426:549–565. 25, 45

Scudder, J. M., Oliver, S., Hurley, P. D., Griffin, M., and Sargent, M. T. e. a. (2016). The multiplicity of 250-μm Herschel sources in the COSMOS field. MNRAS, 460:1119–1130. 49, 81

Shamshiri, S., Thomas, P. A., Henriques, B. M., Tojeiro, R., Lemson, G., Oliver, S. J., and Wilkins, S. (2015). Galaxy formation in the Planck cosmology - II. Star-formation histories and post-processing magnitude reconstruction. MNRAS, 451:2681–2691. 42

Silva, L., Granato, G. L., Bressan, A., and Danese, L. (1998). Modeling the Effects of Dust on Galactic Spectral Energy Distributions from the Ultraviolet to the Millimeter Band. ApJ, 509:103–117. 91

Simpson, J. M., Smail, I., Swinbank, A. M., Chapman, S. C., and Geach, J. E. e. a. (2015). The SCUBA-2 Cosmology Legacy Survey: ALMA Resolves the Bright-end of the Sub-millimeter Number Counts. ApJ, 807:128. 79, 81

Smail, I., Ivison, R. J., and Blain, A. W. (1997). A Deep Sub-millimeter Survey of Lensing Clusters: A New Window on Galaxy Formation and Evolution. ApJ, 490:L5–L8. 13, 48

Smail, I., Swinbank, A. M., Ivison, R. J., and Ibar, E. (2011). The potential influence of far-infrared emission lines on the selection of high-redshift galaxies. MNRAS, 414:L95–L99. 57

Smith, M. W. L., Ibar, E., Maddox, S. J., Valiante, E., and Dunne, L. e. a. (2017). The Herschel-ATLAS Data Release 2, Paper I. Submillimeter and Far-infrared Images of the

South and North Galactic Poles: The Largest Herschel Survey of the Extragalactic Sky. ApJS, 233:26. 16

Smolčić, V., Novak, M., Bondi, M., Ciliegi, P., and Mooley, K. P. e. a. (2017). The VLA-COSMOS 3 GHz Large Project: Continuum data and source catalog release. A&A, 602:A1. 90

Sobral, D., Best, P. N., Smail, I., Geach, J. E., Cirasuolo, M., Garn, T., and Dalton, G. B. (2011). The dependence of star formation activity on environment and stellar mass at z˜ 1 from the HiZELS-Hα survey. MNRAS, 411:675–692. 23

Sobral, D., Best, P. N., Smail, I., Mobasher, B., Stott, J., and Nisbet, D. (2014). The stellar mass function of star-forming galaxies and the mass-dependent SFR function since z = 2.23 from HiZELS. MNRAS, 437:3516–3528. 24

Soifer, B. T., Neugebauer, G., Helou, G., Lonsdale, C. J., and Hacking, P. e. a. (1984). The remarkable infrared galaxy ARP 220 = IC 4553. ApJ, 283:L1–L4. 57

Speagle, J. S., Steinhardt, C. L., Capak, P. L., and Silverman, J. D. (2014). A Highly Consistent Framework for the Evolution of the Star-Forming "Main Sequence" from z ˜ 0-6. ApJS, 214:15. 24

Straatman, C. M. S., Labbé, I., Spitler, L. R., Allen, R., and Altieri, B. e. a. (2014). A Substantial Population of Massive Quiescent Galaxies at z ˜ 4 from ZFOURGE. ApJ, 783:L14. 84

Strandet, M. L., Weiss, A., De Breuck, C., Marrone, D. P., and Vieira, J. D. e. a. (2017). ISM Properties of a Massive Dusty Star-forming Galaxy Discovered at z ˜ 7. ApJ, 842:L15. 48, 64, 65

Strandet, M. L., Weiss, A., Vieira, J. D., de Breuck, C., and Aguirre, J. E. e. a. (2016). The Redshift Distribution of Dusty Star-forming Galaxies from the SPT Survey. ApJ, 822:80. 48, 63, 64, 65

Su, T., Marriage, T. A., Asboth, V., Baker, A. J., and Bond, J. R. e. a. (2017). On the redshift distribution and physical properties of ACT-selected DSFGs. MNRAS, 464:968–984. 55

Symeonidis, M. (2017). What produces the far-infrared/submillimetre emission in the most luminous QSOs? MNRAS, 465:1401–1408. 6, 76

Symeonidis, M., Giblin, B. M., Page, M. J., Pearson, C., and Bendo, G. e. a. (2016). AGN are cooler than you think: the intrinsic far-IR emission from QSOs. MNRAS, 459:257–276. 6, 75, 76

Symeonidis, M., Vaccari, M., Berta, S., Page, M. J., and Lutz, D. e. a. (2013). The Herschel census of infrared SEDs through cosmic time. MNRAS, 431:2317–2340. 57, 64, 69, 70, 71, 72

Taniguchi, Y., Kajisawa, M., Kobayashi, M. A. R., Shioya, Y., and Nagao, T. e. a. (2015). The Subaru COSMOS 20: Subaru optical imaging of the HST COSMOS field with 20 filters*. PASJ, 67:104. 88

Taniguchi, Y., Scoville, N., Murayama, T., Sanders, D. B., and Mobasher, B. e. a. (2007). The Cosmic Evolution Survey (COSMOS): Subaru Observations of the HST Cosmos Field. ApJS, 172:9–28. 88

The Dark Energy Survey Collaboration (2005). The Dark Energy Survey. *ArXiv Astrophysics e-prints*. 107

Tonnesen, S. and Cen, R. (2014). On the Reversal of Star formation Rate-Density Relation at z = 1: Insights from Simulations. ApJ, 788:133. 23

Totsuji, H. and Kihara, T. (1969). The Correlation Function for the Distribution of Galaxies. PASJ, 21:221. 17

Tyler, K. D., Bai, L., and Rieke, G. H. (2014). Star Formation Trends in the Unrelaxed, Post-merger Cluster A2255. ApJ, 794:31. 24

Tyler, K. D., Rieke, G. H., and Bai, L. (2013). Star-forming Galaxy Evolution in Nearby Rich Clusters. ApJ, 773:86. 24

Vaccari, M. (2015). HELP-ing Extragalactic Surveys : The Herschel Extragalactic Legacy Project and the Coming of Age of Multi-Wavelength Astrophysics. *SALT Science Conference 2015 (SSC2015)*, page 17. 25

Vaccari, M. (2016). HELP: The Herschel Extragalactic Legacy Project and The Coming of Age of Multi-wavelength Astrophysics. *The Universe of Digital Sky Surveys*, 42:71. 76

Vieira, J. D., Marrone, D. P., Chapman, S. C., De Breuck, C., and Hezaveh, Y. D. e. a. (2013). Dusty starburst galaxies in the early Universe as revealed by gravitational lensing. Nature, 495:344–347. 15, 48

Viero, M. P., Moncelsi, L., Quadri, R. F., Arumugam, V., and Assef, R. J. e. a. (2013a). HerMES: The Contribution to the Cosmic Infrared Background from Galaxies Selected by Mass and Redshift. ApJ, 779:32. 16, 17, 18, 20, 34, 35, 88, 92, 110

Viero, M. P., Moncelsi, L., Quadri, R. F., Béthermin, M., and Bock, J. e. a. (2015). HerMES: Current Cosmic Infrared Background Estimates Can Be Explained by Known Galaxies and Their Faint Companions at z <4. ApJ, 809:L22. 21, 26, 34, 89, 90, 91, 105, 106, 109

Viero, M. P., Wang, L., Zemcov, M., Addison, G., and Amblard, A. e. a. (2013b). HerMES: Cosmic Infrared Background Anisotropies and the Clustering of Dusty Star-forming Galaxies. ApJ, 772:77. 45, 90

von der Linden, A., Wild, V., Kauffmann, G., White, S. D. M., and Weinmann, S. (2010). Star formation and AGN activity in SDSS cluster galaxies. MNRAS, 404:1231–1246. 24

Vulcani, B., Poggianti, B. M., Finn, R. A., Rudnick, G., Desai, V., and Bamford, S. (2010). Comparing the Relation Between Star Formation and Galaxy Mass in Different Environments. ApJ, 710:L1–L6. 24, 40, 45

Wang, L., Cooray, A., Farrah, D., Amblard, A., and Auld, R. e. a. (2011). HerMES: detection of cosmic magnification of submillimetre galaxies using angular cross-correlation. MNRAS, 414:596–601. 54, 82

Wardlow, J. L., Cooray, A., De Bernardis, F., Amblard, A., and Arumugam, V. e. a. (2013). HerMES: Candidate Gravitationally Lensed Galaxies and Lensing Statistics at Submillimeter Wavelengths. ApJ, 762:59. 55

Webb, T., Noble, A., DeGroot, A., Wilson, G., and Muzzin, A. e. a. (2015). An Extreme Starburst in the Core of a Rich Galaxy Cluster at z = 1.7. ApJ, 809:173. 34

Weiß, A., De Breuck, C., Marrone, D. P., Vieira, J. D., and Aguirre, J. E. e. a. (2013). ALMA Redshifts of Millimeter-selected Galaxies from the SPT Survey: The Redshift Distribution of Dusty Star-forming Galaxies. ApJ, 767:88. 48, 64, 65

Weiß, A., Ivison, R. J., Downes, D., Walter, F., Cirasuolo, M., and Menten, K. M. (2009a). First Redshift Determination of an Optically/Ultraviolet Faint Submillimeter Galaxy Using CO Emission Lines. ApJ, 705:L45–L47. 15

Weiß, A., Kovács, A., Coppin, K., Greve, T. R., and Walter, F. e. a. (2009b). The Large Apex Bolometer Camera Survey of the Extended Chandra Deep Field South. ApJ, 707:1201–1216. 79

Werner, M. W., Roellig, T. L., Low, F. J., Rieke, G. H., and Rieke, M. e. a. (2004). The Spitzer Space Telescope Mission. ApJS, 154:1–9. 87

Wetzel, A. R., Tinker, J. L., Conroy, C., and van den Bosch, F. C. (2013). Galaxy evolution in groups and clusters: satellite star formation histories and quenching time-scales in a hierarchical Universe. MNRAS, 432:336–358. 8, 23

Whitaker, K. E., van Dokkum, P. G., Brammer, G., and Franx, M. (2012). The Star Formation Mass Sequence Out to z = 2.5. ApJ, 754:L29. 24

Wijesinghe, D. B., Hopkins, A. M., Brough, S., Taylor, E. N., and Norberg, P. e. a. (2012). Galaxy And Mass Assembly (GAMA): galaxy environments and star formation rate variations. MNRAS, 423:3679–3691. 24

Wright, E. L., Eisenhardt, P. R. M., Mainzer, A. K., Ressler, M. E., and Cutri, R. M. e. a. (2010). The Wide-field Infrared Survey Explorer (WISE): Mission Description and Initial On-orbit Performance. AJ, 140:1868–1881. 54

York, D. G., Adelman, J., Anderson, Jr., J. E., Anderson, S. F., and Annis, J. e. a. (2000). The Sloan Digital Sky Survey: Technical Summary. AJ, 120:1579–1587. 54

Zavala, J. A., Montaña, A., Hughes, D. H., Yun, M. S., and Ivison, R. J. e. a. (2018). A dusty star-forming galaxy at z = 6 revealed by strong gravitational lensing. *Nature Astronomy*, 2:56–62. 48, 82

Zemcov, M., Blain, A., Cooray, A., Béthermin, M., and Bock, J. e. a. (2013). HerMES: A Deficit in the Surface Brightness of the Cosmic Infrared Background due to Galaxy Cluster Gravitational Lensing. ApJ, 769:L31. 91

Appendix A

Detailed information about the galaxies and templates used in the stack

A.1 The main-sequence fit

To be able to probe the environmental dependence of the MS, we need to obtain the weights in the flux density contribution for every galaxy in this MS. For this purpose we used the fit from Figure A.1.

This fit can be used to predict the flux density for a galaxy with a given mass, and so make an estimate of its weight in the stacking. In combination with the choice of best SED (as shown in Table A.1) we could apply the K-correction weights to determine a weight for every galaxy within the stack. By running `SIMSTACK` with these estimates we are able to investigate the offset of the MS in a certain region of the Universe.

Redshift bin	star-forming template	Quiescent template
0.1 – 0.5	Mod-SF-glx	Cold-glx
0.5 – 1.0	SF-glx-1	Cold-glx
1.0 – 1.5	Ly-break	Cold-glx
1.5 – 2.0	WeakPAH-SF-flx-1	Blue-SF-glx
2.0 – 3.2	Si-break	Spiral

Table A.1: SED templates used in the final run; for detailed information about the templates see Berta et al. (2013).

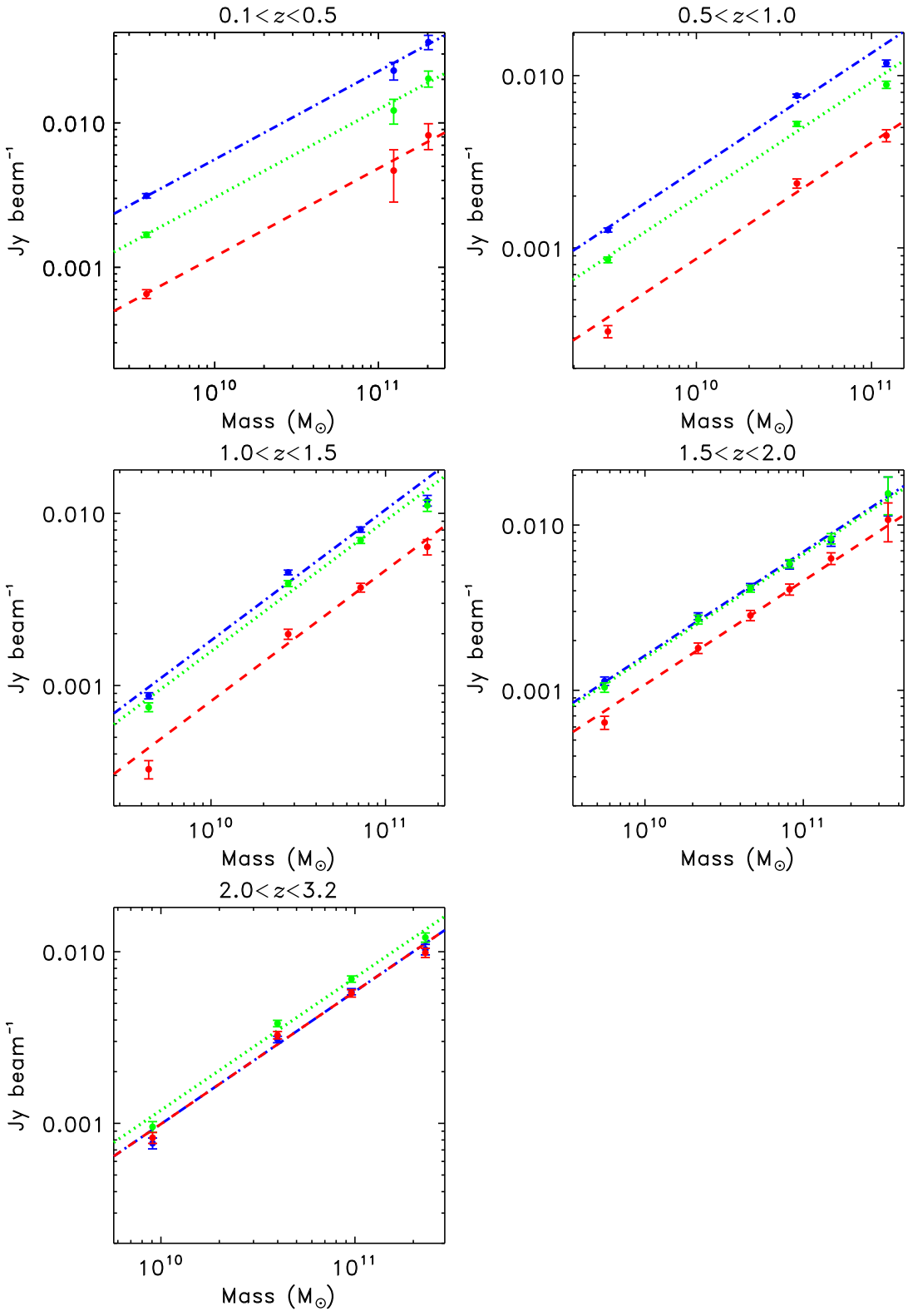

Figure A.1: Stacked flux densities for the three different SPIRE bands, 250 μm (blue, dash-dot), 350 μm (green, dotted) and 500 μm (red, dashed) plotted against the stellar mass of the galaxies for different redshifts. The dashed lines are the best fits of the model (Equation 2.10). For every redshift and every SPIRE band we can see a clear correlation of mass with flux density, so this plot is effectively another way to show the MS.

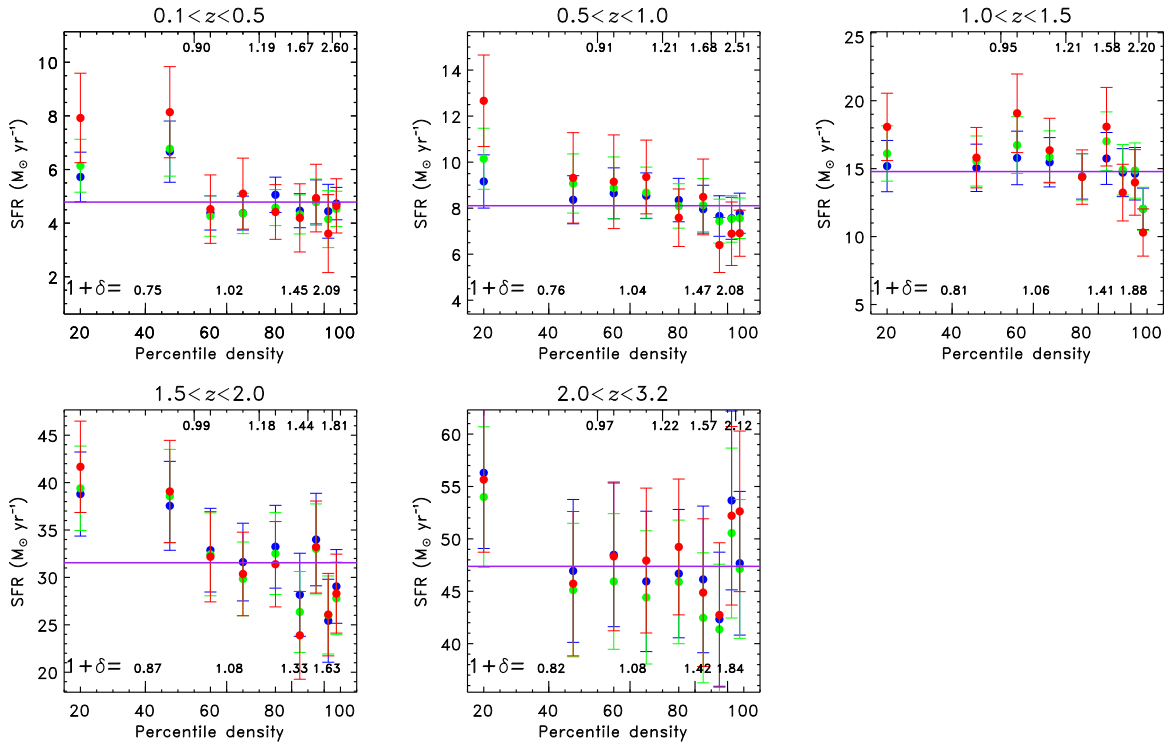

Figure A.2: SFR from the stacked K_s selected star-forming galaxies in the COSMOS field for different redshifts and environments. The blue, red and green symbols represent the estimates from the 250 μm, 350 μm and 500 μm SPIRE bands. The purple line represents the average value, the value of the SFR which would arise from a constant MS over different environments.

Our final result is the MS as function of environment, as measured by each single SPIRE band as shown in Figure A.2. For every data point we constructed the jackknife errors over the map and the errors associated with a re-sampling of the data from the redshift PDF (Equation 2.13). The estimates for the SFR from the three different SPIRE bands are in line with each other (have a reduced $\chi^2 \lesssim 1$), and we combine them to construct Figure 2.3.

Appendix B

Error estimation

For Figure 2.3 we constructed the errors by using both the variance over the map (using jackknife) and in redshift space. In this calculation we assumed that we had the correct SED to transform from the SPIRE flux density to SFR.

If instead we had chosen an SED with an FIR peak with an offset from the intrinsic one, our three SPIRE estimates would have given very different SFR values, allowing us to rule out this FIR peak location. But if the peak is only slightly wrong, or if all three SPIRE bands are longward of the FIR peak, then several SED templates (with different SFRs) would all give a reasonable fit. On the other hand, the K-correction, and the other corrections applied to obtain to our stacking list would still be roughly the same for these "good" SED fits.

Because our corrections are roughly the same, we will find the same result (SPIRE flux density versus density), and so we do not take this error in the SFR into account. If we had picked the wrong SED, then all of our data points would move up or down together, leading to the same conclusion in whether or not the MS is dependent of environment.

For the SFR-density in the COSMOS field we constructed the errors based on a tile-selected jackknife over the map, in combination with the error on the SFR of the stacked galaxies and the error of the mass function, see Ilbert et al. (2013). In this case, we have to take the error in the template into account, because we want to compare with previous results for the SFR-density relation.

We quantified this uncertainty by not only running the `SIMSTACK` code for the best SED template, but also for the second to fifth best templates. These different templates give different SFR estimates. We constructed a weighted mean of these SFRs by weighting each SFR by the reduced χ^2 (on which we based our choice of best templates).

By enforcing the reduced χ^2 of this mean to be 1 we enlarge these errors. These

enlarged errors based on our best templates give a better estimate of the uncertainty in the SFR-density by also including the bias from selecting a specific template for the SED.

For our environmentally dependent SFR we did not take this bias into account. In each of the chosen top five SEDs the same environmental trend can be seen as we observe for our best template; so by taking the bias in SFR into account for this plot, we will wash out any observed correlation. Therefore we can say that there is an extra uncertainty on the SFR estimates (as seen in Figure 2.4), but our environmental results would already be seen in using the higher SPIRE flux densities fitted to the map, justifying the use of the smaller error bars in Figure 2.3.

Appendix C

Table of source detection

Source name	Name	S_{250} [mJy]	S_{350} [mJy]	S_{500} [mJy]	S_{850} [mJy]	phot-z	$\log(L_{FIR}/L_\odot)$
HerMES J004409.9+011823	HELMS_RED_1	108.1 ± 6.9	166.5 ± 6.0	191.8 ± 8.2	82.0 ± 3.9	$4.00^{+0.55}_{-0.52}$	$13.95^{+0.09}_{-0.09}$
HerMES J005258.9+061319	HELMS_RED_2	68.2 ± 6.0	111.6 ± 5.9	131.7 ± 6.9	82.4 ± 4.9	$4.59^{+0.67}_{-0.65}$	$13.92^{+0.09}_{-0.10}$
HerMES J003929.5+002424	HELMS_RED_3	140.8 ± 6.5	152.6 ± 6.3	162.1 ± 7.3	52.3 ± 4.5	$3.10^{+0.58}_{-0.65}$	$13.75^{+0.12}_{-0.17}$
HerMES J002220.8−015521	HELMS_RED_4	62.2 ± 6.1	104.0 ± 5.8	116.3 ± 6.6	52.4 ± 4.4	$4.13^{+0.60}_{-0.57}$	$13.76^{+0.09}_{-0.11}$
HerMES J005047.6+065720	HELMS_RED_5	20.8 ± 6.0	68.2 ± 6.4	112.0 ± 6.8	37.2 ± 4.2	$5.02^{+0.54}_{-0.91}$	$13.70^{+0.07}_{-0.13}$
HerMES J010053.9+030323	HELMS_RED_6	50.1 ± 6.8	83.3 ± 6.1	96.1 ± 7.8	39.3 ± 5.4	$4.10^{+0.63}_{-0.61}$	$13.65^{+0.10}_{-0.11}$
HerMES J003814.0+002250	HELMS_RED_7	73.3 ± 5.5	119.0 ± 6.0	122.9 ± 6.7	58.8 ± 3.6	$4.02^{+0.57}_{-0.57}$	$13.79^{+0.09}_{-0.10}$
HerMES J233802.0−011907	HELMS_RED_8	33.6 ± 6.5	53.8 ± 6.1	90.9 ± 7.6	22.4 ± 3.4	$4.13^{+0.67}_{-0.65}$	$13.46^{+0.10}_{-0.12}$
HerMES J002718.1+023946	HELMS_RED_9	65.2 ± 5.9	76.4 ± 5.7	99.3 ± 6.9	18.2 ± 3.6	$3.27^{+0.59}_{-0.56}$	$13.42^{+0.12}_{-0.13}$
HerMES J000304.4+024111	HELMS_RED_10	33.6 ± 5.7	53.9 ± 6.5	86.5 ± 6.9	37.9 ± 4.4	$4.62^{+0.75}_{-0.63}$	$13.63^{+0.10}_{-0.09}$
HerMES J004747.0+061444	HELMS_RED_11	71.4 ± 5.9	112.0 ± 6.0	114.6 ± 7.8	20.4 ± 6.0	$3.51^{+0.54}_{-0.60}$	$13.57^{+0.10}_{-0.13}$
HerMES J002115.6+013259	HELMS_RED_12	58.5 ± 6.3	80.5 ± 6.7	81.5 ± 7.3	36.7 ± 4.8	$3.67^{+0.64}_{-0.64}$	$13.57^{+0.11}_{-0.13}$
HerMES J002936.4+020706	HELMS_RED_13	77.4 ± 6.4	89.3 ± 6.1	100.0 ± 6.7	30.1 ± 5.0	$3.29^{+0.62}_{-0.64}$	$13.55^{+0.12}_{-0.16}$
HerMES J003847.0−021105	HELMS_RED_14	61.0 ± 5.9	75.1 ± 5.6	100.5 ± 7.0	19.7 ± 3.9	$3.42^{+0.59}_{-0.57}$	$13.45^{+0.11}_{-0.13}$
HerMES J011206.7+031417	HELMS_RED_15	54.4 ± 5.8	78.7 ± 5.9	92.2 ± 7.4	17.8 ± 6.3	$3.60^{+0.61}_{-0.59}$	$13.48^{+0.11}_{-0.13}$
HerMES J002959.4+032138	HELMS_RED_16	47.5 ± 5.8	78.7 ± 6.3	100.0 ± 6.5	26.9 ± 5.7	$3.98^{+0.62}_{-0.61}$	$13.57^{+0.09}_{-0.12}$
HerMES J005352.1+023916	HELMS_RED_17	24.6 ± 6.6	39.7 ± 6.4	72.0 ± 6.7	22.5 ± 3.6	$4.47^{+0.78}_{-0.72}$	$13.46^{+0.11}_{-0.12}$
HerMES J000727.1+015626	HELMS_RED_19	53.9 ± 6.1	72.5 ± 6.4	81.6 ± 7.0	40.9 ± 3.4	$3.90^{+0.67}_{-0.65}$	$13.60^{+0.10}_{-0.13}$
HerMES J003909.3+020247	HELMS_RED_21	41.0 ± 5.9	53.5 ± 6.1	74.3 ± 7.5	33.6 ± 4.6	$4.17^{+0.74}_{-0.71}$	$13.55^{+0.11}_{-0.13}$
HerMES J235411.8−082912	HELMS_RED_22	40.9 ± 6.5	57.8 ± 6.2	71.3 ± 6.8	20.6 ± 5.4	$3.80^{+0.69}_{-0.66}$	$13.43^{+0.11}_{-0.13}$
HerMES J004532.6+000121	HELMS_RED_23	48.2 ± 6.7	87.6 ± 6.3	97.2 ± 7.4	42.1 ± 4.9	$4.20^{+0.63}_{-0.61}$	$13.67^{+0.10}_{-0.11}$
HerMES J234805.1−052135	HELMS_RED_25	18.7 ± 5.6	52.0 ± 6.3	65.2 ± 7.3	22.9 ± 3.5	$4.56^{+0.68}_{-0.78}$	$13.46^{+0.09}_{-0.12}$
HerMES J003750.7+003323	HELMS_RED_28	66.4 ± 5.6	85.3 ± 5.9	92.9 ± 6.6	16.2 ± 4.2	$3.25^{+0.55}_{-0.56}$	$13.42^{+0.11}_{-0.13}$
HerMES J232404.6−055123	HELMS_RED_30	51.0 ± 5.9	76.8 ± 6.5	79.1 ± 7.4	33.5 ± 4.3	$3.82^{+0.64}_{-0.61}$	$13.55^{+0.11}_{-0.12}$
HerMES J002737.4−020801	HELMS_RED_31	42.0 ± 6.9	49.4 ± 6.0	75.3 ± 6.9	31.9 ± 3.9	$4.14^{+0.76}_{-0.73}$	$13.53^{+0.11}_{-0.14}$
HerMES J232133.3−040621	HELMS_RED_32	34.3 ± 5.6	63.5 ± 6.3	77.7 ± 7.0	14.4 ± 4.8	$3.89^{+0.61}_{-0.69}$	$13.40^{+0.10}_{-0.14}$
HerMES J004118.5+015537	HELMS_RED_33	34.7 ± 6.0	39.9 ± 6.1	64.4 ± 7.0	17.6 ± 3.5	$3.75^{+0.76}_{-0.76}$	$13.32^{+0.12}_{-0.16}$
HerMES J004302.6+011416	HELMS_RED_35	30.7 ± 6.6	73.7 ± 6.0	77.4 ± 7.3	26.5 ± 3.5	$4.23^{+0.59}_{-0.71}$	$13.52^{+0.08}_{-0.13}$
HerMES J001848.5−061051	HELMS_RED_36	46.6 ± 5.6	61.0 ± 6.2	66.0 ± 6.9	17.4 ± 4.5	$3.43^{+0.66}_{-0.64}$	$13.35^{+0.12}_{-0.15}$
HerMES J005254.9+032931	HELMS_RED_37	55.4 ± 6.0	90.0 ± 6.0	91.3 ± 7.4	30.6 ± 4.5	$3.79^{+0.59}_{-0.58}$	$13.57^{+0.10}_{-0.12}$
HerMES J000400.8−043103	HELMS_RED_38	53.4 ± 5.3	59.5 ± 5.7	67.4 ± 6.9	21.6 ± 4.6	$3.20^{+0.69}_{-0.74}$	$13.36^{+0.14}_{-0.19}$
HerMES J002822.0−021634	HELMS_RED_39	39.8 ± 6.0	54.7 ± 6.1	64.9 ± 6.9	16.2 ± 4.6	$3.61^{+0.68}_{-0.65}$	$13.34^{+0.12}_{-0.14}$
HerMES J234431.9−061852	HELMS_RED_40	59.5 ± 5.6	89.5 ± 5.8	92.2 ± 7.3	39.8 ± 4.5	$3.83^{+0.60}_{-0.59}$	$13.63^{+0.10}_{-0.12}$
HerMES J234647.8+000525	HELMS_RED_41	74.6 ± 5.8	95.4 ± 5.8	100.5 ± 7.0	23.6 ± 3.4	$3.30^{+0.55}_{-0.54}$	$13.50^{+0.11}_{-0.13}$
HerMES J002741.3−011650	HELMS_RED_42	33.1 ± 5.4	59.0 ± 5.7	64.9 ± 6.5	39.5 ± 3.8	$4.53^{+0.75}_{-0.71}$	$13.60^{+0.10}_{-0.12}$
HerMES J004656.1+013751	HELMS_RED_43	36.1 ± 5.8	43.4 ± 5.9	67.6 ± 6.8	28.7 ± 5.3	$4.24^{+0.82}_{-0.76}$	$13.50^{+0.11}_{-0.13}$
HerMES J004237.7+020457	HELMS_RED_45	49.3 ± 6.2	66.1 ± 6.0	87.6 ± 7.3	17.3 ± 5.1	$3.60^{+0.63}_{-0.60}$	$13.43^{+0.11}_{-0.13}$
HerMES J233247.6+003632	HELMS_RED_46	46.3 ± 5.9	72.9 ± 6.0	75.8 ± 6.8	29.4 ± 3.4	$3.84^{+0.63}_{-0.60}$	$13.52^{+0.10}_{-0.12}$
HerMES J003531.5+001536	HELMS_RED_49	52.2 ± 6.3	75.1 ± 5.7	81.7 ± 6.7	26.9 ± 3.8	$3.69^{+0.62}_{-0.60}$	$13.51^{+0.10}_{-0.12}$
HerMES J002937.6+002617	HELMS_RED_50	50.3 ± 6.1	66.8 ± 6.2	67.5 ± 7.1	16.1 ± 3.6	$3.31^{+0.63}_{-0.61}$	$13.33^{+0.13}_{-0.14}$
HerMES J232908.1−050653	HELMS_RED_51	44.3 ± 6.4	69.1 ± 6.1	76.8 ± 7.0	23.2 ± 4.5	$3.80^{+0.63}_{-0.62}$	$13.47^{+0.11}_{-0.12}$
HerMES J232342.0−035109	HELMS_RED_53	34.3 ± 5.6	36.3 ± 6.2	65.9 ± 7.6	19.1 ± 5.0	$3.87^{+0.80}_{-0.83}$	$13.36^{+0.13}_{-0.16}$
HerMES J234522.9+015601	HELMS_RED_54	46.2 ± 6.4	75.1 ± 5.9	79.6 ± 6.9	19.4 ± 3.6	$3.64^{+0.59}_{-0.61}$	$13.43^{+0.11}_{-0.13}$
HerMES J004600.3+065559	HELMS_RED_56	70.6 ± 6.0	85.6 ± 6.9	98.1 ± 7.6	17.9 ± 4.5	$3.23^{+0.57}_{-0.56}$	$13.44^{+0.11}_{-0.15}$
HerMES J001029.7−025524	HELMS_RED_57	32.5 ± 5.6	56.3 ± 5.9	70.6 ± 7.2	15.1 ± 3.3	$3.80^{+0.62}_{-0.66}$	$13.34^{+0.10}_{-0.13}$
HerMES J233943.0−013939	HELMS_RED_58	51.0 ± 6.2	66.8 ± 6.2	81.2 ± 7.1	19.2 ± 3.6	$3.50^{+0.62}_{-0.59}$	$13.41^{+0.11}_{-0.13}$
HerMES J232849.6+010843	HELMS_RED_60	56.0 ± 5.7	95.3 ± 5.7	99.2 ± 6.9	35.3 ± 4.5	$3.92^{+0.58}_{-0.58}$	$13.62^{+0.10}_{-0.11}$
HerMES J001432.9+014530	HELMS_RED_61	60.7 ± 5.9	75.1 ± 5.8	81.5 ± 6.9	27.7 ± 3.4	$3.42^{+0.63}_{-0.63}$	$13.49^{+0.12}_{-0.14}$
HerMES J002319.1+001557	HELMS_RED_62	47.7 ± 5.9	60.9 ± 6.1	78.4 ± 7.3	20.9 ± 3.6	$3.58^{+0.66}_{-0.62}$	$13.42^{+0.11}_{-0.14}$
HerMES J233755.3−053318	HELMS_RED_64	48.4 ± 6.1	61.2 ± 6.5	66.1 ± 7.5	22.0 ± 6.0	$3.45^{+0.70}_{-0.72}$	$13.40^{+0.13}_{-0.16}$
HerMES J000947.0+034432	HELMS_RED_65	39.4 ± 5.6	57.1 ± 5.9	77.4 ± 6.8	22.9 ± 3.3	$3.88^{+0.66}_{-0.60}$	$13.45^{+0.10}_{-0.13}$
HerMES J235922.9−043705	HELMS_RED_67	37.8 ± 6.4	66.0 ± 6.0	67.0 ± 7.8	28.7 ± 4.1	$4.01^{+0.67}_{-0.65}$	$13.49^{+0.11}_{-0.12}$
HerMES J235808.7+005553	HELMS_RED_68	55.4 ± 5.6	73.9 ± 6.1	76.1 ± 6.5	32.7 ± 3.8	$3.60^{+0.63}_{-0.64}$	$13.52^{+0.11}_{-0.14}$
HerMES J000900.6+050709	HELMS_RED_69	36.6 ± 6.2	43.1 ± 6.0	70.2 ± 6.9	44.7 ± 4.8	$5.19^{+0.89}_{-0.92}$	$13.70^{+0.10}_{-0.13}$
HerMES J004019.0+052714	HELMS_RED_71	28.2 ± 5.6	49.8 ± 6.1	63.8 ± 7.1	10.0 ± 3.6	$3.71^{+0.65}_{-0.68}$	$13.25^{+0.11}_{-0.15}$
HerMES J005227.0+020027	HELMS_RED_72	66.9 ± 6.1	71.6 ± 6.2	84.1 ± 7.1	15.7 ± 4.6	$3.04^{+0.66}_{-0.67}$	$13.36^{+0.14}_{-0.19}$
HerMES J001813.6+053159	HELMS_RED_76	70.7 ± 6.0	75.6 ± 6.0	85.6 ± 6.2	17.5 ± 3.7	$3.02^{+0.63}_{-0.64}$	$13.38^{+0.14}_{-0.16}$
HerMES J000056.0+010231	HELMS_RED_77	70.4 ± 6.4	71.2 ± 6.1	84.4 ± 8.3	17.4 ± 4.9	$2.89^{+0.70}_{-0.80}$	$13.35^{+0.15}_{-0.24}$

Table C.1: Flux densities with instrumental errors, redshifts and luminosities of our targets.

Source name	Name	S_{250} [mJy]	S_{350} [mJy]	S_{500} [mJy]	S_{850} [mJy]	phot-z	$\log(L_{FIR}/\mathrm{L}_\odot)$
HerMES J002552.3+031329	HELMS_RED_79	46.6 ± 6.0	65.7 ± 6.1	73.6 ± 6.8	12.0 ± 3.5	$3.32^{+0.60}_{-0.60}$	$13.30^{+0.12}_{-0.14}$
HerMES J005037.1+014449	HELMS_RED_80	44.2 ± 5.7	59.8 ± 6.1	64.5 ± 7.8	25.1 ± 3.7	$3.63^{+0.68}_{-0.69}$	$13.43^{+0.11}_{-0.15}$
HerMES J004724.4+010119	HELMS_RED_82	47.4 ± 6.9	75.8 ± 6.0	76.2 ± 7.6	36.2 ± 5.0	$3.96^{+0.67}_{-0.65}$	$13.57^{+0.11}_{-0.13}$
HerMES J235020.1−065224	HELMS_RED_84	67.5 ± 6.1	82.4 ± 6.5	84.0 ± 7.3	10.3 ± 4.7	$3.02^{+0.57}_{-0.57}$	$13.34^{+0.13}_{-0.15}$
HerMES J233823.1−042924	HELMS_RED_86	48.9 ± 6.5	58.1 ± 6.1	63.2 ± 7.5	22.5 ± 5.8	$3.37^{+0.73}_{-0.78}$	$13.38^{+0.14}_{-0.18}$
HerMES J002058.4+002114	HELMS_RED_88	36.3 ± 5.9	54.2 ± 6.0	63.8 ± 6.8	24.8 ± 3.5	$3.95^{+0.70}_{-0.66}$	$13.44^{+0.11}_{-0.13}$
HerMES J234940.0−025551	HELMS_RED_89	46.0 ± 6.3	58.5 ± 6.5	85.2 ± 6.5	7.4 ± 5.0	$3.37^{+0.65}_{-0.63}$	$13.32^{+0.12}_{-0.14}$
HerMES J010040.6+051550	HELMS_RED_95	52.0 ± 6.4	62.6 ± 6.1	78.9 ± 7.6	18.3 ± 3.8	$3.40^{+0.65}_{-0.64}$	$13.38^{+0.12}_{-0.15}$
HerMES J001533.3−054652	HELMS_RED_96	37.8 ± 6.3	51.6 ± 6.0	63.9 ± 7.1	19.1 ± 3.8	$3.72^{+0.71}_{-0.68}$	$13.36^{+0.13}_{-0.14}$
HerMES J232014.8−045552	HELMS_RED_98	20.4 ± 6.5	34.4 ± 6.0	74.2 ± 7.4	17.8 ± 4.9	$4.58^{+0.82}_{-0.79}$	$13.41^{+0.11}_{-0.13}$
HerMES J235221.4−043114	HELMS_RED_101	33.7 ± 5.7	58.3 ± 5.4	63.7 ± 7.3	17.8 ± 4.4	$3.87^{+0.65}_{-0.66}$	$13.37^{+0.11}_{-0.13}$
HerMES J004526.1+031638	HELMS_RED_104	48.6 ± 5.8	69.4 ± 5.6	76.6 ± 6.9	29.9 ± 4.3	$3.78^{+0.64}_{-0.63}$	$13.52^{+0.10}_{-0.13}$
HerMES J005134.1+053502	HELMS_RED_105	51.9 ± 5.9	61.2 ± 6.3	73.4 ± 7.6	24.8 ± 5.4	$3.46^{+0.68}_{-0.73}$	$13.43^{+0.13}_{-0.16}$
HerMES J232033.8−020958	HELMS_RED_106	56.9 ± 6.3	72.9 ± 6.5	74.8 ± 7.3	23.7 ± 6.4	$3.41^{+0.66}_{-0.67}$	$13.45^{+0.12}_{-0.15}$
HerMES J233052.3−060958	HELMS_RED_107	52.0 ± 6.3	59.6 ± 6.2	80.1 ± 7.3	21.9 ± 4.7	$3.48^{+0.68}_{-0.71}$	$13.42^{+0.12}_{-0.17}$
HerMES J233554.3−054408	HELMS_RED_108	46.6 ± 6.0	72.3 ± 6.6	86.1 ± 7.5	16.6 ± 4.2	$3.61^{+0.59}_{-0.62}$	$13.42^{+0.11}_{-0.13}$
HerMES J000208.8−015521	HELMS_RED_110	42.9 ± 5.7	57.3 ± 6.3	71.8 ± 6.8	20.9 ± 4.7	$3.72^{+0.67}_{-0.64}$	$13.42^{+0.12}_{-0.12}$
HerMES J235003.0−015825	HELMS_RED_114	41.9 ± 6.2	65.6 ± 6.0	77.8 ± 6.7	23.3 ± 4.9	$3.89^{+0.65}_{-0.62}$	$13.48^{+0.10}_{-0.13}$
HerMES J010631.8+015002	HELMS_RED_117	42.9 ± 6.4	46.8 ± 5.7	63.4 ± 7.4	19.0 ± 4.0	$3.42^{+0.77}_{-0.83}$	$13.32^{+0.15}_{-0.19}$
HerMES J003943.5+003955	HELMS_RED_118	32.7 ± 6.1	57.0 ± 6.1	73.7 ± 7.0	23.5 ± 3.9	$4.13^{+0.67}_{-0.65}$	$13.46^{+0.10}_{-0.12}$
HerMES J233208.3−022211	HELMS_RED_119	34.7 ± 6.0	57.5 ± 6.0	75.4 ± 7.0	25.7 ± 6.4	$4.20^{+0.71}_{-0.66}$	$13.51^{+0.10}_{-0.12}$
HerMES J005708.2+023637	HELMS_RED_123	35.1 ± 5.9	55.3 ± 5.8	79.7 ± 6.8	9.7 ± 4.7	$3.68^{+0.66}_{-0.67}$	$13.33^{+0.11}_{-0.15}$
HerMES J000000.7−054310	HELMS_RED_124	51.8 ± 6.6	62.2 ± 6.2	66.9 ± 6.4	21.8 ± 4.3	$3.35^{+0.69}_{-0.73}$	$13.39^{+0.13}_{-0.18}$
HerMES J233521.4−040227	HELMS_RED_126	39.6 ± 6.2	44.6 ± 6.9	63.9 ± 7.7	21.7 ± 4.6	$3.69^{+0.76}_{-0.81}$	$13.37^{+0.13}_{-0.17}$
HerMES J010433.0+044510	HELMS_RED_127	51.7 ± 6.1	62.1 ± 7.0	75.0 ± 8.7	19.7 ± 4.5	$3.38^{+0.68}_{-0.69}$	$13.38^{+0.12}_{-0.17}$
HerMES J235712.0−041341	HELMS_RED_134	53.6 ± 5.8	60.8 ± 5.5	70.4 ± 8.0	20.6 ± 4.0	$3.21^{+0.70}_{-0.76}$	$13.36^{+0.14}_{-0.19}$
HerMES J235833.6−042150	HELMS_RED_135	62.4 ± 6.2	71.8 ± 6.0	81.8 ± 7.3	12.3 ± 4.1	$3.06^{+0.61}_{-0.59}$	$13.32^{+0.13}_{-0.16}$
HerMES J004700.2+004214	HELMS_RED_136	46.6 ± 5.5	63.3 ± 6.0	63.8 ± 7.5	18.5 ± 3.7	$3.43^{+0.64}_{-0.64}$	$13.35^{+0.11}_{-0.15}$
HerMES J004434.7+070159	HELMS_RED_137	35.2 ± 6.2	42.3 ± 6.2	66.0 ± 7.5	17.3 ± 4.1	$3.75^{+0.76}_{-0.76}$	$13.33^{+0.12}_{-0.16}$
HerMES J011130.9+041443	HELMS_RED_139	44.2 ± 6.8	63.4 ± 6.2	64.2 ± 7.9	23.6 ± 4.6	$3.63^{+0.70}_{-0.69}$	$13.42^{+0.12}_{-0.15}$
HerMES J003651.3−015617	HELMS_RED_140	29.8 ± 6.3	51.8 ± 5.7	65.4 ± 7.6	13.5 ± 4.0	$3.84^{+0.66}_{-0.70}$	$13.31^{+0.11}_{-0.14}$
HerMES J233832.1−040953	HELMS_RED_142	27.3 ± 6.2	42.4 ± 6.1	66.7 ± 7.7	22.9 ± 4.7	$4.35^{+0.79}_{-0.72}$	$13.44^{+0.11}_{-0.12}$
HerMES J000407.6−050014	HELMS_RED_143	33.5 ± 6.6	49.4 ± 6.3	73.8 ± 7.4	15.1 ± 4.4	$3.86^{+0.70}_{-0.67}$	$13.36^{+0.11}_{-0.13}$
HerMES J005213.2+000447	HELMS_RED_146	54.3 ± 5.6	80.6 ± 6.2	81.3 ± 7.8	19.2 ± 5.4	$3.52^{+0.59}_{-0.59}$	$13.44^{+0.11}_{-0.12}$
HerMES J003512.0+010758	HELMS_RED_153	59.0 ± 6.0	72.6 ± 6.2	91.4 ± 7.1	12.5 ± 5.4	$3.32^{+0.60}_{-0.59}$	$13.40^{+0.12}_{-0.13}$
HerMES J235157.2−044058	HELMS_RED_154	29.4 ± 5.7	40.2 ± 6.7	63.4 ± 6.8	20.2 ± 4.4	$4.12^{+0.78}_{-0.70}$	$13.40^{+0.12}_{-0.13}$
HerMES J235752.2−040711	HELMS_RED_155	25.4 ± 5.6	40.3 ± 5.9	68.3 ± 6.7	20.1 ± 4.5	$4.38^{+0.77}_{-0.70}$	$13.42^{+0.10}_{-0.12}$
HerMES J233623.2+000108	HELMS_RED_160	54.7 ± 6.2	58.9 ± 6.4	69.2 ± 7.5	10.8 ± 3.5	$2.93^{+0.67}_{-0.73}$	$13.21^{+0.14}_{-0.22}$
HerMES J232847.2−053724	HELMS_RED_161	46.6 ± 6.5	65.7 ± 5.6	67.4 ± 8.0	33.1 ± 4.5	$3.80^{+0.71}_{-0.69}$	$13.51^{+0.11}_{-0.14}$
HerMES J010906.7+052709	HELMS_RED_163	39.2 ± 6.4	51.9 ± 6.0	63.5 ± 8.3	18.6 ± 5.0	$3.63^{+0.74}_{-0.73}$	$13.36^{+0.12}_{-0.16}$
HerMES J004909.5+005712	HELMS_RED_165	25.6 ± 5.9	43.9 ± 5.5	63.1 ± 6.8	11.7 ± 3.9	$3.91^{+0.71}_{-0.71}$	$13.28^{+0.11}_{-0.14}$
HerMES J235924.0−075406	HELMS_RED_169	30.5 ± 6.8	54.6 ± 6.3	65.0 ± 7.3	17.2 ± 4.0	$3.92^{+0.68}_{-0.69}$	$13.37^{+0.11}_{-0.13}$
HerMES J004623.3+000425	HELMS_RED_173	27.4 ± 5.8	31.1 ± 5.9	64.7 ± 7.1	16.2 ± 3.6	$4.05^{+0.84}_{-0.78}$	$13.31^{+0.13}_{-0.15}$
HerMES J000326.9−041214	HELMS_RED_174	19.4 ± 5.9	56.1 ± 6.3	68.4 ± 7.5	12.8 ± 4.5	$4.20^{+0.63}_{-0.81}$	$13.37^{+0.10}_{-0.15}$
HerMES J233254.6+001616	HELMS_RED_179	62.5 ± 6.3	66.3 ± 6.3	75.4 ± 7.8	10.8 ± 3.2	$2.81^{+0.63}_{-0.68}$	$13.22^{+0.15}_{-0.20}$
HerMES J233927.1−052258	HELMS_RED_180	51.4 ± 6.1	59.4 ± 5.9	66.9 ± 7.9	18.1 ± 4.3	$3.21^{+0.71}_{-0.76}$	$13.33^{+0.14}_{-0.19}$
HerMES J004120.1+015220	HELMS_RED_183	44.4 ± 6.0	65.3 ± 6.4	67.5 ± 7.2	21.5 ± 3.6	$3.63^{+0.64}_{-0.63}$	$13.41^{+0.10}_{-0.14}$
HerMES J235818.3−081029	HELMS_RED_188	45.8 ± 5.5	76.4 ± 5.6	77.0 ± 6.5	26.9 ± 5.6	$3.85^{+0.62}_{-0.60}$	$13.51^{+0.10}_{-0.12}$
HerMES J010733.0+042228	HELMS_RED_191	46.1 ± 6.1	69.3 ± 5.7	80.7 ± 8.1	15.7 ± 4.3	$3.55^{+0.61}_{-0.61}$	$13.38^{+0.11}_{-0.13}$
HerMES J003846.3−033526	HELMS_RED_196	54.7 ± 5.9	63.4 ± 5.7	68.5 ± 6.6	16.3 ± 3.4	$3.16^{+0.66}_{-0.67}$	$13.32^{+0.13}_{-0.17}$
HerMES J235320.4−054743	HELMS_RED_202	35.3 ± 5.7	49.6 ± 6.3	66.3 ± 7.6	13.7 ± 4.5	$3.69^{+0.69}_{-0.66}$	$13.31^{+0.12}_{-0.15}$
HerMES J232711.4−051505	HELMS_RED_206	57.2 ± 6.0	64.8 ± 6.2	75.4 ± 6.8	11.7 ± 4.2	$3.09^{+0.63}_{-0.62}$	$13.29^{+0.12}_{-0.17}$
HerMES J010510.0+044223	HELMS_RED_212	41.3 ± 6.5	54.5 ± 5.8	72.0 ± 7.5	27.5 ± 4.3	$3.91^{+0.72}_{-0.70}$	$13.48^{+0.12}_{-0.14}$
HerMES J001134.9+002738	HELMS_RED_219	46.9 ± 5.6	69.4 ± 6.2	69.7 ± 6.4	23.4 ± 4.4	$3.66^{+0.63}_{-0.61}$	$13.44^{+0.11}_{-0.13}$
HerMES J234106.3−061457	HELMS_RED_223	56.5 ± 6.7	76.7 ± 6.4	83.3 ± 7.3	17.8 ± 4.2	$3.40^{+0.59}_{-0.59}$	$13.41^{+0.11}_{-0.14}$
HerMES J235900.9−062939	HELMS_RED_224	48.2 ± 5.7	54.9 ± 6.2	67.0 ± 7.1	14.9 ± 4.0	$3.24^{+0.69}_{-0.72}$	$13.29^{+0.14}_{-0.19}$
HerMES J235647.0−023312	HELMS_RED_226	29.6 ± 5.7	58.3 ± 5.5	69.2 ± 7.6	20.9 ± 5.1	$4.16^{+0.67}_{-0.69}$	$13.44^{+0.10}_{-0.13}$
HerMES J233838.8+000032	HELMS_RED_228	58.4 ± 5.9	61.9 ± 5.8	67.7 ± 6.9	10.6 ± 3.4	$2.84^{+0.65}_{-0.71}$	$13.21^{+0.15}_{-0.21}$

Table C.1

Source name	Name	S_{250} [mJy]	S_{350} [mJy]	S_{500} [mJy]	S_{850} [mJy]	phot-z	$\log(L_{FIR}/\mathrm{L}_\odot)$
HerMES J002012.1−044523	HELMS_RED_232	44.0 ± 6.2	57.9 ± 6.2	67.4 ± 7.1	20.4 ± 4.1	$3.58^{+0.68}_{-0.67}$	$13.39^{+0.11}_{-0.15}$
HerMES J234707.6+021633	HELMS_RED_235	55.7 ± 6.4	59.4 ± 6.2	67.5 ± 6.6	23.4 ± 3.5	$3.15^{+0.72}_{-0.74}$	$13.37^{+0.14}_{-0.20}$
HerMES J233123.5+000631	HELMS_RED_241	60.3 ± 6.4	71.2 ± 6.8	71.5 ± 7.1	14.3 ± 4.5	$3.08^{+0.63}_{-0.64}$	$13.32^{+0.12}_{-0.17}$
HerMES J234247.3−024555	HELMS_RED_242	60.0 ± 6.6	80.7 ± 5.9	81.0 ± 7.6	13.3 ± 4.6	$3.22^{+0.58}_{-0.59}$	$13.37^{+0.12}_{-0.14}$
HerMES J235512.7−045840	HELMS_RED_249	39.1 ± 5.9	69.2 ± 6.5	73.3 ± 7.7	17.8 ± 4.8	$3.79^{+0.61}_{-0.65}$	$13.41^{+0.10}_{-0.13}$
HerMES J002057.1+051242	HELMS_RED_251	42.5 ± 6.1	46.0 ± 6.0	65.4 ± 7.0	16.4 ± 3.7	$3.37^{+0.75}_{-0.80}$	$13.30^{+0.14}_{-0.20}$
HerMES J003743.6−011423	HELMS_RED_255	48.0 ± 6.2	53.1 ± 5.9	64.4 ± 7.4	16.8 ± 3.4	$3.20^{+0.73}_{-0.80}$	$13.29^{+0.15}_{-0.21}$
HerMES J001618.9−040118	HELMS_RED_258	48.7 ± 6.3	68.0 ± 6.1	90.6 ± 7.1	11.4 ± 4.4	$3.44^{+0.59}_{-0.61}$	$13.36^{+0.11}_{-0.14}$
HerMES J001936.8+025855	HELMS_RED_262	51.6 ± 5.9	63.7 ± 6.3	67.3 ± 7.3	16.6 ± 3.6	$3.26^{+0.64}_{-0.66}$	$13.33^{+0.13}_{-0.16}$
HerMES J005557.4+063518	HELMS_RED_264	54.6 ± 6.5	61.7 ± 6.3	73.5 ± 7.3	6.8 ± 6.1	$3.11^{+0.67}_{-0.67}$	$13.28^{+0.14}_{-0.17}$
HerMES J000831.4+035303	HELMS_RED_266	44.6 ± 6.3	65.7 ± 5.5	69.9 ± 7.1	11.0 ± 3.2	$3.29^{+0.58}_{-0.61}$	$13.27^{+0.11}_{-0.14}$
HerMES J001732.5+031559	HELMS_RED_267	46.5 ± 5.9	59.2 ± 5.8	64.6 ± 8.2	17.5 ± 3.7	$3.35^{+0.68}_{-0.69}$	$13.33^{+0.13}_{-0.17}$
HerMES J004919.4+012439	HELMS_RED_268	53.9 ± 6.2	54.4 ± 6.1	69.7 ± 6.7	21.3 ± 5.7	$3.16^{+0.75}_{-0.79}$	$13.36^{+0.15}_{-0.21}$
HerMES J234220.9−045604	HELMS_RED_269	50.9 ± 6.4	55.3 ± 5.9	67.1 ± 6.8	26.8 ± 4.5	$3.39^{+0.74}_{-0.75}$	$13.41^{+0.14}_{-0.18}$
HerMES J235830.9+005631	HELMS_RED_270	47.8 ± 5.7	62.3 ± 5.8	63.8 ± 7.0	31.5 ± 4.8	$3.64^{+0.72}_{-0.69}$	$13.47^{+0.12}_{-0.15}$
HerMES J003819.5+064505	HELMS_RED_272	47.7 ± 5.8	61.5 ± 6.0	64.4 ± 6.5	13.7 ± 3.9	$3.29^{+0.63}_{-0.62}$	$13.29^{+0.12}_{-0.16}$
HerMES J002943.2+010330	HELMS_RED_277	53.0 ± 5.8	63.7 ± 6.3	67.3 ± 8.0	17.6 ± 3.6	$3.20^{+0.67}_{-0.70}$	$13.33^{+0.13}_{-0.18}$
HerMES J010231.1+005416	HELMS_RED_279	55.1 ± 6.3	61.6 ± 6.2	83.2 ± 7.5	10.5 ± 4.6	$3.16^{+0.65}_{-0.64}$	$13.30^{+0.13}_{-0.17}$
HerMES J232606.3−023610	HELMS_RED_283	34.6 ± 6.8	61.5 ± 5.8	65.6 ± 7.6	11.4 ± 4.6	$3.63^{+0.63}_{-0.68}$	$13.32^{+0.10}_{-0.15}$
HerMES J004811.1+000810	HELMS_RED_287	47.9 ± 6.1	48.6 ± 6.4	63.8 ± 6.9	18.4 ± 4.1	$3.17^{+0.76}_{-0.82}$	$13.30^{+0.16}_{-0.21}$
HerMES J234046.8−051205	HELMS_RED_288	38.5 ± 6.7	44.9 ± 6.3	67.9 ± 7.2	16.8 ± 4.3	$3.65^{+0.76}_{-0.76}$	$13.33^{+0.13}_{-0.16}$
HerMES J002625.4+024405	HELMS_RED_290	31.3 ± 6.3	56.7 ± 6.1	65.8 ± 7.2	16.6 ± 3.7	$3.88^{+0.65}_{-0.68}$	$13.36^{+0.10}_{-0.14}$
HerMES J002148.7+013522	HELMS_RED_293	30.8 ± 6.1	58.1 ± 5.9	68.5 ± 7.1	15.4 ± 3.9	$3.89^{+0.63}_{-0.69}$	$13.36^{+0.10}_{-0.14}$
HerMES J233159.8−025408	HELMS_RED_301	26.6 ± 7.2	48.4 ± 6.2	64.5 ± 7.2	18.2 ± 4.5	$4.14^{+0.74}_{-0.72}$	$13.39^{+0.11}_{-0.14}$
HerMES J003706.2+011634	HELMS_RED_309	31.8 ± 5.9	63.5 ± 6.3	70.3 ± 7.0	21.8 ± 3.6	$4.07^{+0.63}_{-0.67}$	$13.45^{+0.10}_{-0.12}$
HerMES J010151.9+000822	HELMS_RED_314	42.1 ± 6.4	68.4 ± 6.5	69.5 ± 6.7	21.2 ± 5.3	$3.78^{+0.64}_{-0.63}$	$13.43^{+0.10}_{-0.13}$
HerMES J004808.8+040359	HELMS_RED_315	47.4 ± 5.8	65.3 ± 5.8	66.4 ± 7.1	13.5 ± 4.3	$3.34^{+0.62}_{-0.61}$	$13.31^{+0.11}_{-0.14}$
HerMES J000154.4−031845	HELMS_RED_318	33.0 ± 5.4	47.5 ± 5.6	64.4 ± 7.0	8.7 ± 4.5	$3.58^{+0.68}_{-0.67}$	$13.24^{+0.11}_{-0.15}$
HerMES J232656.9−043112	HELMS_RED_319	33.6 ± 6.6	42.5 ± 6.1	63.6 ± 7.7	20.7 ± 4.6	$3.95^{+0.80}_{-0.79}$	$13.38^{+0.12}_{-0.16}$
HerMES J232658.4−021900	HELMS_RED_320	60.5 ± 6.2	60.9 ± 6.0	77.1 ± 7.1	16.3 ± 4.8	$3.01^{+0.71}_{-0.82}$	$13.33^{+0.15}_{-0.23}$
HerMES J003527.5+002227	HELMS_RED_323	51.2 ± 5.8	61.8 ± 6.2	70.3 ± 7.1	27.3 ± 5.8	$3.51^{+0.68}_{-0.73}$	$13.45^{+0.13}_{-0.16}$
HerMES J232856.6−041652	HELMS_RED_324	75.5 ± 6.3	80.0 ± 5.8	80.6 ± 6.8	22.4 ± 4.5	$2.92^{+0.67}_{-0.76}$	$13.41^{+0.15}_{-0.22}$
HerMES J234656.1+002246	HELMS_RED_326	36.3 ± 5.9	58.1 ± 5.9	67.8 ± 7.4	25.0 ± 3.7	$4.00^{+0.68}_{-0.64}$	$13.46^{+0.11}_{-0.12}$
HerMES J233254.7−060301	HELMS_RED_331	42.1 ± 7.4	60.0 ± 5.6	64.0 ± 8.5	10.7 ± 4.7	$3.35^{+0.66}_{-0.67}$	$13.28^{+0.12}_{-0.16}$
HerMES J232414.9−025250	HELMS_RED_333	67.4 ± 5.5	70.8 ± 6.0	74.3 ± 7.2	20.4 ± 4.8	$2.91^{+0.68}_{-0.77}$	$13.36^{+0.15}_{-0.22}$
HerMES J232057.2−044412	HELMS_RED_335	50.9 ± 6.4	63.8 ± 6.2	70.0 ± 7.1	23.7 ± 5.1	$3.47^{+0.68}_{-0.70}$	$13.43^{+0.13}_{-0.16}$
HerMES J001242.5−042634	HELMS_RED_336	53.8 ± 5.9	57.4 ± 5.8	64.4 ± 6.6	9.1 ± 3.6	$2.87^{+0.67}_{-0.72}$	$13.18^{+0.16}_{-0.21}$
HerMES J005008.5+024618	HELMS_RED_339	52.1 ± 6.3	55.6 ± 5.8	64.5 ± 8.1	19.7 ± 4.9	$3.10^{+0.75}_{-0.80}$	$13.32^{+0.15}_{-0.22}$
HerMES J003306.4+030116	HELMS_RED_342	39.5 ± 6.0	53.4 ± 5.9	68.2 ± 7.0	8.7 ± 4.5	$3.41^{+0.66}_{-0.64}$	$13.25^{+0.12}_{-0.15}$
HerMES J235955.2−032724	HELMS_RED_348	44.5 ± 5.6	50.4 ± 5.9	68.4 ± 6.4	10.8 ± 3.8	$3.25^{+0.67}_{-0.66}$	$13.24^{+0.13}_{-0.16}$
HerMES J000742.7+051438	HELMS_RED_350	49.7 ± 5.7	59.4 ± 5.8	65.1 ± 6.8	12.4 ± 3.3	$3.13^{+0.64}_{-0.63}$	$13.57^{+0.12}_{-0.17}$
HerMES J002223.9+025047	HELMS_RED_353	31.6 ± 6.0	46.7 ± 6.5	65.8 ± 7.2	24.1 ± 4.1	$4.15^{+0.75}_{-0.69}$	$13.25^{+0.11}_{-0.13}$
HerMES J003446.0+045549	HELMS_RED_368	44.6 ± 6.4	55.4 ± 6.2	74.0 ± 7.5	24.4 ± 3.7	$3.71^{+0.69}_{-0.70}$	$13.44^{+0.12}_{-0.15}$
HerMES J234723.5−015213	HELMS_RED_369	41.7 ± 5.5	49.1 ± 5.8	63.4 ± 7.1	18.0 ± 4.7	$3.47^{+0.72}_{-0.75}$	$13.44^{+0.14}_{-0.18}$
HerMES J003931.4+014822	HELMS_RED_373	53.6 ± 5.9	70.6 ± 6.2	79.7 ± 7.5	18.5 ± 3.7	$3.42^{+0.61}_{-0.58}$	$13.33^{+0.12}_{-0.13}$
HerMES J005016.4+055923	HELMS_RED_377	51.5 ± 5.6	61.8 ± 6.5	71.0 ± 7.2	24.1 ± 4.7	$3.43^{+0.67}_{-0.71}$	$13.39^{+0.12}_{-0.18}$
HerMES J233755.0−051000	HELMS_RED_379	60.3 ± 6.5	82.0 ± 6.3	85.3 ± 7.8	19.6 ± 4.9	$3.40^{+0.59}_{-0.58}$	$13.42^{+0.11}_{-0.14}$
HerMES J232933.2+003149	HELMS_RED_385	26.7 ± 5.7	34.8 ± 6.1	68.7 ± 7.5	15.6 ± 4.5	$4.11^{+0.81}_{-0.73}$	$13.44^{+0.12}_{-0.13}$
HerMES J232101.9−033260	HELMS_RED_387	37.5 ± 5.9	49.5 ± 5.9	64.6 ± 6.9	11.5 ± 4.8	$3.56^{+0.69}_{-0.67}$	$13.34^{+0.12}_{-0.14}$
HerMES J001016.5−032131	HELMS_RED_389	40.8 ± 6.1	61.3 ± 6.0	65.0 ± 7.2	20.0 ± 3.7	$3.68^{+0.65}_{-0.64}$	$13.28^{+0.11}_{-0.14}$
HerMES J235712.3+022917	HELMS_RED_390	47.0 ± 6.3	55.0 ± 6.3	68.0 ± 7.9	19.5 ± 5.1	$3.42^{+0.72}_{-0.77}$	$13.39^{+0.14}_{-0.18}$
HerMES J001251.7+061210	HELMS_RED_399	78.2 ± 5.8	79.6 ± 6.4	81.8 ± 6.6	23.3 ± 4.4	$2.85^{+0.67}_{-0.75}$	$13.36^{+0.15}_{-0.23}$
HerMES J234602.1+001736	HELMS_RED_402	46.9 ± 6.6	48.1 ± 6.2	64.6 ± 7.2	18.9 ± 3.4	$3.25^{+0.76}_{-0.83}$	$13.41^{+0.14}_{-0.22}$
HerMES J010735.0+032259	HELMS_RED_403	49.1 ± 6.7	52.8 ± 6.1	64.1 ± 7.7	15.0 ± 5.4	$3.14^{+0.77}_{-0.86}$	$13.31^{+0.15}_{-0.23}$
HerMES J234612.3−054812	HELMS_RED_405	23.0 ± 5.5	47.6 ± 6.0	64.2 ± 8.1	8.7 ± 4.6	$3.91^{+0.68}_{-0.75}$	$13.28^{+0.11}_{-0.15}$
HerMES J004414.7+002550	HELMS_RED_420	27.4 ± 6.0	55.6 ± 5.9	68.5 ± 7.6	16.2 ± 3.6	$3.99^{+0.64}_{-0.70}$	$13.27^{+0.10}_{-0.13}$
HerMES J000127.4−010614	HELMS_RED_421	65.4 ± 6.3	69.1 ± 5.9	72.5 ± 7.3	18.5 ± 4.8	$2.93^{+0.70}_{-0.79}$	$13.37^{+0.15}_{-0.23}$
HerMES J004055.2+021131	HELMS_RED_423	45.7 ± 6.1	57.5 ± 5.9	66.0 ± 7.1	22.1 ± 3.5	$3.52^{+0.69}_{-0.71}$	$13.34^{+0.13}_{-0.16}$

Table C.1

Source name	Name	S_{250} [mJy]	S_{350} [mJy]	S_{500} [mJy]	S_{850} [mJy]	phot-z	$\log(L_{FIR}/\mathrm{L}_{\odot})$
HerMES J003136.0−011856	HELMS_RED_428	39.9 ± 6.0	52.6 ± 6.0	64.5 ± 6.4	14.9 ± 4.1	$3.54^{+0.68}_{-0.65}$	$13.39^{+0.12}_{-0.14}$
HerMES J002414.5+035239	HELMS_RED_430	47.8 ± 6.1	52.1 ± 6.3	64.9 ± 7.2	12.1 ± 3.8	$3.09^{+0.72}_{-0.77}$	$13.32^{+0.14}_{-0.22}$
HerMES J233857.1−034441	HELMS_RED_434	59.2 ± 5.6	65.1 ± 5.8	65.7 ± 7.0	16.4 ± 4.4	$2.97^{+0.69}_{-0.76}$	$13.23^{+0.15}_{-0.22}$
HerMES J002000.9−060219	HELMS_RED_440	49.4 ± 6.2	71.7 ± 5.8	76.9 ± 7.2	10.0 ± 4.3	$3.29^{+0.59}_{-0.60}$	$13.30^{+0.12}_{-0.14}$
HerMES J232909.1+003450	HELMS_RED_441	38.0 ± 6.4	50.6 ± 5.9	76.0 ± 7.9	20.2 ± 3.3	$3.83^{+0.71}_{-0.66}$	$13.32^{+0.11}_{-0.14}$
HerMES J232249.3−024437	HELMS_RED_443	52.1 ± 5.9	54.8 ± 6.3	66.9 ± 7.4	21.0 ± 4.7	$3.17^{+0.73}_{-0.78}$	$13.40^{+0.15}_{-0.20}$
HerMES J002824.0−013329	HELMS_RED_447	47.2 ± 5.5	60.1 ± 5.8	69.5 ± 6.6	14.0 ± 3.9	$3.34^{+0.63}_{-0.61}$	$13.34^{+0.11}_{-0.14}$
HerMES J000823.4+012423	HELMS_RED_448	43.7 ± 6.2	58.1 ± 6.7	63.9 ± 6.6	12.5 ± 3.3	$3.32^{+0.63}_{-0.62}$	$13.31^{+0.13}_{-0.14}$
HerMES J234547.9−054412	HELMS_RED_449	52.0 ± 6.7	59.4 ± 6.2	70.7 ± 7.7	19.4 ± 5.2	$3.30^{+0.73}_{-0.78}$	$13.26^{+0.14}_{-0.20}$
HerMES J232619.7−050855	HELMS_RED_451	49.2 ± 6.5	61.3 ± 6.4	65.3 ± 8.1	20.0 ± 4.6	$3.36^{+0.70}_{-0.73}$	$13.37^{+0.13}_{-0.17}$
HerMES J003753.1+050029	HELMS_RED_452	47.5 ± 7.1	61.5 ± 6.0	68.2 ± 7.2	12.1 ± 3.4	$3.22^{+0.63}_{-0.63}$	$13.36^{+0.13}_{-0.15}$
HerMES J233351.1−035745	HELMS_RED_458	54.9 ± 6.2	61.3 ± 6.3	79.6 ± 7.1	8.0 ± 4.7	$3.09^{+0.64}_{-0.63}$	$13.26^{+0.13}_{-0.17}$
HerMES J001638.5+042328	HELMS_RED_463	31.8 ± 6.2	46.5 ± 6.3	63.5 ± 6.8	12.0 ± 3.7	$3.68^{+0.69}_{-0.68}$	$13.27^{+0.11}_{-0.15}$
HerMES J010438.2+002613	HELMS_RED_472	42.4 ± 6.0	55.8 ± 6.3	64.7 ± 7.1	16.9 ± 3.8	$3.51^{+0.68}_{-0.66}$	$13.27^{+0.13}_{-0.15}$

Table C.1